

**Shaft Resistance of Driven Piles  
in Overconsolidated Cohesionless Soils**

Yasir Mohammed Alharthi

A Thesis  
In the Department  
of  
Building, Civil, and Environmental Engineering

Presented in Partial Fulfilment of the Requirements  
For the Degree of  
Doctor of Philosophy (Civil Engineering) at  
Concordia University  
Montreal, Quebec, Canada

April 2018

© Yasir Mohammed Alharthi, 2018

**CONCORDIA UNIVERSITY**

**School of Graduate Studies**

This is to certify the thesis prepared

By: **Yasir Mohammed Alharthi**

Entitled: **Shaft Resistance of Driven Piles in Overconsolidated Cohesionless Soils**

and submitted in partial fulfillment of the requirements for the degree of

**Doctor of Philosophy (Civil Engineering)**

complies with the regulations of the University and meets with the accepted standards with respect to originality and quality.

Signed by the final examining committee:

\_\_\_\_\_ Chair  
Dr. G. Gopakumar

\_\_\_\_\_ External Examiner  
Dr. S. Vanapalli

\_\_\_\_\_ External to program  
Dr. M. Mannan

\_\_\_\_\_ Examiner  
Dr. K. Galal

\_\_\_\_\_ Examiner  
Dr. A. Zsaki

\_\_\_\_\_ Supervisor  
Dr. A. Hanna

Approved by \_\_\_\_\_  
Dr. A. Bagchi, Chair, Department of Building, Civil & Environmental Engineering

July 26, 2018

\_\_\_\_\_  
Dr. A. Asif  
Dean, Faculty of Engineering and Computer Science

# **Abstract**

## **Shaft resistance of driven piles in overconsolidated cohesionless soils**

**Yasir Mohammed Alharthi, Ph.D.**  
**Concordia University, 2018**

Piles are structural members that transfer the applied load of superstructures to deep supportive layers of soil or bedrock. Besides controlling the settlement of structures, piles provide sufficient capacity that other foundations cannot provide or provide only at a high cost. Despite ample research on the shaft resistance of displacement piles in cohesionless soils, the mechanism of such resistance remains unclear. Consequently, theories on shaft resistance have generated several discrepancies in predicting the capacity of displacement piles in cohesionless soils, not only due to the complexity of modeling cohesionless materials and collecting field data but also because the role of overconsolidation in such soils, which is often neglected. Although the critical depth of pile foundation in cohesionless soils has long been debated, definite conclusions have yet to be drawn.

Overconsolidation in cohesionless soils directly affects the lateral earth pressure that acts upon the pile shafts and thus upon pile capacity. Overconsolidation can occur naturally or artificially when the ground surface is subjected to erosion, excavation, or unloading, often due to glacial melting, the demolition of structures, raised water tables, compaction, or vibration.

This thesis presents an experimental investigation into the capacity of driven piles in overconsolidated cohesionless soils. Tests, with an emphasis on the shaft resistance and the critical depth, were conducted on long piles in a setup that permits measuring the overconsolidation ratio in the test tank as well as the total and local shaft resistance on the pile's shaft. Shear stress distribution along the pile's shaft showed some dependency on embedment depth ratio ( $L / D$ ). Also, critical depth

was observed for shaft resistance only when mean shaft resistance was analyzed, and was in line with Meyerhof's (1976) results.

An analytical model was also developed based on limit equilibrium analysis using the horizontal slice method to predict the shaft resistance of a pile driven into normally consolidated cohesionless soils. The model assumes an inclined failure surface around the pile that accounts for the shear and normal stresses upon it. Critical depth was not only observed but also increased linearly as the angle of shearing resistance increased. A three-dimensional numerical model was developed and validated experimentally to perform 200 pile load tests in soils with various densities and at a range of embedment depths.

Design theories to predict the shaft resistance of displacement piles in cohesionless soils and the critical depth were developed, design charts are presented.

## **Acknowledgement**

All praise and thanks are due to the Almighty Allah who always guides me to the right path and has helped me to complete this thesis. Throughout my Ph.D. program, I have been blessed with support and friendship of many whose guidance, companionship, insights and advices have tremendously enlightened my way.

First and foremost, I would like to express my deepest gratitude to my supervisor Dr. Adel M. Hanna for his consistent support, guidance, encouragement, and immense knowledge. I have been fortunate to have him as a supervisor, and without him this dissertation would not have been successful.

Also, I would like to thank the technical staff at Concordia University, including Mr. Riccardo Gioia, Mr. Joseph Hrib, and Mr. Luc Demers, for the consultation and technical assistance. My sincere thanks also goes to my dear colleagues and friends at Concordia University, especially Mahmoud Khalifa, for the many discussions that helped me a lot to advance in my research.

I extend my most gratefulness to my parents for their care and countless prayers. Moreover, I would like to thank my wife, for her extreme support and patience, without which I would not have accomplished my degree successfully. Besides, I would like to thank my daughter and my son for adding joy into my life, and giving me more reasons to work hard.

Special thanks are due to Taif University for granting me a full scholarship to gain my Ph.D. degree, and for supporting the research financially. I also would like to thank the Saudi Arabian Cultural Bureau in Canada and its staff for their unlimited support.

# Table of Contents

List of Tables .....	x
List of Figures .....	xii
List of Symbols .....	xxi
Chapter 1 : Introduction .....	1
1.1 General .....	1
1.2 Problem Definition and Motivation .....	2
1.3 Research Objectives .....	4
1.4 Organization of Thesis .....	6
Chapter 2 : Literature Review .....	8
2.1 General .....	8
2.2 Pile Capacity .....	8
2.2.1 Failure Mechanism .....	10
2.2.2 Tip Resistance ( $Q_T$ ) .....	11
2.2.3 Shaft Resistance ( $Q_S$ ) .....	14
2.2.4 Critical Depth in Piles .....	17
2.2.5 The Mobilized Lateral Earth Pressure Coefficient ( $K_s$ ) .....	20
2.2.6 Pile – Soil Interface Angle ( $\delta$ ) .....	26
2.3 Measurement of Overconsolidation Ratio (OCR) .....	34
2.4 Effect of OCR on Pile Capacity .....	36

2.5 Discussion .....	47
Chapter 3 : Experimental Investigation.....	50
3.1 General.....	50
3.2. Testing Setup .....	53
3.3 Soil Testing.....	55
3.4 Sand Preparation .....	58
3.4.1 Sand-Placing Technique .....	59
3.4.2 Test Results.....	64
3.4.3 Results Analysis.....	70
3.5 Pile Load Testing .....	78
3.5.1 Pile Models .....	78
3.5.2 Testing Procedure and Program.....	82
3.5.3 Test Results.....	86
3.5.4 Repeatability .....	109
3.6 Summary of Pile Load Test Results.....	111
Chapter 4 : Analysis of Results .....	114
4.1 General.....	114
4.2 Ultimate Load .....	114
4.3 Tip Resistance.....	115
4.4 Total Shaft Resistance.....	120

4.4.1 $K_s$ Values .....	123
4.4.2 $\beta$ Values .....	125
4.4.3 ( $K_s/K_0$ ) Values .....	127
4.5 Shear Stress Distribution.....	129
4.5.1 Local Shear Stress.....	129
4.5.2 Lateral Earth Pressure Coefficient at Failure ( $K_s$ ).....	135
4.5.3 Lateral Earth Pressure (LEP).....	141
4.6 Experimental Critical Depth.....	147
4.7 Comparison with Proposed Values in the Literature .....	150
4.8 Empirical Model .....	152
4.8.1 Model Development.....	152
4.8.2 Validation.....	156
4.8.3 Design Procedure.....	158
4.8.4 Design Example.....	159
Chapter 5 : Analytical Model.....	162
5.1 General.....	162
5.2 Model Development.....	163
5.3 Data Analysis .....	176
5.4 Results of Analysis .....	180
5.5 Design Procedure .....	182

5.6 Validation.....	182
5.7 Critical Depth.....	184
5.8 Discussion.....	186
Chapter 6 : Numerical Investigation .....	188
6.1 General.....	188
6.2 Model Development.....	189
6.3 Model Validation .....	204
6.4 Pile Load Tests.....	210
6.5 Analysis.....	216
6.6 Design Charts.....	222
6.7 Validation.....	227
Chapter 7 : Conclusion and Recommendations .....	230
7.1 General.....	230
7.2 Conclusion .....	230
7.3 Recommendation for Future Work .....	233
References .....	234

## List of Tables

Table 2-1: Values of earth pressure coefficient $K_S$ and Pile-Soil friction angle $\delta z$ for different relative densities, after Broms (1966).....	23
Table 2-2: Recommended values for $K_S$ .....	24
Table 2-3: Ratio of $K_S/K_0$ suggested by different researchers .....	26
Table 2-4: Interface angle between the pile material and sand.....	27
Table 2-5: Proposed design parameters and API RP 2A design criteria after Foray et al. (1998) .....	39
Table 2-6: Pile load test for 50.8 mm diameter model pile, after DiCamillo (2014) .....	46
Table 3-1: Silica sand properties.....	56
Table 3-2: Relative density and corresponding angle of shearing resistance .....	57
Table 3-3: Test results for sand at a relative density of 30 %.....	65
Table 3-4: Test results for sand at a relative density of 45 %.....	65
Table 3-5: Test results for sand at a relative density of 60 %.....	66
Table 3-6: Experimental values of OCR.....	67
Table 3-7: Test results: lateral earth pressure coefficient .....	68
Table 3-8: (D/B) Ratios for different experimental investigations.....	81
Table 3-9: Pile load testing program for pile model of 55 mm diameter .....	85
Table 3-10: Pile load testing program for pile model of 30 mm diameter .....	85
Table 3-11: Summary of ultimate, tip and shaft resistance for pile model of 55 mm .....	111
Table 3-12: Section lengths for pile model of 55 mm diameter .....	112
Table 3-13: Summary of the shaft resistance for each section for pile model of 55 mm diameter ..	112
Table 3-14: Summary of ultimate, tip and shaft resistance for pile model of 30 mm .....	113
Table 4-1: Experimental ratio of shaft resistance to ultimate pile load ( $Q_s / Q_u$ ).....	122

Table 4-2: Experimental ratio of pile displacement at peak shaft resistance to pile diameter ( $W_s / D$ )	122
Table 4-3: Local shear stress for pile diameter of 55 mm	130
Table 4-4: Illustration of the calculation steps for the pile load test reported by Beringen et al. (1979)	161
Table 5-1: Summary of the database for pile load tests in sand	178
Table 5-2: Independent database of field pile load tests for validation	183
Table 5-3: The results of the validation database	183
Table 5-4: Shaft resistance of 55 mm pile model at normally consolidated sand	187
Table 6-1: Mesh analysis for X and Y directions	200
Table 6-2: Mesh analysis for Z directions	202
Table 6-3: Factors for Eq.6-7 after (Coduto, 2001)	205
Table 6-4: Material properties	205
Table 6-5: Numerical results and comparison with experimental results using different $K_S$ values	208
Table 6-6: Numerical results and comparison with experimental results using an average $K_S$ values	209
Table 6-7: Soil properties of the sand used for pile load test	211
Table 6-8: Shaft resistance with variable values of $\beta$ for embedment depth ratio (L/D) of 5	212
Table 6-9: Shaft resistance with variable values of $\beta$ for embedment depth ratio (L/D) of 8	213
Table 6-10: Shaft resistance with variable values of $\beta$ for embedment depth ratio (L/D) of 10	214
Table 6-11: Shaft resistance with variable values of $\beta$ for embedment depth ratio (L/D) of 13	215
Table 6-12: Error between the predicted and actual $\beta$ values for the pile model of 30 mm diameter	229

## List of Figures

Figure 1-1 Distribution of $Q_c / Q_m$ with respect to embedment depth ( $L/D$ ), after Jardine et al. (2005) .....	5
Figure 2-1: Component of the pile's capacity.....	9
Figure 2-2: Bearing capacity shear failure modes, after Vesic (1973) adopted from Das (2011).....	11
Figure 2-3: Bearing capacity factors for deep circular foundations after, Prakash and Sharma (1990) .....	13
Figure 2-4: Assumed Failure Patterns under deep foundations, adopted from Prakash & Sharma (1990); (a) after Prandtl, Reissner, Caquot, Busiman, Terzaghi (b) After DeBeer, Jaky, Meyerhof (c) After Berezantsev and Yaroshenko, Vesic (d) After Bishop, Hill and Mott, Skempton, Yassin, and Gibson.....	15
Figure 2-5: Distribution of local unit skin friction, $f_s$ , over the pile shaft, after Randolph et al. (1994) .....	18
Figure 2-6: Values of critical depth for different authors, adopted from Barnes (2016).....	18
Figure 2-7: Coefficient of earth pressure ( $K_s$ ) acting on piles shafts (a) above critical depth versus ( $\phi'$ ) after Meyerhof (1976), and (b) versus ( $L/D$ ) after Coyle and Castello (1981).....	24
Figure 2-8: Values of ( $\beta$ ) versus ( $\phi'$ ) in sand for various type of installations according to (a) Poulos and Davis (1980) (b) Meyerhof (1976).....	25
Figure 2-9: Values of ( $\beta$ ) versus pile depth for different relative densities ( $D_r$ ), after Toolan et al. (1990).....	25
Figure 2-10: Relationship between average particle size and interface angle, adopted from Yang et al. (2015).....	28

Figure 2-11: Relationship between the ratio of roughness ( $R_a$ ) to the average particle size ( $d_{50}$ ) with $\tan \delta$ , adopted from Yang et al. (2015) .....	28
Figure 2-12: Measured profiles of local shear stresses, after Lehane et al. (1993) .....	30
Figure 2-13: (a) Pile instrumentation; (b) local shear stress for pile R2; (c) local shear stress distribution for all pile load tests, after Flynn & McCabe (2015) .....	33
Figure 2-14: (a) Stepped Blade Test, adopted from Sivakugan and Das (2010); (b) Pressuremeter Test, adopted from Potts et al. (2001).....	36
Figure 2-15: Results of Beringen et al. (1979) comparing measured and predicted shaft resistance (a) with limiting, and (b) without limiting shaft resistance value .....	38
Figure 2-16: (a) Influence of overconsolidation on unit end bearing capacity (b) Influence of overconsolidation on average unit skin friction, after Foray et al. (1998).....	39
Figure 2-17: Sand depth versus ultimate pullout load and OCR, after Hanna and Ghaly (1992) .....	41
Figure 2-18: OCR distribution around the pile shaft, after Sabry (2005).....	42
Figure 2-19: (a) Earth pressure distribution around the pile shaft, (b) Idealized earth pressure zones, after Sabry (2005) .....	43
Figure 2-20: Values of OCR at various depths for different compaction effort, after DiCamillo (2014).....	45
Figure 2-21: Failure zone and forces applied around the pile's shaft, after Hanna and Nguyen (2002). .....	47
Figure 2-22: Distribution of $Q_c / Q_m$ with respect to embedment depth ( $L/D$ ), after Jardine et al. (2005).....	48
Figure 3-1: Actual experimental setup.....	52
Figure 3-2: (a) Sketch of the steel tank (b) EC5 electric cylinder actuator, (c) AKD servo driver .....	54

Figure 3-3: Particle size distribution for silica sand 4010 .....	56
Figure 3-4: Relative density and corresponding angle of shearing resistance.....	57
Figure 3-5: Set-up arrangement for soil preparation.....	61
Figure 3-6: Location of (a) cans and (b) sensors in the testing tank.....	62
Figure 3-7: Photos of the (a) can location, (b) sensor location, and (c) compaction plate during testing.....	63
Figure 3-8: Test results: depth versus (a) number of drops, (b) relative density (c) angle of shearing resistance.....	66
Figure 3-9: Theoretical and measured values of the vertical stress versus the depth of soil for (a) $D_r = 30\%$ , (b) $D_r = 45\%$ , and (c) $D_r = 60\%$ . .....	67
Figure 3-10: Test results: OCR versus depth.....	68
Figure 3-11: Test results: lateral earth pressure coefficients versus depth .....	69
Figure 3-12: Accumulated energy versus depth .....	71
Figure 3-13: Experimental results: energy factor versus the relative height .....	74
Figure 3-14: Energy factor versus relative height.....	75
Figure 3-15: Test results of $[\text{OCR} (1 - (D_r)^2)]$ versus relative height .....	76
Figure 3-16: Flow charts for calculating the number of drop and the OCR.....	77
Figure 3-17: Photo and schematic sketch for (a) 55mm pile model, and (b) 30 mm pile model .....	80
Figure 3-18: Values of $(\delta/\phi')$ for different relative densities of Silica Sand after Vakili (2015).....	81
Figure 3-19: Pile load testing program for both pile models .....	83
Figure 3-20: Setup arrangement.....	84
Figure 3-21: Photos for the (a) 55 mm and (b) 30 mm pile models during test .....	87
Figure 3-22: Instrumentation of the 55 mm diameter pile model.....	88

Figure 3-23: Test results of (C-55-30%-5); (a) Load-Cell reading, (b) total, tip, and shaft resistance, and (c) shaft resistance for sections .....	90
Figure 3-24: Test results of (C-55-30%-8); (a) Load-Cell reading, (b) total, tip, and shaft resistance, and (c) shaft resistance for sections .....	91
Figure 3-25: Test results of (C-55-30%-10); (a) Load-Cell reading, (b) total, tip, and shaft resistance, and (c) shaft resistance for sections .....	92
Figure 3-26: Test results of (C-55-30%-13); (a) Load-Cell reading, (b) total, tip, and shaft resistance, and (c) shaft resistance for sections .....	93
Figure 3-27: Test results of (C-55-45%-5); (a) Load-Cell reading, (b) total, tip, and shaft resistance, and (c) shaft resistance for sections .....	96
Figure 3-28: Test results of (C-55-45%-8); (a) Load-Cell reading, (b) total, tip, and shaft resistance, and (c) shaft resistance for sections .....	97
Figure 3-29: Test results of (C-55-45%-10); (a) Load-Cell reading, (b) total, tip, and shaft resistance, and (c) shaft resistance for sections .....	98
Figure 3-30: Test results of (C-55-45%-13); (a) Load-Cell reading, (b) total, tip, and shaft resistance, and (c) shaft resistance for sections .....	99
Figure 3-31: Test results of (C-55-60%-5); (a) Load-Cell reading, (b) total, tip, and shaft resistance, and (c) shaft resistance for sections .....	101
Figure 3-32: Test results of (C-55-60%-8); (a) Load-Cell reading, (b) total, tip, and shaft resistance, and (c) shaft resistance for sections .....	102
Figure 3-33: Test results of (C-55-60%-10); (a) Load-Cell reading, (b) total, tip, and shaft resistance, and (c) shaft resistance for sections .....	103

Figure 3-34: Test results of (C-55-60%-13); (a) Load-Cell reading, (b) total, tip, and shaft resistance, and (c) shaft resistance for sections .....	104
Figure 3-35: Test results of (C-30-30%-19); total, tip, and shaft resistance.....	105
Figure 3-36: Test results of (C-30-30%-23.8); total, tip, and shaft resistance.....	106
Figure 3-37: Test results of (C-30-45%-19); total, tip, and shaft resistance.....	107
Figure 3-38: Test results of (C-30-45%-23.8); total, tip, and shaft resistance.....	107
Figure 3-39: Test results of (C-30-60%-19); total, tip, and shaft resistance.....	108
Figure 3-40: Test results of (C-30-60%-23.8); total, tip, and shaft resistance.....	109
Figure 3-41: Repeated test for (C-55-60%-10).....	110
Figure 3-42: Repeated test for (C-30-60%-23.8).....	110
Figure 4-1: Ultimate load versus the ratio of depth to diameter (L/D) for the 55 mm pile model ...	116
Figure 4-2: Ultimate load versus the ratio of depth to diameter (L/D) for the 30 mm pile model ...	116
Figure 4-3 : Ultimate load distribution for pile of 55 mm diameter at (a) L/D = 5, (b) L/D = 8, (c) L/D = 10, and (d) L/D = 13.....	117
Figure 4-4 : Ultimate load distribution for pile of 30 mm diameter at (a) L/D = 19, and (b) L/D = 23.8.....	118
Figure 4-5: Experimental $N_q$ values compared to proposed $N_q$ values by different authors after, Prakash and Sharma (1990) .....	119
Figure 4-6: Average shaft resistance for pile diameter of 55 mm .....	121
Figure 4-7: Average shaft resistance for pile diameter of 30 mm .....	121
Figure 4-8: $K_s$ values for all tests performed.....	124
Figure 4-9: Experimental values of ( $\beta$ ) for the 55 mm pile model .....	126
Figure 4-10: Experimental values of ( $\beta$ ) for the 30 mm pile model .....	126

Figure 4-11: Experimental values of ( $K_S / K_0$ ) for the 55 mm pile model .....	128
Figure 4-12: Experimental values of ( $K_S / K_0$ ) for the 30 mm pile model .....	128
Figure 4-13 : Local shear stress distribution for $L/D = 5$ .....	131
Figure 4-14: Local shear stress distribution for $L/D = 8$ .....	132
Figure 4-15: Local shear stress distribution for $L/D = 10$ .....	133
Figure 4-16: Local shear stress distribution for $L/D = 13$ .....	134
Figure 4-17: Local lateral earth pressure coefficient at failure for $L/D = 5$ .....	137
Figure 4-18: Local lateral earth pressure coefficient at failure for $L/D = 8$ .....	138
Figure 4-19: Local lateral earth pressure coefficient at failure for $L/D = 10$ .....	139
Figure 4-20: Local lateral earth pressure coefficient at failure for $L/D = 13$ .....	140
Figure 4-21: Local lateral earth pressure at failure for $L/D = 5$ .....	143
Figure 4-22: Local lateral earth pressure at failure for $L/D = 8$ .....	144
Figure 4-23: Local lateral earth pressure at failure for $L/D = 10$ .....	145
Figure 4-24: Local lateral earth pressure at failure for $L/D = 13$ .....	146
Figure 4-25: Variation of $K_s$ values with depth for each relative density .....	148
Figure 4-26: Experimental critical depth results.....	148
Figure 4-27: Comparison between the actual and the calculated shaft resistance using values proposed by different authors .....	151
Figure 4-28: Ratio of ( $h/D$ ) versus the ratio of ( $\sigma'_{rf}/q_c$ ) .....	154
Figure 4-29: Regression analysis for the ratio of ( $h/D$ ) versus the ratio of ( $\sigma'_{rf}/q_c$ ) .....	155
Figure 4-30: Factor (a) and (b) versus the ratio of depth to diameter ( $L/D$ ).....	155
Figure 4-31: Comparison between experimental and predicted shear stress .....	157

Figure 4-32: Calculated values of $(\sigma'_{rf}/q_c)$ for the field pile load test reported by Beringen et al. (1979).....	157
Figure 4-33: The pile load test reported by Beringen et al. (1979), (a) the pile configuration and soil parameter, (b) $q_c$ profile, and (c) the pile load-settlement curve.....	159
Figure 5-1: Assumed failure zone around the pile's shaft .....	164
Figure 5-2: (a) one slice of the failure zone, (b) side and bottom area illustration, and (c) forces on the slice .....	165
Figure 5-3: Three possible cases for the inclination angle .....	169
Figure 5-4: Steps of calculating the inclination angle .....	179
Figure 5-5: Results of the inclination angles .....	181
Figure 5-6: Illustration of the inclination angle behaviour with depth .....	181
Figure 5-7: Error between the predicted and actual shaft resistance .....	184
Figure 5-8: Results of critical depth.....	185
Figure 5-9: Difference between experimental and analytical shaft resistance .....	187
Figure 6-1 Stresses on a soil element in three-dimensional space.....	190
Figure 6-2: Mohr-Coulomb yield model (Hibbitt et al., 2016).....	192
Figure 6-3: Soil layers in model built for pile at 550 mm depth.....	193
Figure 6-4: Boundary conditions .....	194
Figure 6-5: Solid elements: (a) tetrahedron, (b) hexahedra, (c) triangular wedge.....	195
Figure 6-6: (a) Model mesh, (b) inside elements, (c) top view of the model, and (d) pile mesh .....	198
Figure 6-7: Top view of the model for 3D zone mesh size illustration .....	199
Figure 6-8: Influence of the element size outside the 3D zone on the pile capacity .....	200
Figure 6-9: Influence of the element size inside the 3D zone on the pile capacity .....	201

Figure 6-10: Side view of the model for mesh size illustration at Z direction .....	202
Figure 6-11: Influence of the element size on the pile capacity for Z direction around the pile shaft .....	203
Figure 6-12: Influence of the element size on the pile capacity for Z direction underneath the pile tip .....	203
Figure 6-13: Geostatic analysis for (a) $D_r = 45\%$ and $L/D = 5$ , (b) $D_r = 60\%$ and $L/D = 10$ .....	206
Figure 6-14: Results of the numerical pile load test for (C-55-45%-13).....	207
Figure 6-15: Stress distribution at failure (a) vertical, (b) lateral .....	208
Figure 6-16: Stresses before pile load test and at ultimate load on (a & c) the tank sides, and on (b & d) the bottom of the tank.....	210
Figure 6-17: Variation of modulus of elasticity and Poisson's ratio with angle of shearing resistance .....	211
Figure 6-18: Shaft resistance with variable values of $\beta$ for embedment depth ratio ( $L/D$ ) of 5.....	212
Figure 6-19: Shaft resistance with variable values of $\beta$ for embedment depth ratio ( $L/D$ ) of 8.....	213
Figure 6-20: Shaft resistance with variable values of $\beta$ for embedment depth ratio ( $L/D$ ) of 10.....	214
Figure 6-21: Shaft resistance with variable values of $\beta$ for embedment depth ratio ( $L/D$ ) of 13.....	215
Figure 6-22: $\beta$ value versus shaft resistance and OCR for $L/D = 5$ .....	218
Figure 6-23: $\beta$ value versus shaft resistance and OCR for $L/D = 8$ .....	219
Figure 6-24: $\beta$ value versus shaft resistance and OCR for $L/D = 10$ .....	220
Figure 6-25: $\beta$ value versus shaft resistance and OCR for $L/D = 13$ .....	221
Figure 6-26: $\beta$ value versus embedment depth ratio for $\phi' = 33$ degree .....	223
Figure 6-27: $\beta$ value versus embedment depth ratio for $\phi' = 35$ degree .....	224
Figure 6-28: $\beta$ value versus embedment depth ratio for $\phi' = 37$ degree .....	225

Figure 6-29:  $\beta$  value versus embedment depth ratio for  $\phi' = 39$  degree ..... 226

Figure 6-30:  $\beta$  value versus angle of shearing resistance for OCR = 5.5 and L/D = 19..... 229

## List of Symbols

$A_b$	Area of pile's base
$B$	Distance from center of the pile to the tank side
$D$	Pile diameter
$G$	Shear modulus
$h$	Distance from the pile tip
$R$	Pile radius
$C_u$	Uniformity coefficient
$C_c$	Coefficient of curvature
$G_s$	Specific gravity
$R_0$	Radius of influence at tip level
$R_1$	Radius of influence at the ground surface level
OCR	Overconsolidation ratio
CPT	Cone penetration test
$K_0 = K_{0(NC)}$	At-rest lateral earth pressure coefficient
$K_{0(OC)}$	Overconsolidated at-rest lateral earth pressure coefficient
$K_s$	Lateral earth pressure coefficient at failure
$K_p$	Passive lateral earth pressure coefficient
$L$	Pile length
$L_c$	Critical depth
$P_a$	Atmospheric pressure
$q_c$	Cone penetration test (CPT) end resistance

$Q_c$	Calculated shaft resistance
$Q_m$	Measured shaft resistance
$D_r$	Relative density (%)
$m$	Hammer mass
$N$	Number of drops
$g$	Gravity acceleration
$i$	Rank of the layer in the tank
$n$	Total number of soil layers
CLA	Average centerline
$\tau_f$	Ultimate shear resistance at failure
$\phi'$	Effective angle of shearing resistance
$\sigma'_v$	Effective overburden pressure
$\sigma'_h$	Horizontal effective pressure
$\delta_f$	Pile-Soil interface angle
$\sigma'_{rf}$	Radial effective stresses on the shaft at failure
$\sigma'_{rc}$	Stationary horizontal effective stress
$\Delta\sigma'_{rd}$	Dilation component
$\delta_h$	Horizontal displacement of a soil particle at the soil-pile interface
$\gamma_d$	Dry unit weight of the soil
$\gamma'$	Effective unit weight of soil
$\sigma_c$	Measured vertical pressure
$\sigma'_m$	Mean overburden pressure
$N_C^*, N_q^*, N_\gamma^*$	Bearing capacity factors

$F_{Cs}, F_{qs}, F_{\gamma s}$	Shape factors
$F_{Cd}, F_{qd}, F_{\gamma d}$	Depth factors
$Q_T$	Tip capacity
$Q_s$	Shaft resistance
$q'_o$	Effective overburden pressure
$\nu$	Poisson's ratio
$q_b$	Pile tip stress resistance
$\tau_{local}$	Local shear stress
$W_{soil}$	Weight of the soil in the can
$V_{can}$	Can volume
$\gamma_{d min}$	Minimum dry unit weight of the soil
$\gamma_{d max}$	Maximum unit dry weight of the soil
$\sigma_{V(M)}$	Measured vertical pressure at a given depth
$\sigma_{V(Th)}$	Theoretical effective overburden pressure at a given depth
$E_{applied}$	Applied energy
$E_i$	Accumulated energy per unit volume for layer i
$\gamma_i$	Unit weight of layer i
$d_L$	Depth of the middle layer i from the top
$H_r$	Relative height factor
$E_f$	Energy factor
$\beta$	$= (K_s \tan \delta_z)$
$\alpha$	Inclination angle

## **Chapter 1 : Introduction**

### **1.1 General**

Piles are structural members that transfer the applied load of superstructures to deep supportive layers of soil or bedrock to provide sufficient support both axially and laterally. Pile foundations were first used at least more than 2,000 years ago. The Romans, for example, used deep foundations, mainly made of rocks and timber, to support loads and structures in several locations, including Strasbourg Cathedral in present-day Strasbourg, France (Coduto, 2001; Ulitskii, 1995).

Today, piles are typically made of timber, steel, concrete, or a composite of two of those materials. Other than classification by material, piles can be classified according to their load transfer mechanism (e.g., end-bearing piles, friction piles, and combined friction and end-bearing piles), installation method (e.g., displacement or driven piles and replacement or bored piles), shape (e.g., square, circular, tapered, and helical piles), alignment (e.g., vertical and both negative and positive batter piles), and numerous other characteristics (Das, 2012). A more recently popular type of piles is micropiles, which have smaller diameters (i.e., generally 100–250 mm) than conventional piles and consist of a central steel reinforcement surrounded by grout that bonds the piles with the soil (Gogoi et al., 2014).

Piles are necessary when upper soil layers are highly compressible or too weak to support the applied load of superstructures, when superstructures encounter horizontal forces, when a site contains collapsible or expansive soil, and when uplift forces are applied to structures (Das, 2012). They are also necessary when slight movement in a superstructure require rapid response, in which case micropiles are suitable (Gogoi et al., 2014).

Methods used to determine the ultimate resistance of piles include either small- or full-scale static load testing, dynamic analysis based on the dynamics of pile driving or wave propagation, and analytical methods based on soil properties obtained from laboratory or in situ tests (Coduto, 2001). Given major improvements in computer hardware and software during the past two decades, numerical analysis to determine the resistance of piles has become popular as well (Kusakabe & Kobayashi, 2010).

## **1.2 Problem Definition and Motivation**

Various parameters, including pile geometry, soil properties, pile–sand interface angle, residual forces, and soil stress history, affect the bearing capacity of drive piles in cohesionless soil (Wrana, 2015). When a pile is driven into such soil, the stress state of the surrounding soil changes (Rajapakse, 2008). Moreover, for vertically loaded piles in particular, the shaft resistance depends upon the effective radial stress in the surrounding soil which is a function of the mobilized lateral earth pressure coefficient ( $K_s$ ), the pile–soil interface angle, and vertical stress (Randolph et al., 1994).

In particular, the mobilized lateral earth pressure coefficient ( $K_s$ ) is often found empirically by performing laboratory or field pile load tests in normally consolidated cohesionless soils. The coefficient is typically presented either as a factor of the at-rest lateral earth pressure coefficient ( $K_s / K_0$ ) or as a factor combining the friction coefficient ( $\beta = K_s \tan \delta$ ).

Geotechnical engineers traditionally use Jaky's (1944) equation ( $K_0 = 1 - \sin \phi'$ ), which depends solely on the effective friction angle of the soil ( $\phi'$ ), to estimate the at-rest earth pressure coefficient ( $K_0$ ). Although such use is appropriate when soil is normally consolidated (El-Emam, 2011; Mayne & Kulhawy, 1982), the magnitude of the at-rest earth pressure coefficient ( $K_0$ ) is always affected by stress history, represented by the overconsolidation ratio (OCR).

Whether the overconsolidation of cohesionless soil occurs naturally or artificially, it indicates that effective vertical stress in the soil was previously greater than its current magnitude. Overconsolidation can occur when the ground surface is subjected to erosion, excavation, or unloading, often due to glacial melting, the demolition of structures, raised water tables (Coduto, 2001), compaction, or vibration (Hanna & Soliman-Saad, 2001; El-Emam, 2011).

In theory, when soil is overconsolidated, the at-rest earth pressure coefficient ( $K_0$ ) exceeds the value calculated by using Jaky's (1944) equation. Many researchers, including Wroth (1973), Meyerhof (1976), Mayne and Kulhawy (1982), and Hanna and Al-Romhein (2008), have noticed the effect of the OCR and thus proposed empirical equations to calculate the lateral at-rest earth pressure coefficient incorporated with the OCR's effect. Similarly, the mobilized lateral earth pressure coefficient ( $K_s$ ) in overconsolidated soil, presented either as a factor of the at-rest lateral earth pressure coefficient ( $K_s / K_0$ ) or as a combined factor ( $\beta$ ), is greater than that in normally consolidated soil. Because, the pressure acts upon the pile shaft, shaft resistance rises.

In practice, Beringen et al. (1979) performed compressive and tensile field pile load tests on opened- and closed-ended pile at a site with overconsolidated sand and observed that shaft resistance exceeded recommended limits by 100–200%. More recently, Foray et al. (1998) conducted laboratory tests on piles in normally consolidated and overconsolidated sand and observed that shaft resistance values of piles driven into overconsolidated sand were nearly double those driven into normally consolidated sand. However, given the difficulty of measuring stress in undisturbed cohesionless soil with laboratory tests, stress history is not incorporated into any conventional calculation of the ultimate resistance of piles in cohesionless soil (DiCamillo, 2014).

The distribution of shaft resistance was long believed to increase linearly with depth at a constant rate down to a certain embedment depth, also known as critical depth, and remains constant downward

(Vesic, 1964; Meyerhof, 1976). However, recent field pile tests have dispelled that theory (Fellenius, 2002; Kulhawy, 1995), and researchers now attribute critical depth to the effect of the angle of shearing resistance, the fact that it decreases with depth, residual forces, and soil arching development due to driving, and the tendency of the OCR to decrease with depth as well. Although the foregoing theory is now regarded as a fallacy, the lack of any better theory has meant that the concept of critical depth remains in use by geotechnical engineers today (Rajapakse, 2008; Wrana, 2015).

Ultimately, the shaft resistance of driven piles in overconsolidated cohesionless soil remains uncertain. To illustrate such uncertainty, the ratios of calculated field shaft resistance to measured field shaft resistance ( $Q_c / Q_m$ ) for 81 piles were determined by using the American Petroleum Institute's design procedure (Jardine et al., 2005). Although the ratios ideally should have been 1, most were below unity when plotted against the embedment depth ( $L/D$ ), which indicates that shaft resistance was underestimated when calculated (Figure 1-1), partly due to the overconsolidation of cohesionless soil.

### **1.3 Research Objectives**

Because the overconsolidation of cohesionless soil and its variation with depth influences shaft resistance, the research reported in this thesis involved investigating the influence of such overconsolidation, its effect on shaft resistance, the distribution of shaft resistance along the pile shaft, and the possibility of critical depth. Experimental, analytical, and numerical approaches were used to propose a method of predicting the shaft resistance of piles driven into overconsolidated cohesionless soil, and to investigate the existence of critical depth.

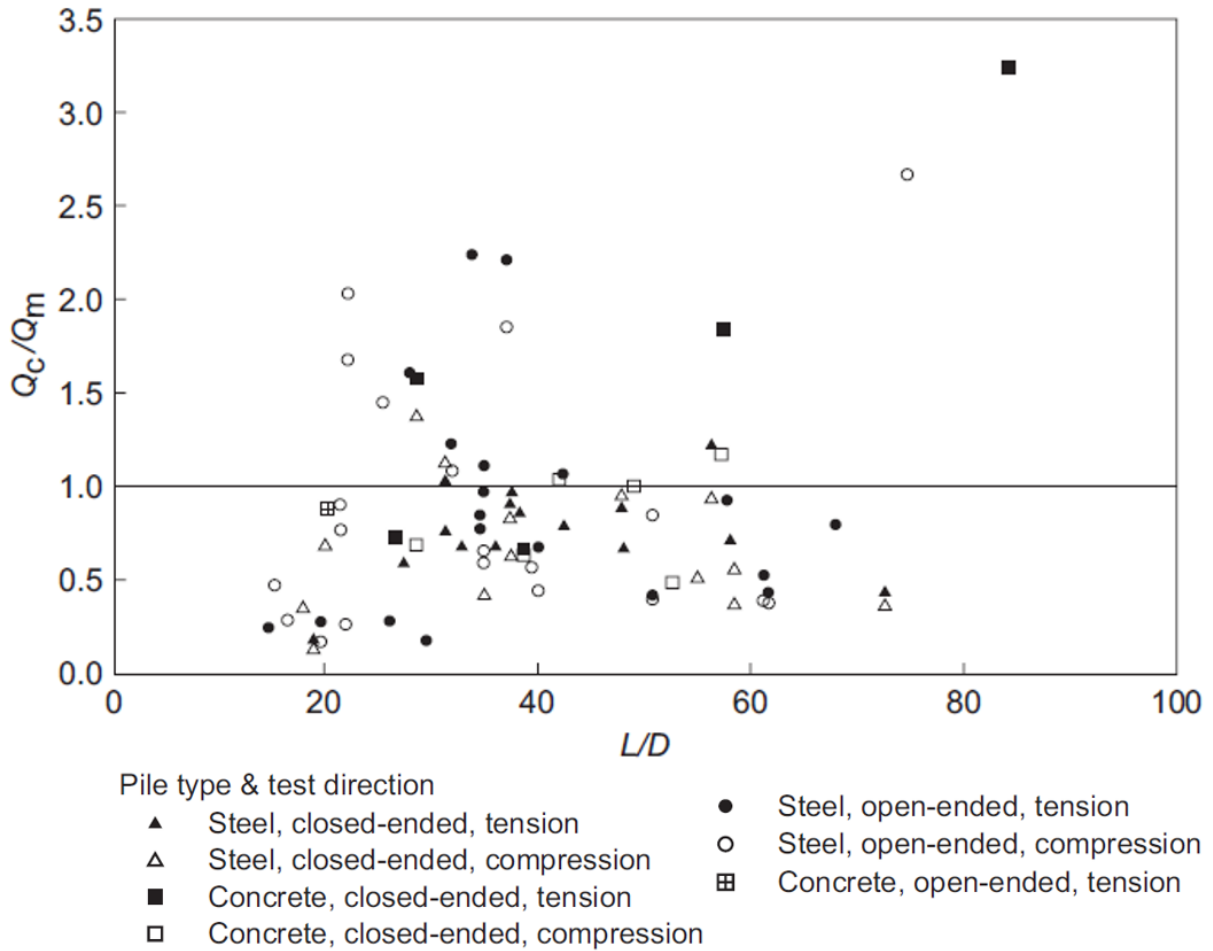


Figure 1-1 Distribution of  $Q_c / Q_m$  with respect to embedment depth ( $L/D$ ), after Jardine et al. (2005)

The objectives of the research were:

- 1- To review literature addressing the bearing capacity of single piles and especially shaft resistance in order to ascertain the current state of the art on the topic;
- 2- To design an experimental setup to measure the OCR, the total shaft resistance of piles, and their distribution; to develop a sand-placing technique to obtain a uniform relative density throughout the test tank and overconsolidate the soil; and to perform pile load tests on overconsolidated cohesionless soil using pile models 55 mm and 30 mm in diameter at different embedment depths and relative densities;

- 3- To examine the critical depth appearance, and study its sensitivity to OCR.
- 4- To develop an analytical model based on the horizontal slice method in order to predict the shaft resistance of driven piles in normally consolidated cohesionless soil;
- 5- To develop three-dimensional numerical models using ABAQUS to study the effect of  $\beta$  variation on the shaft resistance of driven piles in cohesionless soils; and
- 6- To analyze the results of the experiment and of the analytical and numerical models to propose a method of predicting the shaft resistance of driven piles in overconsolidated cohesionless soils and to develop corresponding design charts for practice.

## **1.4 Organization of Thesis**

Following this introductory chapter, Chapter 2 presents a literature review on the bearing capacity of single piles in overconsolidated cohesionless soil. It also presents the methods used to calculate the bearing capacity of piles with an emphasis on shaft resistance and discusses both critical depth and the effect of overconsolidation on shaft resistance.

Chapter 3 presents the experimental work proposed to investigate the problem, illustrates the experimental setup and materials used, and describes the test procedure and test program. Ultimately, the chapter also presents the results of compaction and pile load tests.

Chapter 4 presents the analysis of the experimental pile load tests and of the effect of relative density, embedment depth, pile diameter, and the OCR on shaft resistance and critical depth. It also presents an empirical model developed to estimate shear stress along the pile shaft and its distribution.

Chapter 5 presents an analytical model developed to predict the shaft resistance of driven piles in normally consolidated soils, as well as a design chart and procedure.

Chapter 6 presents the numerical model constructed to investigate the effect of  $\beta$ , a factor that combines the mobilized lateral earth pressure coefficient and friction coefficient ( $K_s \tan \delta$ ), on shaft resistance. Details of the model, as well as its validation, are also presented, as is the analysis of experimental, analytical, and numerical results used to generate design charts to predict  $\beta$  at different OCRs, angles of shearing resistance, and embedment depth ratios.

Last, Chapter 7 discusses the conclusions of the thesis and recommendations for future research.

## **Chapter 2 : Literature Review**

### **2.1 General**

In recent decades, a range of published scientific work supported by field experiments has focused on pile foundations. Nevertheless, predicting the bearing capacity of piles remains challenging and always involves uncertainty given the complexity of the problem, partly due to theoretical concepts derived from soil mechanics and more often due to empirical methods developed from field experiments (Randolph et al., 1994). Adding complexity to the problem of pile capacity is the overconsolidation of cohesionless soil, represented by the OCR.

This chapter reviews the bearing capacity of axially loaded driven piles in cohesionless soil, with an emphasis on methods of calculating shaft resistance and the parameters that influence its value.

### **2.2 Pile Capacity**

Based on the load transfer mechanism, piles are classified into three types: end-bearing piles, friction (i.e., floating) piles, and combined friction and end-bearing piles. With end-bearing piles, the total load applied to piles is borne and resisted by pile end (i.e., pile tip). Friction piles, by contrast, resist the applied load mostly due to frictional forces developed at the interface of the pile shaft and soil. Piles that resist the applied load with the pile end and shaft are classified as combined bearing piles, as shown in Figure 2-1 (Coduto, 2001).

Many methods are used to determine the capacity of piles: static load tests (i.e., full-scale or prototype), dynamic analysis based on the dynamics of pile driving or wave propagation, and analytical methods based on soil properties obtained from laboratory or in situ tests (Coduto, 2001). The research for this

thesis focused on the capacity of single driven, axially loaded piles and possible mechanisms of the failure of pile tip resistance and especially shaft resistance.

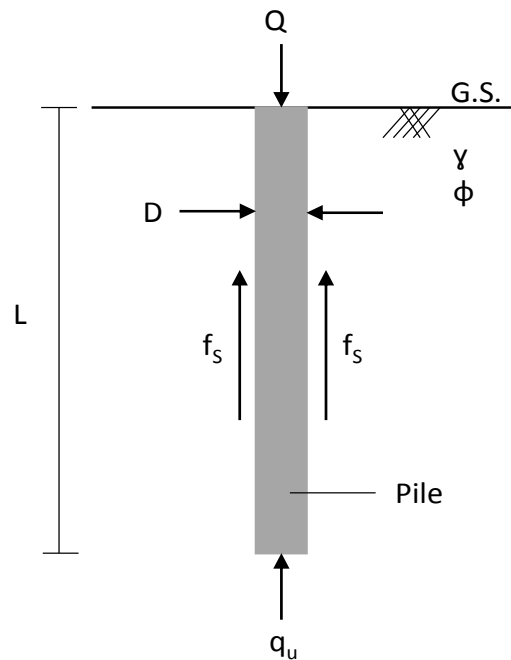


Figure 2-1: Component of the pile's capacity

Conventionally, pile capacity is a component of two types of resistance: tip resistance ( $Q_T$ ) and shaft resistance ( $Q_s$ ), as shown in Figure 2-1. The ultimate pile bearing capacity is expressed as follows:

$$Q = Q_T + Q_s = q_u A_b + f_s A_s \quad (2-1)$$

where:

$Q_T$  = tip resistance.

$Q_s$  = shaft resistance.

$q_u$  = ultimate unit tip resistance.

$f_s$  = ultimate unit skin friction.

$A_b$  = pile cross section area.

$A_s$  = pile surface area.

Values of  $Q_T$  and  $Q_s$  are generally estimated according to theories, while most analytical methods proposed to estimate  $Q_T$  and  $Q_s$  by comparing the measured soil properties with results of static load tests are based on empirical findings (Coduto, 2001).

Shaft resistance is mobilized at a far smaller pile displacement than that required to mobilize tip resistance. Usually, shaft resistance mobilizes at a displacement of 0.5–2.0% of the pile diameter, whereas displacement of 5.0–10.0%, or larger in the case of low displacement, of the pile diameter is needed to fully mobilize tip resistance (Fleming et al., 2008). In what follows, a brief description of the mechanisms of foundation failure is presented and the calculation of tip and shaft resistance is reviewed.

### **2.2.1 Failure Mechanism**

Bearing capacity failure occurs when the supporting soil exhibits a shear failure. Vesic (1973) recognized three modes of bearing capacity shear failure as shown in Figure 2-2. First, a general shear failure that shows a well-defined failure pattern where the slip surface starts from the edge of the foundation and ends at the ground surface as shown in Figure 2-2 (a). Second, a local shear failure that also shows a well-defined failure pattern but only underneath the foundation where the slip surface extends to the ground surface outward of the foundation as shown in Figure 2-2 (b). Last, a punching shear failure that is less well-defined where the slip surface does not extend to the ground surface and is often hard to observe as shown in Figure 2-2 (c). For a single pile, the punching shear failure is what describes its failure mode the most (Das, 2011; Hanna & Nguyen, 2002).

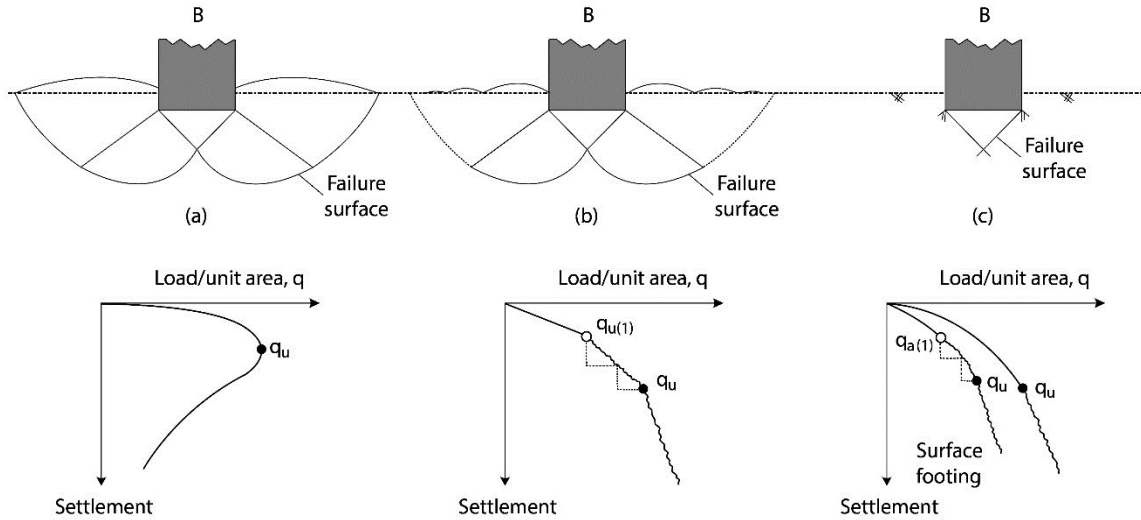


Figure 2-2: Bearing capacity shear failure modes, after Vesic (1973) adopted from Das (2011)

### 2.2.2 Tip Resistance ( $Q_T$ )

Most of the theories proposed to estimate the ultimate unit tip resistance for piles,  $q_u$  are based on the general bearing capacity equation for shallow foundation as follows;

$$q_u = c' N_C F_{Cs} F_{Cd} + q'_0 N_q F_{qs} F_{qd} + 0.5 \gamma' B N_\gamma F_{\gamma s} F_{\gamma d} \quad (2-2)$$

In general, it can be expressed as:

$$q_u = c' N_C^* + q'_0 N_q^* + 0.5 \gamma' B N_\gamma^* \quad (2-3)$$

where  $q'_0$  is effective overburden pressure at the base level of the foundation;  $N_C^*$ ,  $N_q^*$  and  $N_\gamma^*$  are the bearing capacity factors that include the necessary shape ( $F_{Cs}$ ,  $F_{qs}$ ,  $F_{\gamma s}$ ) and depth ( $F_{Cd}$ ,  $F_{qd}$ ,  $F_{\gamma d}$ ) factors;  $c'$  is cohesion of soil;  $\gamma'$  = effective unit weight of soil; and  $B$  is the width of the foundation.

Since piles are deep, different values of  $N_C^*$ ,  $N_q^*$  and  $N_\gamma^*$  are used. Also, piles mostly are circular in shape and have a diameter,  $D$ , rather than a width,  $B$ . Because this research is about cohesionless soils,

$c' = 0$  and the term  $(0.5 \gamma' D N_{\gamma}^*)$  becomes very small in comparison with the term  $(q'_0 N_q^*)$  for deep foundations. As a result, tip bearing capacity ( $Q_T$ ) is expressed generally as follows (Murthy, 2002);

$$Q_T = [q'_0 N_q^*] A_b = q_u A_b \quad (2-4)$$

where:

$q'_0$  = effective overburden pressure

$N_q^*$  = bearing capacity factor

$A_b$  = pile cross section area

Figure 2-3 Presents the ( $N_q$ ) values suggested by many researchers. It can be noted that the ( $N_q$ ) values, which is a function of  $(\phi')$  only, proposed by different researchers have huge variation. This variation is a result of the different assumptions made by each researcher, and the lack of ability to evaluate the state of stresses in the surrounding sand after pile installation (Sabry, 2005).

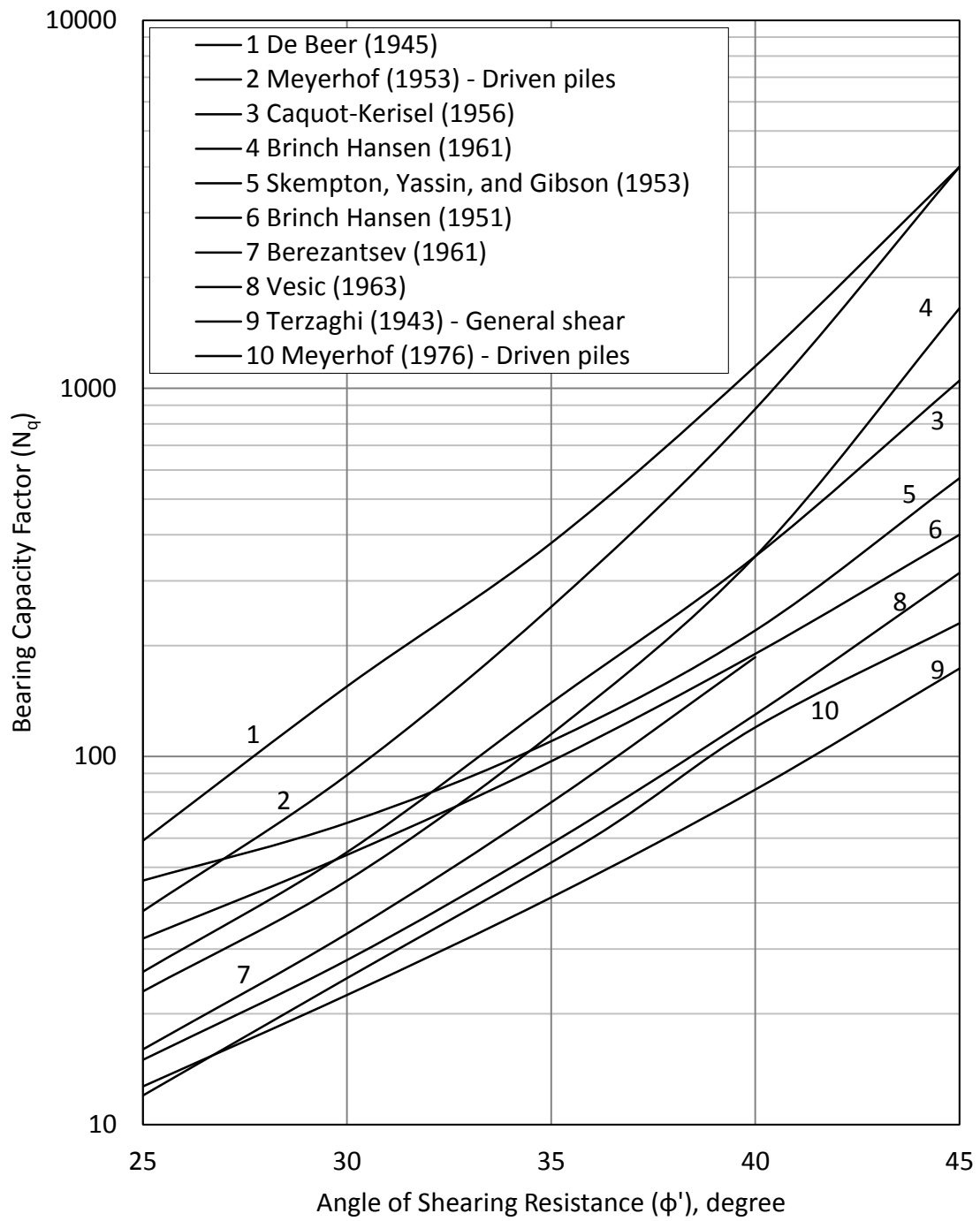


Figure 2-3: Bearing capacity factors for deep circular foundations after, Prakash and Sharma (1990)

### 2.2.3 Shaft Resistance ( $Q_s$ )

The ultimate unit skin friction,  $f_s$ , is developed based on the laws of mechanics considering friction between solid surfaces. In order to estimate the shaft resistance ( $Q_s$ ), Dorr (1922) integrated the shear stress ( $\tau$ ) along the surface of the pile sides as follows;

$$Q_s = \pi D \int_0^L \tau dz \quad (2-5)$$

It is assumed that the shear stress around the pile is proportional to the effective lateral stress ( $\sigma'_h$ ) as follows;

$$\tau = \sigma'_h \tan \delta_z \quad (2-6)$$

where: ( $\delta_z$ ) is the mobilized friction angle on the pile-sand interface at depth  $z$ , and ( $\sigma'_h$ ) is the horizontal effective pressure which also can be represented as function of the vertical effective stress ( $\sigma'_v$ ) as follows;

$$\sigma'_h = K_s \cdot \sigma'_v \quad (2-7)$$

where: ( $K_s$ ) is the lateral earth pressure coefficient. By assuming symmetry around the pile axis, the shaft resistance ( $Q_s$ ) can be obtained as:

$$Q_s = \pi D \int_0^L K_s \cdot \sigma'_v \cdot \tan \delta_z dz \quad (2-8)$$

$$\sigma'_v = \gamma' \cdot L \quad (2-9)$$

where: ( $D$ ) is the pile diameter; ( $\gamma'$ ) is the effective unit weight of soil; and ( $L$ ) is the pile embedment length. Therefore, the outcome of integrating the shear stress along the pile is expressed as follows;

$$Q_s = (0.5 K_s \cdot \gamma' \cdot L \cdot \tan \delta) A_s = f_s A_s \quad (2-10)$$

where ( $A_s$ ) is the pile surface area.

Even though tip and shaft resistances are calculated in two independent steps to find the total pile bearing capacity, many researchers argue that this approach is simplified and lacks the accuracy of the calculation. The simplicity of this approach along with other factors caused a wide range of discrepancies between design theories. Based on this concept, many theories were proposed to estimate the capacity of piles. Figure 2-4 shows some of the failure patterns for pile foundations that were proposed by different authors. It is of interest to know that most of these failure models are following either the general shear failure or local shear failure modes.

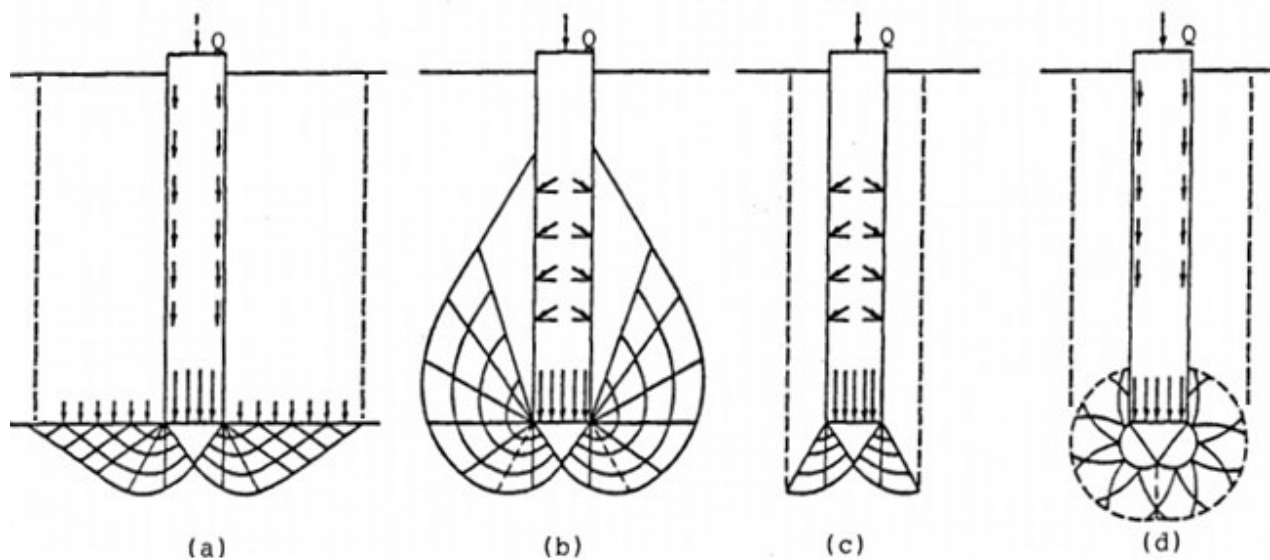


Figure 2-4: Assumed Failure Patterns under deep foundations, adopted from Prakash & Sharma (1990); (a) after Prandtl, Reissner, Caquot, Busiman, Terzaghi (b) After DeBeer, Jaky, Meyerhof (c) After Berezantsev and Yaroshenko, Vesic (d) After Bishop, Hill and Mott, Skempton, Yassin, and Gibson.

Terzaghi (1943) proposed a three-dimensional analytical model to calculate the pile capacity (Figure 2-4 (a)) that combines the shaft resistance and the tip resistance at the same failure mechanism. He extended his theory for the bearing capacity of shallow foundations by assuming a circular failure zone around the pile shaft. The movement of the soil at the tip level due to the pile loading is resisted by

the weight of the soil in the cylindrical zone, the shaft resistance of the pile, and the mobilized shear along the outer surface of the cylindrical failure surface. Although Terzaghi proposed an equation to calculate the tip resistance based on the shaft resistance and the mobilized shear along the outer surface of the cylindrical zone, he did not propose a procedure to estimate the shaft resistance nor the mobilized shear along the outer surface of the cylindrical zone.

Meyerhof (1951) proposed a general bearing capacity theory for shallow foundations based on an assumed failure surface that extends to the ground surface. For deep foundations, he assumed that the failure surface returns to the foundation shaft. To calculate the shaft resistance, the mobilized lateral earth pressure coefficient ( $K_s$ ) is presumed to be 0.5 for loose sand and 1 for dense sand.

Skempton et al., (1953) proposed another analytical model to predict the capacity of a single pile. He assumed a circular failure surface, of a center that lies at the tip level, which extends from the cone apex underneath the tip to a vertical line that extends to the ground surface. This vertical line represents the side of a cylindrical failure zone assumed around the pile's shaft. The forces that are applied in this analytical model include the shaft resistance, the weight of the soil inside the failure zone, the shear forces applied on the side of the cylindrical surface around the pile, the reaction force applied on the circular surface under the tip level, and the resultant force on the triangular wedge underneath the tip. The shear stress applied on the cylindrical surface is calculated based on the at rest lateral earth pressure assuming full mobilization ( $\delta = \phi'$ ). Also, shear stress is applied only to the lower part of the cylindrical surface where the length of this part is a function of the pile length and the relative density. In this model, the mobilized shear stresses along the circular failure surface underneath the tip level are not considered.

Hanna and Nguyen (2002) proposed a three-dimensional analytical model, similar to Vesic's (1967) model, which accounts for the interaction between tip and shaft resistance using the punching shear

failure mode. This model consists of three zones; a triangular wedge under the pile's tip, a radial shear zone which passes through the apex of the triangular wedge and terminates at a horizontal distance that equals the radius of influence, and a trapezoidal shaped zone around the pile bounded by the piles shaft and the external boundary which is assumed to equal the radius of influence. The radius of influence is a function of the angle of shearing resistance and the diameter of the pile. The radial zone and the trapezoidal shaped zone intercepts at an angle which is a function of the pile depth and the angle of shearing resistance. In this model, the shear forces at the external vertical boundary of the failure zone are ignored. This model requires more comprehensive studies to investigate the interaction of tip and shaft resistance in different soil conditions for single piles and pile groups.

#### 2.2.4 Critical Depth in Piles

Unit shaft resistance ( $f_s$ ) is a function of effective overburden pressure in cohesionless soil and increases linearly with depth. However, Vesic (1964), Meyerhof (1976) among others found that the unit shaft resistance remains almost constant beyond a certain depth of embedment ( $L$ ). It is stated that in cohesionless soils, the unit shaft resistance ( $f_s$ ) increases with the ratio of ( $L/D$ ) until it reaches a critical depth and remains constant downward as shown in Figure 2-5, and usually has a ratio of 10-20 based on the soil density. Based on Vesic's (1964) experimental study, the critical depth ( $L/D$ ) is expressed as a function of  $\phi'$  as shown in equation (2-11) and (2-12) (Poulos & Davis, 1980). Figure 2-6 presents the critical depth observed by Vesic (1964) and Meyerhof (1976).

$$L/D = 5 + 0.24 (\phi' - 28) \quad \text{For } 28 \text{ degree} < \phi' < 36.5 \text{ degree} \quad (2-11)$$

$$L/D = 7 + 2.35 (\phi' - 36.5) \quad \text{For } 36.5 \text{ degree} < \phi' < 42 \text{ degree} \quad (2-12)$$

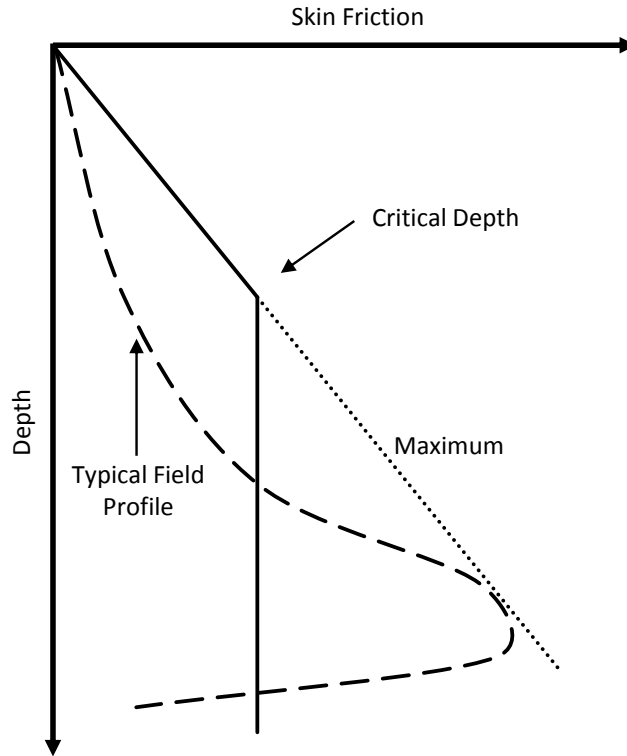


Figure 2-5: Distribution of local unit skin friction,  $f_s$ , over the pile shaft, after Randolph et al. (1994)

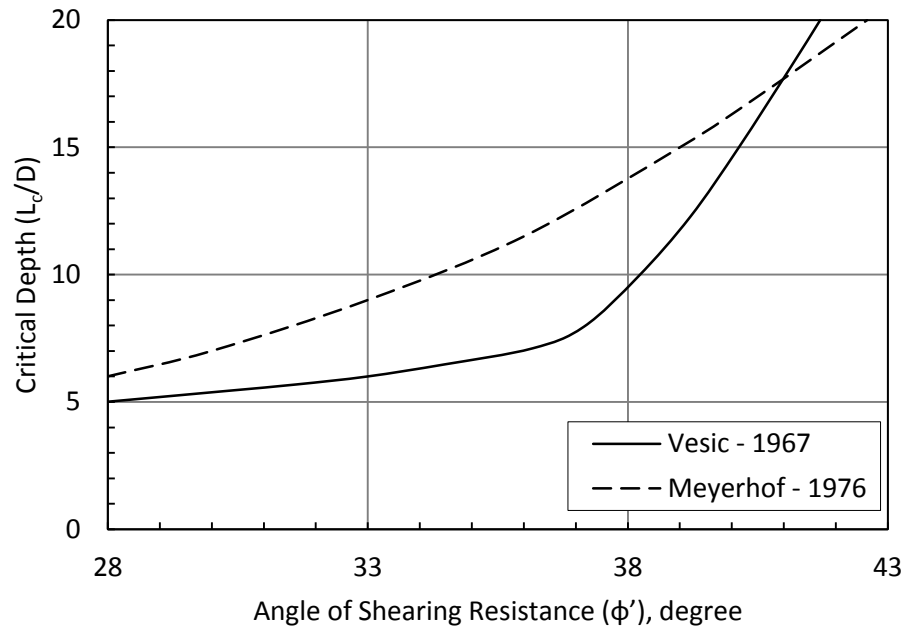


Figure 2-6: Values of critical depth for different authors, adopted from Barnes (2016)

However, several researchers look at the critical depth as a fallacy. Recent researchers proved that the critical depth does not exist, and the unit shaft resistance has a peak close to the pile tip as shown in Figure 2-5. Fellenius and Altaee (1995), Kulhawy (1995), and Kim and Chung (2012) among others are arguing that the existence of residual forces, which affect the resistance of piles, is the reason behind the appearance of the critical depth. Generally, residual load develops in soft clay when negative skin friction exists. Nevertheless, many researchers observed that residual load might exist in driven piles in cohesionless soil. Residual load in a pile could be the result of the soil recovery after the disturbance of the installation, or the result of the pile-soil shear stress (locked-in load) caused by driving. When it exists and ignored, the shaft and tip resistances obtained can be deceiving (Fellenius, 2002).

Fellenius (2002) refers this fallacy to the incorrect common practice to which considers the residual load very small and can be ignored, consequently, setting all gages to zero before the beginning of load tests. Kim and Chung (2012) stated that this error does not affect the bearing capacity of the pile, but it may influence the interpretation of the shaft resistance distribution.

In a discussion paper, Kulhawy (1995) reported that Vesic described the critical depth which he introduced in his 60s research as a “tentative working hypothesis” and he disregarded this hypothesis in mid-70s. Because the critical depth concept was simple, attractive and requires minim geotechnical knowledge, it spread and adopted by many investigators. Kulhawy agreed with Fellenius that residual load affects the so-called critical depth, but in-situ soil characteristics such as ( $K_0$ ) and (OCR) (Kulhawy, 1984) are way more important factors than residual loads to dispel the concept of critical depth.

Kraft (1991) relays the appearance of critical depth to the effect of sand arching around the piles. When a pile is pushed into the soil, the soil underneath the tip is densified. As the pile goes deeper, it

drags the soil in its vicinity which creates a loose sleeve of sand around the pile which makes an ideal condition for arching. Thus, the development of full lateral earth pressure on the pile is prevented (Iskander, 2011).

### **2.2.5 The Mobilized Lateral Earth Pressure Coefficient ( $K_s$ )**

One of the main difficulties associated with Eq.2-10 for axially loaded piles is the selection of the mobilized lateral earth pressure coefficient, ( $K_s$ ). Many factors affect the value of ( $K_s$ ) such as (Fleming et al., 2008; El-Emam, 2011);

- In-situ earth pressure coefficient,
- The method of installation of the pile,
- Initial density of the sand,
- The angle of shearing resistance  $\phi'$ ,
- Soil deformation characteristics,
- Pile shape,
- Loading direction, and
- Stress history.

Fore bored piles, the mobilized lateral earth pressure coefficient ( $K_s$ ) equals the at-rest lateral earth pressure coefficient ( $K_0$ ) which can be calculated for normally consolidated soils as follow (Jaky, 1944);

$$K_{0(NC)} = 1 - \sin \phi' \quad (2-13)$$

For overconsolidated cohesionless soil, Wroth (1975) presented an empirical equation (2-14) as a function of the effective angle of internal friction of the soil ( $\phi'$ ), Overconsolidation ratio (OCR) and Poisson's ratio ( $\nu$ );

$$K_{0(OC)} = (1 - \sin \phi') \text{OCR} - \left[ \frac{\nu}{(\nu - 1)} \right] (\text{OCR} - 1) \quad (2-14)$$

Also, Meyerhof (1976) proposed an equation (2-15) to find a value for lateral earth pressure in OC cohesionless soil.

$$K_{0(OC)} = (1 - \sin \phi') \sqrt{\text{OCR}} \quad (2-15)$$

Mayne and Kulhawy (1982) proposed another equation (2-16) based on statistical analysis method.

$$K_{0(OC)} = (1 - \sin \phi') (\text{OCR})^{(\sin \phi')} \quad (2-16)$$

More recent experimental study was performed on overconsolidated soil by Hanna and Al-Romhein (2008). It was reported that the measured lateral earth pressure agrees with that calculated using Eq. 2-14, 15, and 16 up to an OCR of 3 only. Accordingly, they proposed a new equation (2-17) that agrees with a wider range of OCRs.

$$K_{0(OC)} = (1 - \sin \phi') (\text{OCR})^{(\sin \phi' - 0.18)} \quad (2-17)$$

On the other hand, the value of the mobilized lateral earth pressure coefficient ( $K_s$ ) is higher than the value of ( $K_0$ ) due to the driving effort. If the sand is initially loose, driving a pile densify the sand along the shaft to an extent of about 6 to 8 times the diameter of the pile, whereas driving a pile in dense sand decreases the relative density because of the dilatancy of the sand to an extent of about 5 times the diameter of the pile (Murthy, 2002).

Based on field data, it was found that the sand friction angle decreases from a maximum value ( $\phi'_2$ ) underneath the pile tip to a minimum value ( $\phi'_1$ ) linearly at 3.5 times the diameter of the pile, as expressed in equation (2-18) (Kishida, 1967). For the determination of the ( $K_s \tan \delta$ ), the value of ( $\phi'$ )

along the pile shaft should be taken as the mean of the values prior to, and subsequent to, driving (Poulos & Davis, 1980) as in equation (2-19).

$$(\phi'_2) = 0.50 (\phi'_1 + 40) \quad (2-18)$$

$$(\phi'_2) = (0.75 \phi'_1) + 10 \quad (2-19)$$

where  $(\phi'_1)$  is the soil friction before the driving the pile.

Shalabi and Bader (2014) studied the effect of pile-driving on densification of the sand around the pile experimentally. Part of their results shows that the horizontal movement of sand, which is corresponding to the process of driving piles, extends to almost three times the pile diameter. The extent of this zone increases as the initial relative density increases. Contrasting, other researchers like Tomlinson (1986) reported that it is not valid to increase the value of the friction angle around the pile. It is claimed that driving a pile in sand may not compact it, or in case of loose sand the compaction may be of a little value. Those researchers suggest using the same value of  $(\phi')$  that is obtained on field without any change (Murthy, 2002).

It is difficult to estimate the value of  $(K_s)$  for driven piles since it is influenced by many factors as explained earlier. Therefore, the mobilized lateral earth pressure coefficient  $(K_s)$  for driven piles is mostly found empirically by performing laboratory or field pile load tests in normally consolidated cohesionless soils. Meyerhof (1976) proposed typical values of  $(K_s)$  acting on pile shafts above the critical depth in sand based on the effective angle of shearing resistance  $(\phi')$  as shown in Figure 2-7 (a). For different type of pile materials, Broms (1966) had linked the value of  $(K_s)$  to the effective angle of shearing resistance  $(\phi')$  and to the relative density  $(D_r)$  as shown in Table 2-1. Coyle and Castello (1981) found a correlation between the value of  $(K_s)$  and embedment depth  $(L/D)$  for an angle of shearing resistance range  $(\phi')$  between 30 to 36 degree as shown in Figure 2-7 (b). Table 2-2 also shows some of the  $(K_s)$  values recommended by different authors and organizations.

Meyerhof (1976) and Poulos and Davis (1980) among others represented the earth pressure coefficient ( $K_s$ ) and the friction factor using the pile soil interface angle ( $\tan \delta_z$ ) as a combined factor ( $\beta$ ).

Therefore, Eq.2-10 can be written as follows;

$$Q_s = f_s A_s = (0.5 K_s \gamma' L \tan \delta) A_s = \beta \sigma'_v A_s \quad (2-20)$$

where  $\beta = (K_s \tan \delta_z)$ ;

$$\sigma'_v = 0.5 \gamma' L;$$

$$A_s = \pi DL$$

Figure 2-8a and b shows the values of ( $\beta$ ) versus the effective angle of shearing resistance ( $\phi'$ ) in sand for various type of installations according to Poulos and Davis (1980) and Meyerhof (1976), respectively. The values presented in Figure 2-8a are considered very high values to be used for design (Poulos and Davis, 1980). Based on a field pile load tests database, Toolan et al. (1990) proposed a design chart to estimate the value of ( $\beta$ ) according to the relative density of soil and the depth of the pile as shown in Figure 2-9.

Other researchers such as Stas and Kulhawy (1984) and Kulhawy (1991) linked the value of ( $\phi'$ ) to the ratio of ( $K_s/K_0$ ). Values suggested for the ratio of ( $K_s/K_0$ ) are presented in Table 2-3. With ( $K_s/K_0$ ), equation (2-10) then becomes;

$$Q_s = f_s A_s = \left(0.5 K_0 \frac{K_s}{K_0} \gamma' L \tan \delta\right) A_s \quad (2-21)$$

Table 2-1: Values of earth pressure coefficient  $K_s$  and Pile-Soil friction angle  $\delta_z$  for different relative densities, after Broms (1966)

Pile Material	$K_s$	
	Low relative density	High relative density
Steel	0.5	1.0
Concrete	1.0	2.0
Wood	1.5	4.0

Table 2-2: Recommended values for  $K_s$

$K_s$	NAVFAC (1986)	Mansur and Hunter (1970)	API (2000)
Driven H-pile	0.5–1.0	1.65	-
Driven Low displacement pile	1	-	0.8
Driven High displacement pile	1.5	-	1
Bored Pile	0.7	-	-
Jetted Pile	0.4-0.9	-	-
Steel pile	-	1.26	-
Pre-Cast Pile	-	1.5	-

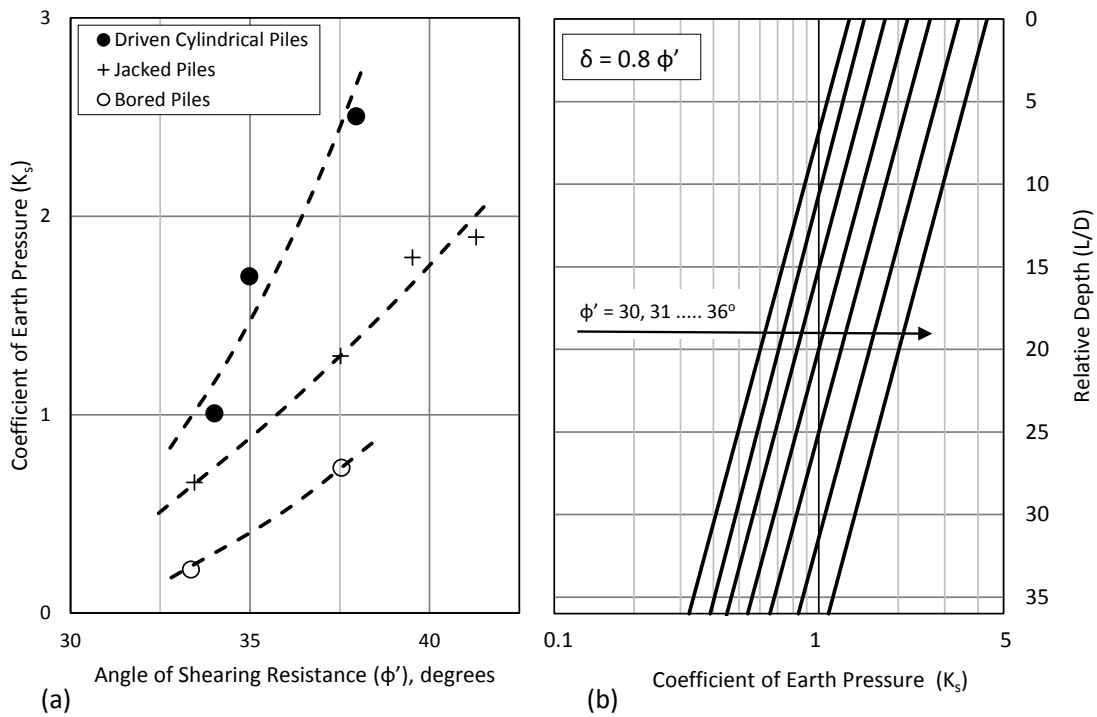


Figure 2-7: Coefficient of earth pressure ( $K_s$ ) acting on piles shafts (a) above critical depth versus ( $\phi'$ ) after Meyerhof (1976), and (b) versus ( $L/D$ ) after Coyle and Castello (1981)

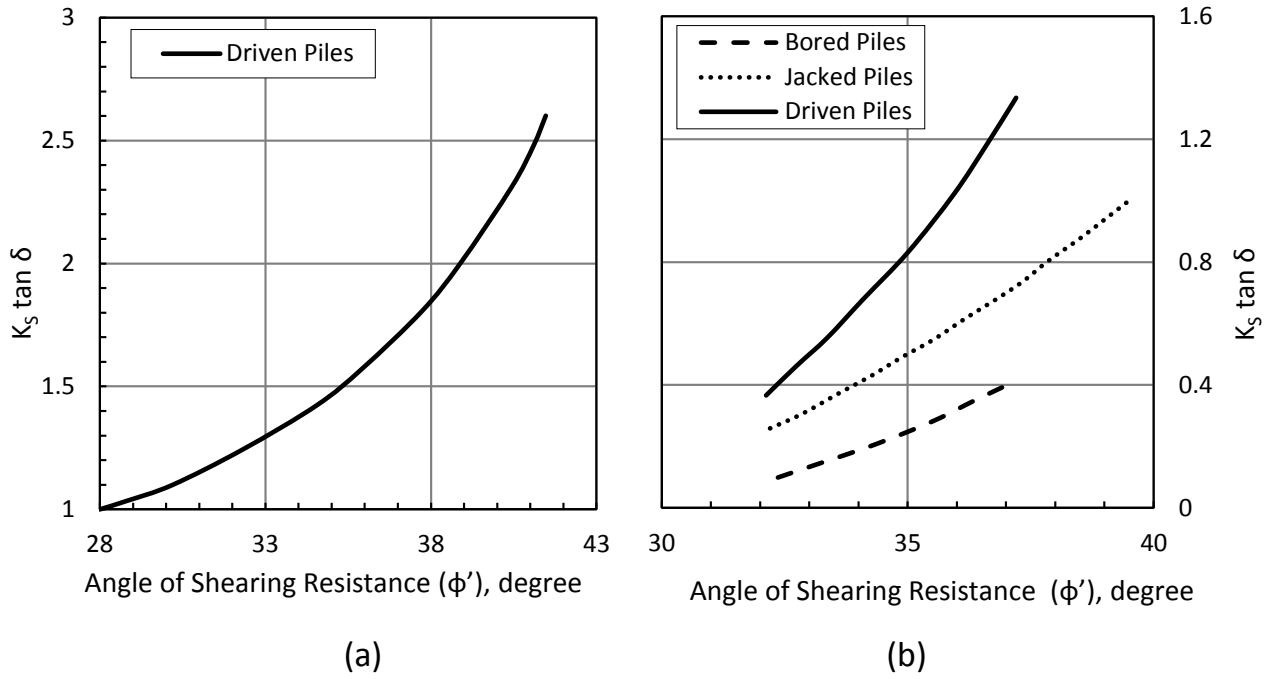


Figure 2-8: Values of ( $\beta$ ) versus ( $\phi'$ ) in sand for various type of installations according to (a) Poulos and Davis (1980) (b) Meyerhof (1976).

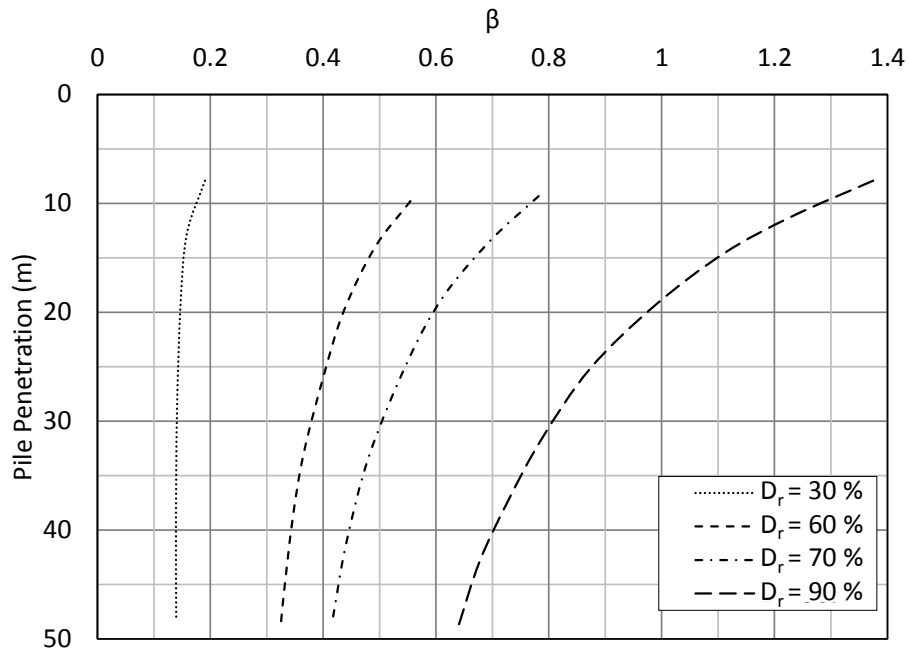


Figure 2-9: Values of ( $\beta$ ) versus pile depth for different relative densities ( $D_r$ ), after Toolan et al. (1990)

Table 2-3: Ratio of  $K_s/K_0$  suggested by different researchers

Foundation Type and Method of Construction	$K_s/K_0$		
	Kulhawy (1991)	Tomlinson and Woodward (2014)	Das (2011)
Pile jetted	0.5-0.7	0.5 – 0.7	-
Driven pile-small displacement	0.7-1.2	0.75 – 1.25	1.4
Driven pile-large displacement	1.0-2.0	1 – 2	1.8
Bored Pile	-	0.7 – 1	
Drilled shaft-built using dry method with minimal sidewall disturbance and prompt concreting	0.9-1.0	-	-
Drilled shaft-slurry construction with good workmanship	0.9-1.0	-	-
Drilled shaft-slurry construction with poor workmanship	0.6-0.7	-	-

### 2.2.6 Pile – Soil Interface Angle ( $\delta$ )

The pile-soil interface angle is an important parameter that controls the shaft resistance. It depends on the pile’s surface roughness and hardness and the soil’s grain size, shape, and the mineral type (Yang et al., 2015). This value is best obtained by direct shear test between the material of the pile and the site-specific soil material. It is usually presented as a percentage of the soil angle of shearing resistance ( $\phi'$ ). Table 2-4 presents the values proposed by Potyondy (1961), Broms and Silberman (1966), and Stas and Kulhawy (1984).

Table 2-4: Interface angle between the pile material and sand

Pile Material	Surface Condition	$\delta$ (degree)		
		Potyondy (1961)	Broms and Silberman (1966)	Stas and Kulhawy (1984)
Concrete	Smooth	$0.76 \phi'$	$0.66 \phi'$	$0.8-1 \phi'$
	Grained	$0.88 \phi'$		-
	Rough	$0.89 \phi'$		1
Steel	Smooth	$0.54 \phi'$	20	$0.5-0.7 \phi'$
	Rough	$0.76 \phi'$		$0.7-0.9 \phi'$
Wood	Parallel to grain	$0.76 \phi'$	$0.75 \phi'$	$0.8-0.9 \phi'$
	Perpendicular to grain	$0.88 \phi'$		

Jardine et al. (1992) showed experimentally that the value of ( $\delta$ ) is independent of the relative density (or soil unit weight) and tends to decrease with the increase of average grain size ( $d_{50}$ ) for a certain pile surface roughness. For a roughness of  $10 \mu\text{m}$  CLA, they found that it is ranged between  $36 - 23$  degree as shown in Figure 2-10. Ho et al. (2011) performed large-displacement ring shear interface tests on various materials and grain sizes. The results showed a similar trend to Jardine et al.'s (1992) results but lower values and less reduction with the increase of the average grain size ( $d_{50}$ ). These results show that the interface angle is between  $31 - 26$  degree. Regardless of the average grain size, CUR (2001) recommended using an interface angle of 29 degree for steel piles. For concrete piles, Barmopoulos et al. (2009) found a relationship between the interface angle and the ratio of the pile roughness ( $R_a$ ) to the average grain size ( $d_{50}$ ) as shown in Figure 2-11. This relation mostly yields an interface angle of 29 degree.

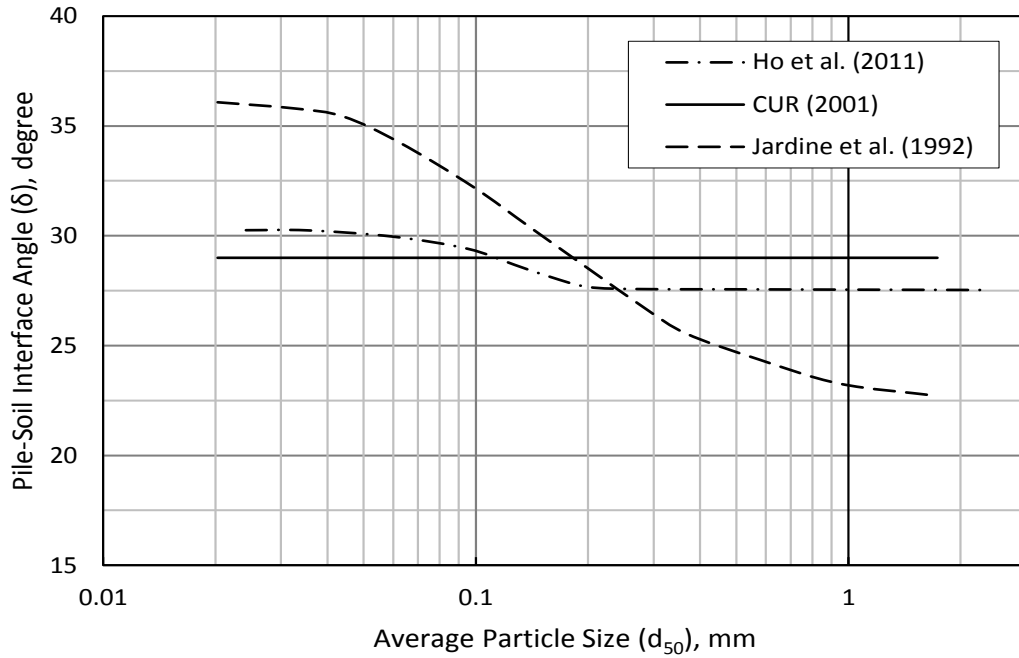


Figure 2-10: Relationship between average particle size and interface angle, adopted from Yang et al. (2015)

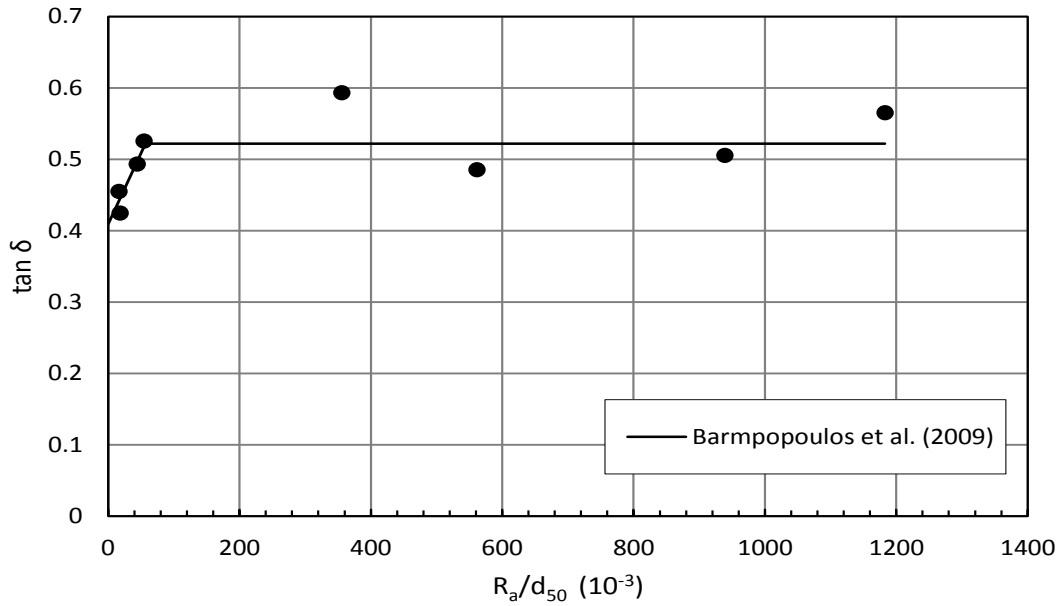


Figure 2-11: Relationship between the ratio of roughness ( $R_a$ ) to the average particle size ( $d_{50}$ ) with  $\tan \delta$ , adopted from Yang et al. (2015)

Lehane et al. (1993) conducted an experimental study about the stresses developed around displacement piles in loose and medium dense sand. In their study, two piles were prepared with highly sensitive pile instrumentation to find the magnitude and distribution of the effective stresses acting on the shafts of driven piles. Also, laboratory tests such as triaxial test and direct shear test were performed on the soil samples to determine the soil properties.

It was realized through the qualitative work of Meyerhof (1976), Vesic (1977) and other researchers that the local shaft friction at a certain depth decreases as the pile penetrates further. Interestingly, the authors were able to quantify this decrease through well-instrumented field pile tests. The reduction of local shaft friction, as presented in Figure 2-12, was measured using 3 instrumented clusters at different distances (h) from the pile tip;  $(h/D) = 4, 14, \text{ and } 25$ .

Their study shows that the experimental pile-sand friction angle correlates well with the laboratory results. It, also, shows that Coulomb failure may be used to describe the ultimate shear resistance at failure as follows;

$$\tau_f = \sigma'_{rf} \tan \delta_f \quad (2-22)$$

The radial effective stresses on the shaft at failure ( $\sigma'_{rf}$ ) is different than the equilibrium values ( $\sigma'_{rc}$ ) by an amount of ( $\Delta\sigma'_r$ ) and expressed as follows;

$$\sigma'_{rf} = \sigma'_{rc} + \Delta\sigma'_r \quad (2-23)$$

where ( $\Delta\sigma'_r$ ) was found as a component of the principal stress rotation ( $\Delta\sigma'_{rp}$ ) in the sand and the dilation due to slipping at the interface ( $\Delta\sigma'_{rd}$ ). A small reduction in ( $\sigma'_{rc}$ ) was observed at the early stages of the compressive load testing because of the principal stress rotations associated with pile loading. A considerable increase in ( $\sigma'_{rc}$ ) was observed as each section of the pile approached local failure because of dilation and soil displacement. Therefore, the authors concluded that dilation phenomena at pile-soil interface during installation and pile loading induces radial effective stress.

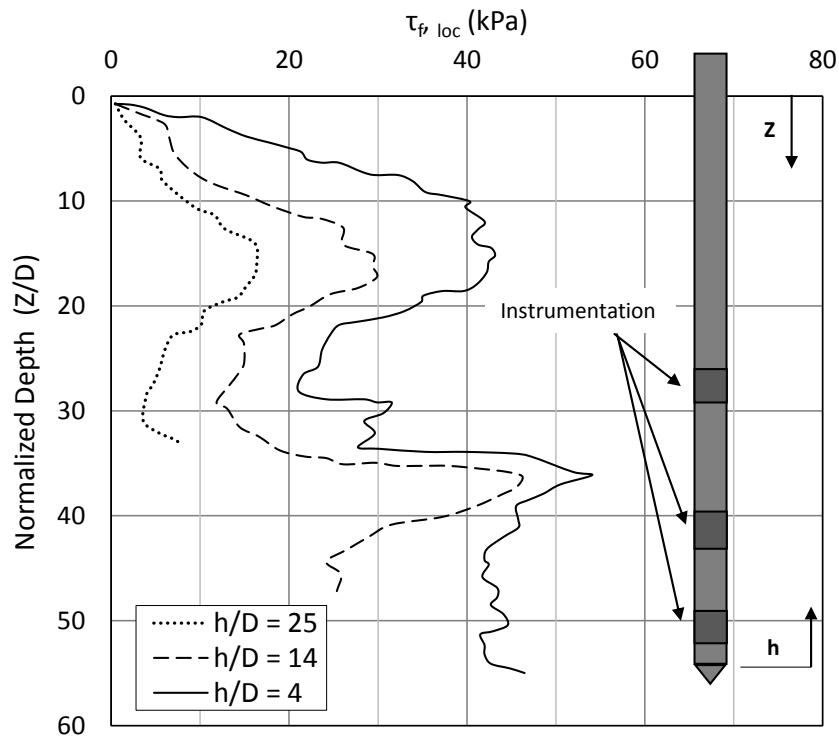


Figure 2-12: Measured profiles of local shear stresses, after Lehane et al. (1993)

Concerning the initial state of soil ( $\sigma'_{rc}$ ), it is noted that ( $\sigma'_{rc}$ ) is a function of the pile tip resistance and the relative position of the pile tip ( $q_b$  and  $h/D$ ). Thus, the authors concluded that the initial state of soil ( $\sigma'_{rc}$ ) and distance from the pile tip have a great impact on the stress on any soil horizon. In addition, the results and analysis show that the constant volume friction angle ( $\delta_{cv}$ ), which is independent of relative density, controls the shaft resistance. It is noticed that the highest stresses are mobilized close to the pile tip, whereas the stabilization of the average ultimate local shear stress ( $\tau_{av}$ ) with pile depth results from the tendency of the initial state of soil ( $\sigma'_{rc}$ ) to reduce at all levels as the relative pile-tip depth ( $h/D$ ) increases.

Chaw (1997) used the same Imperial College Pile (ICP) pile that was used by Lehane et al. (1993) at a different site where the soil density was higher. Both found that ( $\sigma'_{rc}$ ) values at a given level on the

pile were almost directly proportional to the value of the cone penetration test (CPT) end resistance ( $q_c$ ) at the same level and the normalized distance from the tip ( $h/D$  or  $h/R$ ). Interestingly, it is found that ( $\sigma'_{rc}$ ) at a given level decreases as the distance from the tip ( $h$ ) increases which is referred to as friction fatigue. Jardine et al. (2005) evolved these findings to propose best-fit relationship to estimate ( $\sigma'_{rc}$ ), known as Imperial College Pile (ICP) design method, as follows;

$$\sigma'_{rc} = 0.029q_c (\sigma'_v/P_a)^{0.12} (h/R)^{-0.38} \quad (2-24)$$

where ( $\sigma'_v$ ) is the vertical effective stress, ( $P_a$ ) is the atmospheric pressure, and ( $R$ ) is pile radius. The ( $h/R$ ) in equation (2-24), which has a minimum value of 8, considers the friction fatigue effect.

Jardine et al. (2005) listed few factors that explain the friction fatigue phenomena, including (1) reduction in the horizontal stress at a given level because of the migration of the high stress field available around the pile tip as the pile is penetrating past the level concerned; (2) cyclic loading during installation; (3) soil arching which reduces the radial effective stress from acting on the pile shaft. Gavin and O'Kelly (2007) stated that the maximum shear stress on the shaft of displacement piles is near the tip because of the driving effect where high residual stresses build up around the base during the installation. Based on a large database, Lehane et al. (2005) proposed a best-fit relationship to the field data known as the University of Western Australia (UWA) design method which is expressed as follows;

$$\sigma'_{rc} = a q_c (h/D)^b \quad (2-25)$$

where factor “a” and “b” are 0.03 and -0.5, respectively. In equation (2-25), a minimum ratio ( $h/D$ ) of 2 should be used.

White and Lehane (2004) investigated the effect of the number of load cycles ( $N$ ) on the stationary horizontal effective stress ( $\sigma'_{rc}$ ) through a series of centrifugal tests. They found that ( $\sigma'_{rc}/q_c$ ) does not produce a unique relationship with  $h/D$ , rather, it varies with the number of loading cycles ( $N$ )

experienced during installation. They concluded that friction fatigue does not occur in the absence of loading cycles.

Gavin and O’Kelly (2007) provided data based on field pile load tests that agree with White and Lehane’s results where the value of  $(\sigma'_{rc}/q_c)$  was the highest when  $(N=1)$  and decreases as the  $(N)$  increases. These findings were used by Basu et al. (2011) as a base to study the shaft resistance of piles jacked into sand using one-dimensional finite element analysis. As a result, they proposed equations to quantify the effect of using different number of jacking strokes on shaft resistance.

Flynn and McCabe (2015) studied the shaft resistance of driven piles cast-in-situ piles in sand by performing three field pile load tests. All piles were instrumented with strain gages at different levels of the piles to find the local shear stress generated on the pile shaft. The local shear stress, in this case, would be the difference between two strain gauges. The pile load tests showed a reduction in the normalized local shear stress  $(\tau_{local} / q_c)$  at failure, and consequently the effective radial stress, with the distance from the pile tip which is in line with concept of friction fatigue that was introduced by Lehane et al. (1993). Figure 2-13 shows the one pile used in this test and its corresponding local shear stress. The same figure shows the local shear stress distribution along the shaft of the pile.

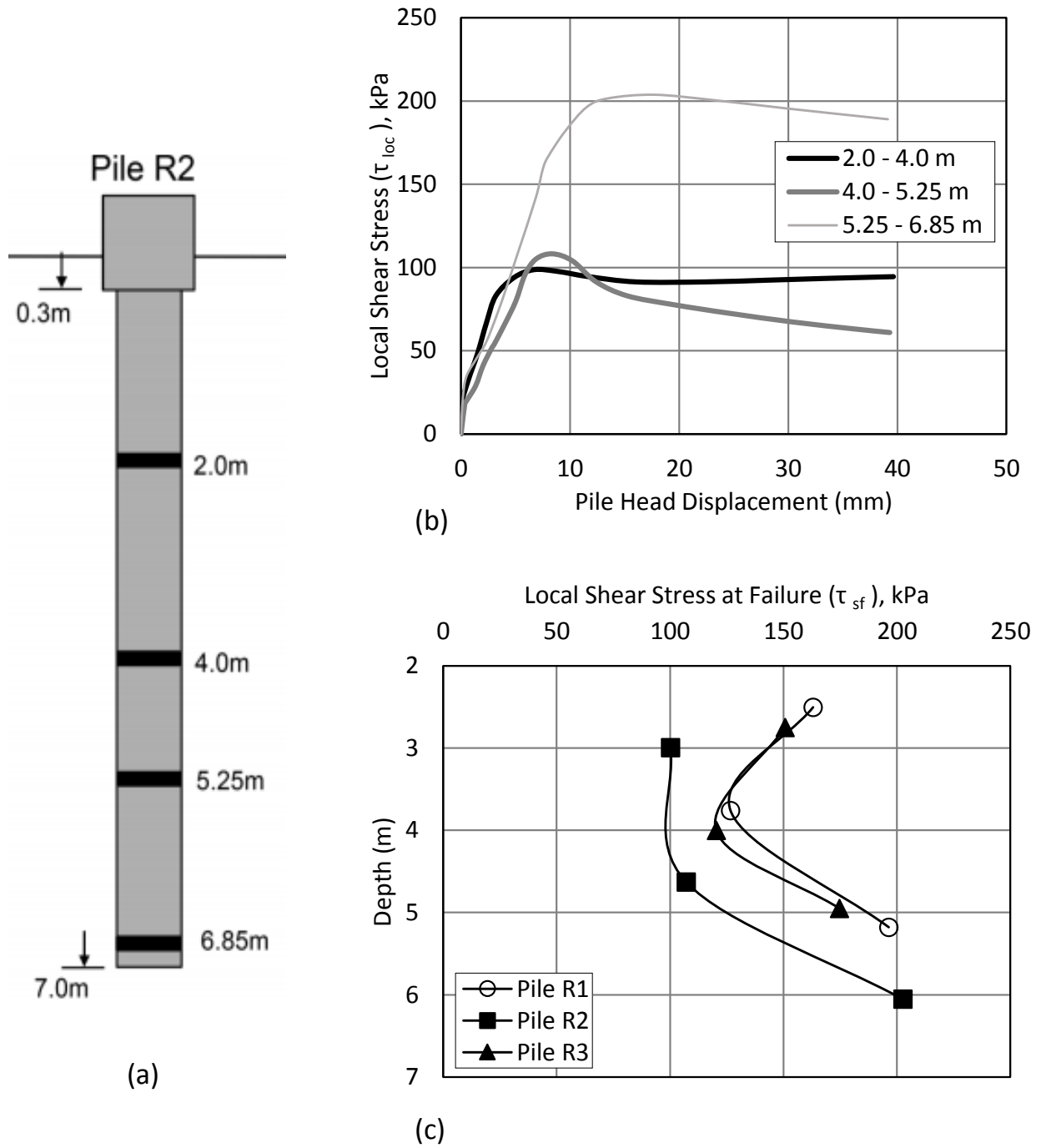


Figure 2-13: (a) Pile instrumentation; (b) local shear stress for pile R2; (c) local shear stress distribution for all pile load tests, after Flynn & McCabe (2015)

## 2.3 Measurement of Overconsolidation Ratio (OCR)

Retrieving an undisturbed cohesionless soil sample to measure the stresses with laboratory tests is difficult. This problem forced researchers to seek alternative methods to measure the horizontal forces to quantify earth pressure coefficient ( $K_0$ ), and accordingly the overconsolidation. There are many field tests that can reveal good estimation of the overconsolidation ratio such as Cone Penetration Test (CPT), Stepped Blade Test, and Pressuremeter Test (Sivakugan & Das, 2010).

Based on field data of (CPT), Mayne (1991) proposed an equation to find ( $K_0$ ) in cohesionless soil as expressed in equation (14).

$$K_0 = \frac{(P_a / \sigma'_v) (q_c / P_a)^{1.6}}{145 \exp \left\{ \left[ \frac{(q_c / P_a) / (\sigma'_v / P_a)^{0.5}}{12.2 \text{ OCR}^{0.18}} \right]^{0.5} \right\}} \quad (2-26)$$

where ( $K_0$ ) is the at rest lateral earth pressure, ( $q_c$ ) is the cone tip resistance, ( $P_a$ ) is a reference stress equal to one atmosphere (1 bar = 100 kPa), ( $\sigma'_v$ ) is the vertical effective stress, and (OCR) is the overconsolidation ratio. When any equation presented earlier for ( $K_0$  (OC)) is substituted to the left side of this equation, the OCR can be calculated.

Another field test proposed to find the value of lateral earth pressure coefficient ( $K_0$ ) is  $K_0$  Stepped-Blade test. This test was developed by Richard Handy (1970). It consists of a long blade that has four steps. Each step is 100 mm long and every step has different thickness. The top step is 7.5 mm thick and the bottom step is 3 mm thick. A pneumatic pressure cell flush with the flat surface is placed in every step. Because of these thin thicknesses, the soil disturbance is minimized when these blades are pushed into the soil. To perform this test, the first step of the blade is pushed into the soil where the soil pressure  $P_1$  is recorded by the pneumatic pressure cell. Then, the second step is pushed into the soil where the pressures  $P_1$  and  $P_2$  are measured. This process continues until all steps are pushed into

the soil and then an extra push is made to have a total of 14 measurements for  $P_1$ ,  $P_2$ ,  $P_3$  and  $P_4$ . To find  $(K_0)$ , the logarithm of measured pressure is plotted versus the blade thickness as shown in Figure 2-14 (a). The pressure correspond to Zero blade thickness ( $P_0$ ) is extrapolated from the figure. This pressure  $P_0$  represent the actual horizontal pressure, which is used to calculate  $(K_0)$ . The (OCR) can be determined using any equation presented earlier for  $(K_{0(OCR)})$  knowing the value of lateral earth pressure coefficient ( $K_0$ ) obtained in this test.

Pressuremeter test is also used to find the lateral earth pressure ( $K_0$ ) which can be correlated to the OCR. In a borehole, the pressuremeter device applies a uniform pressure to the walls and measures stresses and deformations of the wall. These stresses and deformations measured during the test are used to interpret the soil properties and the soil stress state. Conceptually, the pressuremeter device consist of deformable rubber membrane in a cylindrical form which inflates laterally to deform the soil as shown in Figure 2-14 (b). Interpretation of the resulted stresses and deformations in a pressuremeter test is based on cavity expansion theory. The parameters that are used in this test are presented in Figure 2-14 (b).

The radius of the cavity ( $\rho_0$ ) is found when pressure ( $P$ ) is equal to the initial horizontal stress in the soil ( $\sigma_h$ ). Once the cavity pressure ( $P$ ) becomes larger than ( $\sigma_h$ ), the cavity starts to deform initiating a new radius ( $\rho$ ). Therefore, the pressure ( $P$ ) just before the deformation of the cavity can be used to estimate the lateral earth pressure coefficient at rest ( $K_0$ ). This measurement can only be found using the self-boring types of pressuremeter (Potts et al., 2001).

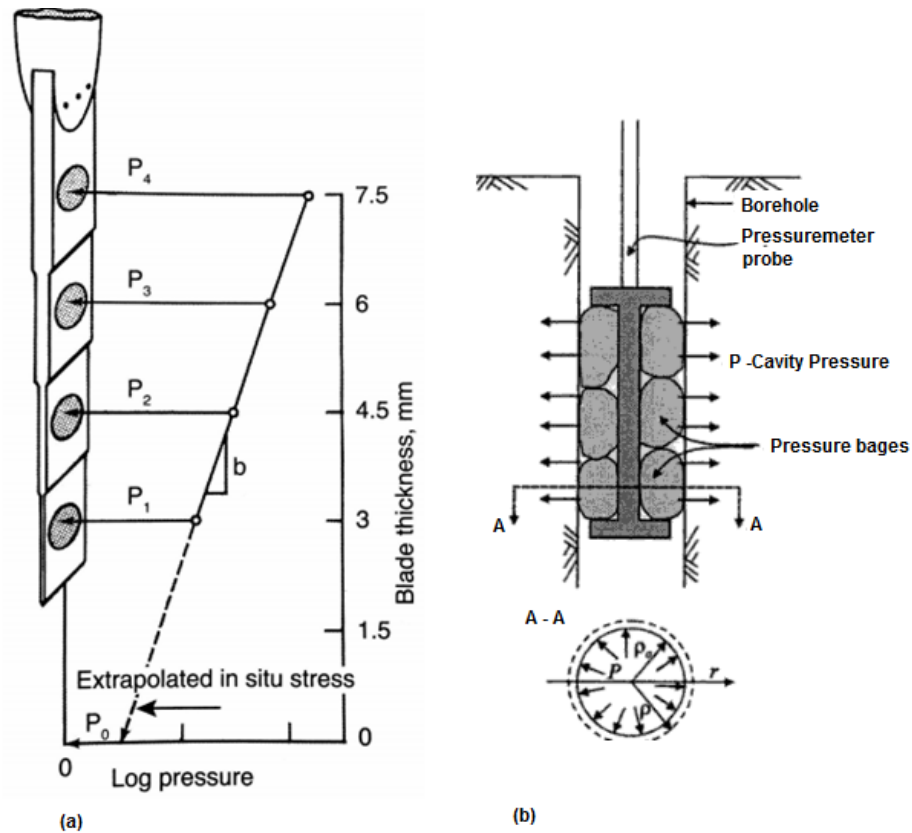


Figure 2-14: (a) Stepped Blade Test, adopted from Sivakugan and Das (2010); (b) Pressuremeter Test, adopted from Potts et al. (2001)

## 2.4 Effect of OCR on Pile Capacity

Beringen et al. (1979) performed compressive and tensile field pile load tests in Hoogzand in the Netherlands. The site contains dense overconsolidated sand. Both open and closed-ended piles are 356 mm diameter where the embedment depth is 7 m and 6.75 m, respectively. Comparing the test results with four designing methods, it was observed that the shaft resistance exceeded the recommended limits by 100 to 200 %. Figure 2-15 illustrates the compression test results for an open-ended pile (I-c) and a closed-ended pile (II-c) in comparison with the predicted shaft resistance obtained from the

four designing methods with and without applying the limiting value of shaft resistance recommended by each designing method.

Foray et al. (1998) studied the effect of overconsolidation on the bearing capacity of driven piles experimentally. Their intention is to improve the American Petroleum Institute (API) design parameters of piles to provide a safe and less conservative bearing capacity and reduce the construction cost of piles. The experimental investigation was performed on dense and very dense sand which represent the North Sea soil condition since many offshore structures are involved in that zone. Their design procedure considered that there is no limiting value “no critical depth” for tip and shaft resistance, also that an optimistic value is chosen for lateral earth pressure coefficient ( $K_0$ ) which is a higher value than that suggested by American Petroleum Institute (API).

Experimentally, an open-ended model pile of 70 mm diameter was used. Pile load tests were conducted in a large calibration chamber for both compression and tension for 0.75 and 1.00 m embedment length. Using a servo-jack attached to the calibration chamber to impose regulated boundary conditions, a lateral earth pressure coefficient ( $K_0$ ) of 1 and 2 were reached. Pluviation method was used to prepare the sand where a relative density of 80% was obtained by a constant free fall flow. For a relative density of 100%, vibration was used. Their experiment showed the effect of overconsolidation for both tip and shaft unit resistances as shown in Figure 2-16.

The general equations that the API uses to calculate unit shaft and unit tip resistance are presented in equation (2-27) and (2-28). The authors presented, in Table 2-5, a comparison between the proposed design parameters that consider the increase of ultimate bearing capacity due to the overconsolidation and the API design parameters which do not account for overconsolidation. Moreover, the authors proposed different values for designing parameter of  $\beta$  and  $\alpha$  when (CPT) is used.

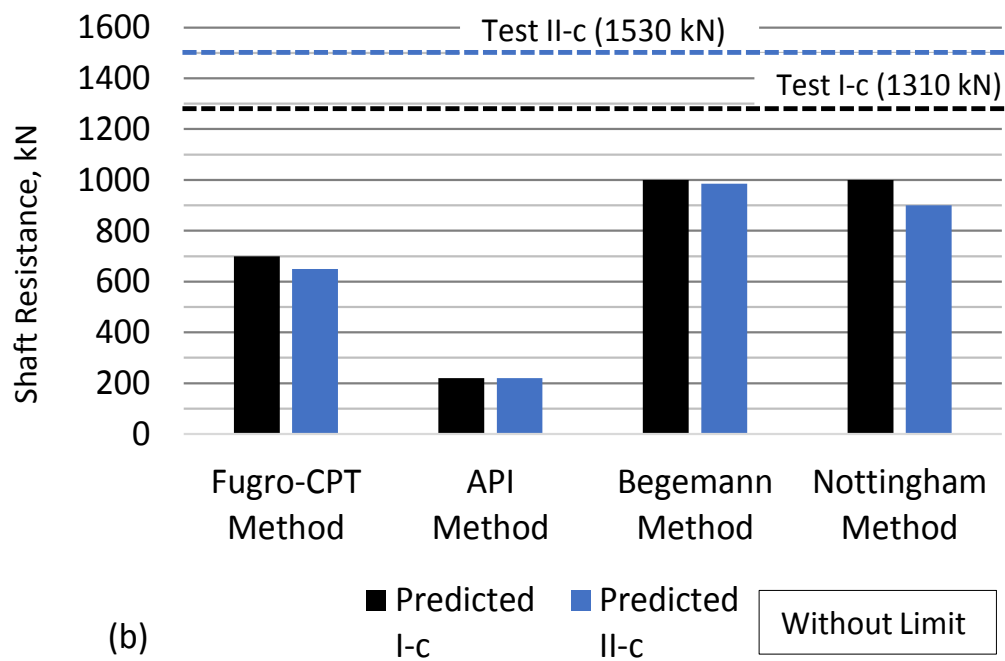
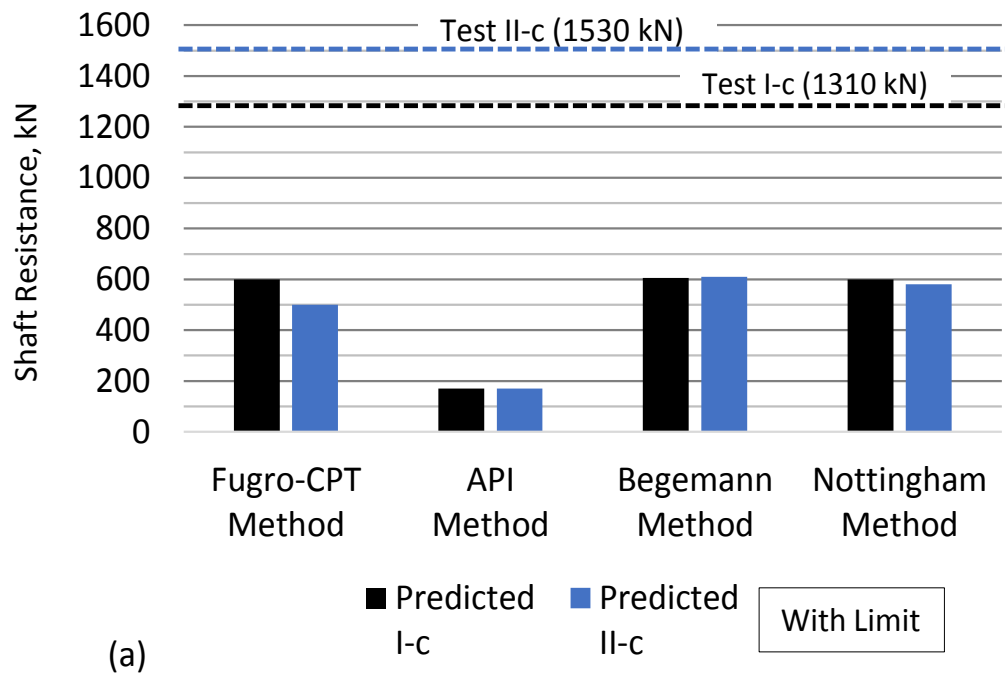


Figure 2-15: Results of Beringen et al. (1979) comparing measured and predicted shaft resistance (a) with limiting, and (b) without limiting shaft resistance value

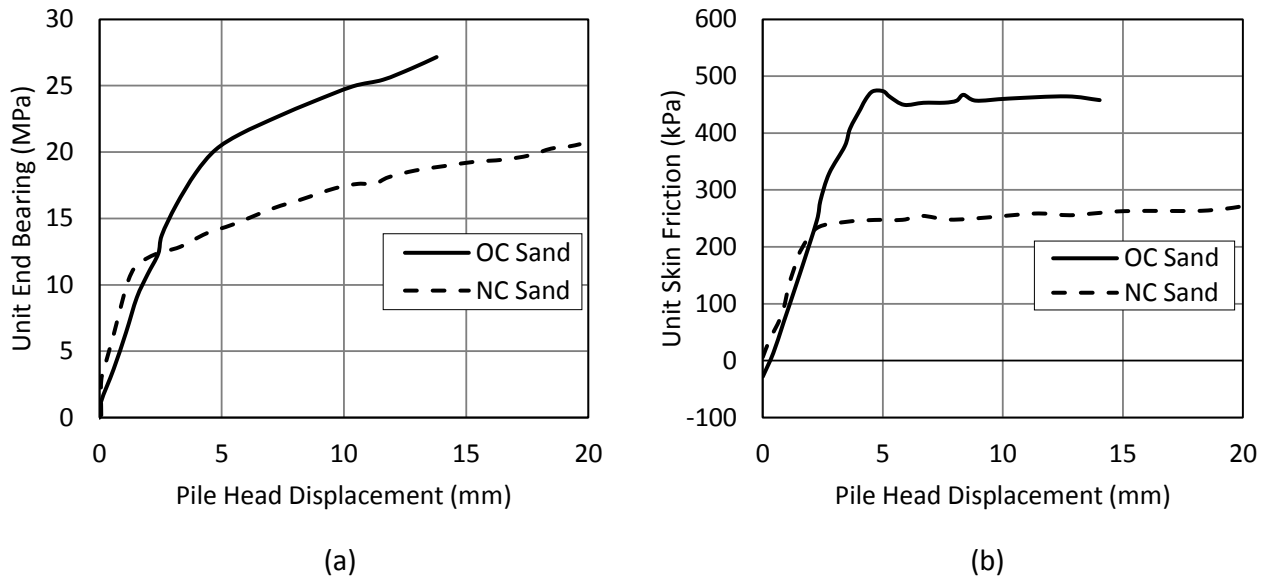


Figure 2-16: (a) Influence of overconsolidation on unit end bearing capacity (b) Influence of overconsolidation on average unit skin friction, after Foray et al. (1998)

Table 2-5: Proposed design parameters and API RP 2A design criteria after Foray et al. (1998)

Soil	$D_r$	$q_c$ (MPa)	K	$\delta$ (degree)	$N_q$	$q_{lim}$ (MPa)	$f_{lim}$ (kPa)
NC dense sand	65-85%	>20 at 20 m >30 at 60 m	C = 1 T = 0.9	30	40	12	C = 120 T = 100
		<b>API</b>	(C = T = 0.8)	(30)	(40)	(9.6)	(C = T = 96)
OC	85-100%	>30 at 20 m >45 at 60 m	1	35	60	15	C = 150 T = 135
NC very dense sand	65-85%	>35 at 20 m >45 at 60 m	C = 1 T = 0.9	35	60	16	C = 150 T = 135
		<b>API</b>	(C = T = 0.8)	(35)	(50)	(12)	(C = T = 115)
OC	85-100%	>45 at 20 m >60 at 60 m	1 to 2	40	80	20	C = 200 T = 180

$$f = K \sigma'_v \tan \delta \quad (2- 27)$$

$$q = \sigma'_v N_q \quad (2- 28)$$

This study shed some light on the effect of overconsolidation on the bearing capacity of driven piles in cohesionless soil. However some drawback points were noticed. This study represented the overconsolidation as a high value of ( $K_0$ ) without representing the actual (OCR). Furthermore, this study was performed on dense and very dense sand where lower densities were not investigated.

Another experimental and theoretical studies were performed by Hanna and Ghaly (1992) on the effects of ( $K_0$ ) and overconsolidation on the uplift capacity of an anchor piles screwed in sand. Although their study is not about compression load, but it is worth mentioning because of the valuable results achieved that show the influence of (OCR) on the shaft resistance. Experimentally, the soil was subjected to vibratory compaction which induces high horizontal stresses. Due to this vibration process, the lateral earth pressure coefficient ( $K_0$ ) as well as the (OCR) was increased. It was found that the uplift capacity of the anchor pile increases with increasing the (OCR) as shown in Figure 2-17. Sabry (2005) developed a 2 D numerical model, using cavity expansion technique, to simulates the pile installation and perform pile load test to study the shaft resistance of single piles. Plaxis software was used in this study. It was found that the ( $K_s$ ) values around the shaft of piles as well as the OCR values were increased due to installation as shown in Figure 2-18. It is of interest to know that the OCR values were found according to the passive earth pressure developed due to installation. Based on the results of the pile load test performed numerically, the distribution of the earth pressure and accordingly the shaft resistance along the pile shaft was found to consist of three zones as shown in Figure 2-19 (a) and (b). The extent of each zone is a function of pile diameter (D), pile length (L) and the angle of shearing resistance ( $\phi'$ ). According to this finding, an analytical model was proposed to find the shaft resistance using limit equilibrium analysis.

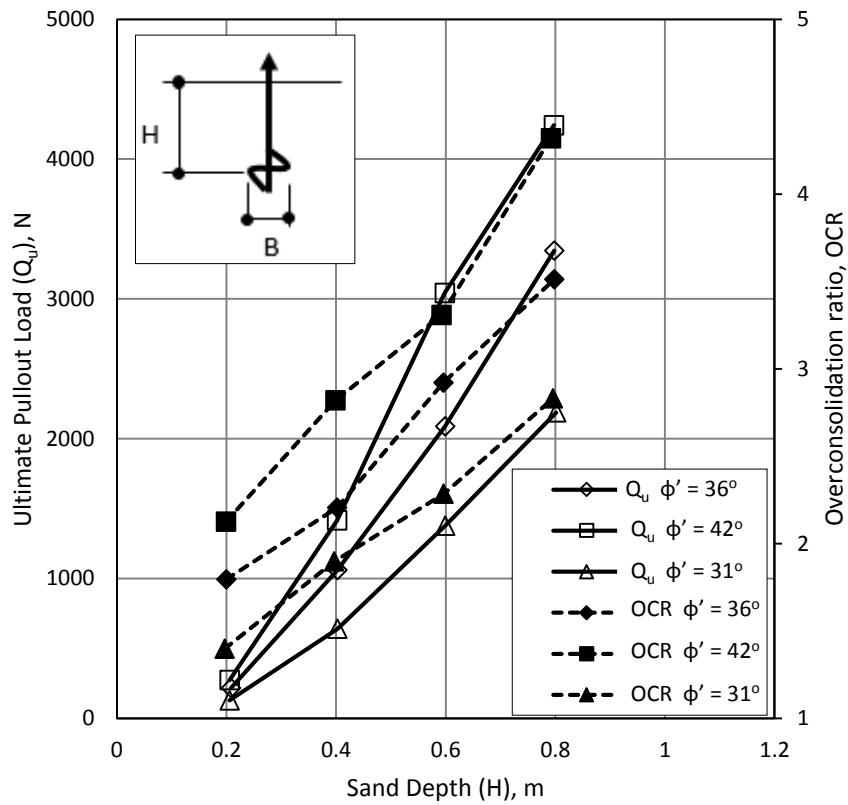


Figure 2-17: Sand depth versus ultimate pullout load and OCR, after Hanna and Ghaly (1992)

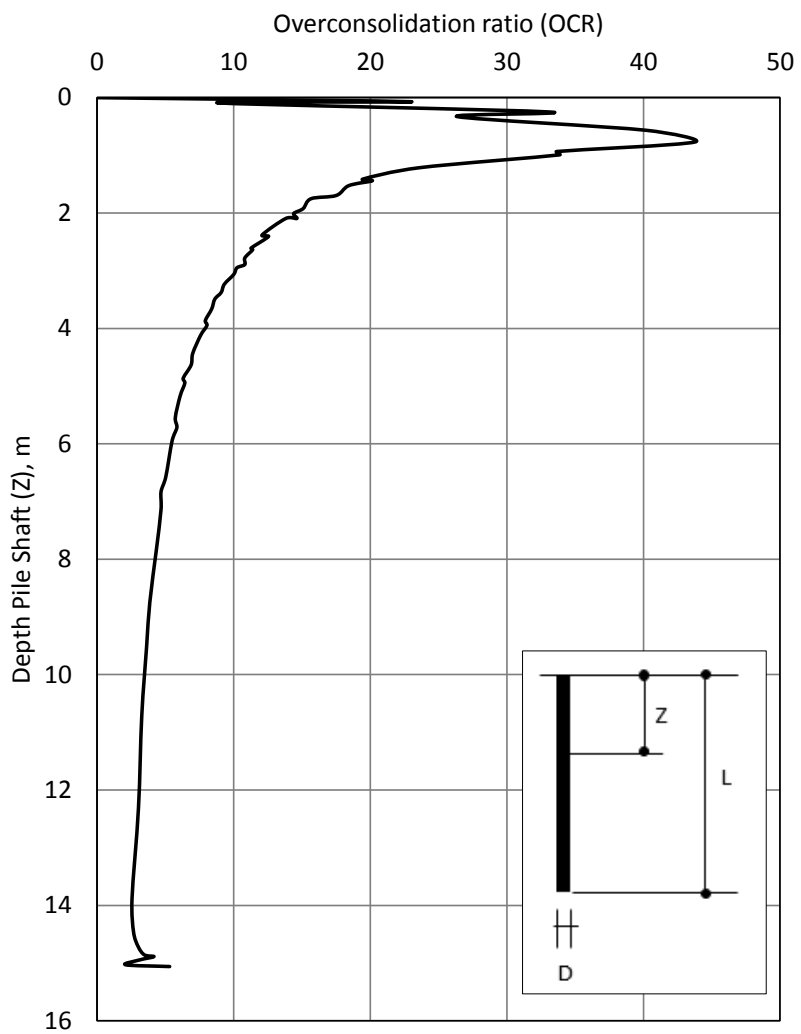


Figure 2-18: OCR distribution around the pile shaft, after Sabry (2005)

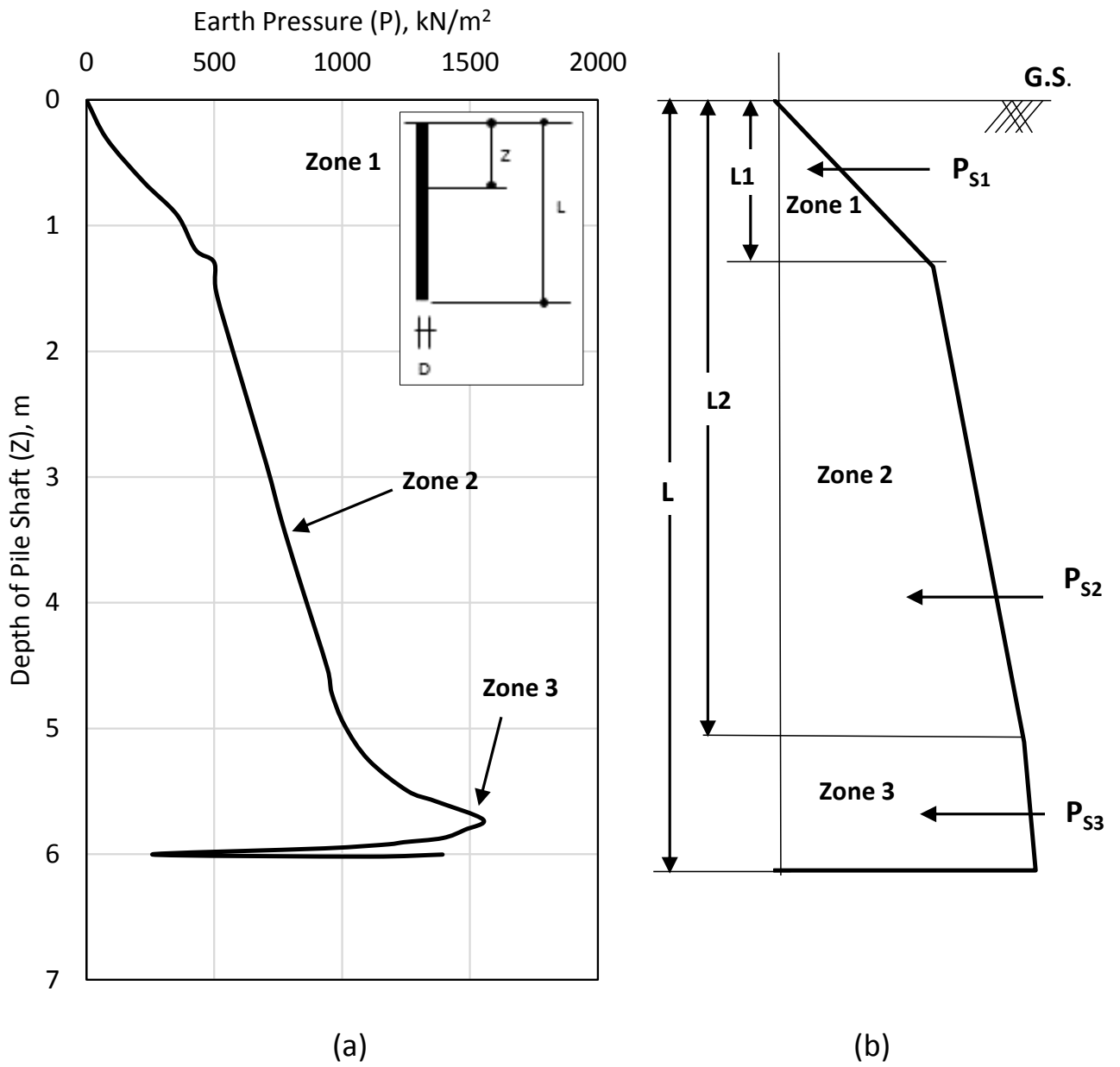


Figure 2-19: (a) Earth pressure distribution around the pile shaft, (b) Idealized earth pressure zones, after Sabry (2005)

DiCamillo (2014) studied experimentally the effect of stress history in sand, which is represented by the over-consolidation ratio (OCR), on shaft resistance of piles. The (OCR) affects lateral earth pressure which consequentially affects the shaft resistance of single piles. He designed a setup that can measure the applied load at the top and the base of piles where the shaft resistance is found as the difference between these two values.

In his experiment, he used a steel tank with an area of 1 m X 1 m and a depth of 1.25 m. Four vertical and horizontal load transducers were installed at the sides of this tank to capture the vertical and horizontal applied load. The tank was filled with sand up to a height of 1.05 m in layers (0.15 m) where each layer was introduced to a constant compaction effort. The density was found after the fill was completed by the cans that were placed in every layer. The (OCR) was measured by the load cell attached to the sides as presented in Figure 2-20. The diameters of the two piles he used were 28.6 mm and 50.8 mm and both are 800 mm in length where two load transducers were installed at both ends to measure the applied load and the base resistance. Both piles were attached to selected sandpapers in which the pile-soil friction angle is a unity. The experimental results, as shown in Table 2-6 for the 50.8 mm diameter, show the influence of the OCR on the shaft resistance.

Analytically, he adopted a model that was proposed by Hanna and Nguyen (2002), which accounts for the interaction between tip and shaft resistance in normally consolidated sand. DiCamillo (2014) was only concerned about the shaft resistance which he quantified experimentally. Therefore, the experimental results for the shaft resistance were fitted in Hanna and Nguyen's model to come up with an analytical procedure which can calculate the shaft resistance of piles in overconsolidated sand.

The analytical analysis for shaft resistance that DiCamillo (2014) used considers the external and internal forces applied to the pile and its zone of influence in a way that accounts for the dependency of tip resistance and shaft resistance on each other as shown in Figure 2-21. If the value of ( $\beta'$ ) angle

changes with depth, both tip and shaft resistances will change accordingly. Therefore, the main challenge in DiCamillo's analytical work was to find the appropriate ( $\beta'$ ) angle that corresponds well with the experimental results. To involve the (OCR) in this model, the overconsolidation ( $K_0$ ) at rest that was proposed by Hanna and Al-Romhein (2008) was used.

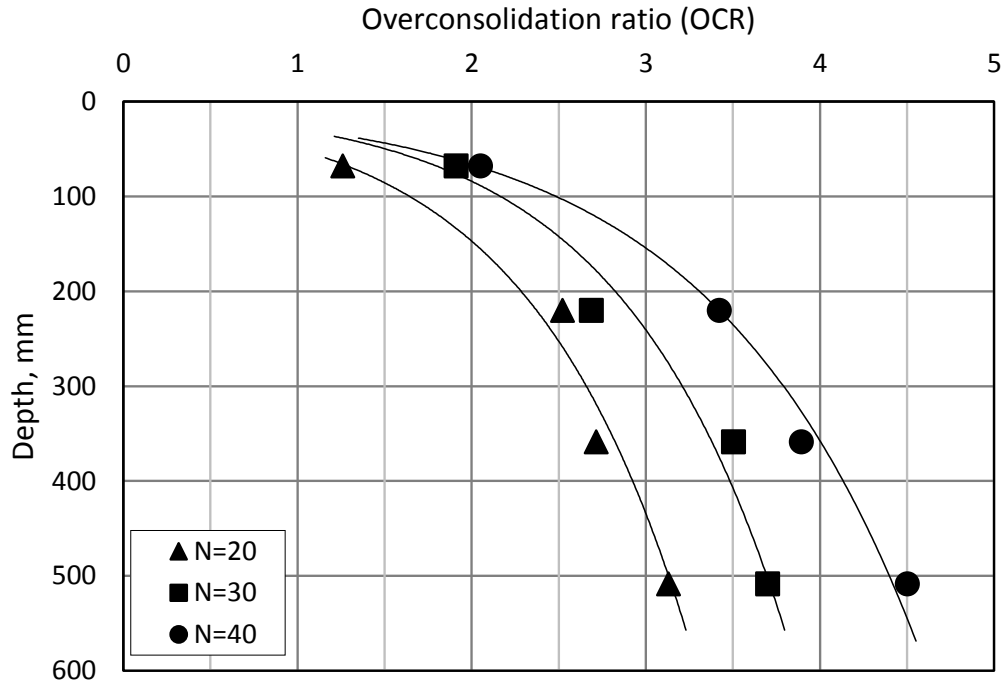


Figure 2-20: Values of OCR at various depths for different compaction effort, after DiCamillo (2014)

According to Hanna and Nguyen's (2002) model, the lateral earth pressure inside the zone of influence is a hydrostatical pressure where the active earth pressure coefficient ( $K_{ac}$ ) was used. The lateral earth pressure at rest for normally consolidated sand was used to calculate the forces applied on the zone of influence from the soil surrounding this zone as shown in Figure 2-21. DiCamillo (2014) followed the same steps to calculate the shaft resistance, but assuming the normally consolidated lateral earth

pressure coefficient at rest for sand ( $K_{0(NC)}$ ) inside the zone of influence, and the overconsolidated lateral earth pressure coefficient at rest for sand ( $K_{0(OC)}$ ) outside the zone of influence.

Table 2-6: Pile load test for 50.8 mm diameter model pile, after DiCamillo (2014)

Model Pile	Compaction (Drops)	Relative depth (L/D)	Ultimate Capacity, $Q_u$	Tip Resistance, $Q_t$	Shaft Resistance, $Q_s$
			(N)	(N)	(N)
50.8 mm Diameter	20	5.4	1814.85	1761.87	52.97
		8.4	3075.43	2913.57	161.86
		11.4	4336.02	3943.62	392.40
		13	5209.11	4581.27	627.84
	30	5.4	2223.92	2151.33	72.59
		8.4	3899.47	3673.84	225.63
		11.4	5689.80	5169.87	519.93
		13	6670.80	5856.57	814.23
	40	5.4	2398.54	2305.35	93.19
		8.4	3904.38	3619.89	284.49
		11.4	5890.90	5233.63	657.27
		13	6847.38	5745.71	1098.72

DiCamillo (2014) found that relative depth of piles in OC sand influences shaft resistance and the coefficient of earth pressure around the pile. Also, he found that the stress history (OCR) has a significant effect on the coefficient of earth pressure which in turn affects the shaft resistance. He proposed a relation between the relative length of piles and the (OCR) of sand to find the appropriate ( $\beta'$ ) angle which is used in the proposed analytical procedure to calculate the shaft resistance.

Experimentally, DiCamillo (2014) measured the vertical stress after compaction, using sensors fixed at the sides of the tank, to quantify the OCR at deferent levels across the tank. Unfortunately, this approach raises doubt about the values and accuracy of the OCR deduced. Fixing the sensors on the sides of the tank causes the soil above the sensors to be more compacted than the rest of the tank. Accordingly, the sensors measure higher values because the sensors do not move with the soil

vertically during compaction. Also, the sensors should have been placed far from the sides of the tank to avoid the boundary effect (Ansari et al., 2018).

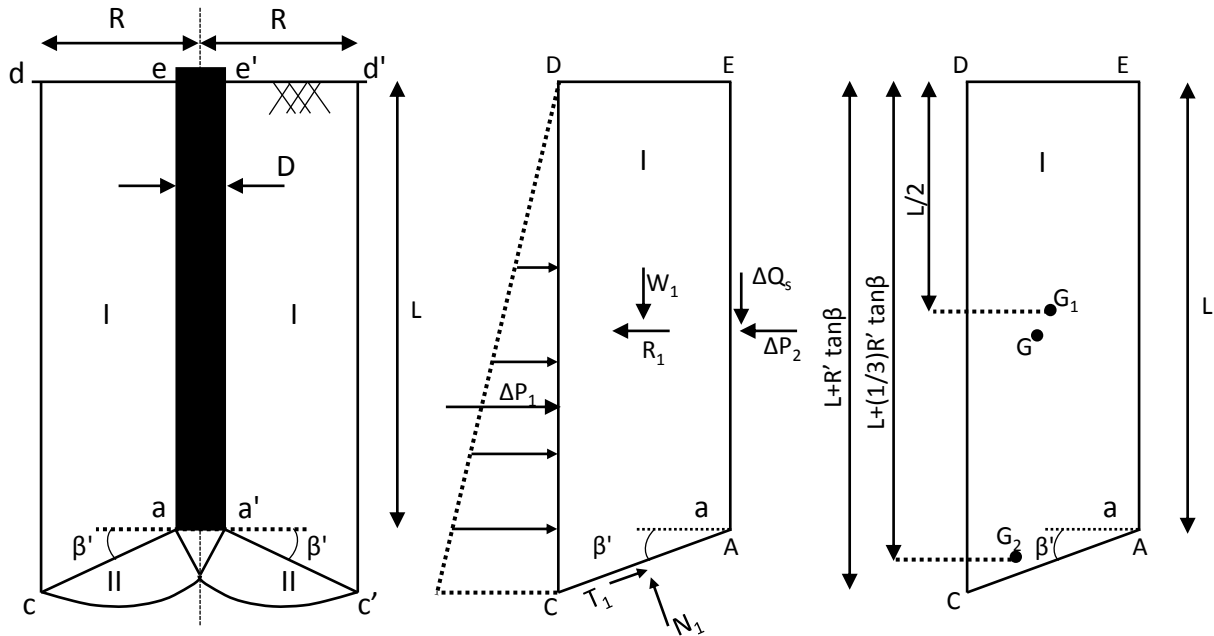


Figure 2-21: Failure zone and forces applied around the pile's shaft, after Hanna and Nguyen (2002).

## 2.5 Discussion

Literature addressing parameters that affect the shaft resistance of driven piles in cohesionless soils reveals that conventional methods of predicting the capacity of a single pile in sand have prompted a range of discrepancies (Hanna & Nguyen, 2002; Poulos & Davis, 1980). Moreover, no proposed method of calculating such shaft resistance takes all parameters into account (Niazi & Mayne, 2013). Values proposed for  $(K_s)$  and  $(\delta)$  by different researchers to calculate shaft resistance range widely and thus cast doubt on their estimation, as does limiting shaft resistance to various values according to different methods. To illustrate such uncertainty, the ratios of calculated field shaft resistance to measured field shaft resistance ( $Q_c / Q_m$ ) for 81 piles were determined by using the American

Petroleum Institute's design procedure (Jardine et al., 2005). Although the ratios ideally should have been 1, most were below unity when plotted against the embedment depth ( $L/D$ ), which indicates that shaft resistance was underestimated when calculated, partly due to the overconsolidation of cohesionless soil (Figure 2-22). The literature also suggests that the OCR increases the shaft resistance of driven piles in cohesionless soil, although few investigations into the effect of overconsolidation on shaft resistance have been performed. Therefore, more experimental, analytical, and numerical studies are needed to develop design charts and design procedures that consider the effect of overconsolidation, as well as to make the ( $Q_c / Q_m$ ) ratio closer to 1.

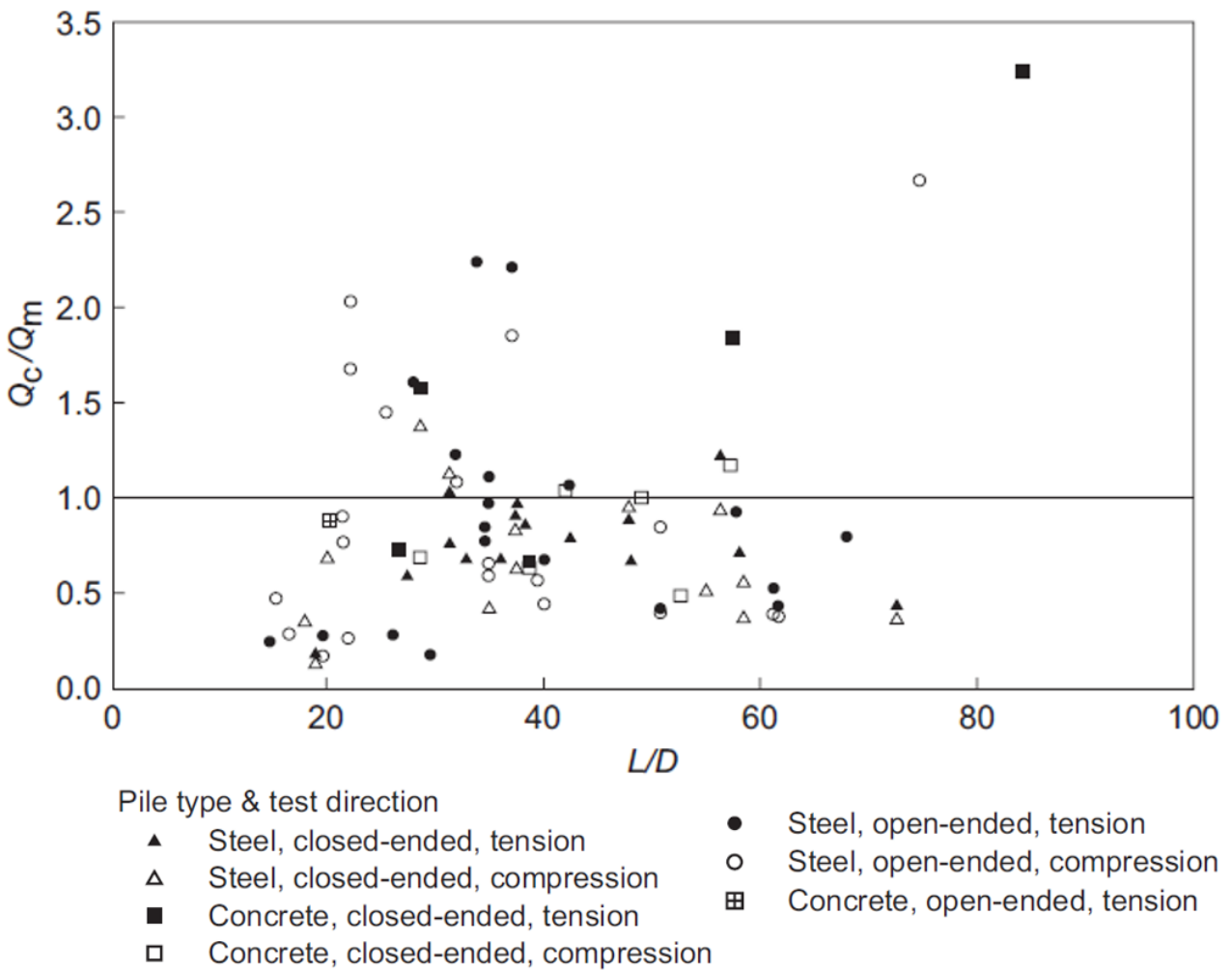


Figure 2-22: Distribution of  $Q_c / Q_m$  with respect to embedment depth ( $L/D$ ), after Jardine et al. (2005)

Last, the critical depth has remained controversial since its introduction several decades ago. Literature on the concept presents arguments both for and against its use, which continues given the lack of consensus.

In response to those concerns, the key objective of the research conducted for this thesis was to investigate the effect of overconsolidation on the shaft resistance of driven piles in cohesionless soil. Experimentally, a large tank was designed to measure the OCR and stresses in sand. A sand-placing technique and compaction method were developed to identify a uniform relative density and overconsolidation of the soil, after which 18 pile load tests were performed in overconsolidated sand using two pile models at three uniform relative densities with different OCR values. The total load applied to the pile was measured at different heights using load cells embedded in the pile models. Those measurements were used to partition the shaft resistance and determine its distribution along the length of the shaft.

Next, the horizontal slice method was applied to develop a model to predict the capacity of shaft resistance of driven piles in normally consolidated cohesionless soil. A database of laboratory and field pile load tests collected from extensive published geotechnical data was entered into the model. Last, a three-dimensional numerical model was also developed using ABAQUS to establish the relationship between  $\beta = K_s \tan \delta$  and shaft resistance. Experimental results were used to validate the model, after which results from experimental, analytical, and numerical research were used to generate a design procedure and design charts to predict shaft resistance in overconsolidated cohesionless soil.

## Chapter 3 : Experimental Investigation

### 3.1 General

Pile load tests are usually performed for three reasons; (i) as part of field investigations to inform adequate design, (ii) in proof tests to determine the capacity of a specific pile as a means to ensure its compliance with design values, and (iii) in research investigations to study the behaviour of piles, from which theories are developed to predict pile capacity and settlement (Fellenius, 1975). The pile load tests performed for this thesis were purely for research to examine the effect of overconsolidation on the shaft resistance of pile foundations.

Pile load tests in laboratories require the identification of soil properties, and the soil-placing technique should be determined beforehand. The experimental investigation reported here consisted of three phases: soil tests, sand placing and compaction tests, and pile load tests. For soil tests, a series of laboratory tests (e.g., sieve analysis, specific gravity tests, relative density, and direct shear tests) were performed on the soil to identify its properties.

To perform pile load tests, an experimental setup was designed in the Foundations Lab at Concordia University that consisted of a steel tank  $1\text{ m} \times 1\text{ m}$  in area and 1.25 m high to contain the soil and a reaction beam at the top to carry an electronic actuator to drive the piles and perform the tests. A soil-placing technique and compaction method were developed to determine the amount of energy required to achieve a certain relative density for a large tank. Stresses induced in the soil mass due to compaction were quantified by using load cells placed inside the soil mass to capture the vertical stresses. Accordingly, the variation of the OCR for uniform cohesionless soil by the number of drops was determined.

Two pile models were fabricated. With the first pile model, 55 mm in diameter, the load–settlement behaviour of driven piles in cohesionless soil was determined for the pile head (i.e., total), pile tip (i.e., base), and two other locations in between. Shaft resistance of the total pile was calculated as the difference between the top and bottom load cells, and shaft resistance for each of the three pile sections was calculated as the difference between the load cells attached to both ends of each section. The second pile model, with a diameter of 30 mm and height of 800 mm, was used to determine the load–settlement behaviour for the pile head (i.e., total) and pile tip (i.e., base), and total shaft resistance was calculated as the difference between the top and bottom load cells. Both piles were tested in three uniform relative densities (i.e., 30%, 45%, and 60%) and at different embedment depths.

The experimental investigation involved various pieces of equipment and materials (Figure 3-1). A steel tank was designed to contain the soil, and pile models were fabricated and instrumented to measure the load at different locations. Silica sand was chosen to represent the cohesionless soil. An electronic actuator was also used to drive the pile and perform the pile load tests. Details of the equipment, materials, and procedure used for the pile load tests, as well as the results, are explained in what follows.



Figure 3-1: Actual experimental setup

### 3.2. Testing Setup

To contain the soil, a steel tank 1 m × 1 m in area and 1.25 m tall was constructed of 6.5-mm thick steel plates braced at the middle by a steel angle to deter buckling. On top of the steel tank, two C 8-column sections were mounted, to which a reaction beam (W 8 × 5 – ¼) was attached by height-adjustable bolts to carry the loading system vertically (Figure 3-2a).

Two tests are used to apply compressive load upon piles. First, in the constant rate of penetration (CRP) test, the applied load on the pile head is continuously increased to force the pile to penetrate the soil at a constant rate until failure is reached. The CRP test is commonly used in investigations because it is quick, defined well, and easy to interpret and can have a clear peak value. Second, in the maintained load test, the load applied to the pile head is increased in stages to multiples of the working load, and the settlement time is recorded for each stage. The maintained load test can be slow or quick based on the amount of working load fraction used in each stage of loading and its duration (Tomlinson & Woodward, 2014). Therefore, the CRP method was chosen to perform all tests in the research reported here.

To drive the pile to the selected depth and perform pile load tests, an electronic loading system was adopted that consisted of an EC5 Electric Cylinder Actuator and an AKD Servo Driver (Figure 3-2b, c). The actuator could apply a maximum load of 25 kN, and the servo drive could control the movement of the actuator stroke by using the software Kollmorgen WorkBench, which permitted strain-controlled tests.

A data acquisition system manufactured by Agilent Technologies (34972A) was used to collect all test results. Once collected, all data were transmitted and saved in a computer. Initially, the system was used to collect vertical stresses after soil preparation; later, it monitored the driving process and recorded pile resistance during the pile load tests.

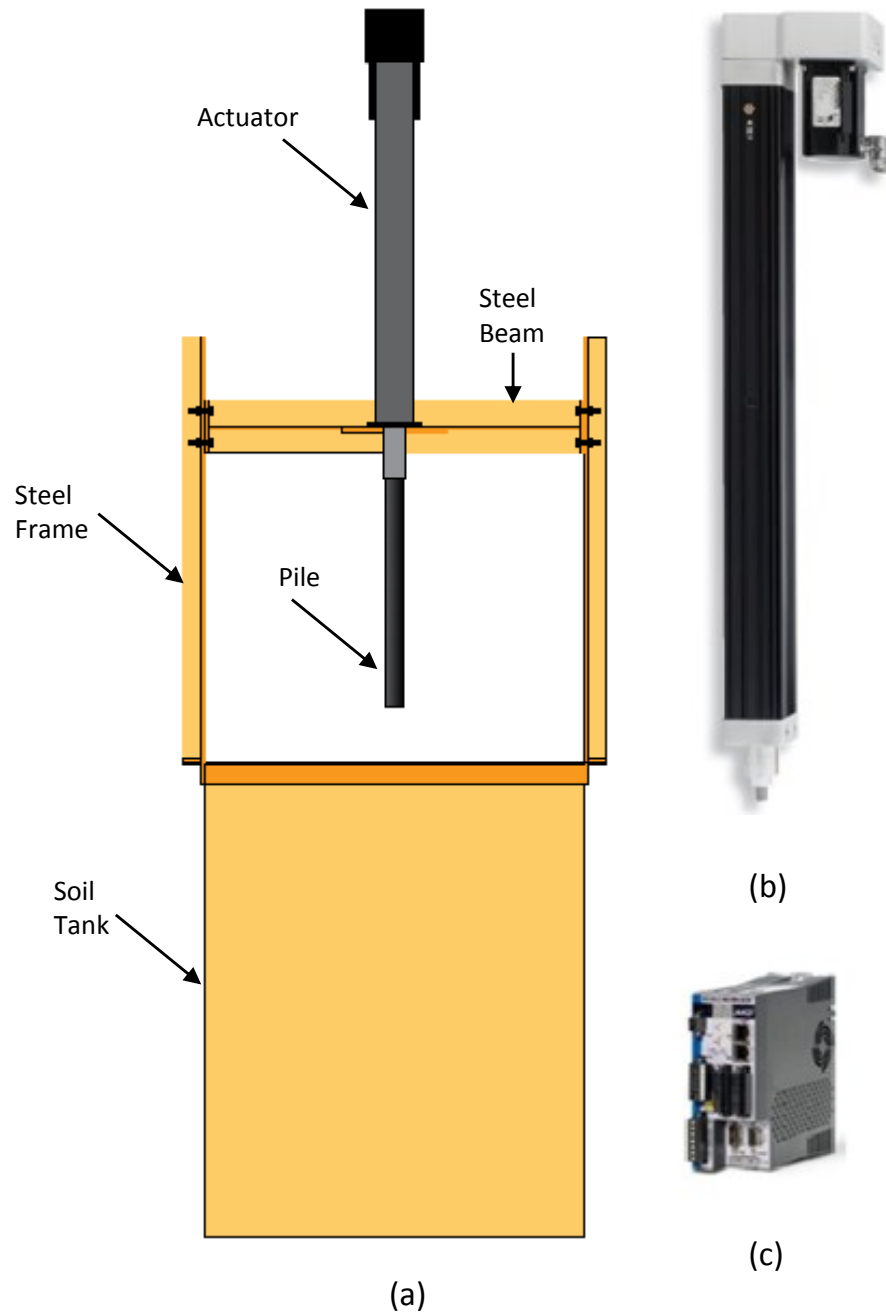


Figure 3-2: (a) Sketch of the steel tank (b) EC5 electric cylinder actuator, (c) AKD servo driver

### 3.3 Soil Testing

Silica Sand 4010, a sub-rounded material, was used to represent the cohesionless soil. DiCamillo (2014) and Vakili (2015) performed a series of laboratory tests (e.g., sieve analysis, specific gravity tests, relative density, and direct shear tests) on Silica Sand 4010 to determine its soil properties and angle of shearing resistance at different relative densities. Verification laboratory tests were performed to check their results.

Results of the sieve analysis, which is presented in Figure 3-3 and compared to that obtained by Vakili (2015) who also performed the sieve analysis test on the same type of soil, indicated that the soil was uniformly graded, with a uniformity coefficient ( $C_u$ ) and coefficient of curvature ( $C_c$ ) of 1.88 and 1.01, respectively. According to the Unified Soil Classification System, the soil is classified as SP. A specific gravity ( $G_s$ ) test was also performed, which revealed specific gravity to be 2.62, and the maximum and minimum unit weights were 17.16 (kN / m<sup>3</sup>) and 13.98 (kN / m<sup>3</sup>), respectively. The physical and mechanical properties of Silica Sand 4010 are summarized in Table 3-1.

Direct shear tests were also performed on Silica Sand 4010. By calculating the weight of the soil required to fill the shear box for a specific relative density and by applying different compaction energy, four different relative densities were achieved and tested; 30%, 45%, 60%, and 75%. The shear box results appear in Table 3-2 and Figure 3-4.

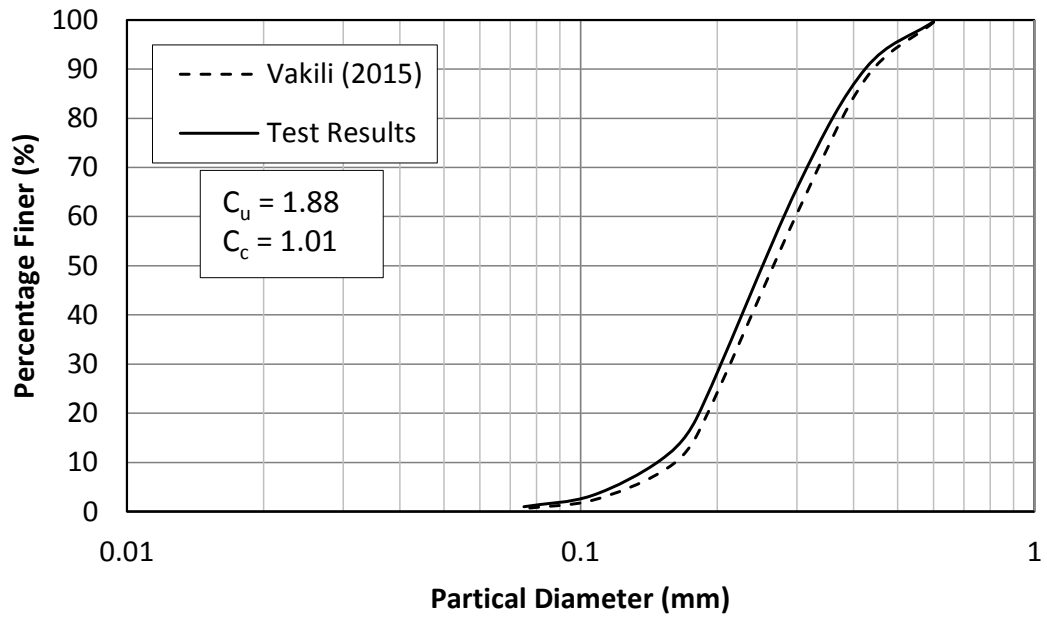


Figure 3-3: Particle size distribution for silica sand 4010

Table 3-1: Silica sand properties

Test	Soil Property	Silica Sand 4010
Sieve Analysis Test	$d_{10}$ (mm)	0.15
	$d_{30}$ (mm)	0.21
	$d_{50}$ (mm)	0.26
	$d_{60}$ (mm)	0.29
	Coefficient of uniformity ( $C_u$ )	1.88
	Coefficient of curvature ( $C_c$ )	1.01
	Soil Classification (USCS)	SP
Specific Gravity Test	Specific Gravity ( $G_s$ )	2.62
Maximum and Minimum Unit Weight Test	Maximum Dry Unit Weight ( $kN/m^3$ )	17.16
	Minimum Dry Unit Weight ( $kN/m^3$ )	13.98
	Minimum Void Ratio	0.50
	Maximum Void Ratio	0.84

Table 3-2: Relative density and corresponding angle of shearing resistance

Relative Density	Void Ratio	Angle of Shearing Resistance (degree)
30%	0.74	32.96
45%	0.69	34.93
60%	0.63	36.80
75%	0.58	38.79

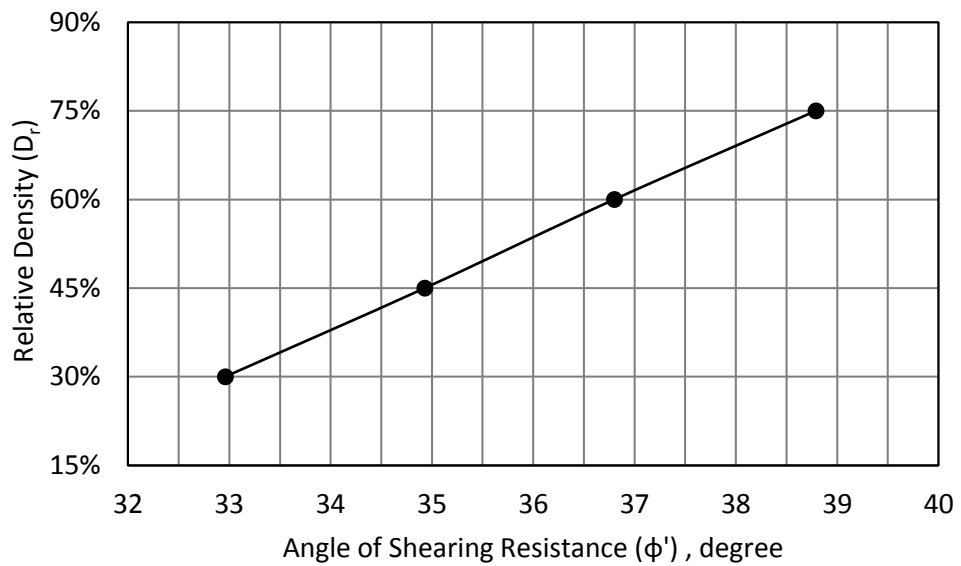


Figure 3-4: Relative density and corresponding angle of shearing resistance

### 3.4 Sand Preparation

Of the several techniques available to prepare sand beds for desired states, pluviation ranks among the most widely used in laboratories to prepare uniform cohesionless soil in a test tank. In that method, an air-dried cohesionless soil falls from a constant height through a funnel or diffuser; increased fall height and flow rate increase the gravity energy and thus the density of the sand (Meyerhof & Hanna, 1978; Cresswell et al., 1999; Hanna & Al-Romhein, 2008).

El-Emam (2011) used vibration to prepare cohesionless soil in a test tank by placing sand in layers, each subjected to a static load on top during vibration. Previously, Hanna and Soliman–Saad (2001) applied vibratory energy directly on top of each layer as well.

Also widely used, dynamic compaction places sand in equal layers, each subjected to a dynamic load that drops from a constant height. When the same number of drops are made for all layers, denser layers emerge at the bottom of the test tank (Towhata, 2008). Ladd (1978) proposed applying a few drops at lower layers, progressively increasing the number of drops at upper layers, and using trial and error until the desired relative density for all layers is achieved.

After Duncan and Seed (1986) reported that 40–90% of lateral pressure induced due to compaction might remain in the soil as residual stress, Hanna and Soliman–Saad (2001), Hanna and Al-Romhein (2008), and El-Emam (2011) studied the influence of compaction techniques on soil and reported on the stress level in the soil mass. Those residual stresses are usually represented by the OCR, which signifies the level of particle interlocking in soil. Because the OCR directly affects lateral earth pressure, the method of compaction was used in the research presented here in order to achieve a uniform relative density across the test tank and overconsolidation of the sand.

### 3.4.1 Sand-Placing Technique

Figure 3-5 schematically illustrates the setup of the investigation. The test began by placing the tank under a crane pulley system and the sand in a container equipped with an extendable hose. The container was lifted by the crane and moved atop the tank, where the hose length was adjusted to maintain a minimum falling distance of sand particles. The sand was slowly released inside the tank via the hose, the location of which was continually moved during the filling to evenly distribute the sand within the tank.

Eight layers of soil, each 150 mm deep, were placed on top each other to fill the tank. A 7.12-kg hammer was manually lifted to a height of 200 mm and dropped repeatedly onto a rigid plate in order to compact each layer. To achieve the desired uniform relative density across the tank, less energy (i.e., drops) was applied to the lower layers and more energy applied to the upper ones (Hanna & Al Khoury, 2005; Hanna & Soliman-Saad, 2001).

The unit weight of sand in the test tank was measured by placing two cans with known volumes in a staggered arrangement in the middle of each layer 250 mm from the sides of the tank (Figure 3-6a). The cans were retrieved at the end of each test, and the unit weight was calculated. Because the bottom layer was expected to be affected by the reflection of compacting energy from the rigid base of the tank, the unit weight was not measured for that layer. The cans were weighed to determine the relative density for each layer according to the following equation:

$$D_r (\%) = \left[ \frac{\left[ \frac{W_{soil}}{V_{can}} \right] - \gamma_{d \min}}{\gamma_{d \max} - \gamma_{d \min}} \right] \cdot \left[ \frac{\gamma_{d \max}}{\left[ \frac{W_{soil}}{V_{can}} \right]} \right] \quad (3-1)$$

where

( $W_{soil}$ ) = weight of the soil in the can,

( $V_{can}$ ) = can volume,

$(\gamma_{d \min})$  = minimum dry unit weight of the soil, and

$(\gamma_{d \max})$  = maximum unit dry weight of the soil.

After compacting all layers, vertical stresses in the sand due to compaction were measured using six sensors (SingleTact) placed individually in the middle of each of the first six layers 300 mm from the sides of the tank in a staggered arrangement (Figure 3-6b). Photos of the cans, sensors, and compaction plate during the test appear in Figure 3-7. The bottom two layers were not instrumented in order to avoid any influence of stress due to the reflection of compacting energy from the rigid base of the tank. Results were recorded with a data acquisition system, and the OCR was calculated for each layer according to the following equation:

$$\text{OCR} = \left[ \frac{\sigma_{V(M)}}{\sigma_{V(Th)}} \right] \quad (3-2)$$

where:

$\sigma_{V(M)}$  = vertical pressure at a given depth as measured by the corresponding sensor, and

$\sigma_{V(Th)}$  = theoretical effective overburden pressure at that depth.

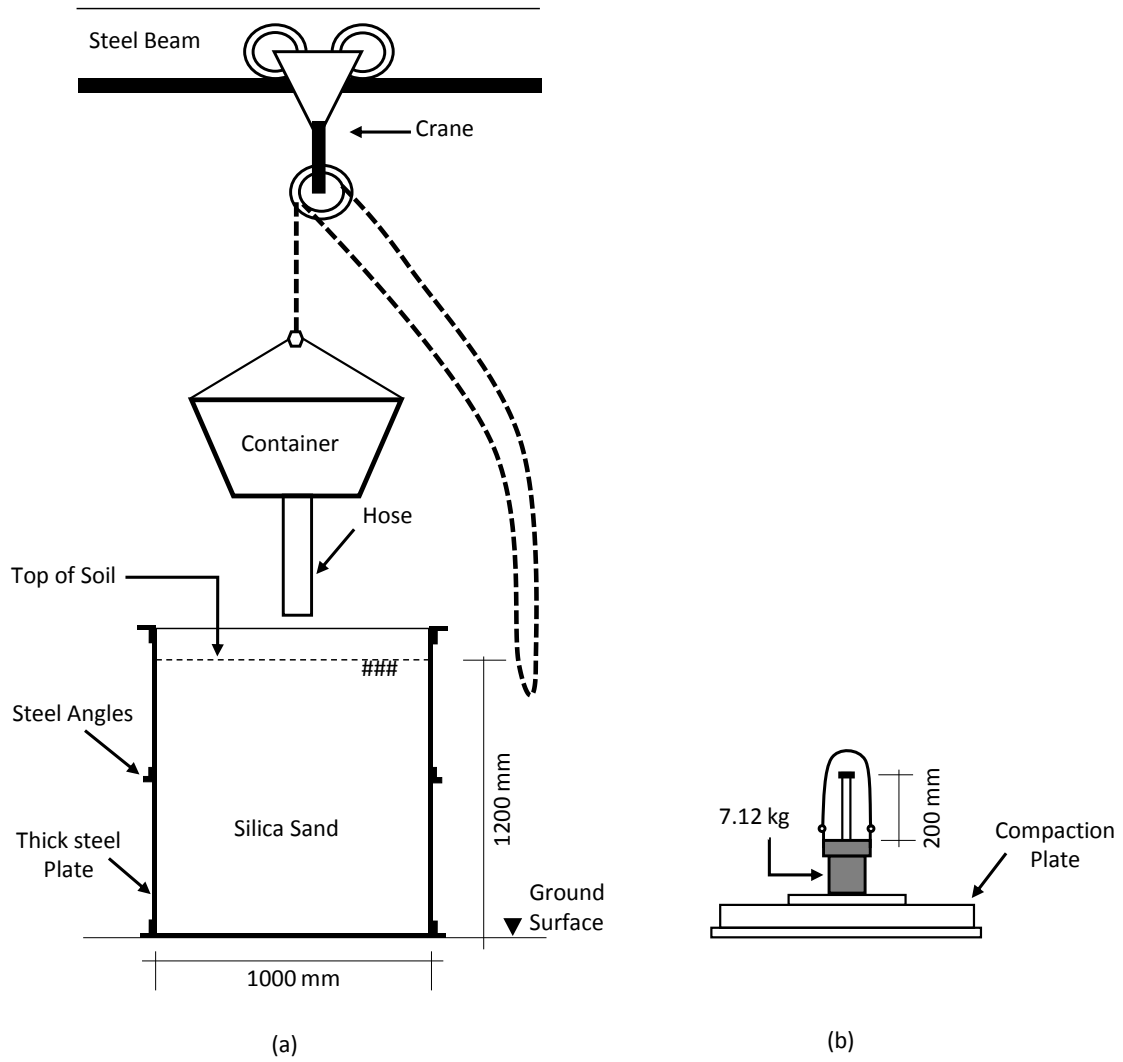


Figure 3-5: Set-up arrangement for soil preparation

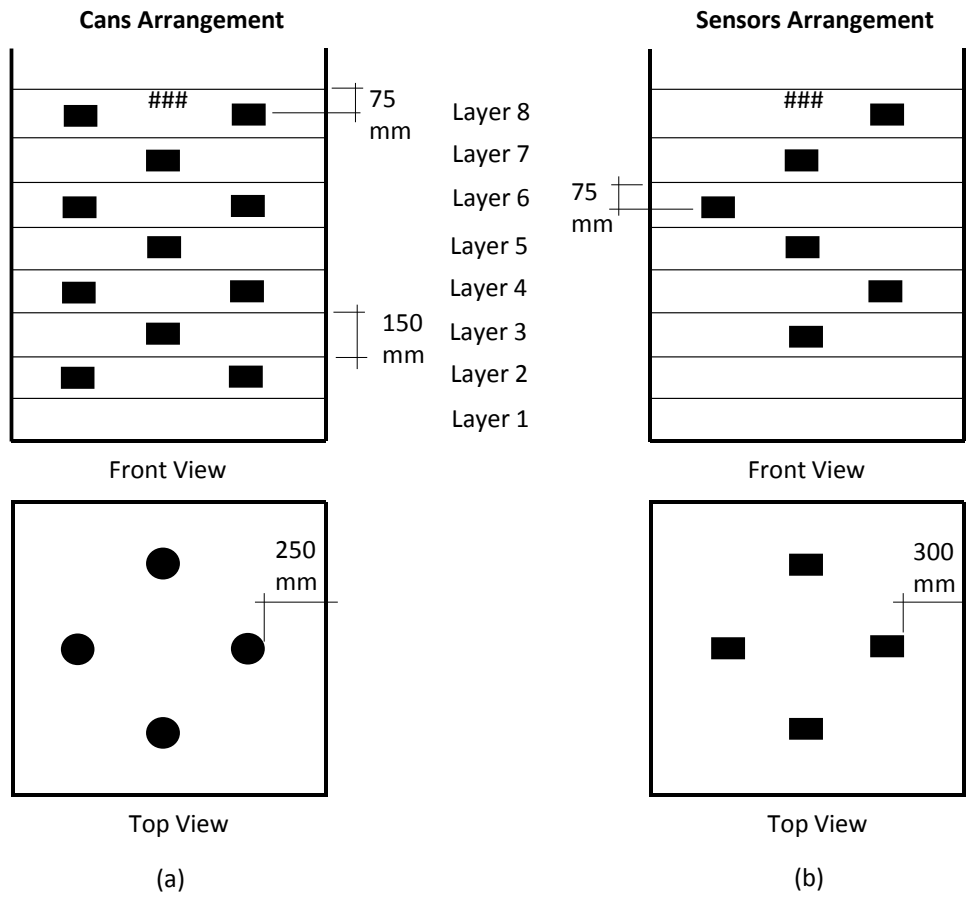


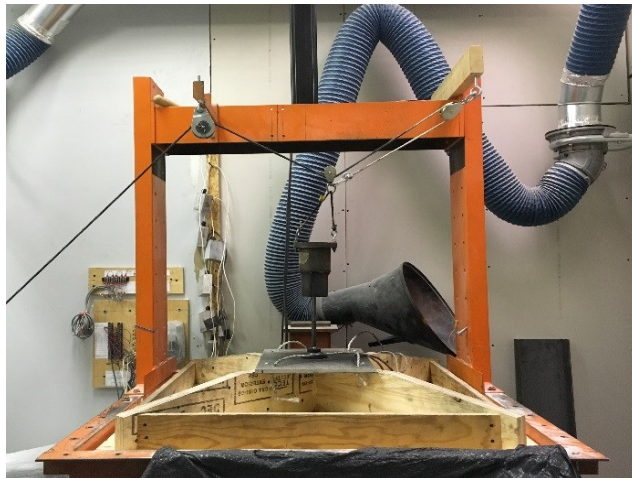
Figure 3-6: Location of (a) cans and (b) sensors in the testing tank



(a)



(b)



(c)

Figure 3-7: Photos of the (a) can location, (b) sensor location, and (c) compaction plate during testing

### 3.4.2 Test Results

To determine the compaction effort to be applied to each layer in order to achieve predetermined relative density, tests were performed using trial and error where the number of drops was adjusted in every test until the desired relative density was achieved. Tests were repeated to ensure the repeatability of the results. The number of drops ( $N$ ), corresponding unit weight ( $\gamma_d$ ), angle of shearing resistance ( $\phi'$ ), theoretical vertical stress ( $\sigma_{V(Th)}$ ), and measured vertical stress ( $\sigma_{V(M)}$ ) for the tests produced relative densities of 30%, 45%, and 60%, which appear in Table 3-3, Table 3-4, and Table 3-5, respectively. The unit weight ( $\gamma_d$ ) was determined from the weight of the cans embedded in the layers of soil, and the relative density ( $D_r$ ) was calculated for each layer. The angle of shearing resistance ( $\phi'$ ) was calculated for each layer according to the relationship of relative density and angle of shearing resistance (Figure 3-4). Figure 3-8 presents the number of drops versus relative density, as well as the angle of shearing resistance with the depth of soil in the test tank.

Values of theoretical and measured vertical stress after compaction appear in Figure 3-9a, b, and c for the relative densities of 30%, 45%, and 60%, respectively. At all levels, the measured vertical stress exceeded theoretical value due to the locked-in stresses that remained in the soil after the compaction, or by the so-called over consolidation represented by the overconsolidation ratio (OCR). Moreover, the measured values increased along with relative density. Overconsolidation of sand increases the efficiency of particle interlocking, which consequently, increases the tendency of soil particles expand during shear (Terzaghi et al, 1996; Lambe & Whitman, 1969; Lee et al. 2013).

Table 3-6 and Figure 3-10 present the calculated OCR values for 30% relative density, 45%, and 60%. OCR values were greater at the top layers and decreased with depth, as well as increased along with relative density, due to both the compaction pattern used, in which top layers received more drops than lower ones, and the fact that the overburden pressure at top layers was less than that at lower ones.

To illustrate the OCR's effect, lateral earth pressure coefficients ( $K_0$ ) for normally consolidated and overconsolidated soil were calculated for relative densities of 30%, 45%, and 60% using experimental data and Equations 2.13 and 2.16, respectively. The results of that analysis appear in Table 3-7 and are illustrated graphically in Figure 3-11.

Table 3-3: Test results for sand at a relative density of 30 %

Layer No	Layer Thickness	Depth at mid layer	Target Relative Density	No. of Drops	Dry Unit Weight	Relative Density	Angle of Shearing Resistance	Theoretical Vertical Stress	Measured Vertical Stress
i	D (mm)	$d_L$ -	$D_r$ (%)	N -	$\gamma_d$ (kN/m <sup>3</sup> )	$D_r$ (%)	$\phi'$ (degree)	$\sigma_{v(Th)}$ (kPa)	$\sigma_{v(M)}$ (kPa)
8	150	75	30	76	14.82	30.48	33.0	1.11	3.89
7	150	225	30	76	14.93	34.38	33.5	3.34	9.16
6	150	375	30	76	14.90	33.16	33.3	5.58	14.66
5	150	525	30	70	14.88	32.63	33.3	7.81	17.63
4	150	675	30	57	14.92	33.84	33.4	10.05	21.28
3	150	825	30	57	14.72	27.14	32.6	12.27	21.51
2	150	975	30	55	14.89	33.00	33.3	14.49	-
1	150	1125	30	55	-	-	-	-	-

Table 3-4: Test results for sand at a relative density of 45 %

Layer No	Layer Thickness	Depth at mid layer	Target Relative Density	No. of Drops	Dry Unit Weight	Relative Density	Angle of Shearing Resistance	Theoretical Vertical Stress	Measured Vertical Stress
i	D (mm)	$d_L$ -	$D_r$ (%)	N -	$\gamma_d$ (kN/m <sup>3</sup> )	$D_r$ (%)	$\phi'$ (degree)	$\sigma_{v(Th)}$ (kPa)	$\sigma_{v(M)}$ (kPa)
8	150	75	45	183	15.34	47.77	35.3	1.15	4.68
7	150	225	45	172	15.34	47.91	35.3	3.45	12.06
6	150	375	45	170	15.23	44.38	34.8	5.74	16.61
5	150	525	45	155	15.34	47.89	35.3	8.04	20.14
4	150	675	45	110	15.27	45.72	35.0	10.33	25.59
3	150	825	45	95	15.15	41.82	34.5	12.62	29.60
2	150	975	45	92	15.23	44.30	34.8	14.89	-
1	150	1125	45	70	-	-	-	-	-

Table 3-5: Test results for sand at a relative density of 60 %

Layer No	Layer Thickness	Depth at mid layer	Target Relative Density	No. of Drops	Dry Unit Weight	Relative Density	Angle of Shearing Resistance	Theoretical Vertical Stress	Measured Vertical Stress
i	D (mm)	$d_L$ -	$D_r$ (%)	N -	$\gamma_d$ (kN/m <sup>3</sup> )	$D_r$ (%)	$\phi'$ (degree)	$\sigma_{v(TH)}$ (kPa)	$\sigma_{v(M)}$ (kPa)
8	150	75	60	380	15.58	55.50	36.2	1.17	6.58
7	150	225	60	345	15.78	61.46	37.0	3.52	13.28
6	150	375	60	340	15.58	55.29	36.2	5.87	21.47
5	150	525	60	325	15.74	60.28	36.9	8.22	29.49
4	150	675	60	240	15.61	56.20	36.4	10.57	34.25
3	150	825	60	220	15.61	56.21	36.3	12.91	32.28
2	150	975	60	210	15.60	56.06	36.3	15.25	-
1	150	1125	60	185	-	-	-	-	-

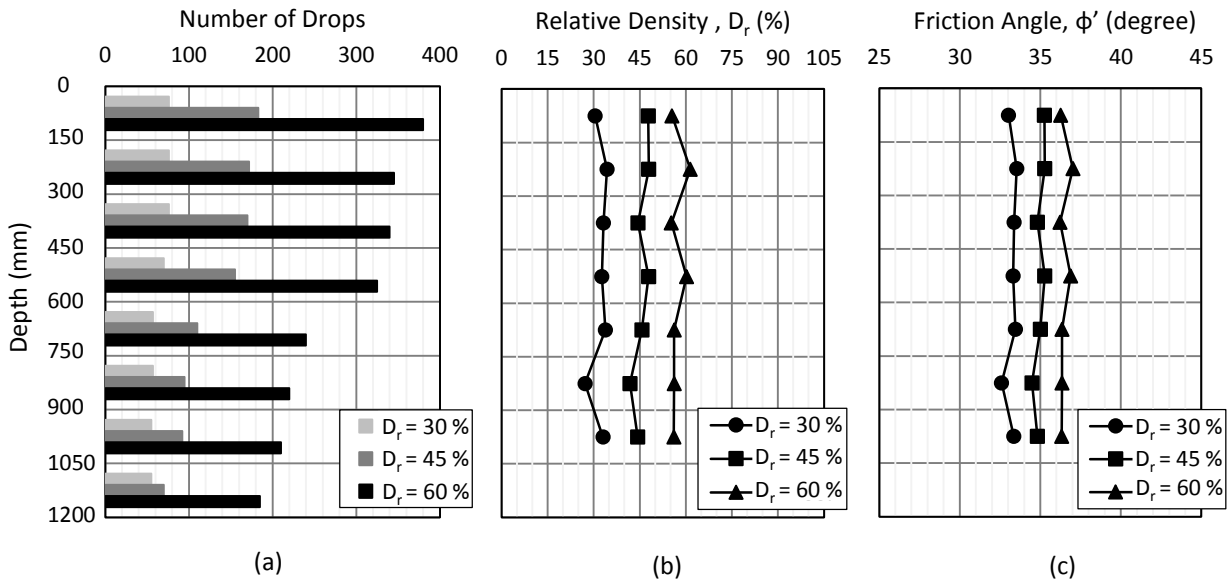


Figure 3-8: Test results: depth versus (a) number of drops, (b) relative density (c) angle of shearing resistance

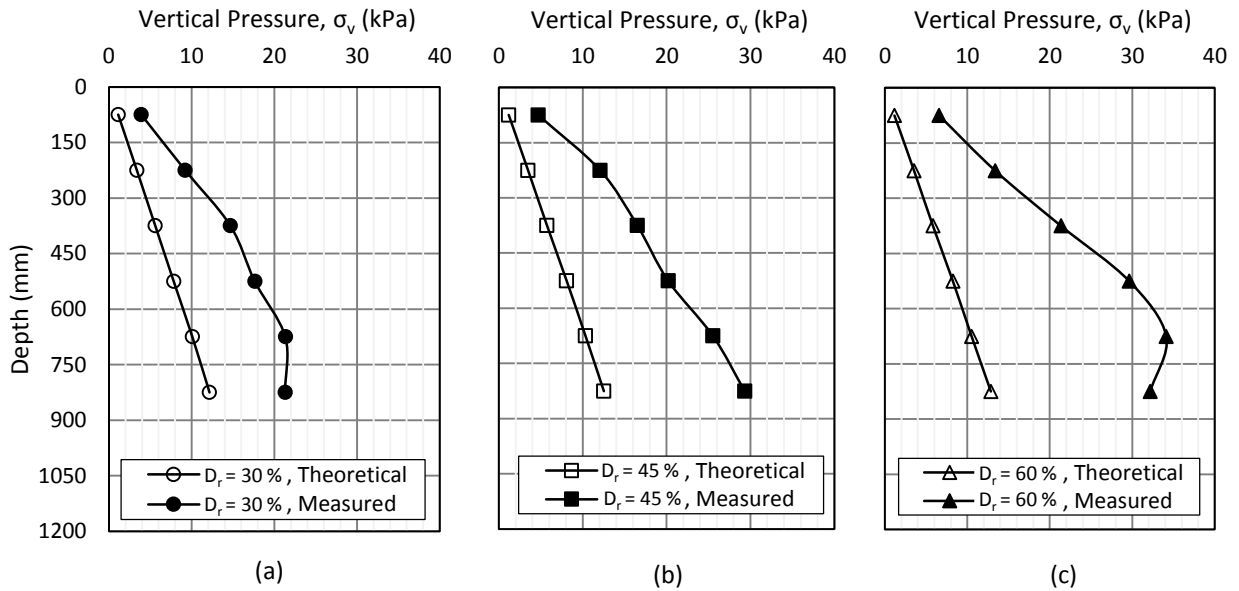


Figure 3-9: Theoretical and measured values of the vertical stress versus the depth of soil for (a)  $D_r = 30\%$ , (b)  $D_r = 45\%$ , and (c)  $D_r = 60\%$ .

Table 3-6: Experimental values of OCR

Layer No <i>i</i>	Layer Thickness <i>D</i> (mm)	Depth at mid layer <i>d<sub>L</sub></i> -	Overconsolidation Ratio OCR		
			$\sigma_{v(M)} / \sigma_{v(Th)}$		
			$D_r = 30\%$	$D_r = 45\%$	$D_r = 60\%$
8	150	75	3.50	4.07	5.63
7	150	225	2.74	3.50	3.77
6	150	375	2.63	2.89	3.66
5	150	525	2.26	2.51	3.59
4	150	675	2.12	2.48	3.24
3	150	825	1.75	2.35	2.50
2	150	975	-	-	-
1	150	1125	-	-	-

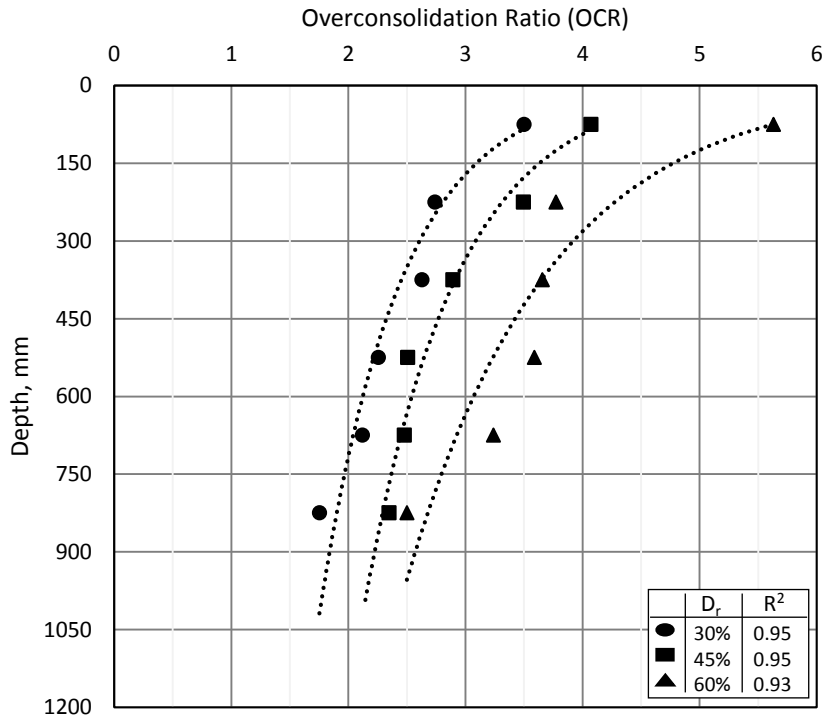


Figure 3-10: Test results: OCR versus depth

Table 3-7: Test results: lateral earth pressure coefficient

Layer No <i>i</i>	Layer Thickness <i>D</i> (mm)	Depth at mid layer <i>d<sub>L</sub></i> -	Lateral Earth Pressure (Normally Consolidated)			Lateral Earth Pressure (Overconsolidated)		
			$K_{0(NC)} \cdot 1 - \sin \phi'$			$K_{0(OC)} \cdot K_{0(NC)} \cdot OCR^{\sin \phi'}$		
			<i>D<sub>r</sub></i> = 30%	<i>D<sub>r</sub></i> = 45%	<i>D<sub>r</sub></i> = 60%	<i>D<sub>r</sub></i> = 30%	<i>D<sub>r</sub></i> = 45%	<i>D<sub>r</sub></i> = 60%
8	150	75	0.455	0.423	0.409	0.901	0.951	1.135
7	150	225	0.448	0.422	0.398	0.781	0.870	0.885
6	150	375	0.450	0.429	0.409	0.766	0.787	0.880
5	150	525	0.451	0.422	0.400	0.705	0.718	0.861
4	150	675	0.449	0.426	0.407	0.679	0.717	0.818
3	150	825	0.461	0.434	0.407	0.624	0.703	0.701
2	150	975	0.450	0.429	0.408	-	-	-
1	150	1125	-	-	-	-	-	-

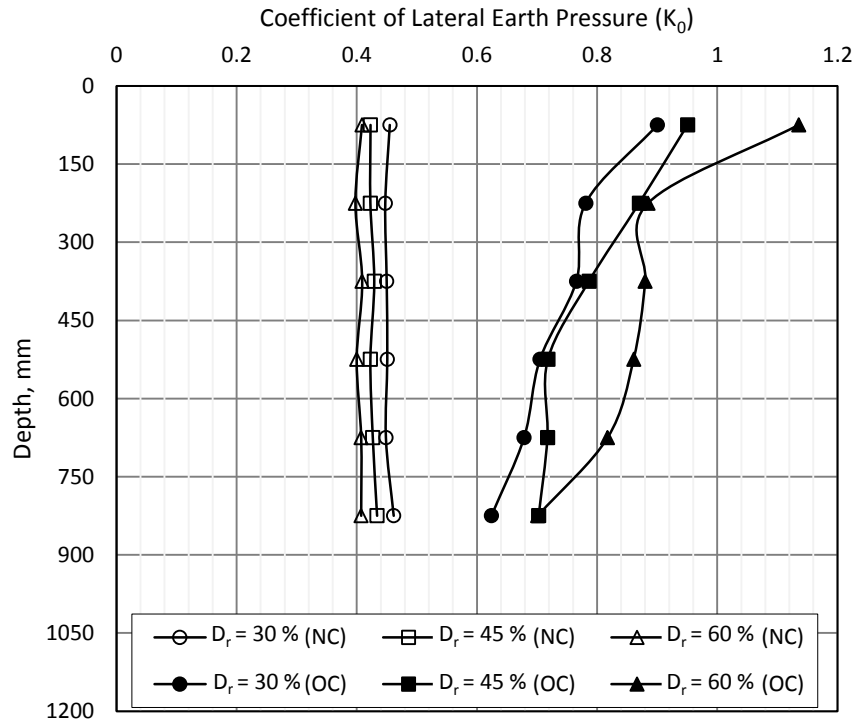


Figure 3-11: Test results: lateral earth pressure coefficients versus depth

Laboratory experiments often require a uniform relative density throughout the test tank. Although the compaction method is popular for soil preparation, no guideline is available to predict the compaction effort required to achieve a uniform relative density or to estimate the resulting increase in stress levels. Alternatively, a time-consuming trial-and-error approach could be followed, which is physically demanding for large test tanks. Therefore, the compaction results were analyzed to develop a guideline that can be followed to produce a uniform sand bed in the test tank and to estimate the level of overconsolidation in the soil mass.

### 3.4.3 Results Analysis

The applied energy per unit of volume at each stage of compaction was calculated by using the following equation:

$$E_{\text{applied}} = \frac{N m g h}{V} \quad (3-3)$$

where:

N = number of drops,

m = hammer mass (kg),

g = gravity acceleration,

h = height of drop, and

V = total volume of sand mass below the compacting plate.

Assuming that the energy applied was uniformly distributed, the accumulated energy for each layer was calculated according to the following equation:

$$E_i = E_{\text{applied,(i)}} + E_{\text{applied,(i+1)}} + \dots + E_{\text{applied,(n)}} \quad (3-4)$$

where;

i = rank of the layer in the tank (Figure 3-6), and

n = total number of soil layers.

Figure 3-12 presents the results of the accumulated energy versus the depth of the soil in the test tank. The energy required increased along with the relative density and depth of the layer.

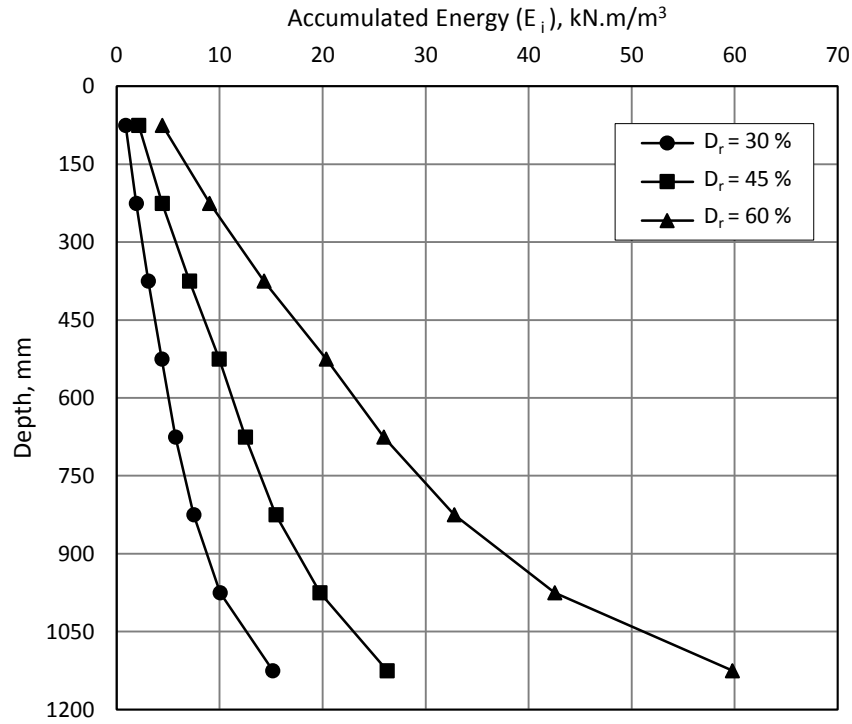


Figure 3-12: Accumulated energy versus depth

A dimensionless energy factor ( $E_f$ ), defined as the ratio of accumulated energy for a given layer and the vertical stress in the middle of that layer, was introduced following a similar approach successfully used by Hanna and Soliman–Saad (2001). The energy factor for each layer was calculated according to the following equation:

$$E_f = \frac{E_i}{\sum_1^n \gamma_i d_L} \quad (3-5)$$

where:

$E_i$  = accumulated energy per unit volume for layer  $i$ ,

$\gamma_i$  = unit weight of layer  $i$ ,

$d_L$  = depth of the middle layer  $i$  from the top,

$i$  = rank of the layer in the tank (Figure 3-6), and

$n$  = total number of layers.

To incorporate the depth of a layer into the total thickness of the deposit, a relative height dimensionless factor ( $H_r$ ), defined as the ratio of the depth of a sand layer measured from the top of the soil to the total height of the soil inside the test tank, was introduced:

$$H_r = \frac{d_L}{H} \quad (3-6)$$

where:

$H$  = total height of the soil.

The experimental results were analyzed using Equations 3.5 and 3.6, and the energy factor ( $E_f$ ) was determined for a given relative height ( $H_r$ ). Figure 3-13 presents the energy factor versus the relative height. The energy factor increased due to the increase of relative density; however, at the top layers, the energy factor decreased with the increase of relative height, whereas the energy factor at the lower layers increased with the increase of relative height due to the influence of the rigid base of the tank.

The relationship of the energy factor and relative height can be represented as follows:

$$E_f = a (H_r)^3 + b (H_r)^2 + c (H_r) + d \quad (3-7)$$

where;

$$a = -0.0079 (D_r)^2 + 0.313 (D_r) - 4.646$$

$$b = 0.0152 (D_r)^2 - 0.692 (D_r) + 11.458$$

$$c = -0.0078 (D_r)^2 + 0.353 (D_r) - 5.888$$

$$d = 0.0023 (D_r)^2 - 0.094 (D_r) + 1.622$$

$D_r$  = Relative density (%)

Figure 3-14 presents the energy factor ( $E_f$ ) versus the relative densities using Equation 3.7, which can be used as a guideline to determine the energy level for a given relative density and sand layer. Accordingly, the number of drops can be determined for each layer.

Figure 3-15 presents  $[\text{OCR}(1 - (D_r)^2)]$  versus the relative height ( $H_r$ ), in which a logarithmic relationship among the OCR, relative height ( $H_r$ ), and the desired relative density ( $D_r$ ) was determined according to the following equation:

$$\text{OCR} = \frac{-0.65 \ln H_r + 1.55}{(1 - (D_r)^2)} \quad (3-8)$$

where;

$D_r$  = relative density (%/100)

Equation 3.8 could thus be used to determine the value of the OCR at a given layer that resulted from compaction. Figure 3-16 presents a flow chart used to determine the number of drops required to be applied at each layer in a test tank and the corresponding value of the OCR for the desired relative density throughout the tank. The steps presented in the flow chart can be easily implemented in any programming software (e.g., MATLAB and Excel).

It should be reported herein that due to lack of published records in the subject matter, it was difficult to validate the procedure proposed. However, in this experiment, tests were repeated to assure repeatability of the test data. These besides the fact that the procedure developed in this investigation is based dimensionless parameters using a common silica sand, which can be tested at any set-up.

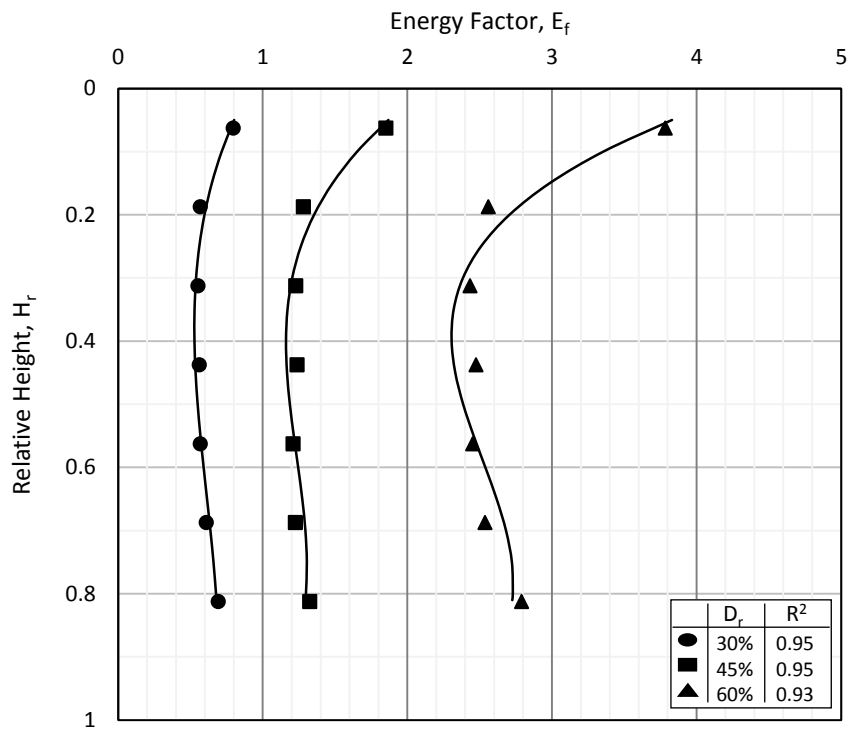


Figure 3-13: Experimental results: energy factor versus the relative height

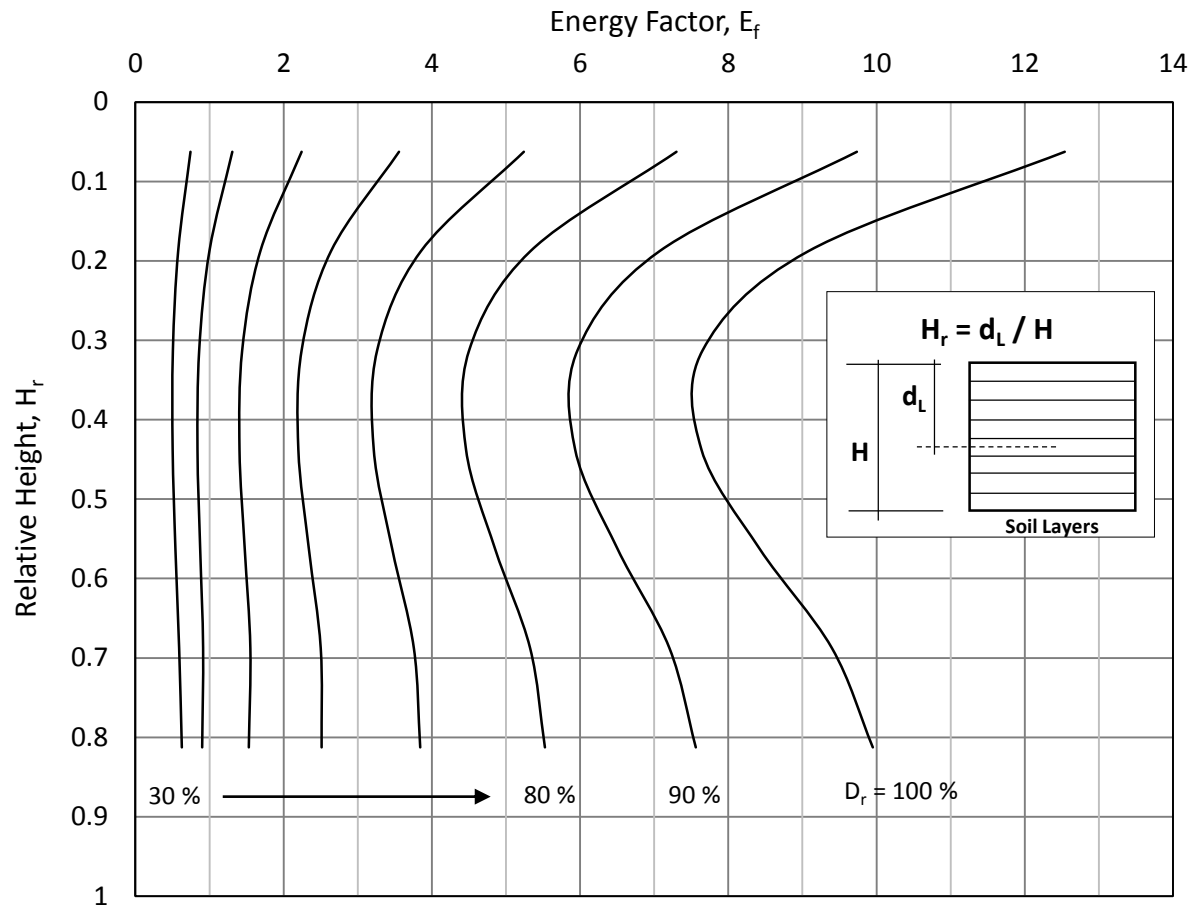


Figure 3-14: Energy factor versus relative height

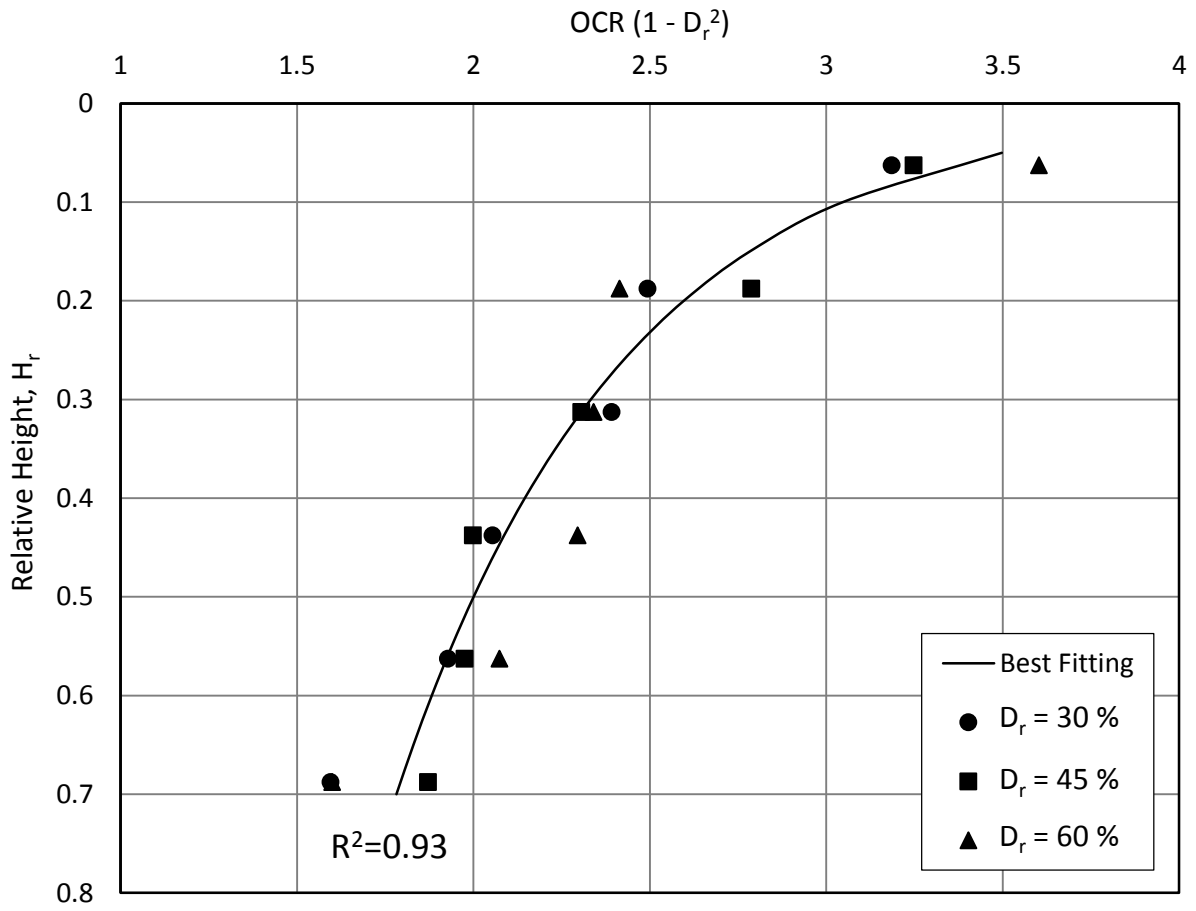


Figure 3-15: Test results of  $[OCR (1 - (D_r)^2)]$  versus relative height

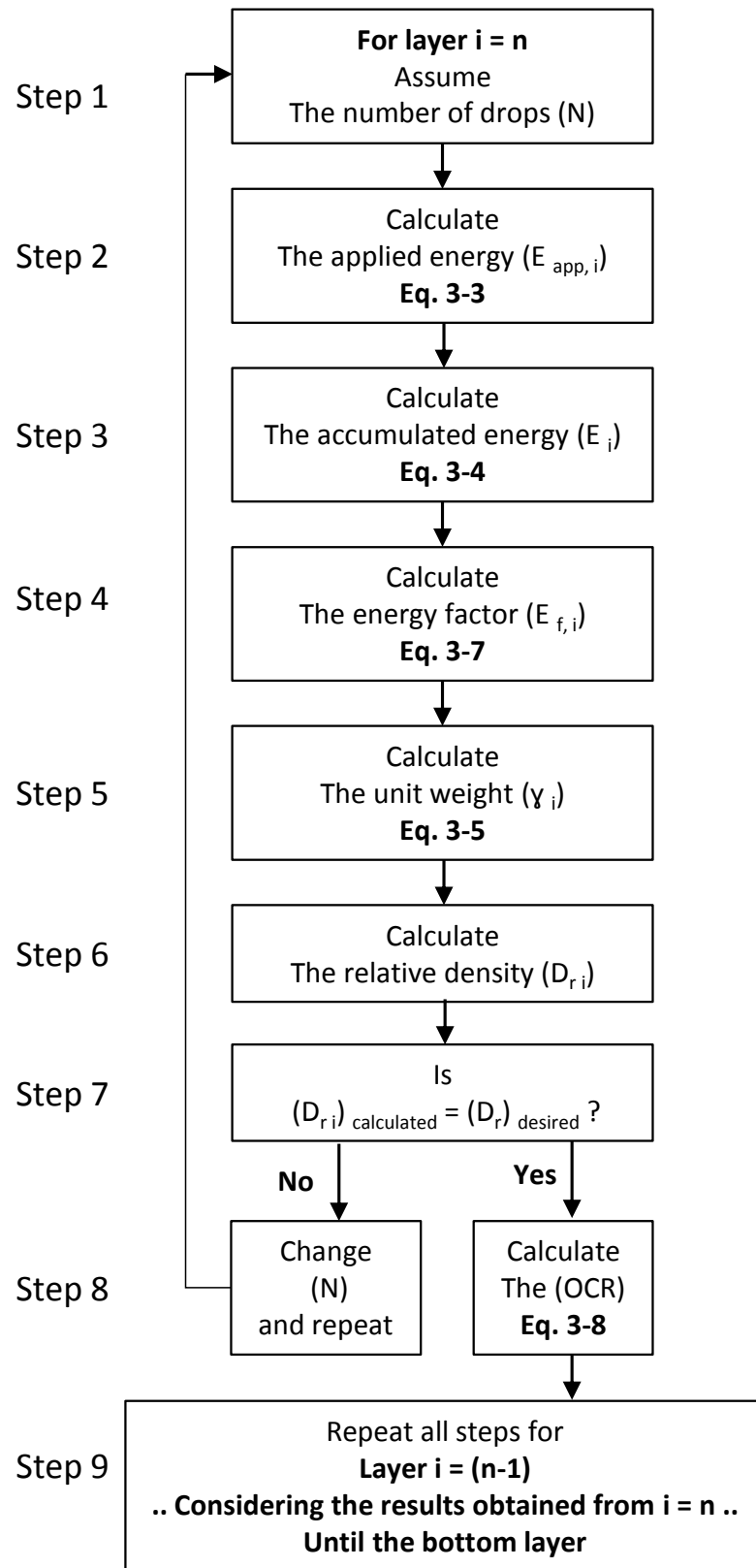


Figure 3-16: Flow charts for calculating the number of drop and the OCR

## 3.5 Pile Load Testing

### 3.5.1 Pile Models

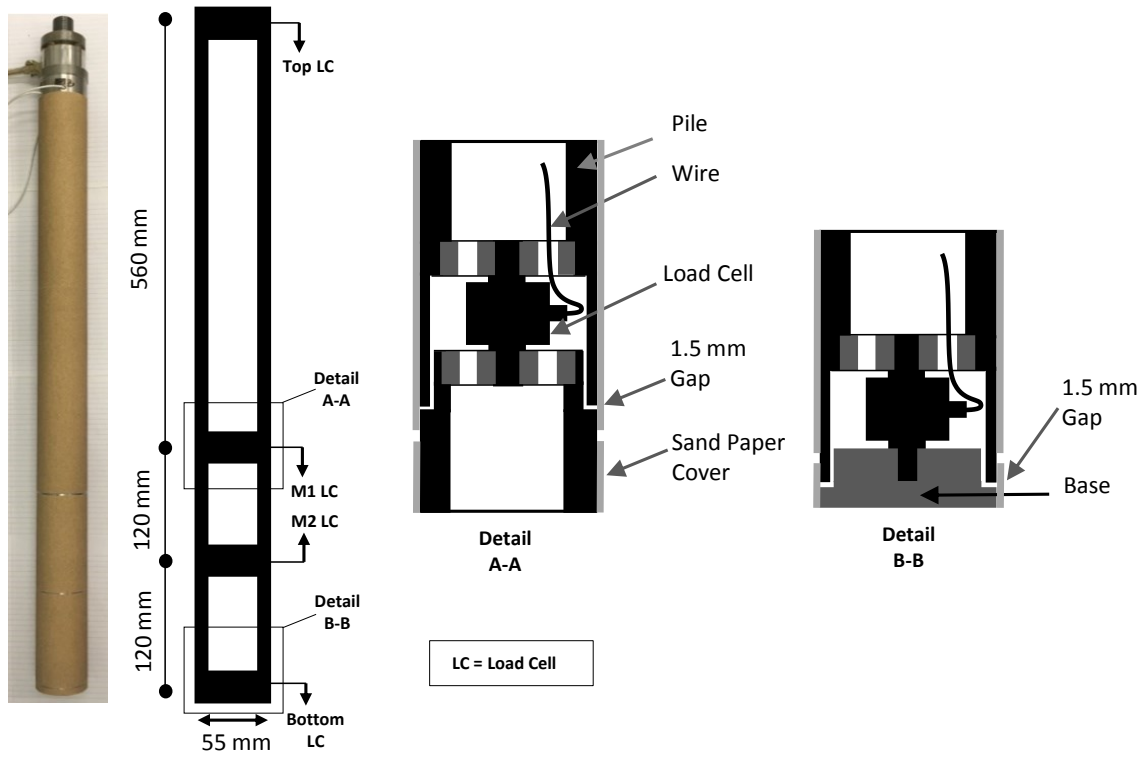
To investigate the effect of overconsolidation on shaft resistance, two pile models were fabricated with a mechanical steel pipe. The first model, 0.8 m in length and 55 mm in diameter, was instrumented with four load cells to measure the applied load, tip resistance, and shaft resistance: one from the top that was attached to the actuator to measure the total applied load, another from the bottom to measure tip resistance, and the two others inside the pile at 120 mm and 240 mm, respectively, from the pile base to measure the total load at those levels. The load cells had a maximum capacity of 22.25 kN with an accuracy of  $\pm 0.25\%$ . The top load cell measured tip resistance plus total shaft resistance, the second load cell measured tip resistance plus shaft resistance from the sections beneath it, the third load cell measured tip resistance plus shaft resistance from the sections beneath it, and the last load cell measured tip resistance only. The difference between every two adjacent load cells indicated the shaft resistance for the pile section between them.

By contrast, the second pile, 0.8 m long and 30 mm in diameter, was instrumented with two load cells: one with a capacity of 22.25 kN to measure the total applied load and another with a capacity of 8.9 kN (with an accuracy of  $\pm 0.25\%$ ) connected to the pile tip at the bottom to measure tip resistance. For the second pile, different mechanisms of instrumentation had to be adopted given the limitations of the 30-mm diameter, and accordingly, the pile consists of four parts: a rounded steel box, a mechanical pipe, a drilling rod, and the tip. The load cell with a capacity of 8.9 kN was fastened inside the rounded steel box, whereas the one with a capacity of 22.25 kN was fastened at the top of the rounded steel box attached to the actuator. The drilling rod was threaded and fastened to the load cell with a capacity of 8.9 kN and inserted inside the mechanical steel pipe threaded at the top and attached to the rounded

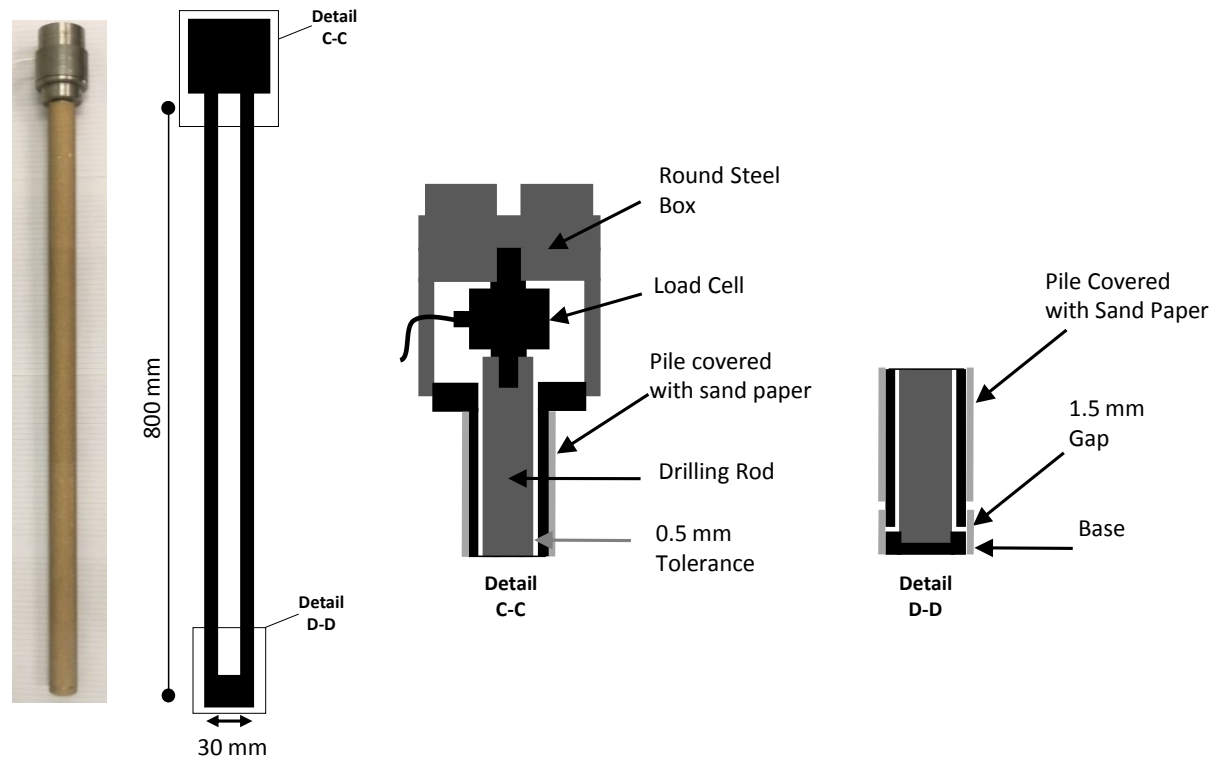
steel box. Ultimately, the tip was attached to the drilling rod at the bottom of the pile. Because the drilling rod made no contact with the steel pipe from inside, shaft resistance could be determined as the difference between tip resistance and the total load applied. Figure 3-17 presents photos and cross-sections of both models.

The interface angle ( $\delta$ ) between the pile and the soil varies according to the roughness of the pile (Murthy, 2002). Vakili (2015) performed several trials to establish the degree of roughness of sandpaper to be glued to a pile shaft to maintain a ratio of interface angle to angle of shearing resistance ( $\delta / \phi'$ ) equal to 1. As a result of those tests, Grade 150 sandpaper satisfied the unit ratio at different relative densities. Figure 3-18 depicts the results of the shear test for the sandpaper.

Experimental investigations on piles are significantly influenced by the scale effect unless an appropriate pile diameter is chosen. Based on the pile diameter, the boundary of the experimental tank may influence the pile load test results. To avoid that influence, the pile center and side of the test tank should be sufficiently distanced ( $B$ ) from each other. Based on various experiments, the appropriate distance ( $B$ ) was determined to be 10 times the pile diameters (Garnier et al., 2007); therefore, the distance between the center of the pile and any hard boundary should be equal to or greater than 10. Literature addressing the capacity of piles in sand material has shown that the  $B / D$  ratio varies, starting at a minimum of 6 (Table 3-8). For the research reported here, the  $B / D$  ratio was 9.1. Theoretically, a distance 4 times the pile diameter would eliminate the effect of the bottom side of the tank on the results; in an experiment, the soil beneath the tip at a depth of 4.5 times the diameter did not experience any deformation (Rakotonindriana et al., 2010). In the study conducted for this thesis, the distance from the tip of the pile with the greatest depth to the bottom of the tank was 485 mm ( $\gg 4.5 D$ ).



(a) 55 mm pile model



(b) 30 mm pile model

Figure 3-17: Photo and schematic sketch for (a) 55mm pile model, and (b) 30 mm pile model

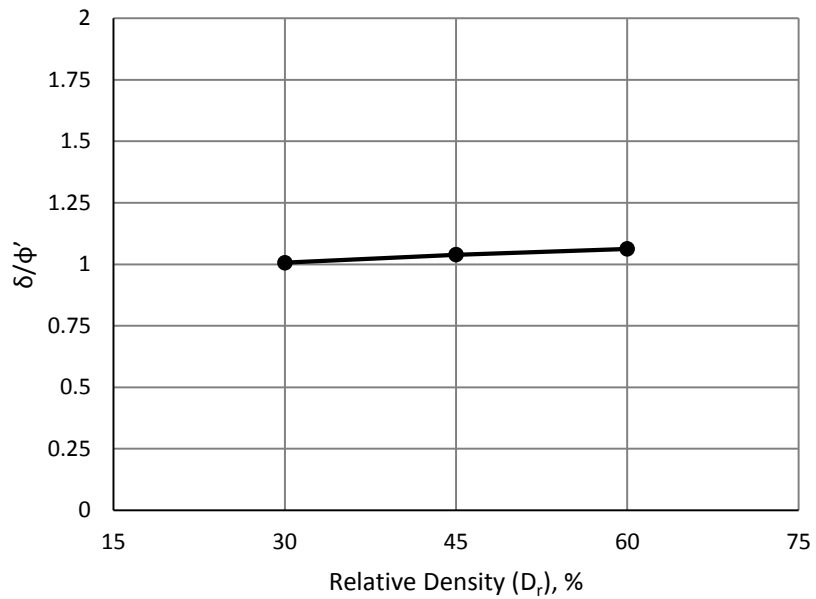


Figure 3-18: Values of  $(\delta/\phi')$  for different relative densities of Silica Sand after Vakili (2015)

Table 3-8: (D/B) Ratios for different experimental investigations

Pile Foundation	Author	Pile Diameter (D) (mm)	Distance from Pile Center to the Side (B) (mm)	Ratio B / D	
Single	Chari and Meyerhof (1983)	75	460	6.1	
	Lehane and Gavin (2001)	114	840	7.4	
	Al-Mhaidib (2012)	25	250	10.0	
	Shalabi and Bader (2014)	50	300	6.0	
	Current Study		55	500	9.1
			30	500	16.7

Pile load tests are also affected by the mean particle size ( $d_{50}$ ) of the soil. Results of an experiment revealed that increasing the ratio of the pile diameter to the mean particle size ( $D / d_{50}$ ) reduced the particle size effect and thus the scale effect. Garnier and Konig (1998) and Fioravante (2002) have suggested that the scale effect can be avoided when the  $D / d_{50}$  ratio exceeds 100 and 50, respectively. In the study reported here, the  $D / d_{50}$  ratio was 211 for the pile 55 mm in diameter and 115 for the pile 30 mm in diameter.

### **3.5.2 Testing Procedure and Program**

The test was commenced by placing the pile model vertically once the desired relative density was achieved and using the actuator to drive it into the compacted soil at the center of the tank down to the desired depth (Figure 3-19) at a rate of 25 mm per minute (Hanna & Nguyen, 2003). The actuator movement was controlled by the software Kollmorgen WorkBench. Next, the driving load was released, all sensors were set to 0, and the actuator drove the pile at a rate of 5 mm per minute (Le Kouby et al., 2013) to commence the pile load test, which ended when the pile was displaced by 20 mm. All readings of the measuring devices were collected by the data acquisition system at a regular interval of one reading per second. Preliminary tests were conducted to ensure the repeatability of the results.

Three soil relative densities were chosen in this experimental investigation; 30%, 45%, and 60% to represent loose, medium dense and dense soil, respectively. Due to the limitation of the tank dimension and the maximum stroke length of the actuator, the maximum embedment depth ratio ( $L/D$ ) was set to 13 for the pile model of 55 mm. To examine the critical depth, higher embedment depth ratio ( $L/D$ ) was chosen for the pile model of 30 mm.

Table 3-9 and Table 3-10 summarize the test program. In those tables, all tests are labeled according to type, pile diameter, relative density, and embedment depth ratio; for example, the label “C-30-45%-10” means that the test involved compression for pile with a diameter of 30 mm at 45% relative density and an embedment depth ratio depth of 10. The setup is illustrated in Figure 3-20.

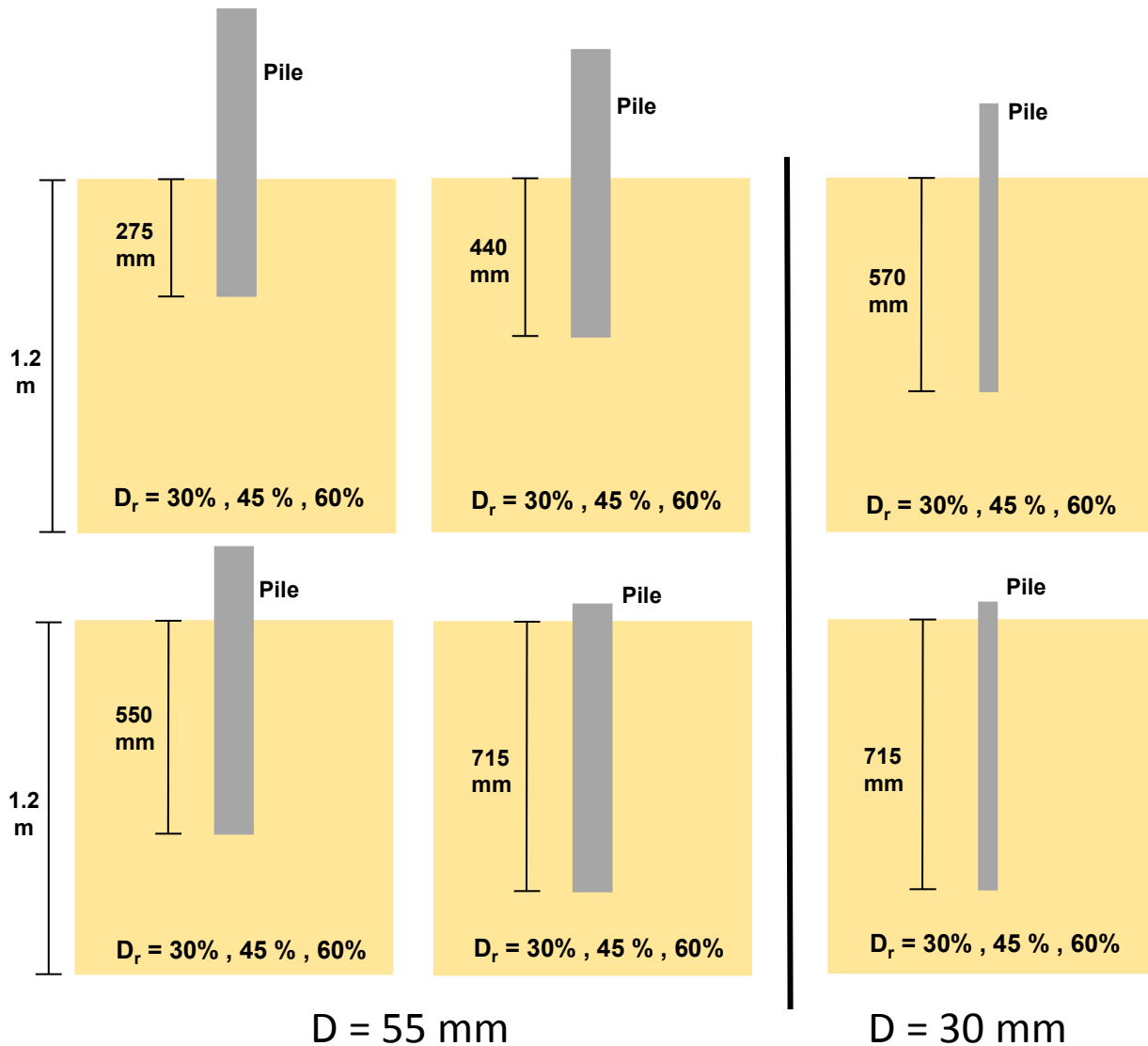


Figure 3-19: Pile load testing program for both pile models

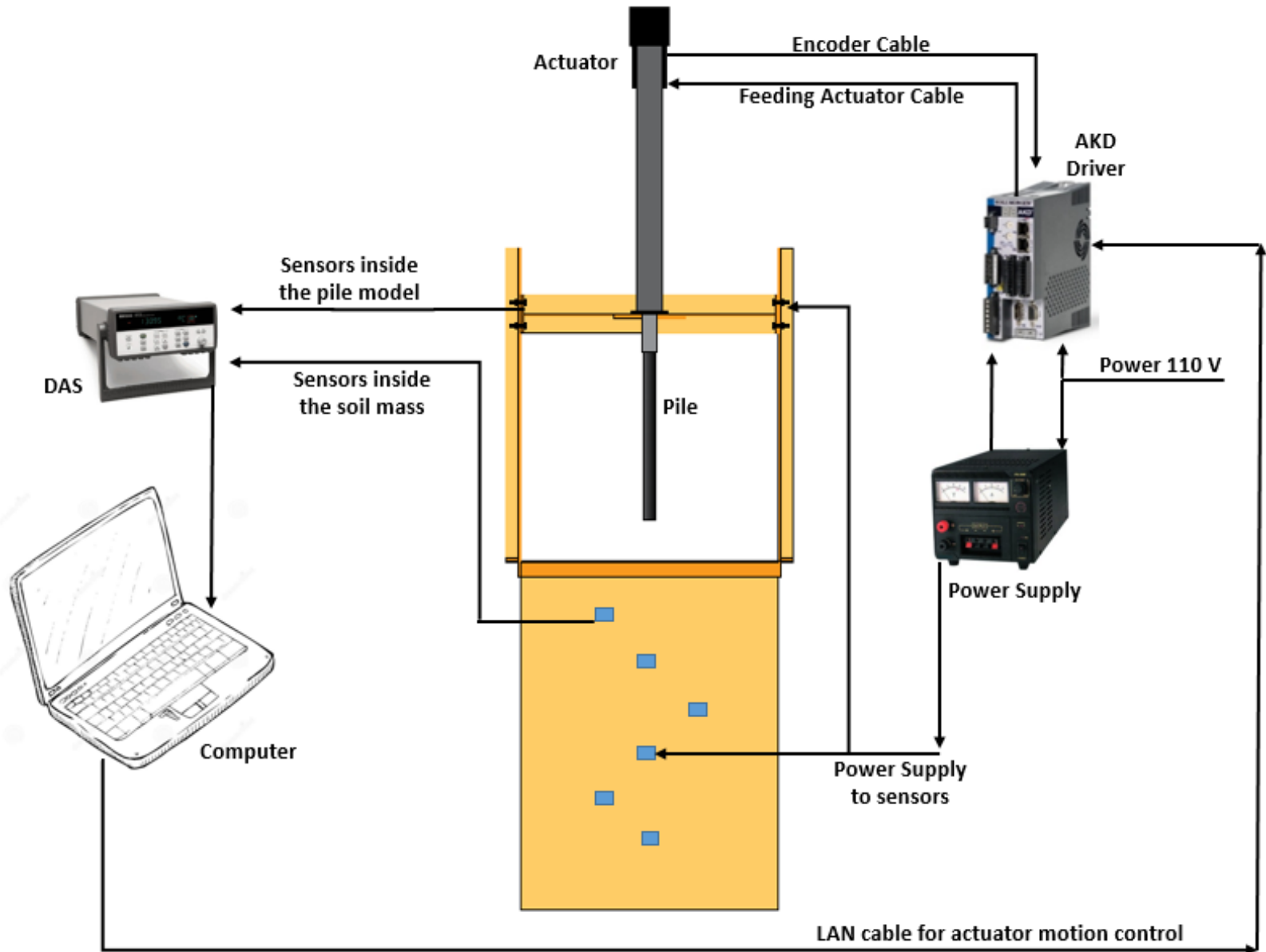


Figure 3-20: Setup arrangement

Table 3-9: Pile load testing program for pile model of 55 mm diameter

Diameter (mm) D	Relative Density (%) D <sub>r</sub>	Relative depth L/D	Embedment Depth, (mm) L	Test Name
55	30	5	275	C-55-30%-5
		8	440	C-55-30%-8
		10	550	C-55-30%-10
		13	715	C-55-30%-13
	45	5	275	C-55-45%-5
		8	440	C-55-45%-8
		10	550	C-55-45%-10
		13	715	C-55-45%-13
	60	5	275	C-55-60%-5
		8	440	C-55-60%-8
		10	550	C-55-60%-10
		13	715	C-55-60%-13

Table 3-10: Pile load testing program for pile model of 30 mm diameter

Diameter (mm) D	Relative Density (%) D <sub>r</sub>	Relative depth L/D	Embedment Depth, (mm) L	Test Name
30	30	19	570	C-30-30%-19
		23.8	715	C-30-30%-23.8
	45	19	570	C-30-45%-19
		23.8	715	C-30-45%-23.8
	60	19	570	C-30-60%-19
		23.8	715	C-30-60%-23.8

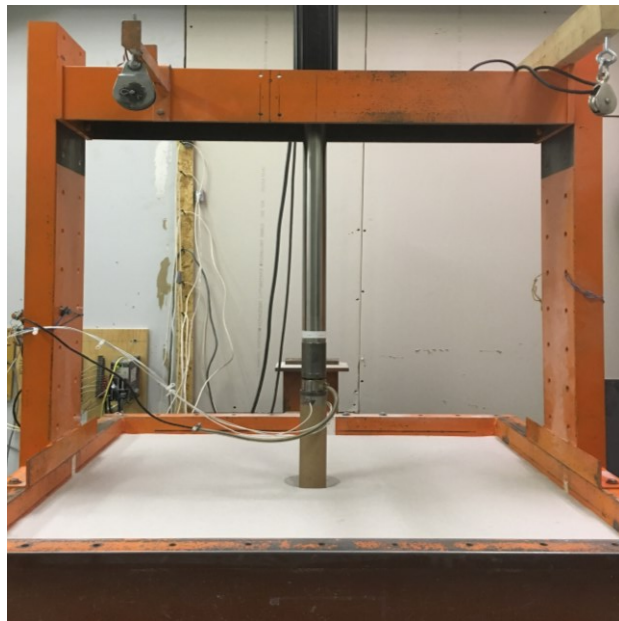
### 3.5.3 Test Results

Figure 3-21 presents photos of both pile models during testing. For the pile model 55 mm in diameter, the results of the top, two middle, and bottom load cells appear in the form of load–settlement curves, as is the total shaft resistance for the entire pile and each of its sections. For the pile model 30 mm in diameter, the results of the top and bottom load cells are presented as load–settlement curves combined with total shaft resistance. All results concerning shaft resistance are summarized in tabular format for both piles.

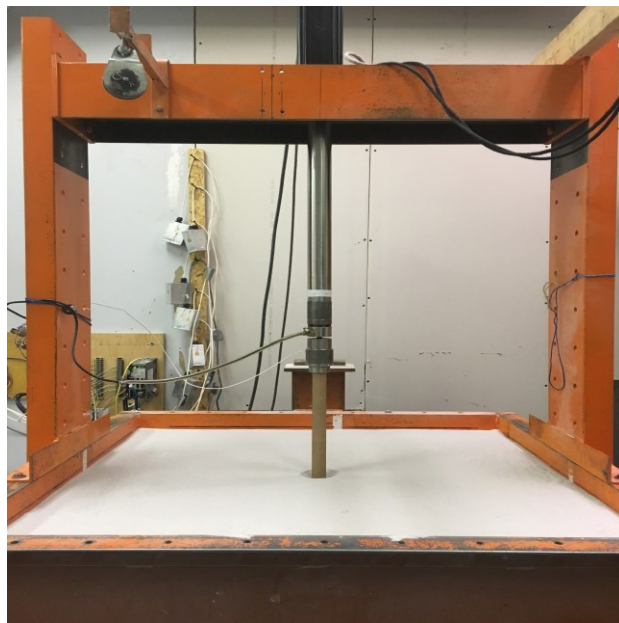
Pile load tests provided data only, meaning that the ultimate load (i.e., failure) needed to be defined. The ultimate load for a pile is defined as the load that causes the pile to plunge or to settle rapidly under a sustained load for which a large settlement might be required. Several researchers (Vesic, 1977; Randolph et al., 1994) have also described ultimate load according to arbitrary settlement limits (e.g., 10% of the pile diameter), whereas other researchers and engineers have defined it as the intersection of the initial tangent to the load–settlement curve and the tangent or extension of the final portion of the curve in what is called the *tangential method*. Still other researchers have argued that those definitions are judgmental and that failure depends on expert opinion. Consequently, failure should be defined based on a mathematical rule that yields reproducible results (Prakash & Sharma, 1990), and accordingly, many mathematical methods have been proposed to determine the ultimate load, including the 90% criterion suggested by the Swedish Pile Commission (Brinch, 1963), Mazurkiewicz’s (1972) method and Davison’s (1972) method.

Because the CRP method was used to perform all pile load tests in the research reported here, well-defined load–settlement curves resulted. The tangential method was thus convenient to interpret the test results and define the ultimate load. According to ultimate load, ultimate shaft resistance could also be found. All load–settlement curves drawn from the experimental pile load tests consisted of 240

points, and a load reading was recorded every 0.0833 s (i.e., 5 mm / min). Because a large number of load points were recorded for such a small displacement (i.e., 20 mm) and given the proximity of the point values, the points were connected without using any curve-fitting function.



(a)



(b)

Figure 3-21: Photos for the (a) 55 mm and (b) 30 mm pile models during test

### 3.5.3.1 Pile Model of 55 mm Diameter

The experimental results are presented for the pile model 55 mm in diameter for relative densities of 30%, 45%, and 60% and sorted accordingly. As explained previously, the pile was instrumented with four load cells. The bottom load cell (Bottom LC) measured the pile's tip resistance, the middle 2 load cells (Mid 2 LC) measured the tip resistance and shaft resistance for Section 3, the middle 1 load cell (Mid 1 LC) measured the tip resistance and the shaft resistance for Sections 2 and 3, and the top load cell (Top LC) measured the total resistance of the pile, which consisted of the tip resistance and shaft resistance for Section 1, 2, and 3 (Figure 3-22). Accordingly, the difference between any two load cells allowed the identification of the shaft resistance for the section or sections in between.

For each pile load test, the load cell readings are depicted, and accordingly, two figures are generated. The first presents the resistance of the total pile, the tip, and the total shaft, whereas the second presents the shaft resistance for each section of the pile. All figures are in the form of load–settlement curves. The ultimate shaft force for each section was selected based on the ultimate load of the pile.

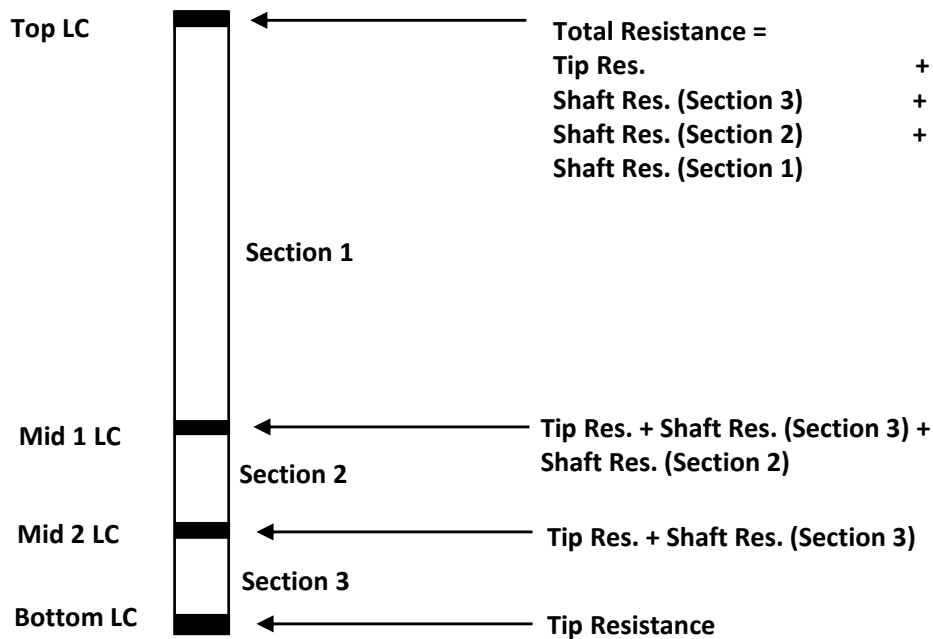


Figure 3-22: Instrumentation of the 55 mm diameter pile model

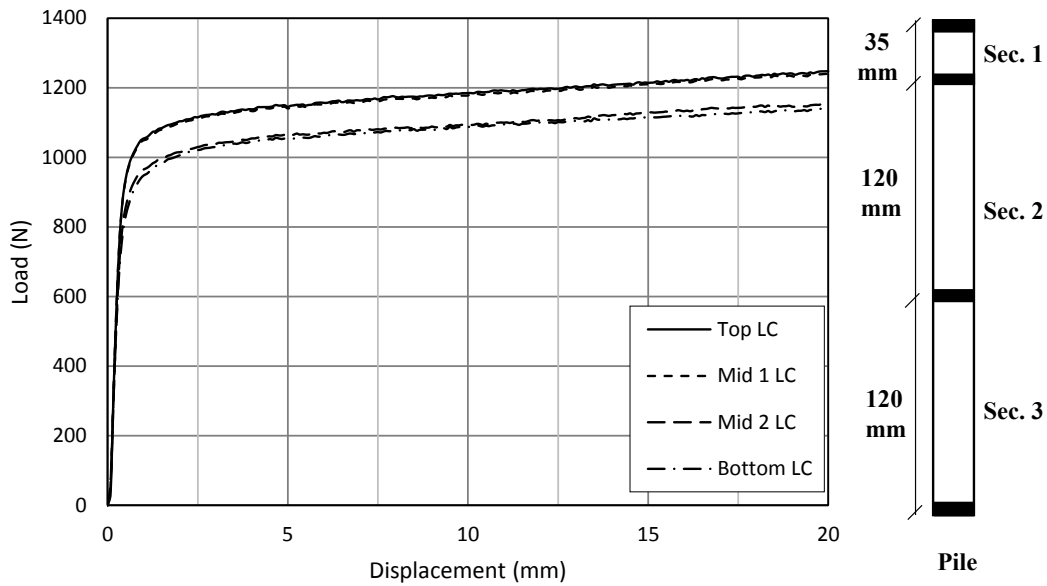
### **Relative Density (30%)**

The load–settlement curves from the pile load test at the first embedment depth ratio of  $L / D = 5$  appear in Figure 3-23. The bottom load cell values were close to the (Mid 2) load cell values, which indicates small friction resistance for Section 3. Meanwhile, the top and the (Mid 1) load cell values were approximate to each other. According to results found by using the tangential method, the ultimate shaft resistance was 93.9 (N). The shaft resistance for each section indicates that Section 2 contributed more to shaft resistance than Sections 1 and 2.

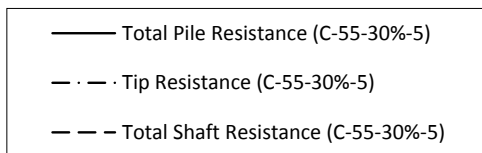
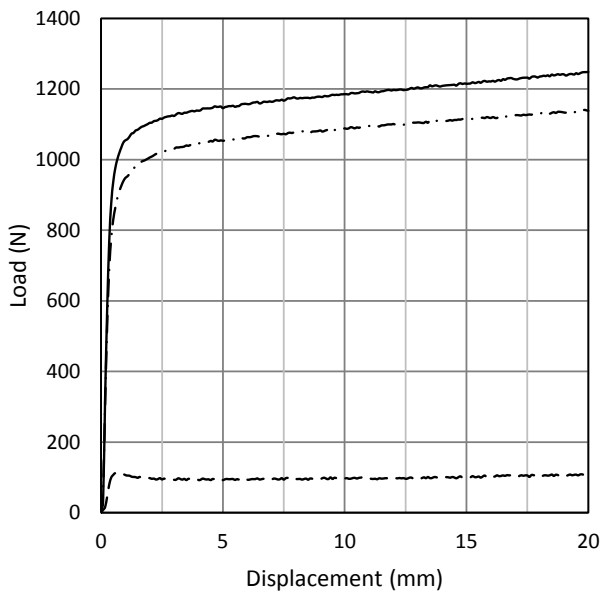
The load–settlement curves of the pile load test at an embedment depth ratio of  $L / D = 8$  appear in Figure 3-24, in which the load cell results are separated and indicate the contribution of the shaft to every section of the pile. The total shaft resistance and shaft resistance of each section increased compared to results at the embedment depth ratio of  $L / D = 5$ .

The load–settlement curves of the pile load test at an embedment depth ratio of  $L / D = 10$  appear in Figure 3-25. Compared with results of the embedment depth ratio of  $L / D = 8$ , all resistance values increased, and the curves were more separated, which indicates the greater contribution of the shaft.

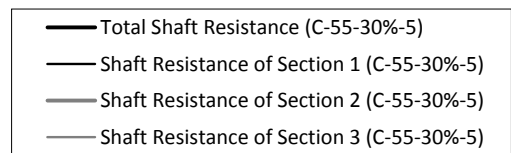
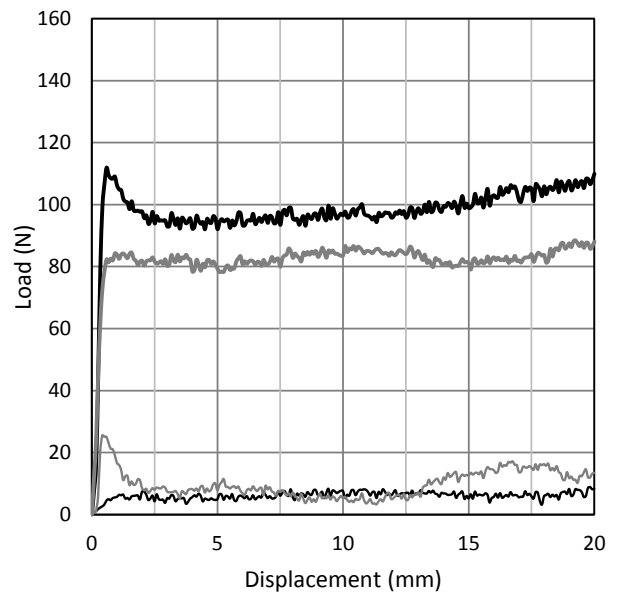
Figure 3-26 shows the load–settlement curves for the pile load test at the embedment depth ratio of  $L / D = 13$ , which was the last test of the test program for 30% relative density. The figure shows a greater tip and shaft resistance than those found at the embedment depth ratio of  $L / D = 10$ . Importantly, the greatest value of total shaft resistance occurred at this embedment depth ratio. The series of tests performed at 30% relative density revealed that total shaft resistance and the shaft resistance of each section increased with depth. The ultimate shaft resistance observed in all tests is summarized in a tabular format at the end of this section.



(a)

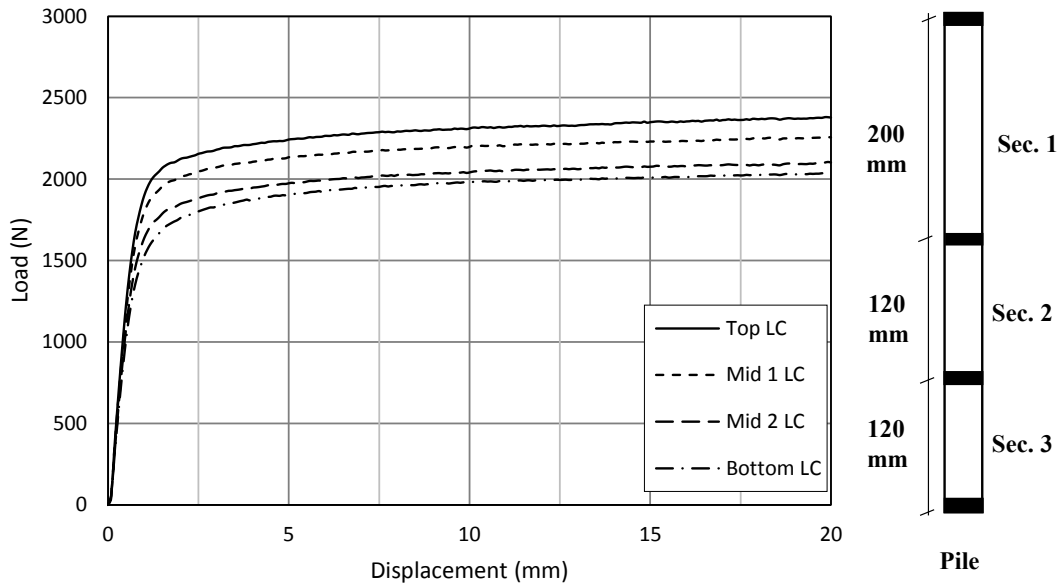


(b)

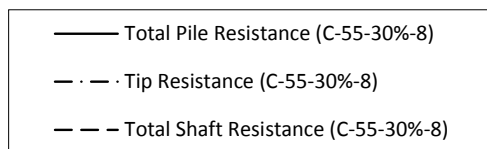
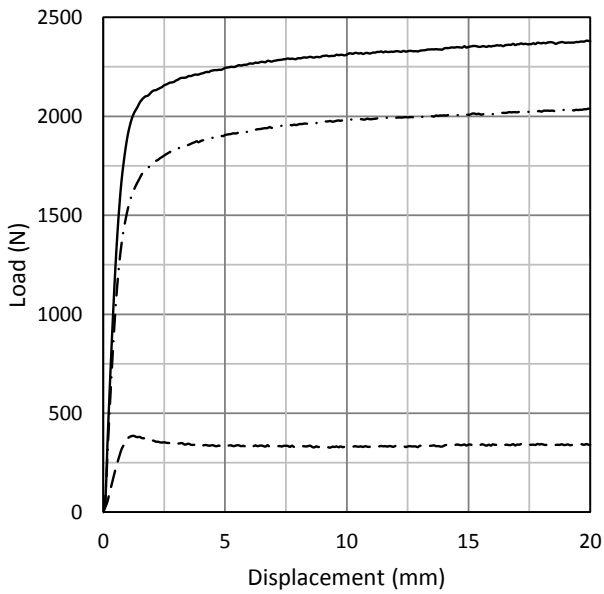


(c)

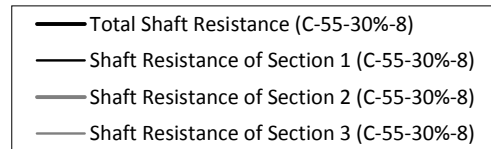
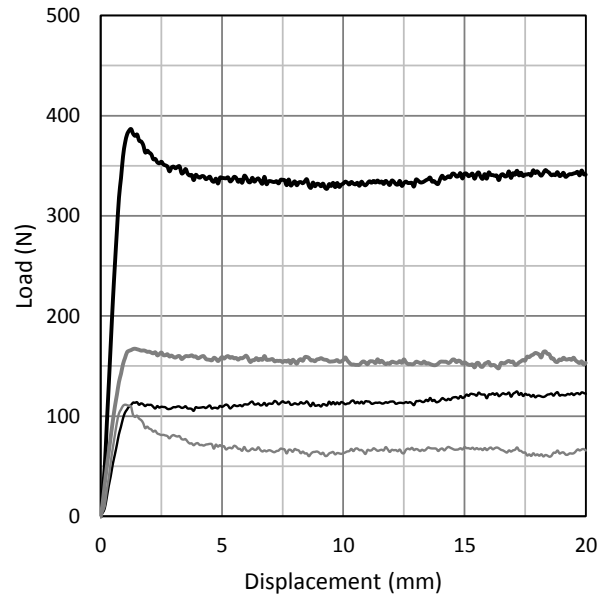
Figure 3-23: Test results of (C-55-30%-5); (a) Load-Cell reading, (b) total, tip, and shaft resistance, and (c) shaft resistance for sections



(a)

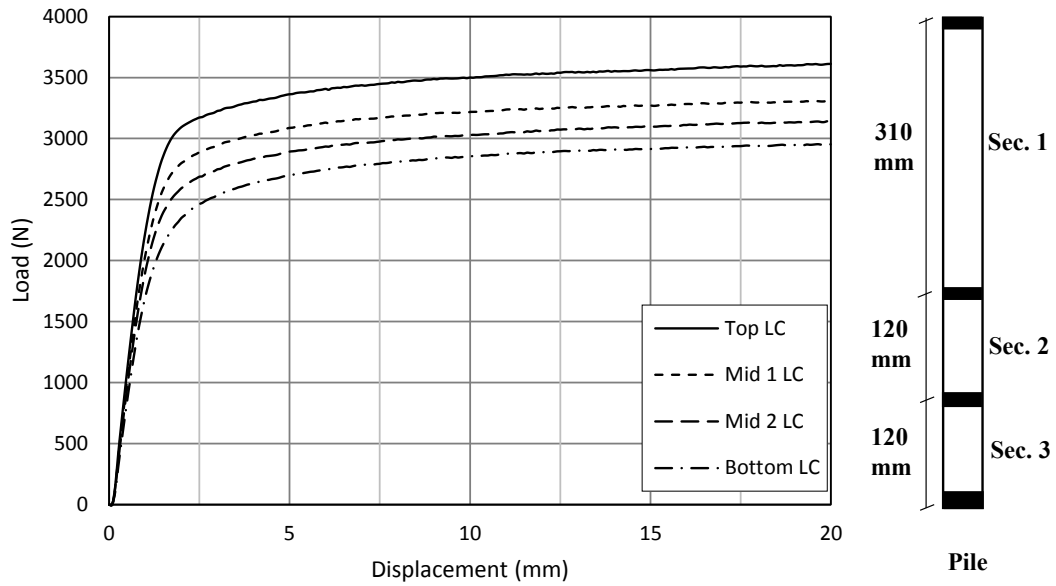


(b)

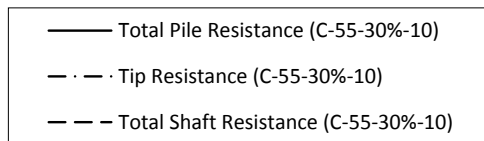
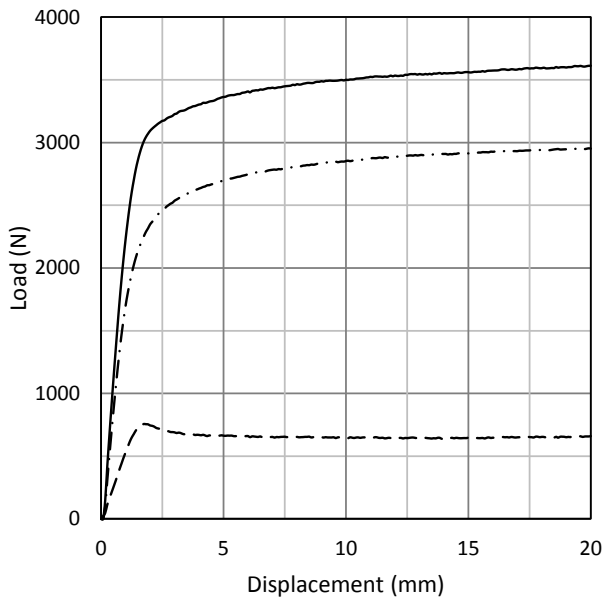


(c)

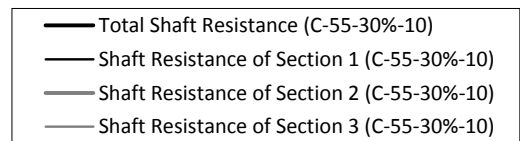
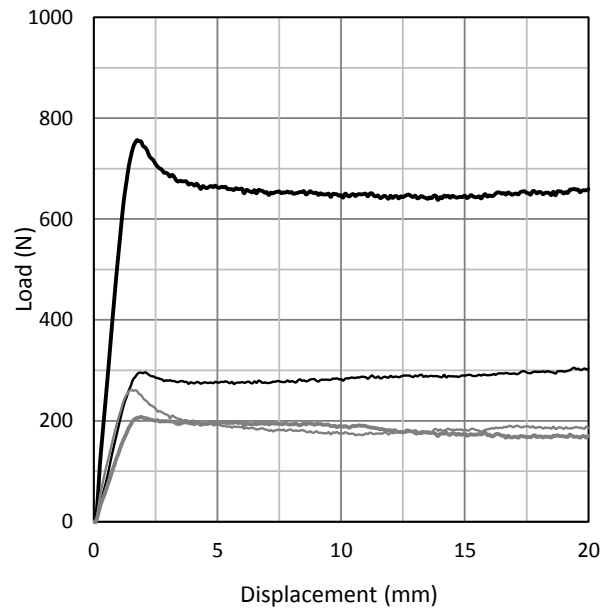
Figure 3-24: Test results of (C-55-30%-8); (a) Load-Cell reading, (b) total, tip, and shaft resistance, and (c) shaft resistance for sections



(a)

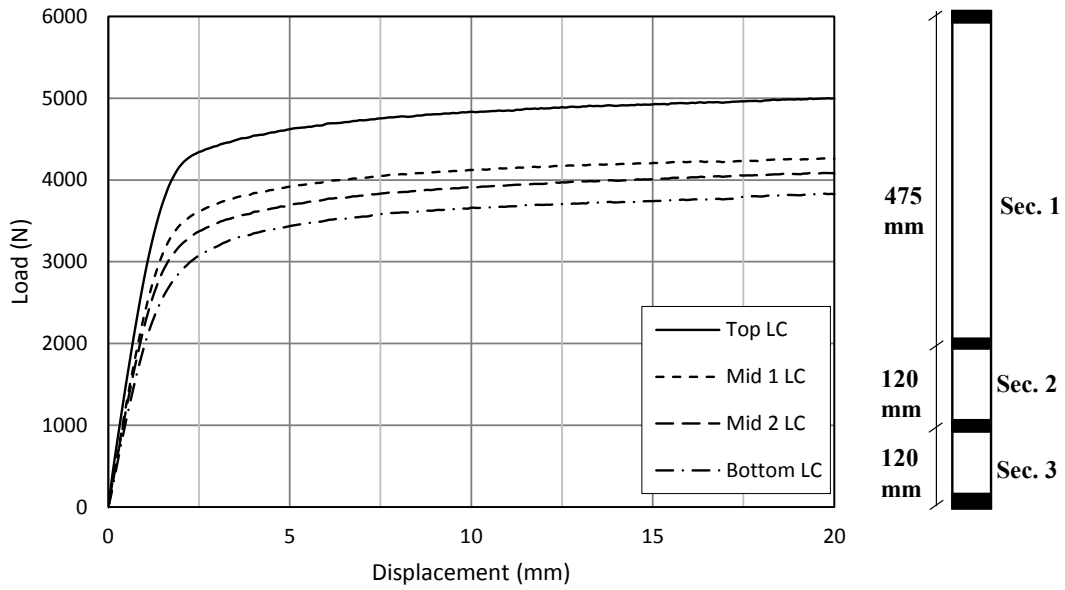


(b)

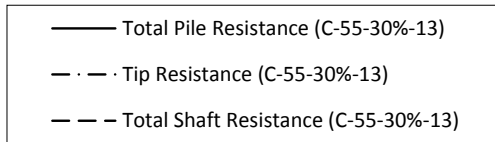
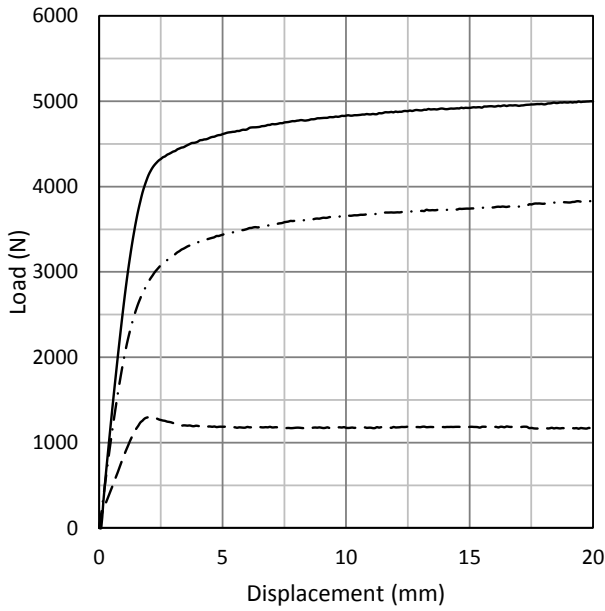


(c)

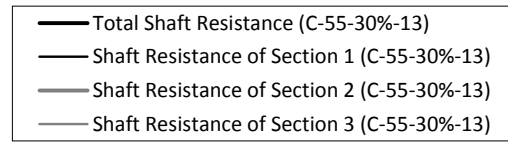
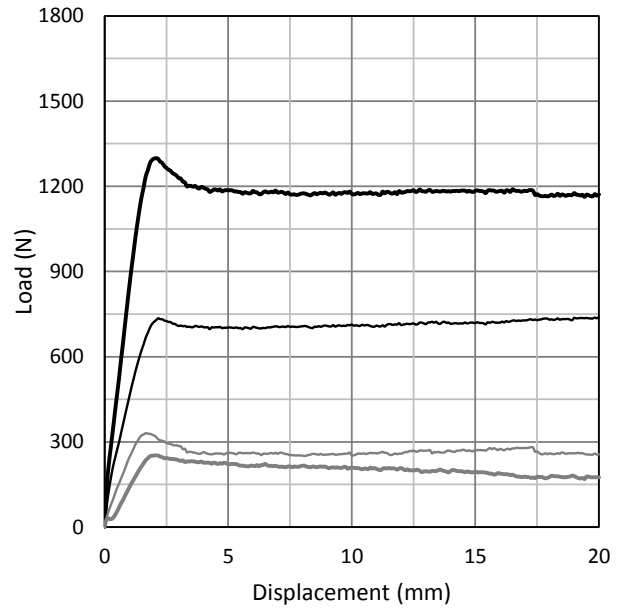
Figure 3-25: Test results of (C-55-30%-10); (a) Load-Cell reading, (b) total, tip, and shaft resistance, and (c) shaft resistance for sections



(a)



(b)



(c)

Figure 3-26: Test results of (C-55-30%-13); (a) Load-Cell reading, (b) total, tip, and shaft resistance, and (c) shaft resistance for sections

### **Relative Density (45%)**

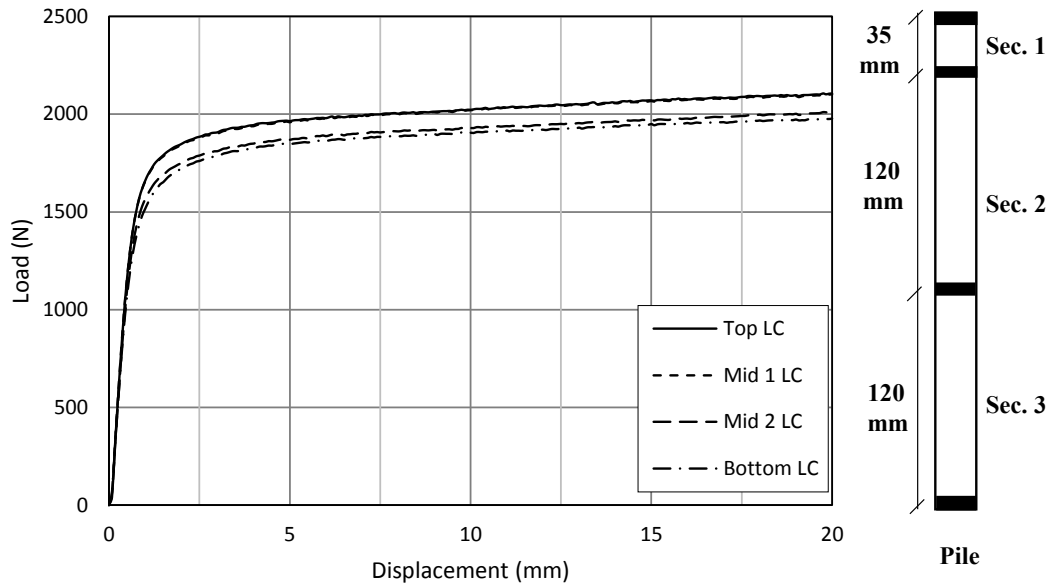
At 45% relative density, the load–settlement curves from the pile load test at the embedment depth ratio of  $L / D = 5$  appear in Figure 3-27. The load–settlement behaviour was similar to that presented for 30% relative density (Figure 3-23); however, the resistance values were greater for 45% relative density. Section 2 of the pile contributed more to shaft resistance than Sections 1 and 2, as was observed at 30% relative density at the same depth.

The load–settlement curves from the pile load test at the embedment depth ratio of  $L / D = 8$  appear in Figure 3-28 and indicate greater resistance than that found for 30% relative density (Figure 3-24). The results also reveal an increase in the shaft resistance for each section of the pile compared to results at the embedment depth ratio of  $L / D = 5$  with the same relative density.

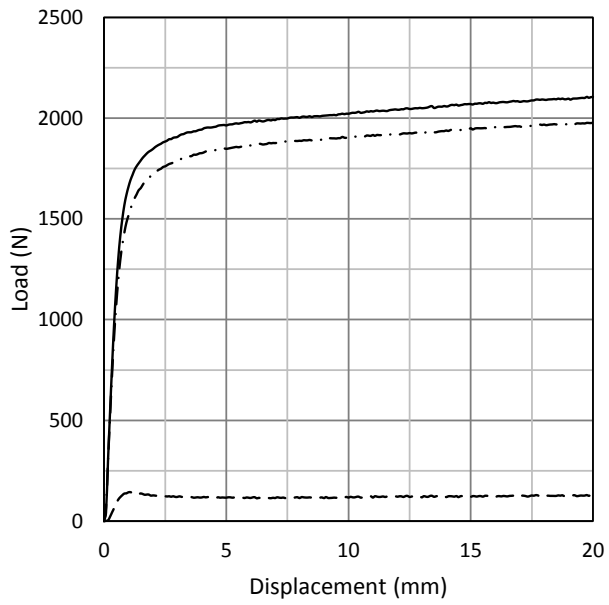
Figure 3-29 presents the load–settlement curves from the pile load test at the embedment depth ratio of  $L / D = 10$ , which achieved greater resistance than that at the embedment depth ratio of  $L / D = 8$  and that at the same depth for 30% relative density (Figure 3-25). Sections 2 and 3 yielded approximate values that resembled the behaviour of the pile load test performed at the same depth for 30% relative density. Total shaft resistance and the shaft resistance of the sections were greater than the total shaft resistance for 30% relative density at the same depth.

Figure 3-30 shows the load–settlement curves from the last embedment depth ratio,  $L / D = 13$ , for 45% relative density. Resistance from the tip and shaft were greater than that found at an embedment depth ratio of  $L / D = 10$  for the same relative density and greater than that at the same embedment depth ratio for 30% relative density (Figure 3-26). It also achieved the greatest value of total shaft resistance for all tests for 45% relative density.

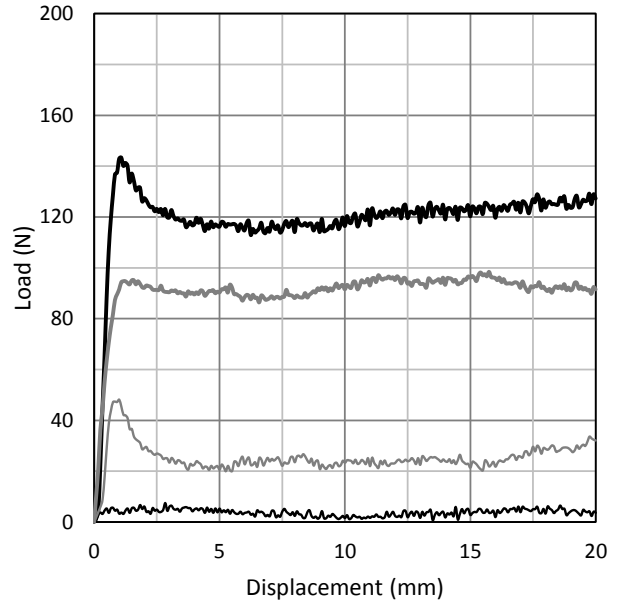
The series of tests for 45% relative density revealed that total shaft resistance, as well as the shaft resistance for each section, increased with depth, as well as that shaft resistance values were greater than those found for 30% relative density. The ultimate shaft resistance observed in all tests is summarized in a tabular format at the end of this section.



(a)

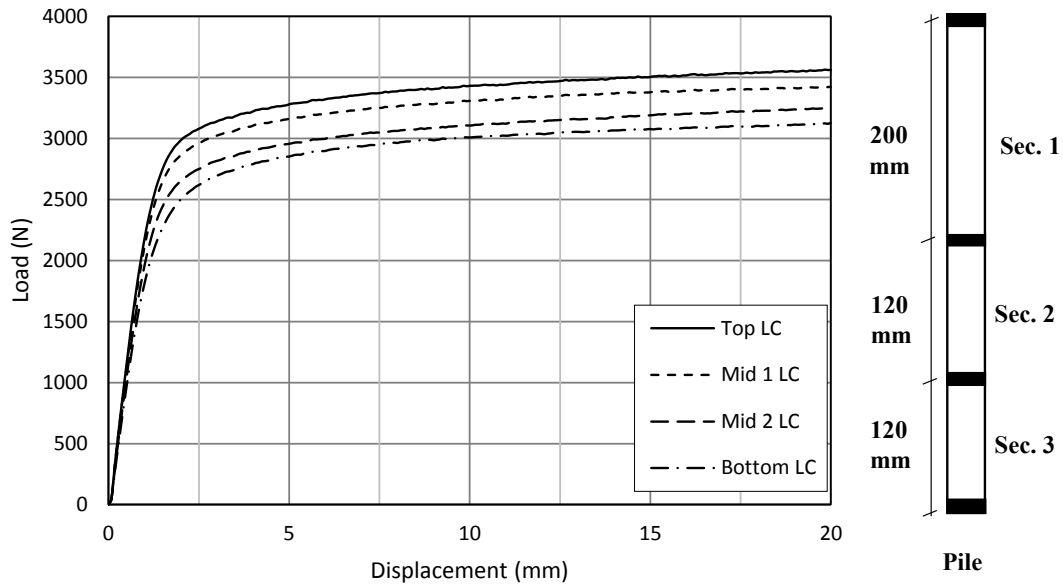


(b)

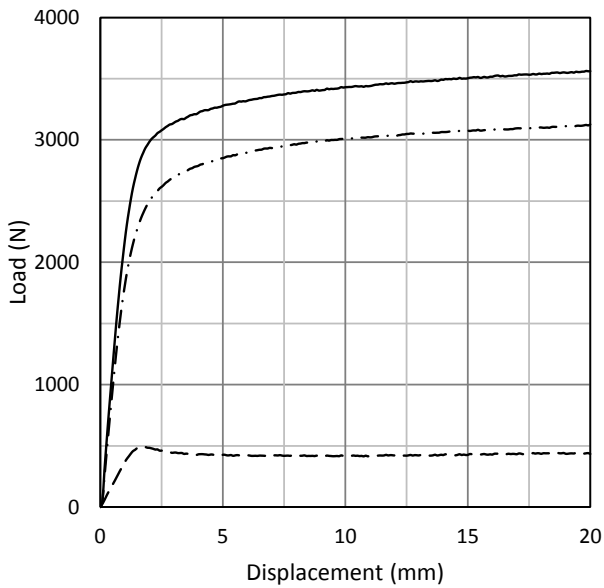


(c)

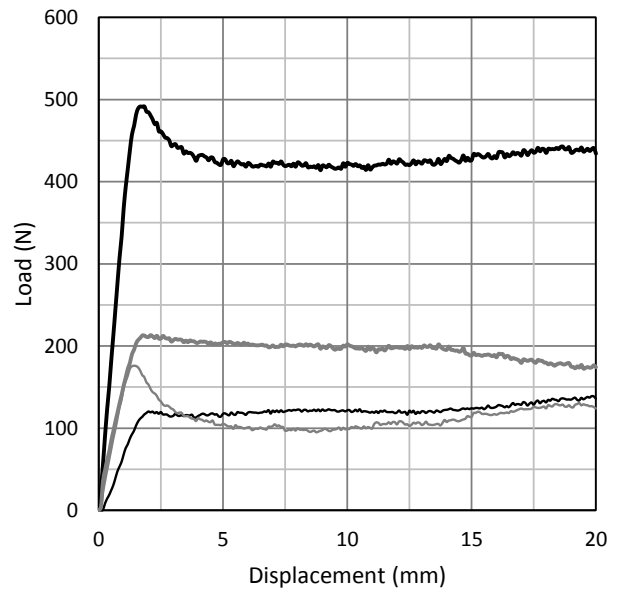
Figure 3-27: Test results of (C-55-45%-5); (a) Load-Cell reading, (b) total, tip, and shaft resistance, and (c) shaft resistance for sections



(a)

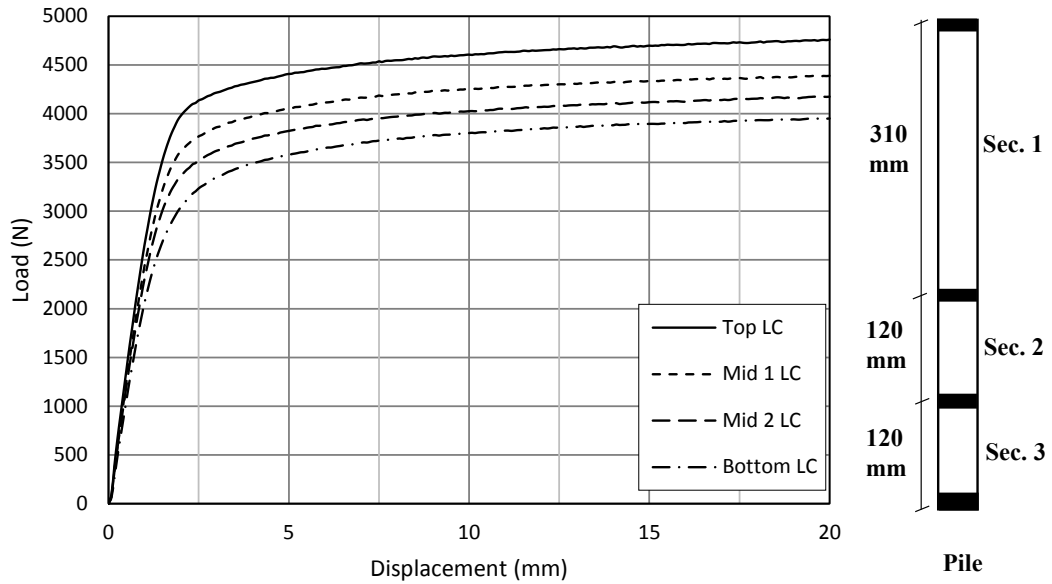


(b)

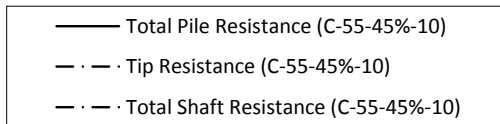
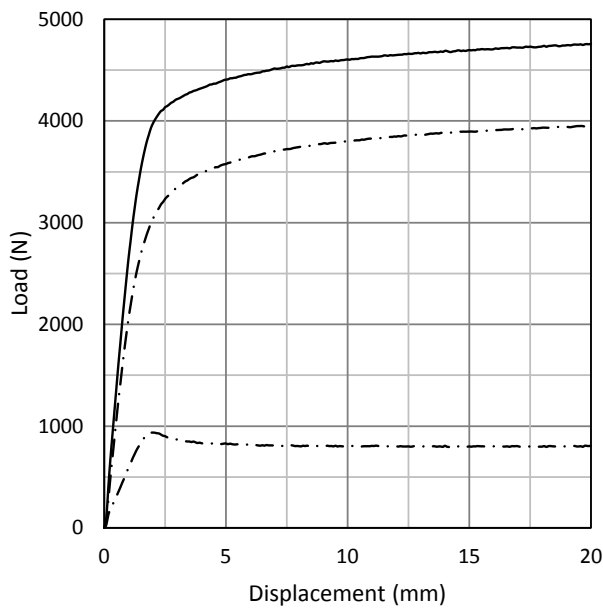


(c)

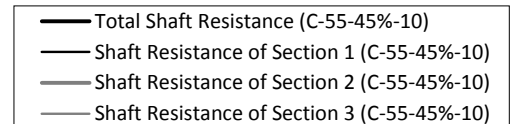
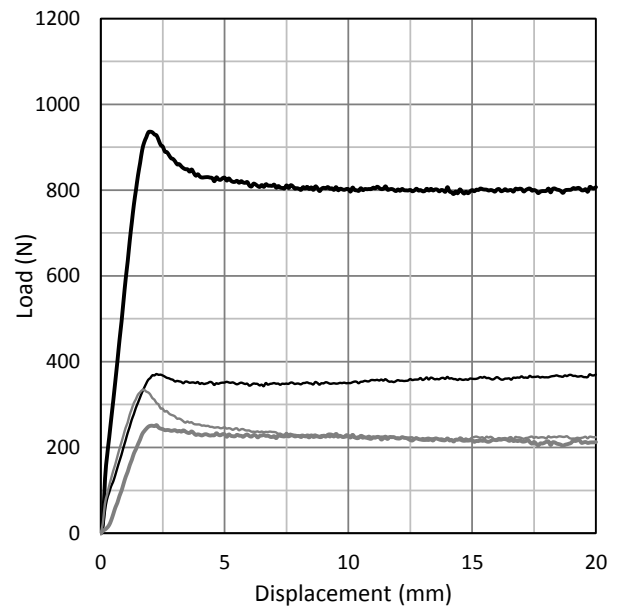
Figure 3-28: Test results of (C-55-45%-8); (a) Load-Cell reading, (b) total, tip, and shaft resistance, and (c) shaft resistance for sections



(a)

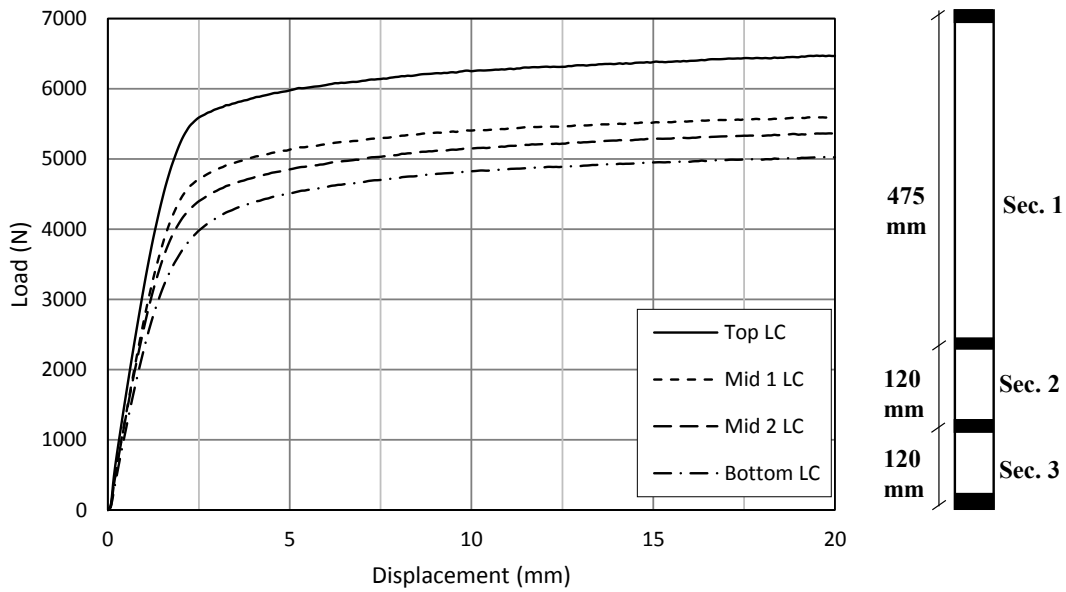


(b)

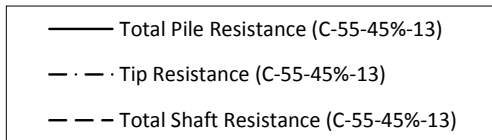
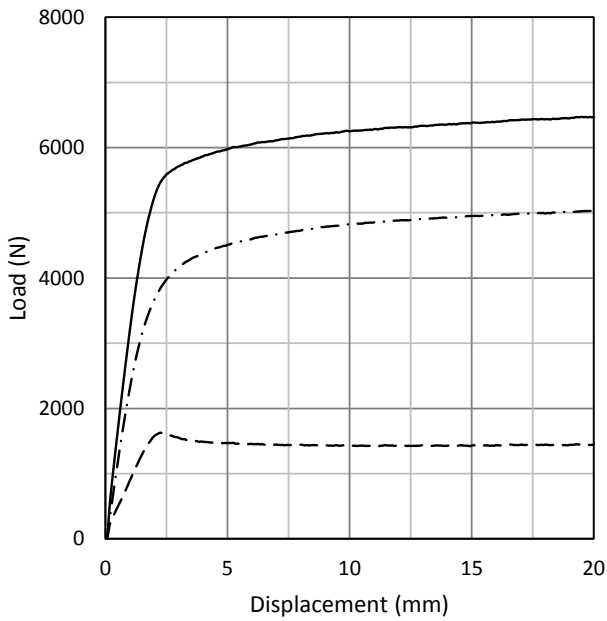


(c)

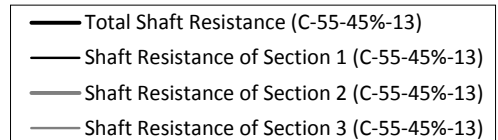
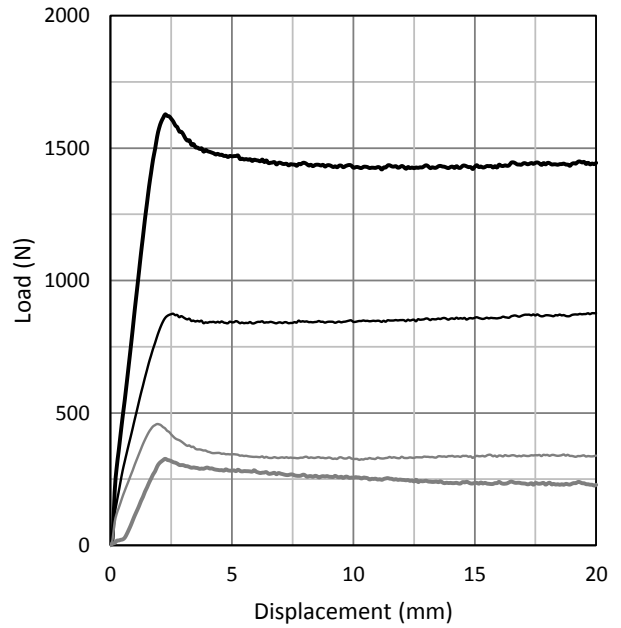
Figure 3-29: Test results of (C-55-45%-10); (a) Load-Cell reading, (b) total, tip, and shaft resistance, and (c) shaft resistance for sections



(a)



(b)



(c)

Figure 3-30: Test results of (C-55-45%-13); (a) Load-Cell reading, (b) total, tip, and shaft resistance, and (c) shaft resistance for sections

### **Relative Density (60%)**

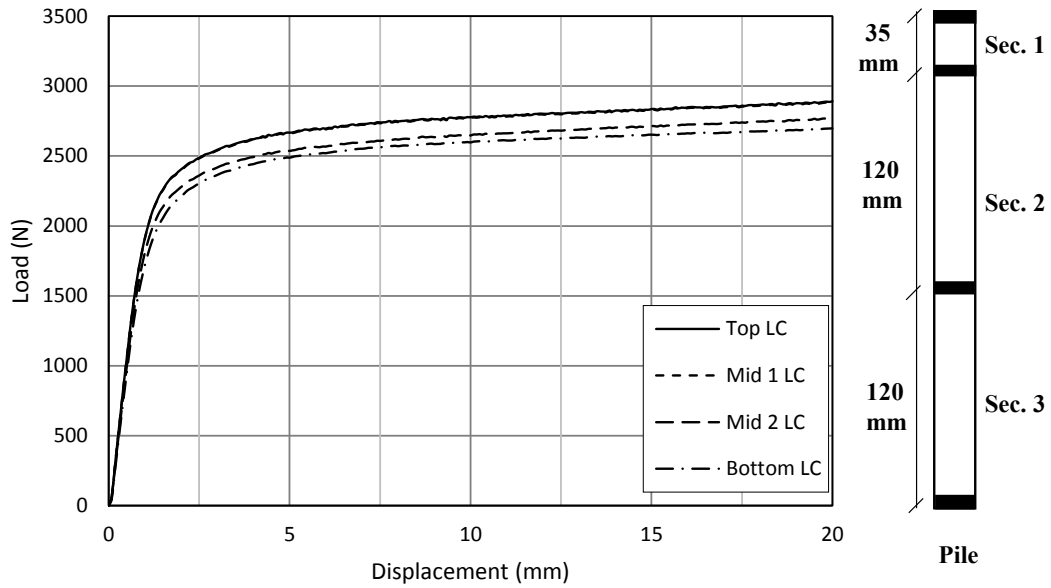
The load–settlement curves from the pile load test at 60% relative density and an embedment depth ratio of  $L / D = 5$  appear in Figure 3-31. Although they indicate behaviour similar to that at 30% relative density (Figure 3-23) and 45% relative density (Figure 3-27), the resistance values were greater at 60% relative density.

For the embedment depth ratio of  $L / D = 8$ , the load–settlement curves from the pile load test appear in Figure 3-32. The relative density of 60% showed greater tip and shaft resistance than found for 30% relative density (Figure 3-24) and 45% relative density (Figure 3-28) at the same embedment depth ratio.

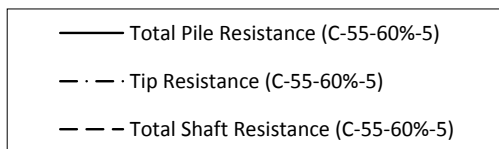
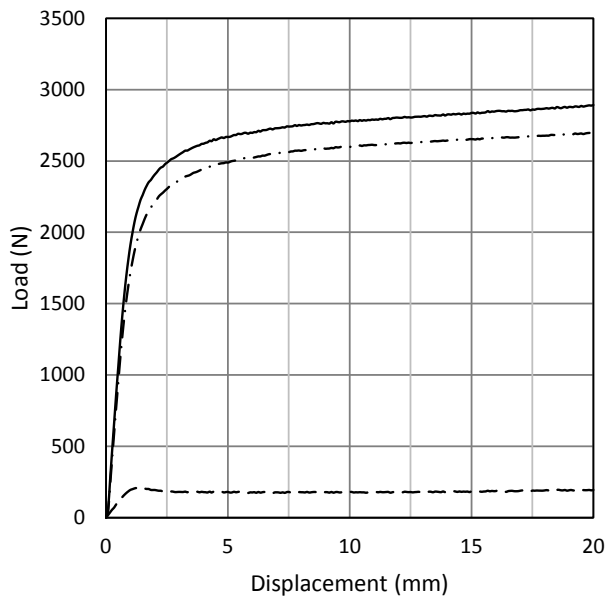
For the embedment depth ratio of  $L / D = 10$ , the load–settlement curves from the pile load test appear in Figure 3-33. That embedment depth ratio showed greater resistance than found at an embedment depth ratio of  $L / D = 8$  with the same relative density, as well as greater values than those found for 30% relative density (Figure 3-25) and 45% relative density (Figure 3-29) at the same embedment depth ratio.

Figure 3-34 presents the load–settlement curves from the pile load test at the last embedment depth ratio,  $L / D = 13$ , for 60% relative density. That embedment depth ratio showed a greater tip and shaft resistance than found at an embedment depth ratio of  $L / D = 10$  for the same relative density, 30% relative density (Figure 3-26), and 45% relative density (Figure 3-30). It also achieved the greatest value of total shaft resistance for tests at 60% relative density.

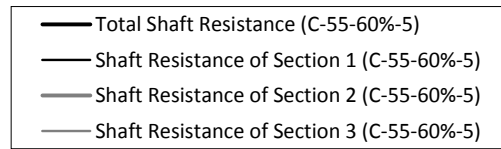
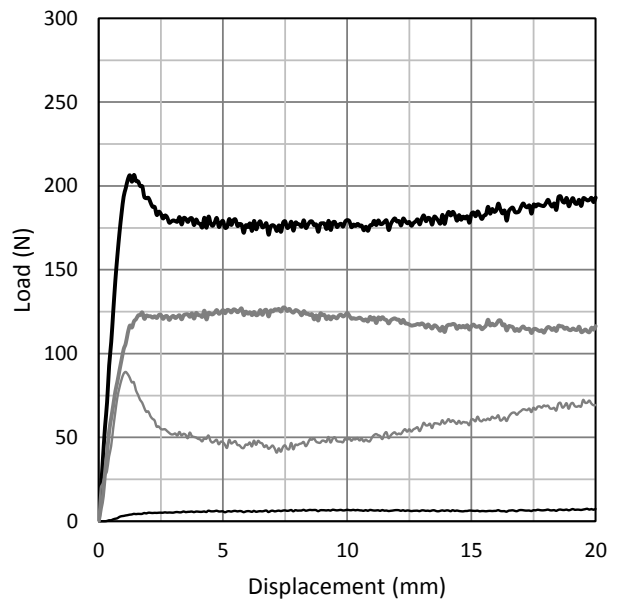
The series of tests performed at 60% relative density revealed that total shaft resistance and shaft resistance for each section increased with depth. Moreover, all values of shaft resistance were greater than those found at 45% and 60% relative densities. Ultimate shaft resistance observed in all tests is summarized in a tabular format at the end of this section.



(a)

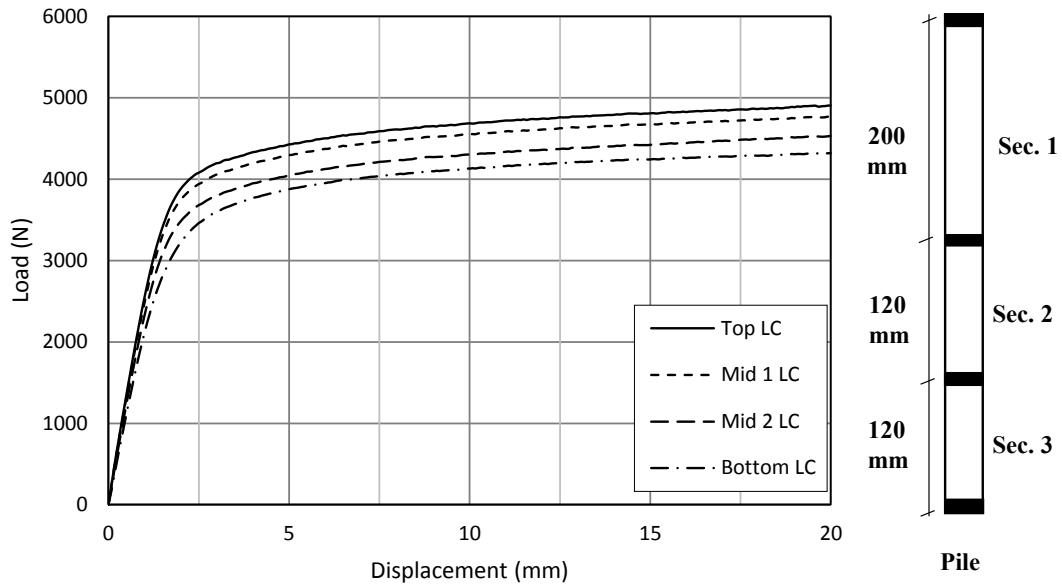


(b)

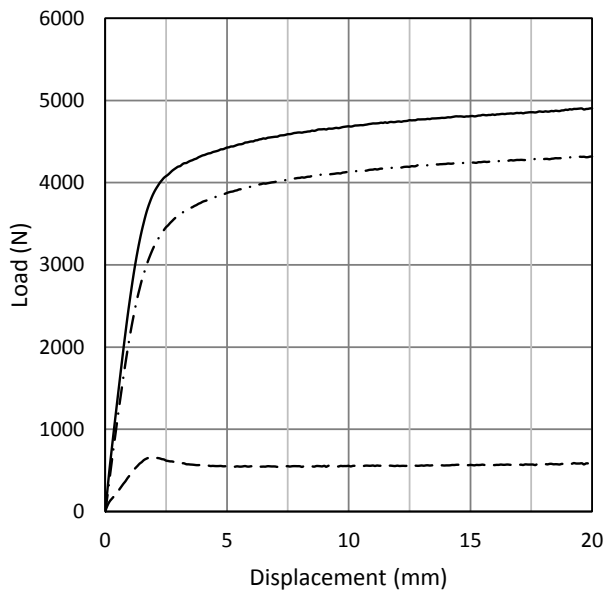


(c)

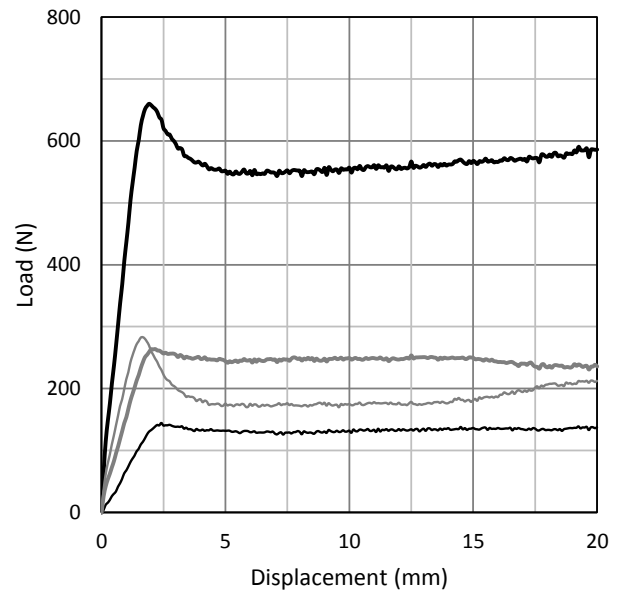
Figure 3-31: Test results of (C-55-60%-5); (a) Load-Cell reading, (b) total, tip, and shaft resistance, and (c) shaft resistance for sections



(a)

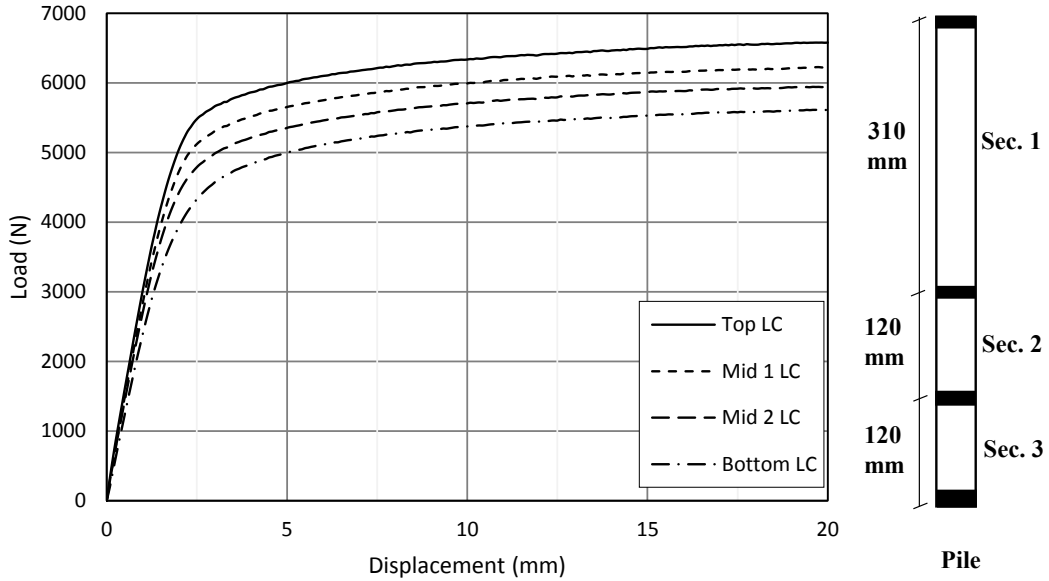


(b)

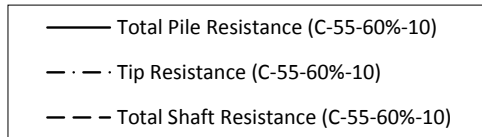
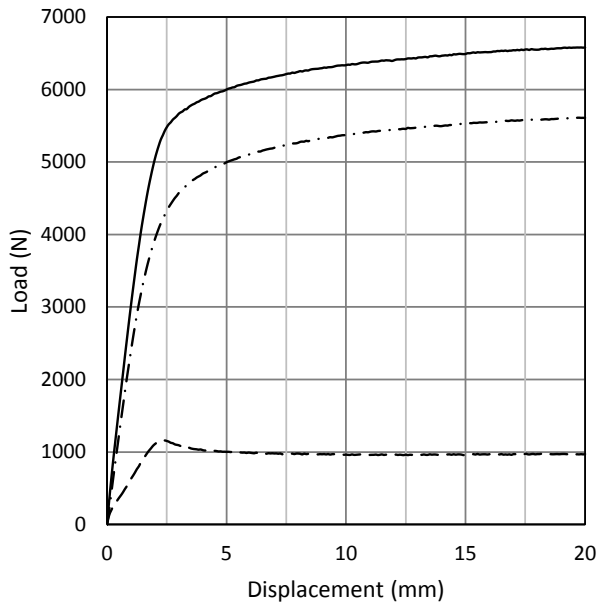


(c)

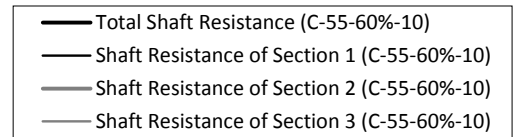
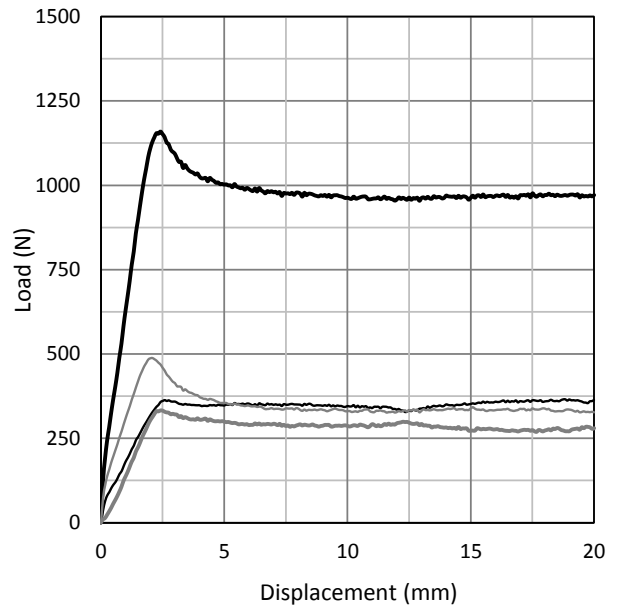
Figure 3-32: Test results of (C-55-60%-8); (a) Load-Cell reading, (b) total, tip, and shaft resistance, and (c) shaft resistance for sections



(a)

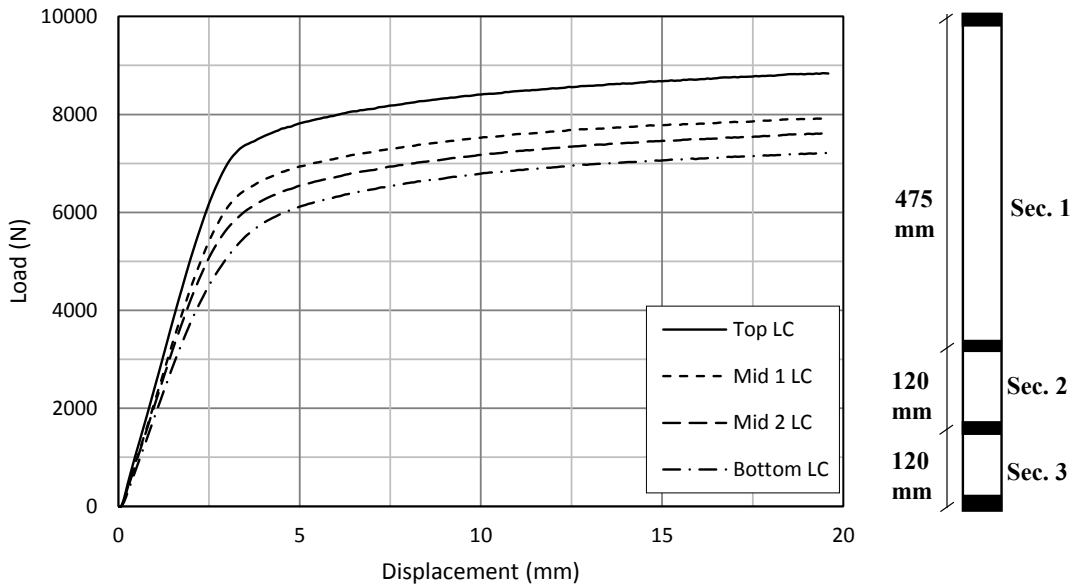


(b)

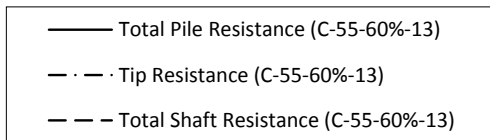
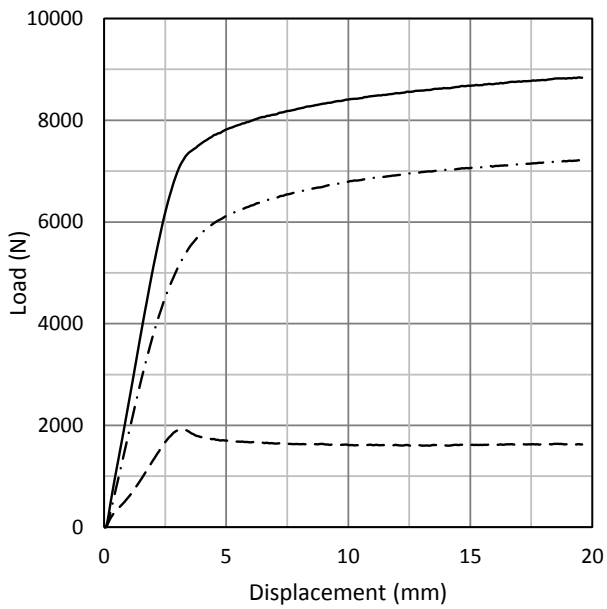


(c)

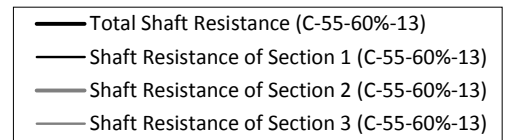
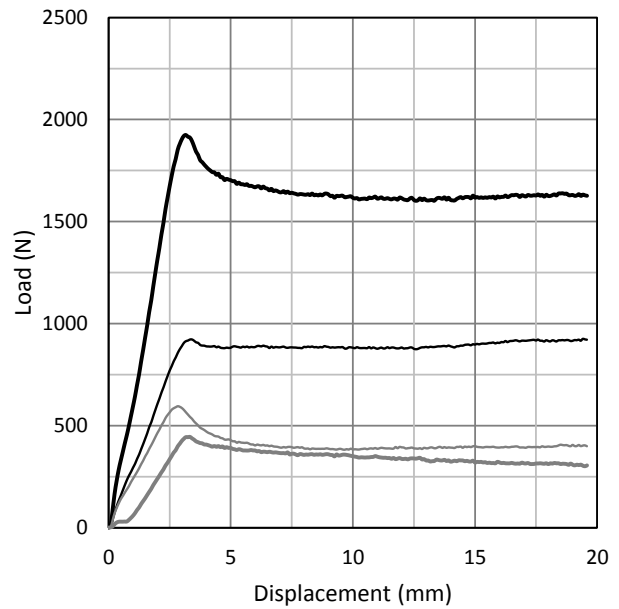
Figure 3-33: Test results of (C-55-60%-10); (a) Load-Cell reading, (b) total, tip, and shaft resistance, and (c) shaft resistance for sections



(a)



(b)



(c)

Figure 3-34: Test results of (C-55-60%-13); (a) Load-Cell reading, (b) total, tip, and shaft resistance, and (c) shaft resistance for sections

### 3.5.3.2 Pile Model of 30 mm Diameter

This section presents the experimental results for the pile model 30 mm in diameter at relative densities of 30%, 45%, and 60%. The model was instrumented with two load cells; the bottom load cell measured the tip resistance of the pile, whereas the top load cell measured the total resistance of the pile, which combines tip resistance and shaft resistance. The difference between the two load cells indicated the shaft resistance for the entire pile.

#### Relative Density (30%)

Figure 3-35 presents the load–settlement curves for the embedment depth ratio of  $L / D = 19$ , whereas Figure 3-36 presents the load–settlement curves for the embedment depth ratio of  $L / D = 23.8$  for 30% relative density. Shaft resistance contributed to total pile resistance almost as much as tip resistance did. In those tests performed at 30% relative density, total shaft resistance increased with depth. Ultimate shaft resistance for all tests is summarized in a tabular format at the end of this section.

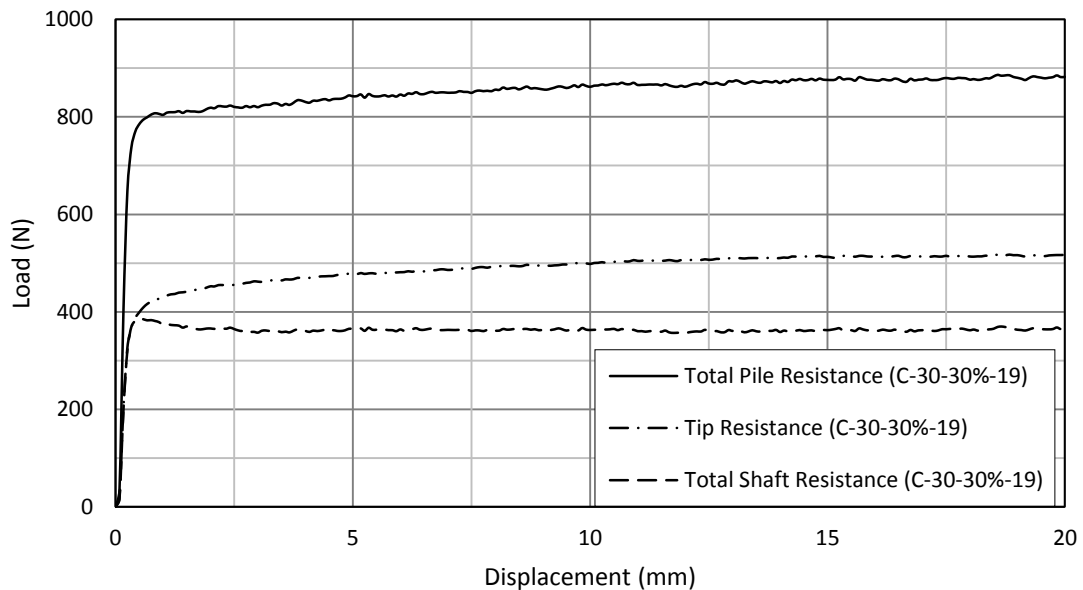


Figure 3-35: Test results of (C-30-30%-19); total, tip, and shaft resistance

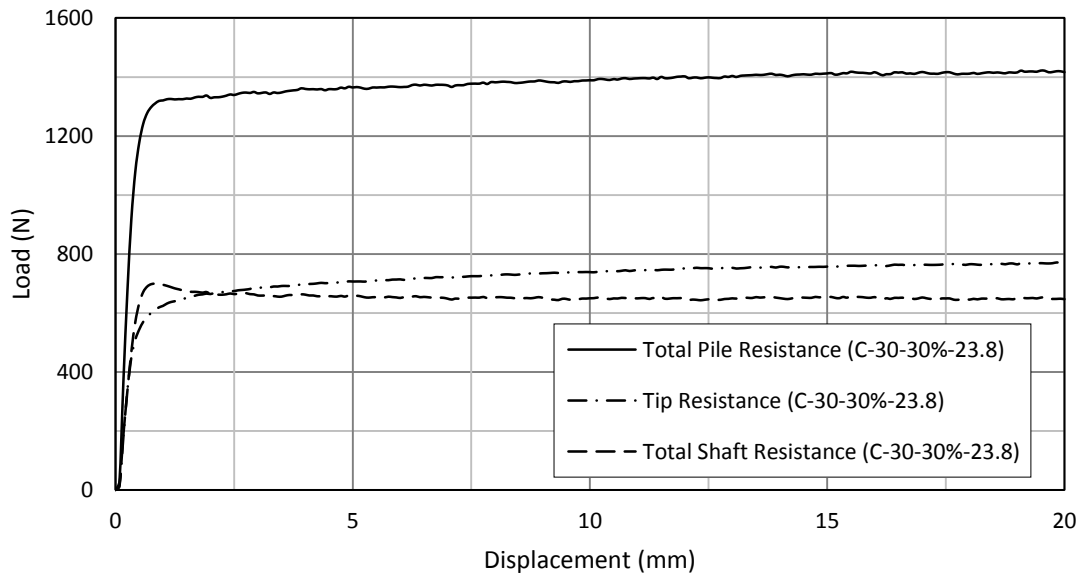


Figure 3-36: Test results of (C-30-30%-23.8); total, tip, and shaft resistance

### Relative Density (45%)

Figure 3-37 presents the load–settlement curves for the embedment depth ratio of  $L / D = 19$  for 45% relative density. Shaft resistance increased more than that at the same depth for 30% relative density. Figure 3-38 presents the load–settlement curves for the embedment depth ratio of  $L / D = 23.8$  for 45% relative density. That embedment depth ratio showed greater shaft resistance than that at the embedment depth ratio of  $L / D = 19$  for the same relative density and that at the same embedment depth ratio for 30% relative density. Those two tests performed at 45% relative density revealed that total shaft resistance increased with depth and exceeded that observed for 30% relative density. Ultimate shaft resistance in all tests is summarized in a tabular format at the end of this section.

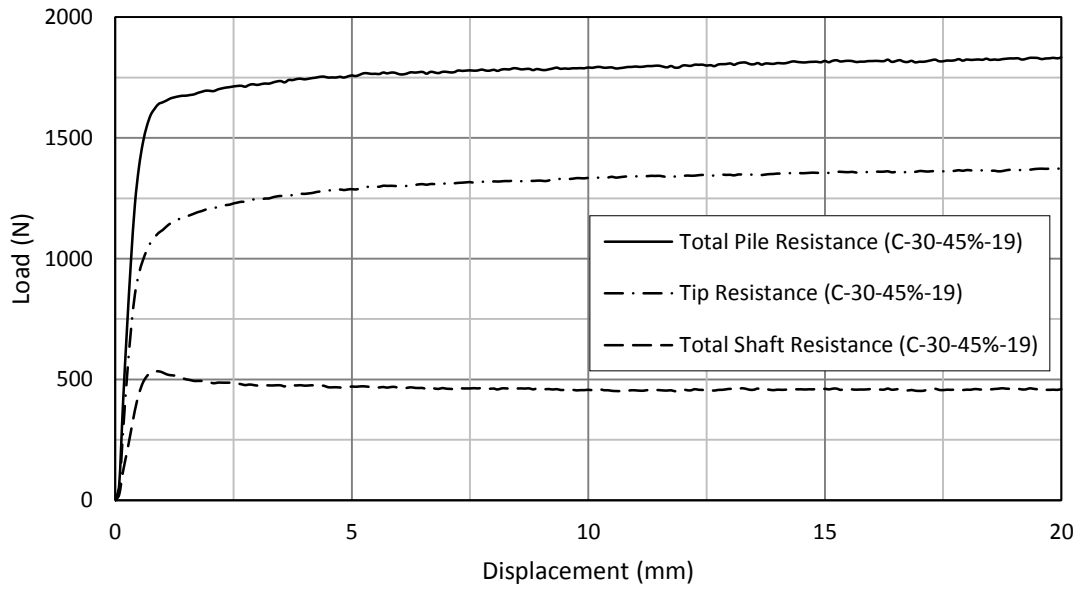


Figure 3-37: Test results of (C-30-45%-19); total, tip, and shaft resistance

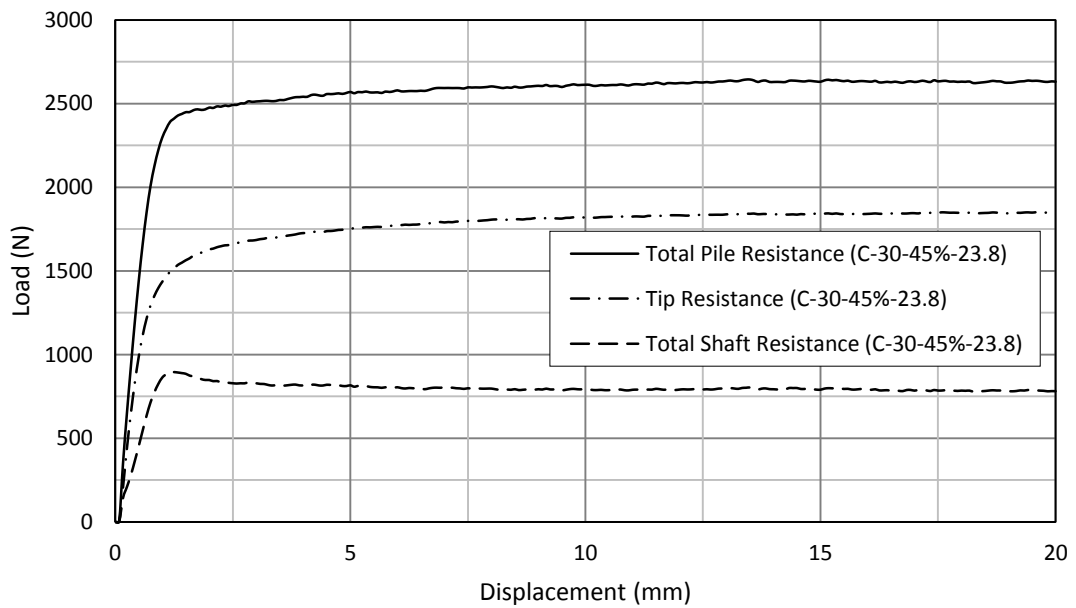


Figure 3-38: Test results of (C-30-45%-23.8); total, tip, and shaft resistance

### Relative Density (60%)

Figure 3-39 presents the load–settlement curves for the embedment depth ratio of  $L / D = 19$  for 60% relative density. Shaft resistance increased more than that observed at the same depth for 30% and 45% relative densities. Figure 3-40 presents the load–settlement curves for the embedment depth ratio of  $L / D = 23.8$  for 60% relative density. That embedment depth ratio showed greater shaft resistance than that found at the embedment depth ratio of  $L / D = 19$  for the same relative density and greater shaft resistance than that found at the same depth for 30% and 45% relative densities. Those two tests performed at 60% relative density revealed that total shaft resistance increased with depth and exceeded that observed for 30% and 45% relative densities. Ultimate shaft resistance in all tests is summarized in a tabular format at the end of this section.

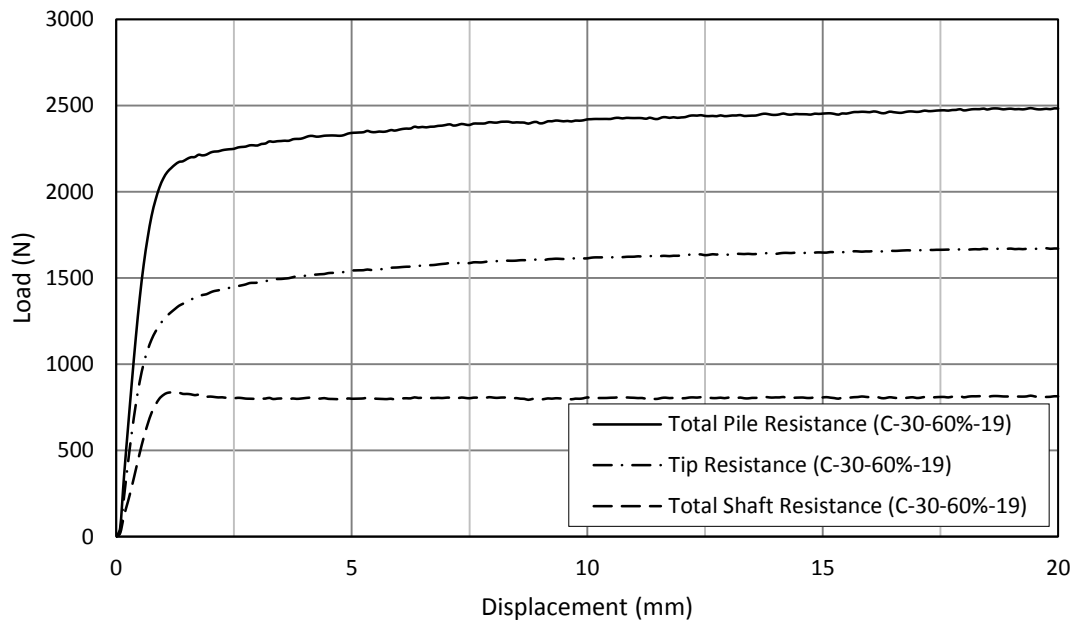


Figure 3-39: Test results of (C-30-60%-19); total, tip, and shaft resistance

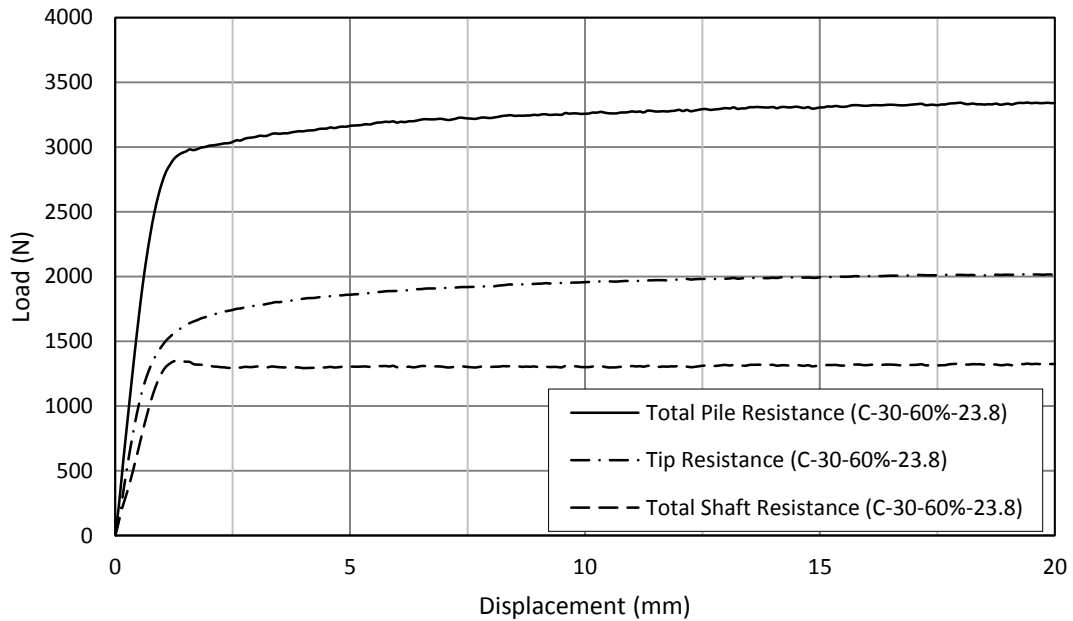


Figure 3-40: Test results of (C-30-60%-23.8); total, tip, and shaft resistance

### 3.5.4 Repeatability

Two tests were repeated to illustrate the repeatability of the test results. The first test repeated was for the pile model 55 mm in diameter at 60% relative density at an embedment depth ratio of 10 L / D (C-55-60%-10). Figure 3-41 presents the results of the original and repeated tests. The second test repeated was for the pile model 30 mm in diameter at 60% relative density at an embedment depth ratio of 10 L / D (C-55-60%-23.8). Figure 3-42 presents the results of the original and repeated tests. Both figures indicate that the results were almost identical, which indicates their consistency and reproducibility.

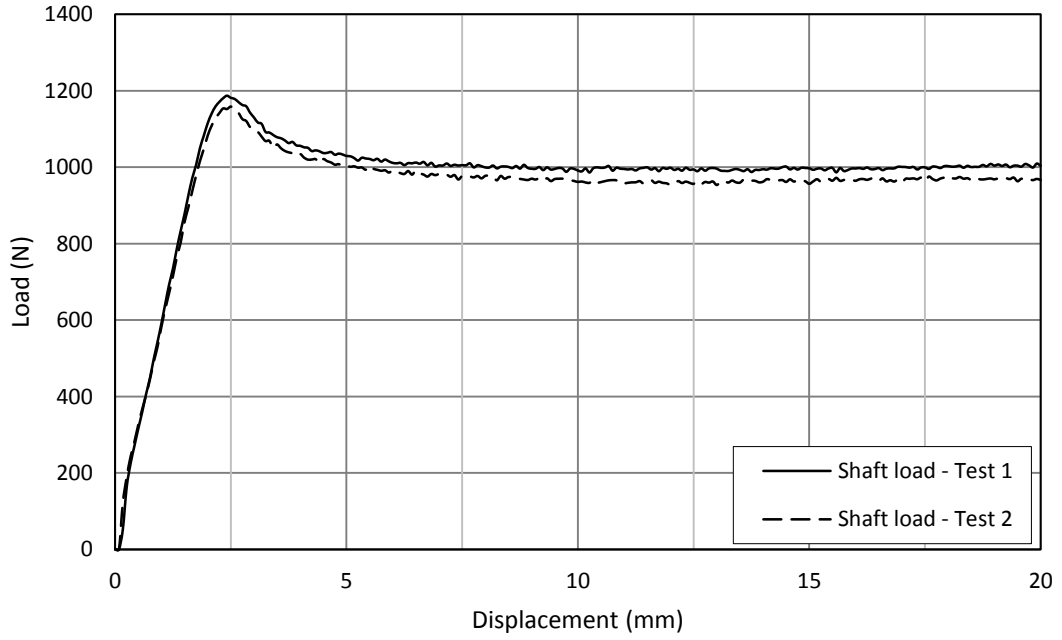


Figure 3-41: Repeated test for (C-55-60%-10)

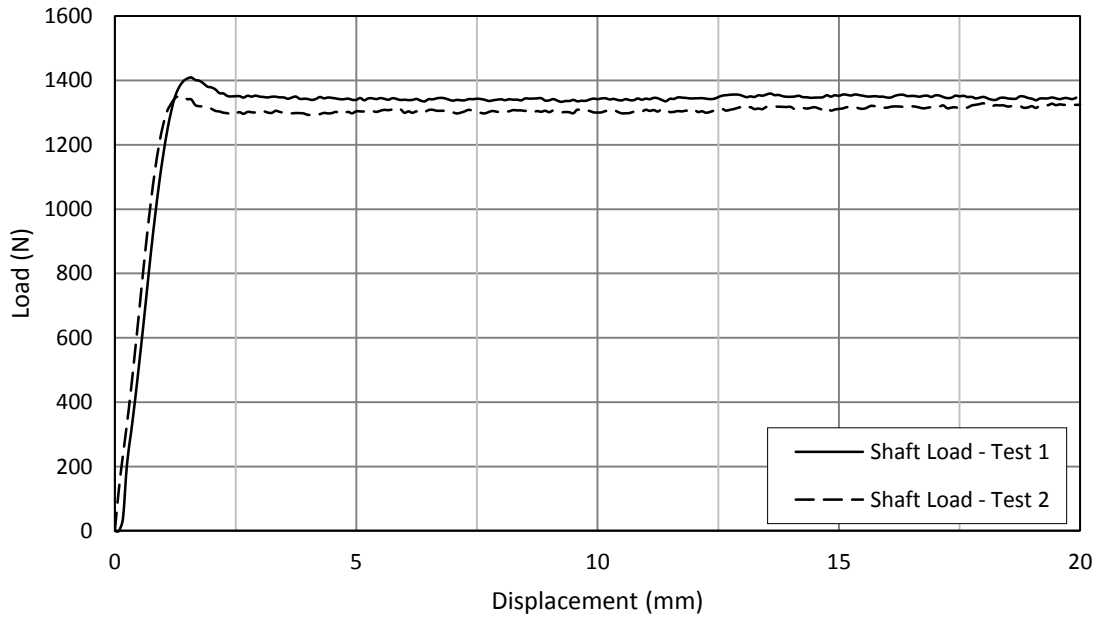


Figure 3-42: Repeated test for (C-30-60%-23.8)

### 3.6 Summary of Pile Load Test Results

Pile load test results presented in this chapter are summarized in tabular format. Results of ultimate load and corresponding tip and shaft resistance for the pile model 55 mm in diameter appear in Table 3-11, and results concerning length and shaft resistance for each section of that model appear in Table 3-12 and Table 3-13, respectively. For the pile model 30 mm in diameter, ultimate load and corresponding tip and shaft resistance appear in Table 3-14.

Table 3-11: Summary of ultimate, tip and shaft resistance for pile model of 55 mm

Pile Diameter	Relative Density	Relative Depth	Depth	Test Name	Ultimate Pile Capacity	Ultimate Tip Capacity	Ultimate Shaft Capacity
D (mm)	D <sub>r</sub> (%)	L/D	L (mm)		Q <sub>u</sub> (N)	Q <sub>t</sub> (N)	Q <sub>s</sub> (N)
55	30	5	275	C-55-30%-5	1115.11	1021.21	93.90
		8	440	C-55-30%-8	2238.34	1900.12	338.23
		10	550	C-55-30%-10	3376.07	2712.61	663.46
		13	715	C-55-30%-13	4750.42	3581.10	1171.96
	45	5	275	C-55-45%-5	1920.72	1801.75	118.97
		8	440	C-55-45%-8	3358.32	2933.91	424.41
		10	550	C-55-45%-10	4523.75	3719.91	803.83
		13	715	C-55-45%-13	6209.80	4773.07	1436.73
	60	5	275	C-55-60%-5	2650.52	2468.78	177.75
		8	440	C-55-60%-8	4529.19	3983.12	547.43
		10	550	C-55-60%-10	6058.28	5062.12	996.16
		13	715	C-55-60%-13	8232.10	6600.04	1632.06

Table 3-12: Section lengths for pile model of 55 mm diameter

Embedment depth ratio	Length		
	Section 1 (mm)	Section 2 (mm)	Section 3 (mm)
L/D			
5	35	120	120
8	200	120	120
10	310	120	120
13	475	120	120

Table 3-13: Summary of the shaft resistance for each section for pile model of 55 mm diameter

Pile Diameter D (mm)	Relative Density D <sub>r</sub> (%)	Relative Depth L/D	Test Name	Ultimate Shaft Capacity	Ultimate Shaft Capacity	Ultimate Shaft Capacity
				Section 1 (N)	Section 2 (N)	Section 3 (N)
55	30	5	C-55-30%-5	4.25	81.61	8.04
		8	C-55-30%-8	110.18	156.99	71.05
		10	C-55-30%-10	276.93	196.83	189.70
		13	C-55-30%-13	705.07	213.83	253.06
	45	5	C-55-45%-5	4.87	91.17	22.94
		8	C-55-45%-8	121.30	200.52	102.60
		10	C-55-45%-10	348.13	225.73	229.97
		13	C-55-45%-13	844.66	260.77	331.29
	60	5	C-55-60%-5	5.91	123.79	48.06
		8	C-55-60%-8	129.00	244.51	173.92
		10	C-55-60%-10	351.79	294.29	350.08
		13	C-55-60%-13	886.55	357.13	388.38

Table 3-14: Summary of ultimate, tip and shaft resistance for pile model of 30 mm

Pile Diameter	Relative Density	Relative Depth	Depth	Test Name	Ultimate Pile Capacity	Ultimate Tip Capacity	Ultimate Shaft Capacity
D (mm)	D <sub>r</sub> (%)	L/D	L (mm)		Q <sub>u</sub> (N)	Q <sub>t</sub> (N)	Q <sub>s</sub> (N)
30	30	19	570	C-30-30%-10	833.46	473.50	359.97
		23.83	715	C-30-30%-13	1365.12	707.12	658.00
	45	19	570	C-30-45%-10	1749.60	1275.42	474.18
		23.83	715	C-30-45%-13	2569.54	1753.15	816.38
	60	19	570	C-30-60%-10	2378.57	1574.20	804.36
		23.83	715	C-30-60%-13	3221.29	1918.96	1302.32

## **Chapter 4 : Analysis of Results**

### **4.1 General**

Analyzed in this chapter, the experimental results presented in Chapter 3 clearly show that the shaft resistance of piles driven into overconsolidated cohesionless soils was greater than that obtained by using theoretical and empirical methods presented in the literature. When total shaft resistance was analyzed, critical depth limiting the shear stress tended to affect both pile models. However, local shear stress distribution for the pile model 55 mm in diameter showed that shear stress increased with depth and decreased near the tip of the pile.

In what follows, the behaviour of tip resistance and total shaft resistance is analyzed, local shear stress distribution along the shaft of the piles with a 55-mm diameter is discussed, and the effect of relative density, pile diameter, and the OCR on shaft resistance is scrutinized. As a result of this analysis, an empirical model is proposed to estimate shaft resistance and its distribution along the pile shaft.

### **4.2 Ultimate Load**

Ultimate capacity versus the embedment depth ratio ( $L / D$ ) is presented in Figure 4-1 and Figure 4-2 for the pile models 55 mm and 30 mm in diameter, respectively. Ultimate load increased with embedment depth ratio and relative density. Since the research conducted for this thesis focused on shaft resistance during pile failure, tip and shaft resistance were analyzed according to ultimate load. Instrumenting the pile model 55 mm in diameter allowed the identification of the distribution of total force between the pile base and along the shaft. Assuming a linear reduction in load between load cell levels, the difference between two levels refers to shaft resistance for the corresponding section of the

pile. Figure 4-3 illustrates the total force distribution for all pile load tests for the pile model 55 mm in diameter. As for the pile 30 mm in diameter, only two load cells were used to identify total load applied and tip resistance, the difference of which signified shaft resistance. Figure 4-4 illustrates the distribution of ultimate load for all pile load tests performed using the pile 30 mm in diameter. Figure 4-3 and Figure 4-4 group pile load tests for the same depth ( $L / D$ ) performed at different relative densities.

### 4.3 Tip Resistance

Tip resistance for all pile load tests, summarized in Table 3-11 and Table 3-13, was analyzed to determine the bearing capacity factor,  $N_q$ , which is commonly represented as the following equation:

$$N_q = \frac{Q_t/A_b}{\sigma'_v} = \frac{Q_t/A_b}{\gamma L} \quad (4-1)$$

where:

$Q_t$  = tip resistance,

$A_b$  = tip area,

$\sigma'_v$  = effective overburden pressure at the tip level,

$\gamma$  = unit weight of soil, and

$L$  = embedded depth of the pile.

To take the effect of overconsolidation into account,  $N_q$  values were calculated using mean overburden pressure ( $\sigma'_m$ ), which uses the lateral earth pressure coefficient ( $K_0$ ), instead of the vertical overburden pressure ( $\sigma'_v$ ), as shown in the following equation:

$$\sigma'_m = \frac{(1+2 K_0) \sigma'_v}{3} \quad (4-2)$$

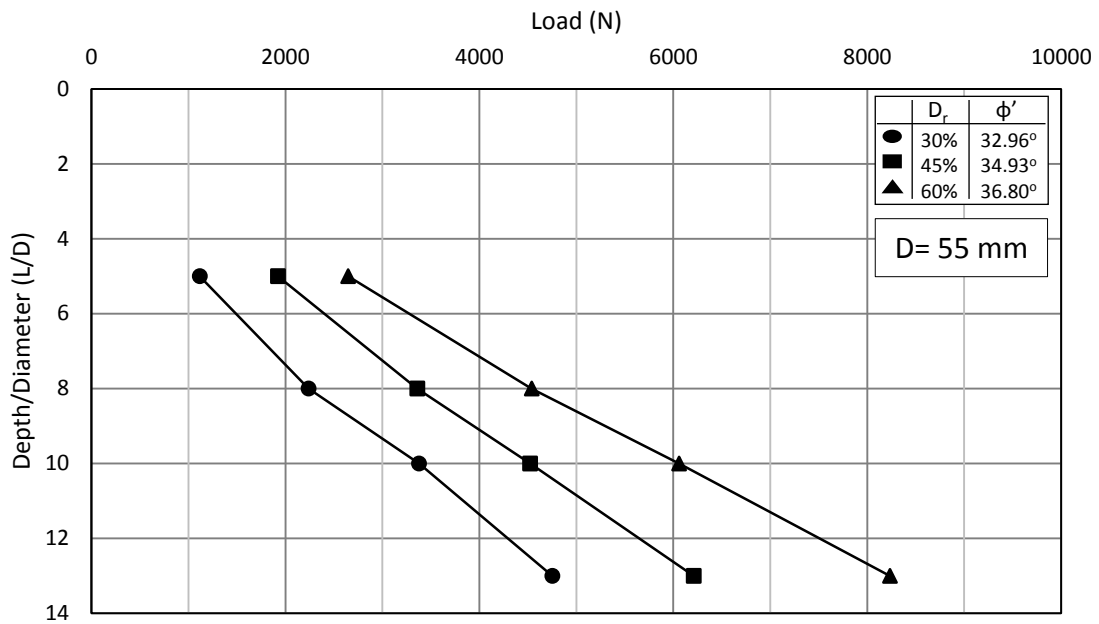


Figure 4-1: Ultimate load versus the ratio of depth to diameter (L/D) for the 55 mm pile model

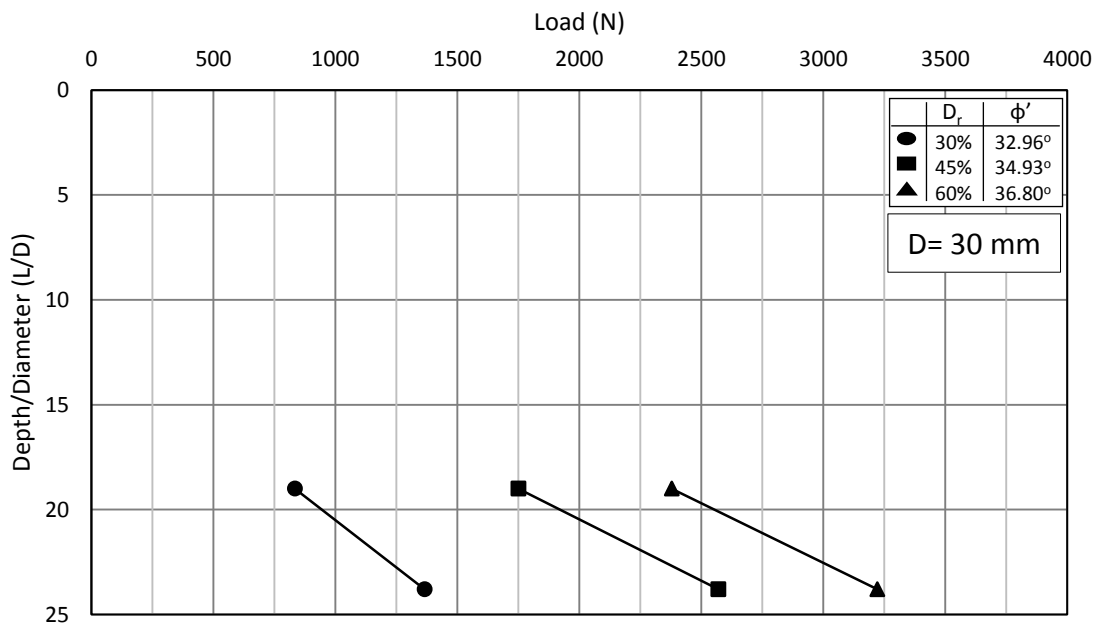
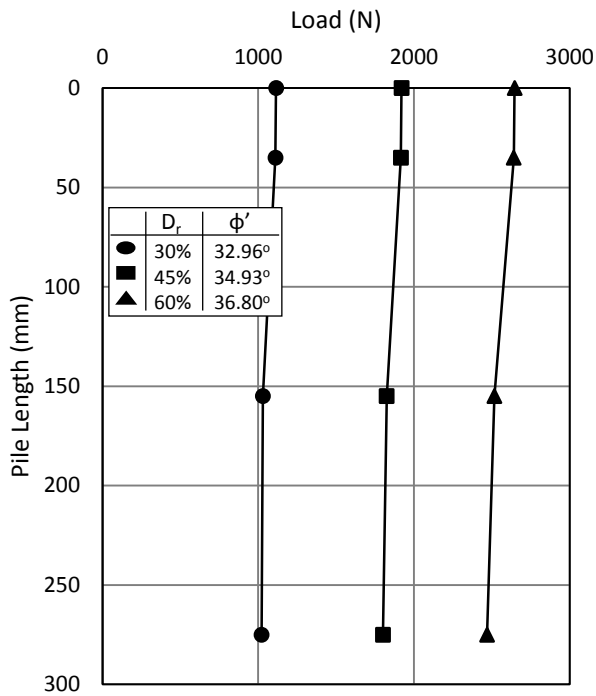
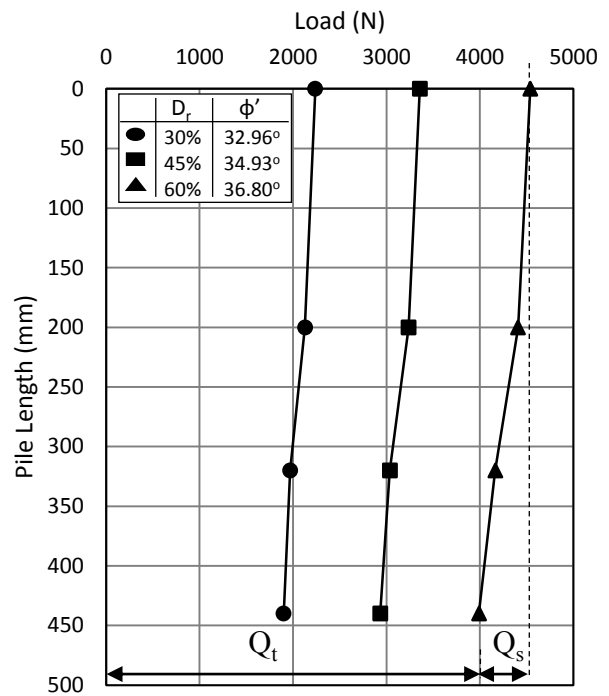


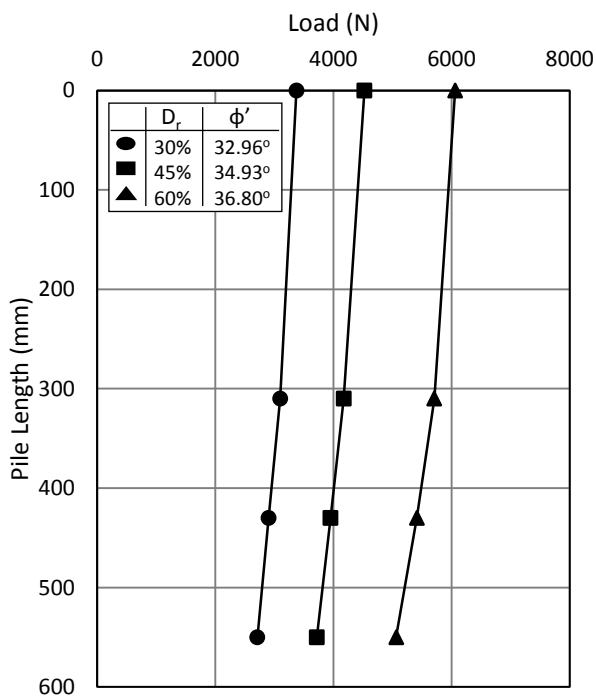
Figure 4-2: Ultimate load versus the ratio of depth to diameter (L/D) for the 30 mm pile model



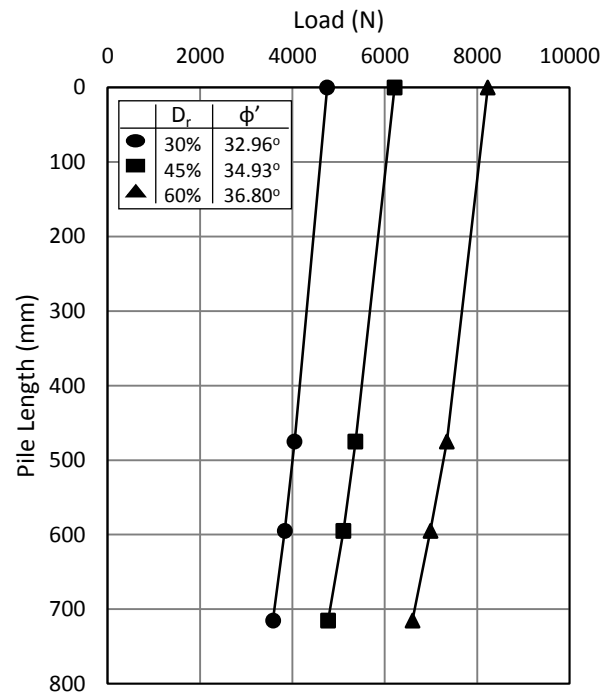
(a)



(b)



(c)



(d)

Figure 4-3 : Ultimate load distribution for pile of 55 mm diameter at (a)  $L/D = 5$ , (b)  $L/D = 8$ , (c)  $L/D = 10$ , and (d)  $L/D = 13$

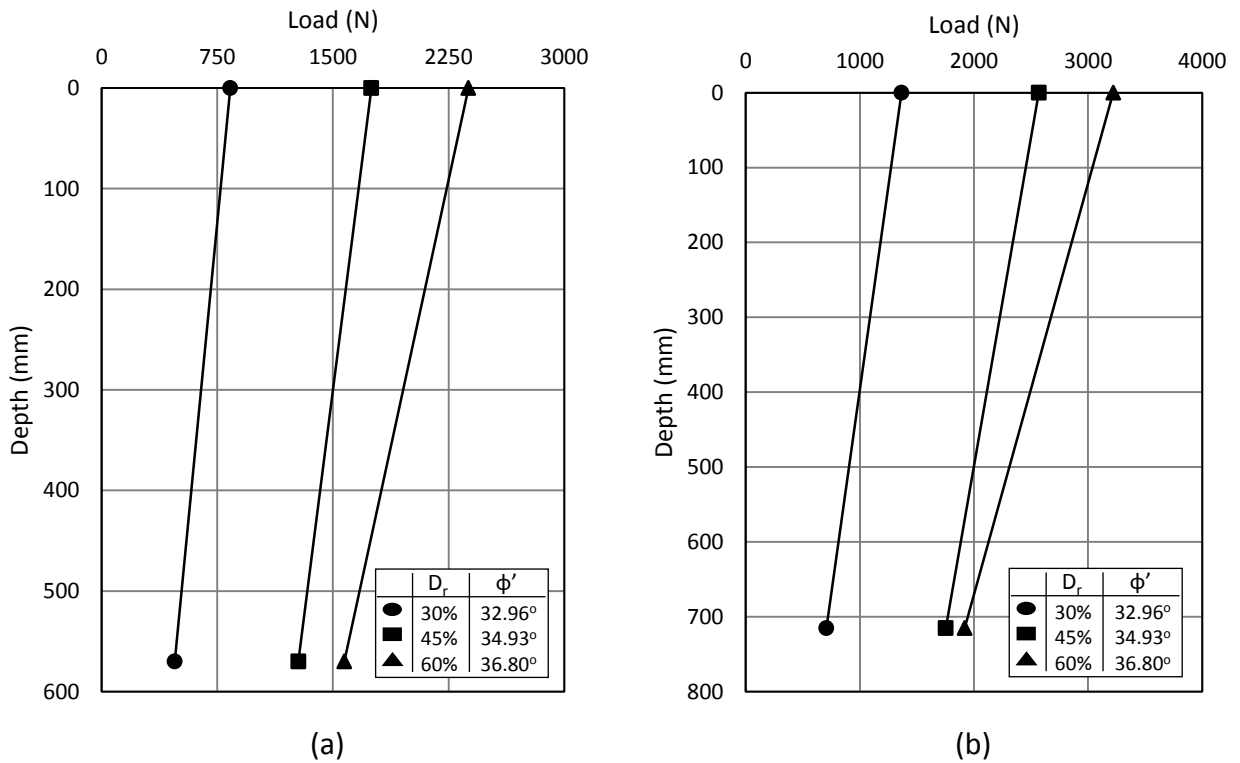


Figure 4-4 : Ultimate load distribution for pile of 30 mm diameter at (a) L/D = 19, and (b) L/D = 23.8

Regarding the pile 55 mm in diameter,  $N_q$  values for the tests performed at relative densities of 30%, 45%, and 60% had coefficients of variation equal to 16.5%, 4.3%, and 4.6%, respectively. For the pile 30 mm in diameter, the coefficients of variation for piles tested at relative densities of 30%, 45%, and 60% were 13.6%, 7.8%, and 0.2%, respectively. Consequently, the  $N_q$  values at a low relative density (i.e., low angle of shearing resistance) were significantly influenced by embedment depth. As relative density increased,  $N_q$  values relied less upon embedment depth.

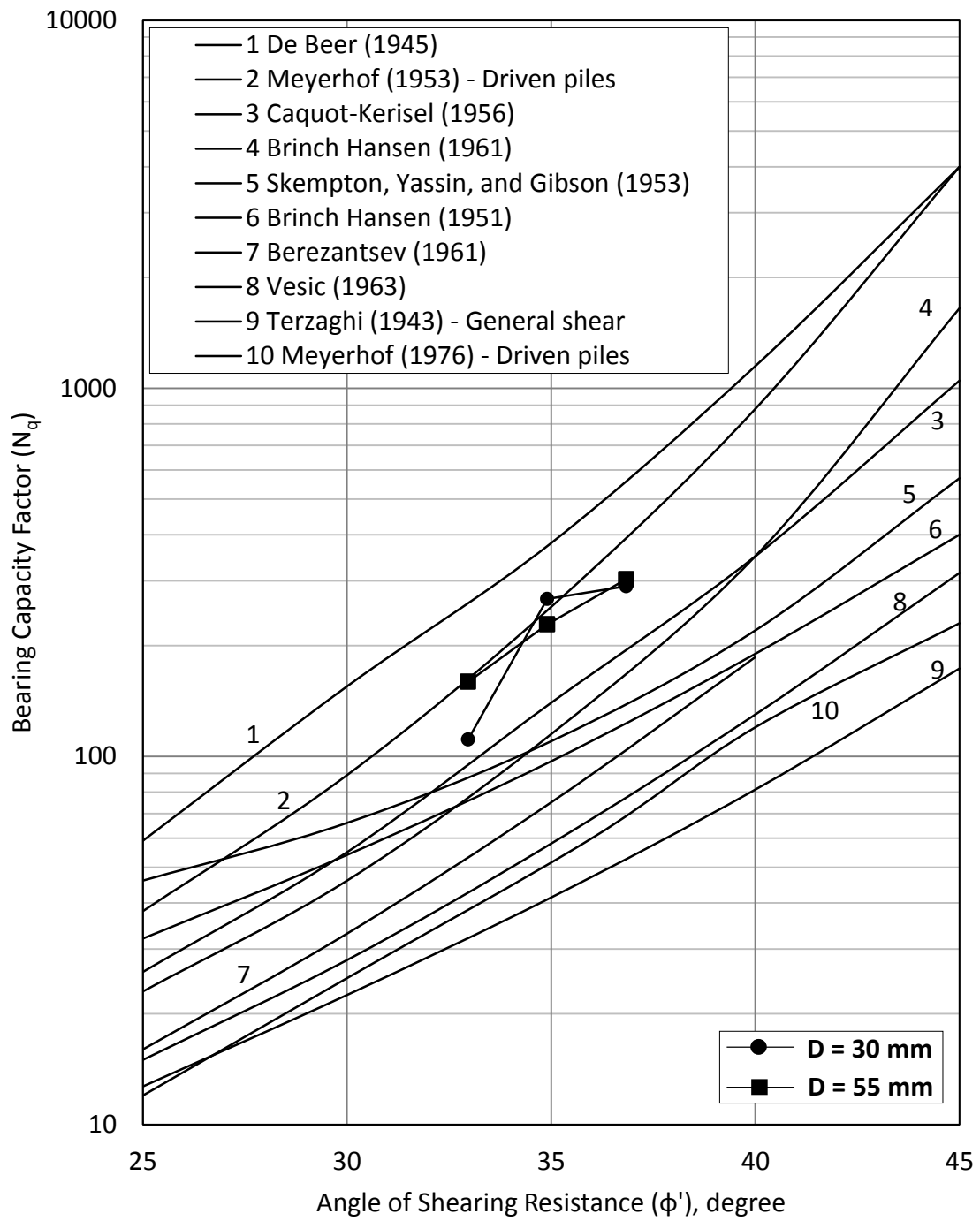


Figure 4-5: Experimental  $N_q$  values compared to proposed  $N_q$  values by different authors after, Prakash and Sharma (1990)

#### 4.4 Total Shaft Resistance

Figure 4-6 and Figure 4-7 present the mean shaft resistance versus the  $L / D$  ratio and depth for the pile models 55 mm and 30 mm in diameter, respectively. Average shaft resistance increased with pile depth and relative density. From the load–settlement curves presented in the previous chapter, the shaft resistance dropped only slightly, after peaking, as pile displacement increased and stabilized by the end of the test. Such behaviour aligns with the results of Foray et al. (1998) for a model pile tested in overconsolidated sand.

The ratios of shaft resistance to total pile resistance ( $Q_s / Q_u$ ) for both pile models appear in Table 4-1. In general, the contribution of shaft resistance increased with pile embedment depth. The greatest contributions occurred in pile load tests performed at 30% relative density, presumably due to the low bearing capacity of soil at tip level at 30% relative density, which reduced tip resistance and prompted the greater contribution of the shaft. Among other results, the  $Q_s / Q_u$  ratio decreased with relative density, although at 60% relative density with the pile model 30 mm in diameter exceeded that found at 45% relative density, likely given the contribution of unit tip resistance. Unit tip resistance for the pile model 55 mm in diameter increased considerably as relative density increased, though only slightly as the relative density increased from 45% to 60%, as  $N_q$  values indicate.

Although shaft resistance was primarily analyzed according to the ultimate load of piles, the ratio of pile displacement to pile diameter ( $W_s / D$ ) at peak shaft resistance was also recorded for all tests (Table 4-2). Compared with the typical value of displacement pile—that is, 2% (Fleming et al., 2008)— $W_s / D$  values increased as embedment depth ratio and relative density increased. The deviation of  $W_s / D$  from the typical value could have resulted from the dilation and high pile–soil interface angles (Lehane et al., 2005).

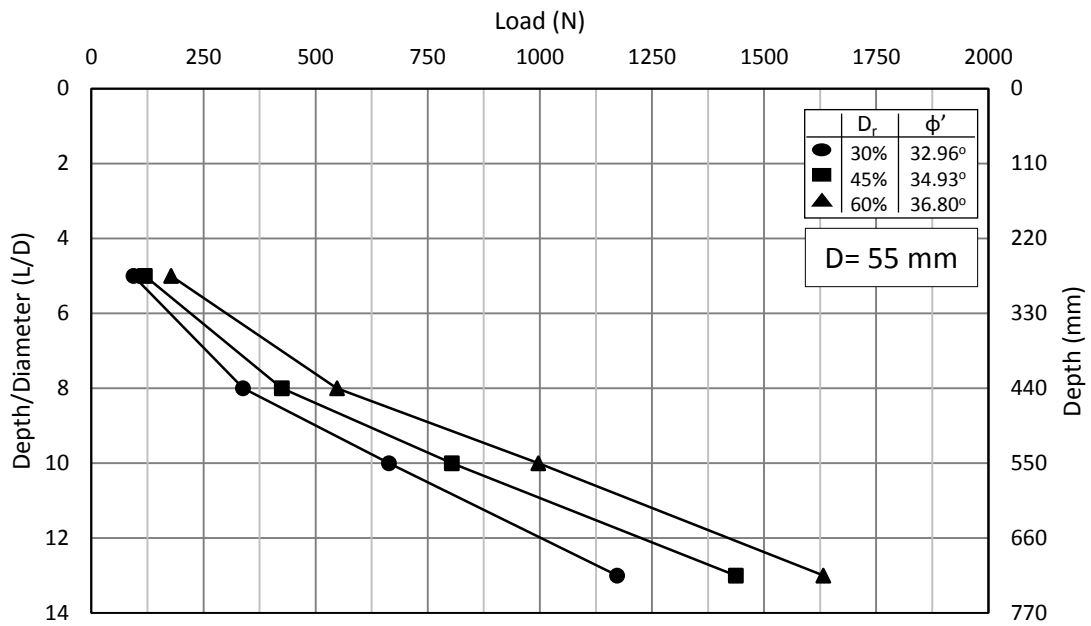


Figure 4-6: Average shaft resistance for pile diameter of 55 mm

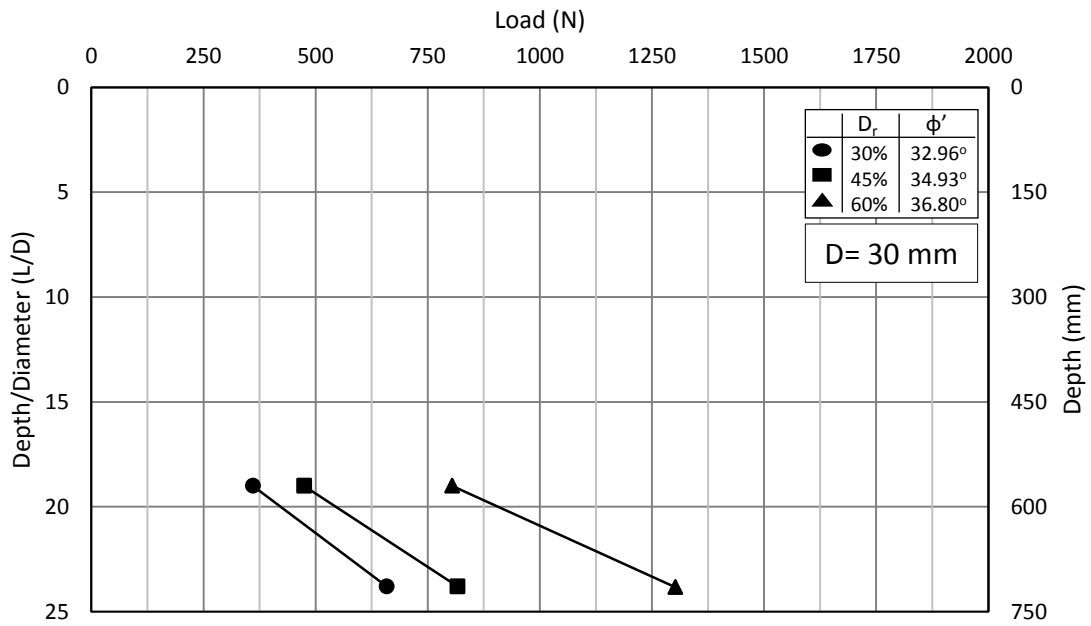


Figure 4-7: Average shaft resistance for pile diameter of 30 mm

Table 4-1: Experimental ratio of shaft resistance to ultimate pile load ( $Q_s / Q_u$ )

D (mm)	D <sub>r</sub> (%)	30	45	60
	φ' (degree)	32.97	34.90	36.84
	L/D	(Q <sub>s</sub> / Q <sub>u</sub> ) - %		
55	5	8.42	6.19	6.72
	8	15.11	12.64	12.06
	10	19.65	17.77	16.44
	13	24.67	23.14	19.83
30	19	43.19	27.10	33.82
	23.8	48.20	31.77	40.43

Table 4-2: Experimental ratio of pile displacement at peak shaft resistance to pile diameter ( $W_s / D$ )

D (mm)	D <sub>r</sub> (%)	30	45	60
	φ' (degree)	32.97	34.90	36.84
	L/D	Peak (W <sub>s</sub> / D) - %		
55	5	1.05	1.96	2.58
	8	2.27	3.33	3.49
	10	3.18	3.64	4.40
	13	3.78	4.09	5.76
30	19	1.67	3.07	4.17
	23.8	2.77	3.90	4.43

#### 4.4.1 $K_s$ Values

The values of the lateral earth pressure coefficients ( $K_s$ ) were back-calculated according to total shaft resistance, pile geometry, and soil properties using Equation 2.10

$$Q_s = (0.5 K_s \gamma' L \tan \delta) A_s = f_s A_s \quad (\text{Repeated 2-10})$$

Where

( $K_s$ ) = averaged lateral earth pressure coefficient,

( $\gamma'$ ) = effective unit weight of soil,

( $L$ ) = pile embedment length,

( $\delta$ ) = mobilized pile-sand friction angle,

( $A_s$ ) = pile surface area.

$K_s$  values for the piles with diameters of 55 mm and 30 mm appear in Figure 4-8. Since most  $K_s$  values recommended for displacement piles range from 0.5 to 2.0 (Table 2-1, Table 2-2, Table 2-3),  $K_s$  values for driven piles in overconsolidated cohesionless soils clearly have values exceeding those recommendations.

$K_s$  values for tests performed at each relative density (30%, 45%, and 60%) increased linearly with depth and remained nearly constant after a certain embedment depth ratio.  $K_s$  values for the pile model 30 mm in diameter at 60% relative density were significantly greater than those found at 30% of 45% relative density, possibly due to greater confinement around the pile shaft as relative density increased, the minor disturbance that occurred during installation, and the contribution of unit tip resistance.

Unit tip resistance for the pile model 55 mm in diameter increased considerably as relative density increased, whereas for the pile model 30 mm in diameter it increased only slightly as the relative

density increased from 45% to 60%, as emphasized by  $N_q$  values. Therefore, the increase in total load for the pile 30 mm in diameter as relative density increased most likely resulted from increased shaft resistance.

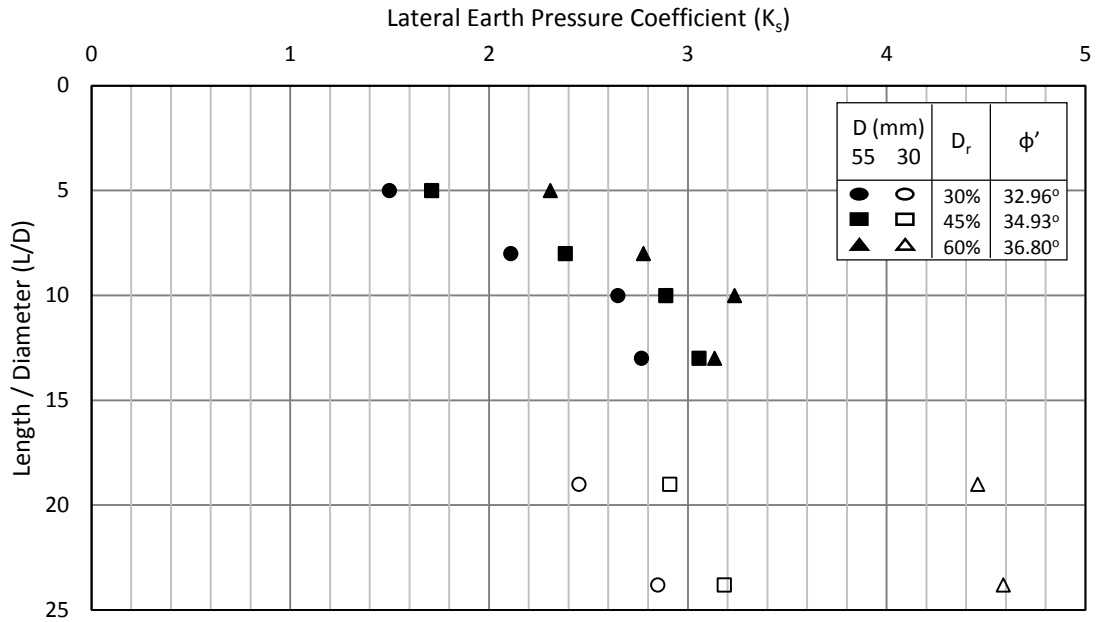


Figure 4-8:  $K_s$  values for all tests performed

#### 4.4.2 $\beta$ Values

A widely used method to calculate the shaft shear stress of piles is the beta ( $\beta$ ) method, in which  $\beta$  is coefficient that combines the lateral earth pressure coefficient ( $K_s$ ) and the friction coefficient ( $\tan \delta_z$ ).

The value of  $\beta$  was back-calculated for every pile load test according to Equation 2.20:

$$Q_s = \beta \sigma'_v A_s \quad (\text{Repeated 2-20})$$

$$\text{Where } \beta = (K_s \tan \delta_z) ;$$

$$\sigma'_v = 0.5 \gamma' L ;$$

$$A_s = \pi D L$$

Figure 4-9 and Figure 4-10 present all  $\beta$  values for pile load tests performed at all relative densities with the pile models 55 mm and 30 mm in diameter, respectively. Clearly, the values of  $\beta$  for piles driven into overconsolidated cohesionless soil are greater than those values proposed in the literature (i.e. Figure 2-8 and Figure 2-9). The  $\beta$  values increased linearly with the mean vertical pressure. The  $\beta$  values for the pile model 30 mm in diameter at 60% relative density were significantly greater than those found at 30% of 45% relative density, due to the greater confinement around the pile shaft, not only given the increased relative density and the small disturbance that occurred during installation but also because of the contribution of unit tip resistance, which increased slightly for the pile model 30 mm in diameter unlike for the one 55 mm in diameter, since relative density increased from 45% to 60%, as emphasized by  $N_q$  values.

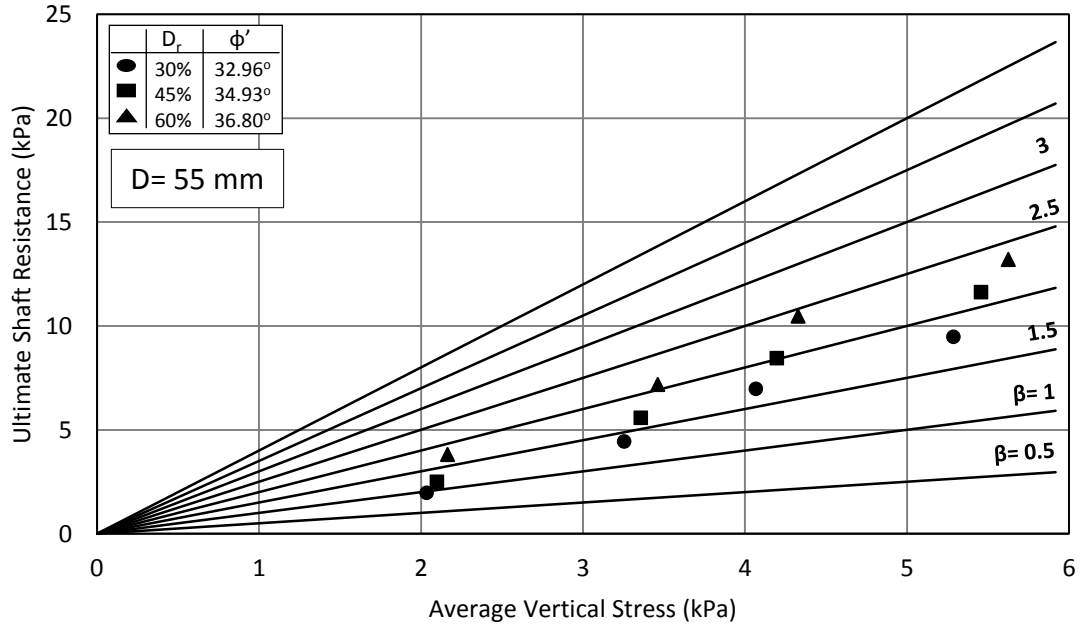


Figure 4-9: Experimental values of ( $\beta$ ) for the 55 mm pile model

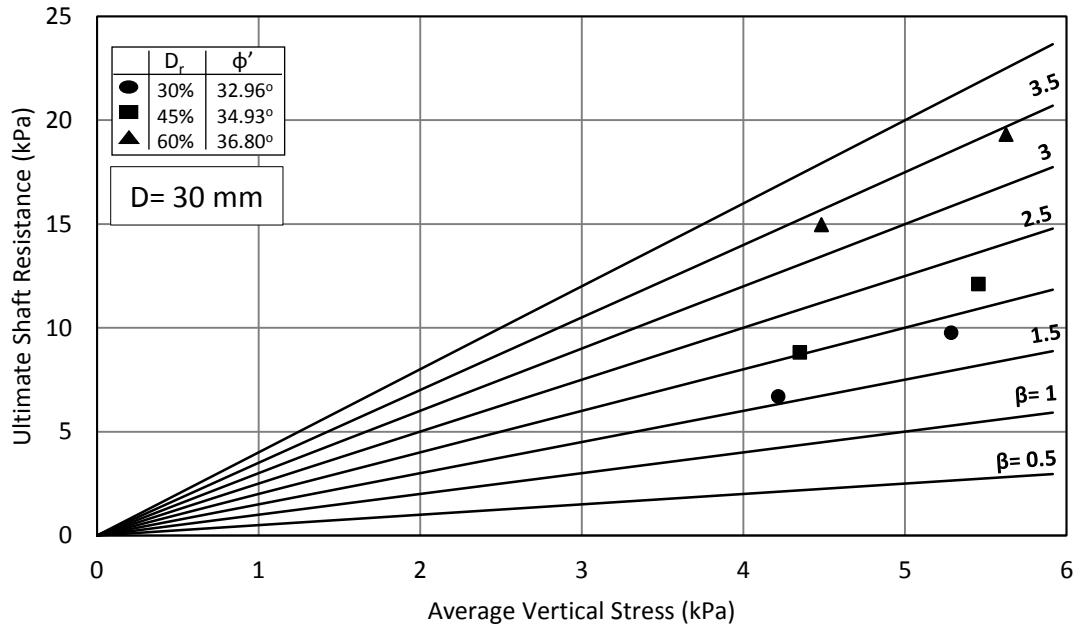


Figure 4-10: Experimental values of ( $\beta$ ) for the 30 mm pile model

### 4.4.3 ( $K_s/K_0$ ) Values

Proposals have been made to estimate  $K_s$  based on the  $K_s / K_0$  ratio (Kulhawy, 1991; Tomlinson & Woodward, 2014; Das, 2012). Following the pile load tests, the values of that ratio were back-calculated for each test by using Equation 2.21:

$$Q_s = f_s A_s = \left( 0.5 K_0 \frac{K_s}{K_0} \gamma' L \tan \delta \right) A_s \quad (\text{Repeated 2-21})$$

Where

( $K_s$ ) = averaged mobilized lateral earth pressure coefficient,

( $K_0$ ) = lateral earth pressure coefficient at rest,

( $\gamma'$ ) = effective unit weight of soil,

( $L$ ) = pile embedment length,

( $\delta$ ) = mobilized pile-sand friction angle, and

( $A_s$ ) = pile surface area.

Figure 4-11 and Figure 4-12 show the  $K_s / K_0$  values for pile load tests performed at all relative densities with the pile models 55 mm and 30 mm in diameter, respectively. The  $K_s / K_0$  ratio had higher values than that traditionally suggested (i.e., 1-2 for displacement piles). At 30% relative density, the ratio had a low value of 3.0 and increased to 6.0 at the highest mean vertical pressure. Similarly, at 45% relative density, the ratio increased from 4.0 to 7.5. As for the relative density of 60%, the  $K_s / K_0$  ratio for the pile model 55 mm in diameter varied from 6.0 to 8.0, whereas for the pile model 30 mm in diameter it began at 11.0 and ended at 11.5.

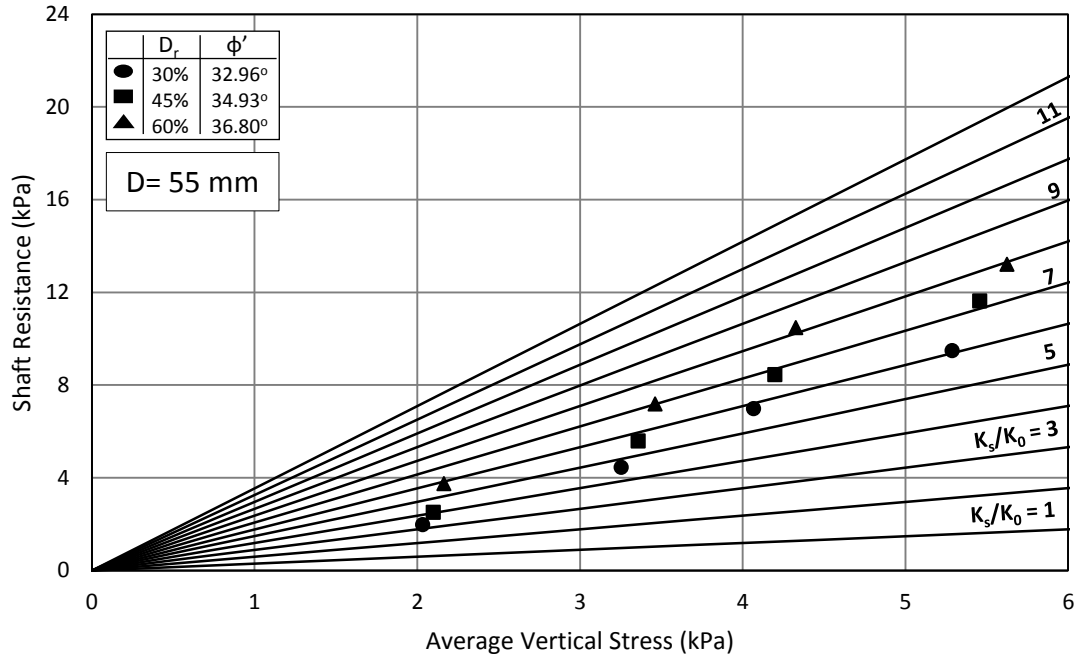


Figure 4-11: Experimental values of  $(K_s / K_0)$  for the 55 mm pile model

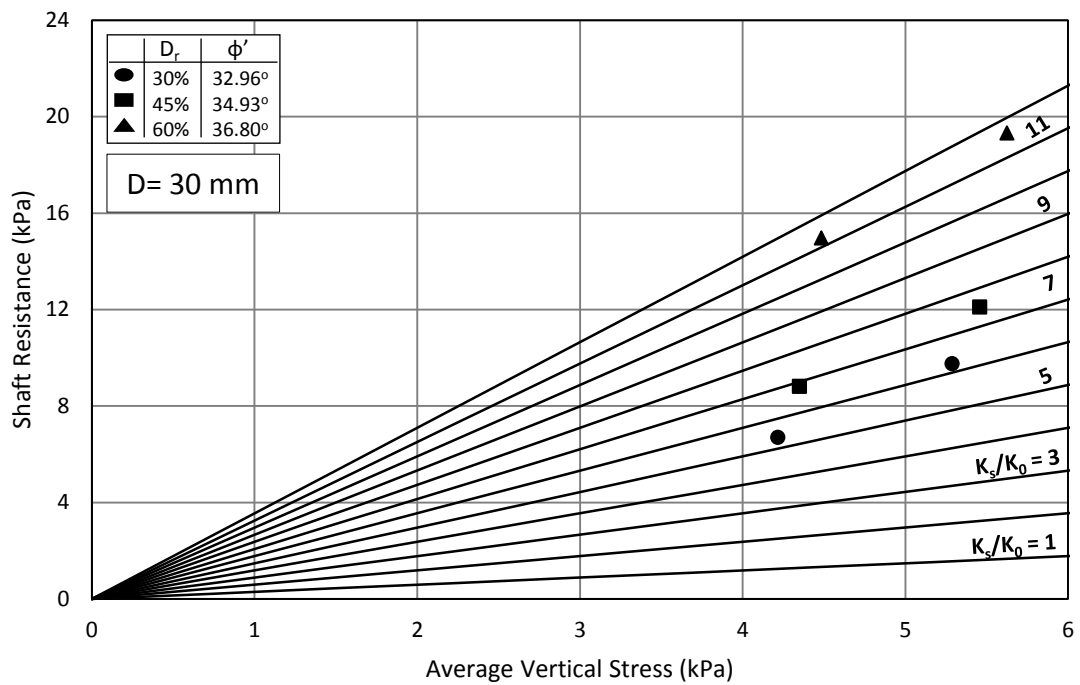


Figure 4-12: Experimental values of  $(K_s / K_0)$  for the 30 mm pile model

## 4.5 Shear Stress Distribution

Shear stress distribution was identified for the pile 55 mm in diameter because, unlike the pile 30 mm in diameter, it was instrumented in the middle of the pile. Therefore, only results of the pile 55 mm in diameter are discussed in this section.

### 4.5.1 Local Shear Stress

Local shear stress distribution, measured as load divided by the corresponding area (Table 4-3), on the total length of the pile model 55 mm in diameter is presented in Figure 4-13–Figure 4-16 for the embedment depth ratios ( $L / D$ ) of 5, 8, 10, and 13, respectively. Local shear stress is presented as a mean value in the middle of each section. Clearly, the distribution of shear stress along the pile shaft was nonlinear. Local shear stress at a certain depth decreased as pile depth increased, which generally agrees with the results of Vesic (1970), Lehane et al. (1993), and Flynn and McCabe (2015). Local shear stress for tests performed at the same embedment depth ratio behaved similarly by increasing with relative density.

At the lowest embedment depth ratio (i.e.,  $L / D = 5$ ), local shear stress showed a low value at the top of the pile (Section 1), high value at the middle of the pile (Section 2), and a low value close to the tip (Section 3). The reduction close to the tip was due to the built-up residual forces in the vicinity of the pile tip due to installation (Gavin et al., 2009), as well as due to the influence of the high OCR, especially in the top layers of the soil, which helped to increase residual forces. As embedment depth ratio increased, shear stress similarly increased.

For Section 3 (i.e., close to the tip), shear stress increased as embedment depth ratio increased until it peaked along the pile shaft at an embedment depth ratio of  $L / D = 13$ . Such behaviour related to the influence of the effective overburden pressure, which increased as embedment depth ratio increased,

which in turn increased the lateral earth pressure applied to the pile shaft. At the same time, the influence of the OCR on residual forces decreased given the reduced OCR value with increased depth. Tests performed at an embedment depth ratio of  $L / D = 13$  did not show any drop in shear stress near the tip due to the way in which the pile was instrumented, in which the length of the last section of the pile (Section 3) equaled  $2.18 D$ ; local shear stress for that section was a mean of that length. Therefore, the peak location was lost along the length of the last section, which Flynn and McCabe (2015) also observed during three field pile load tests with a similar instrumentation.

Table 4-3: Local shear stress for pile diameter of 55 mm

Pile Diameter D (mm)	Relative Density D <sub>r</sub> (%)	Relative Depth L/D	Test Name	Local Shear Stress	Local Shear Stress	Local Shear Stress
				Section 1 (kPa)	Section 2 (kPa)	Section 3 (kPa)
55	30	5	C-55-30%-5	0.70	3.94	0.39
		8	C-55-30%-8	3.19	7.57	3.43
		10	C-55-30%-10	5.17	9.49	9.15
		13	C-55-30%-13	8.59	10.31	12.20
	45	5	C-55-45%-5	0.80	4.40	1.11
		8	C-55-45%-8	3.51	9.67	4.95
		10	C-55-45%-10	6.50	10.89	11.09
		13	C-55-45%-13	10.29	12.58	15.98
	60	5	C-55-60%-5	0.98	5.97	2.32
		8	C-55-60%-8	3.73	11.79	8.39
		10	C-55-60%-10	6.57	14.19	16.88
		13	C-55-60%-13	10.80	17.22	18.73

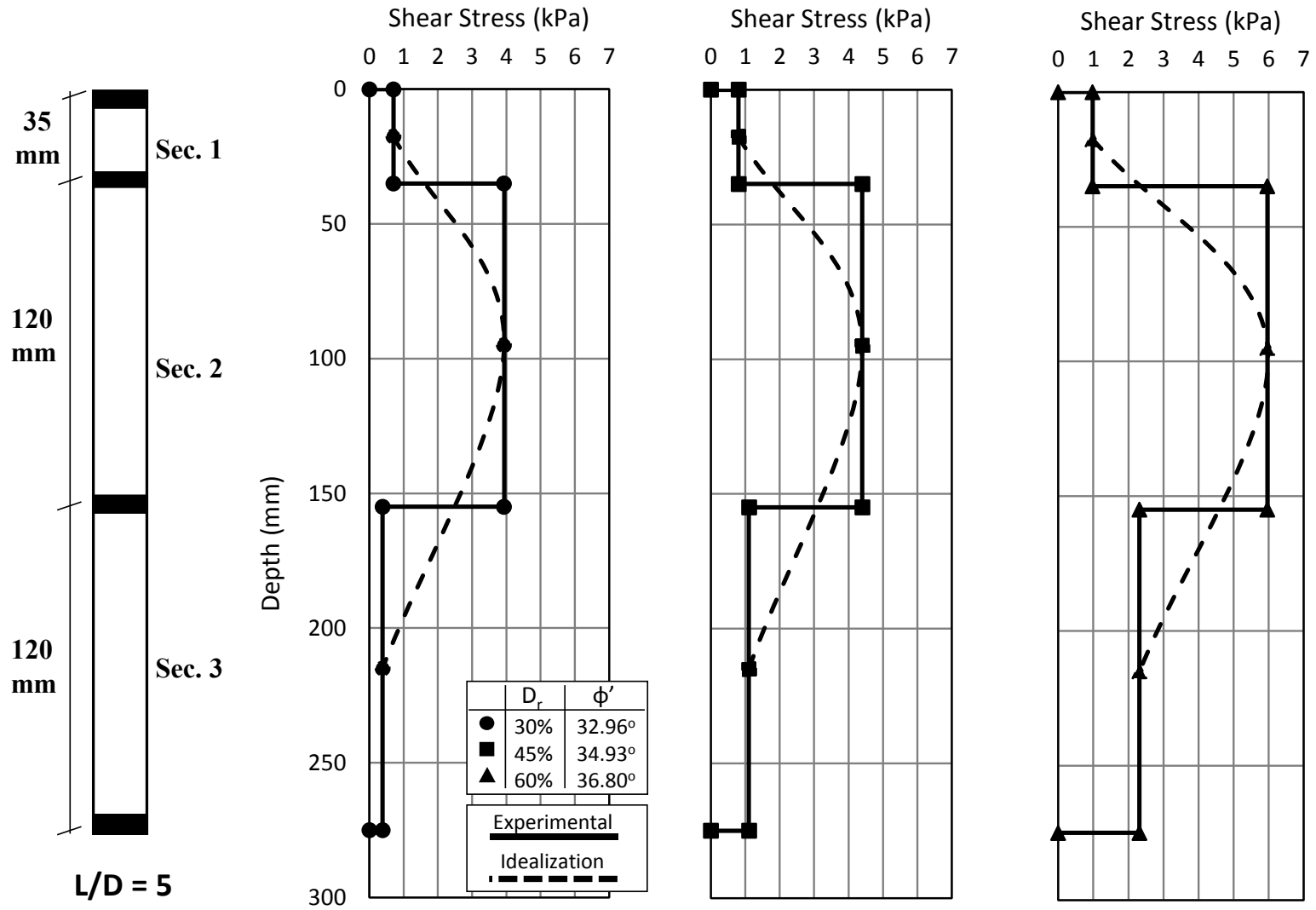


Figure 4-13 : Local shear stress distribution for  $L/D = 5$

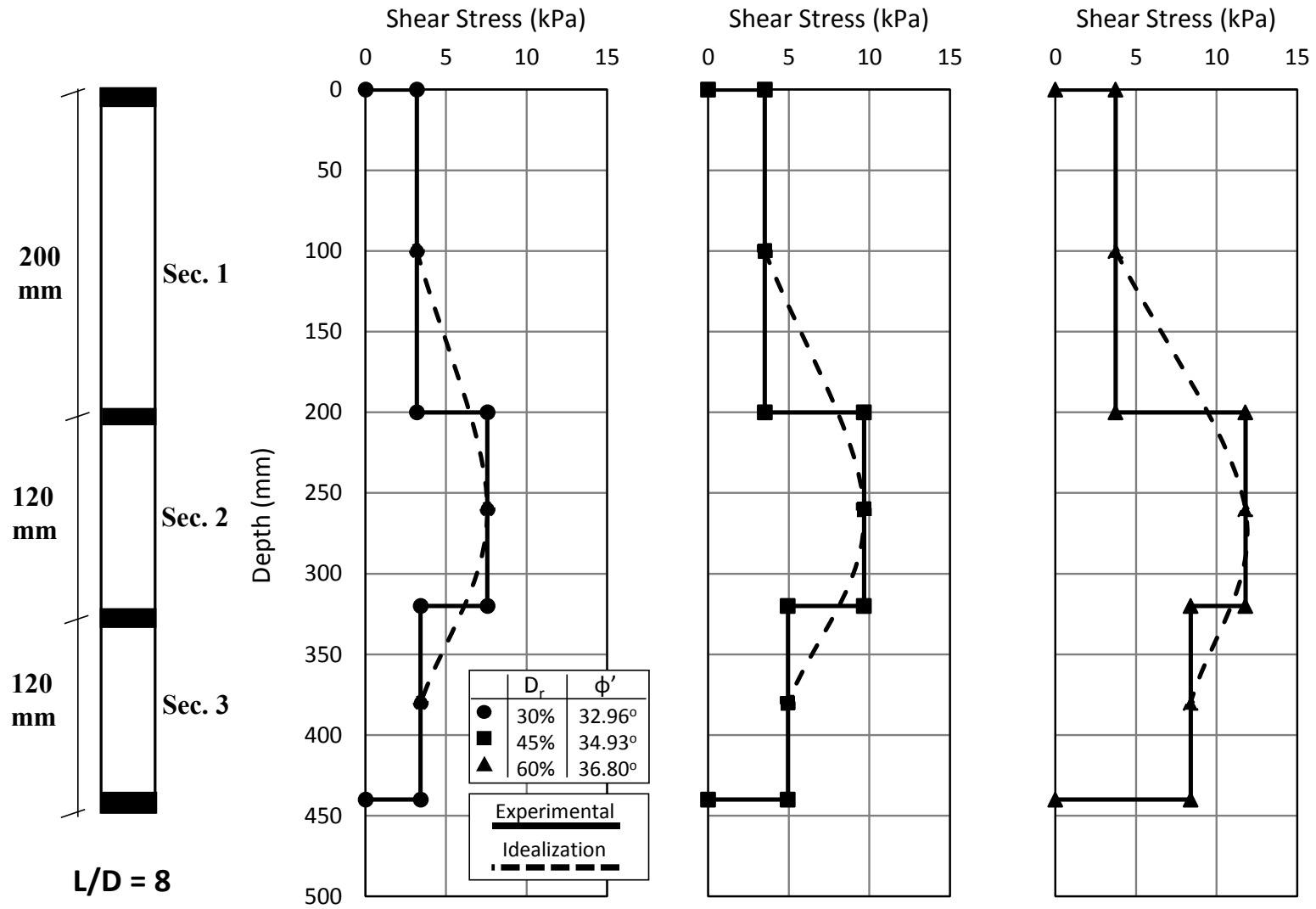


Figure 4-14: Local shear stress distribution for  $L/D = 8$

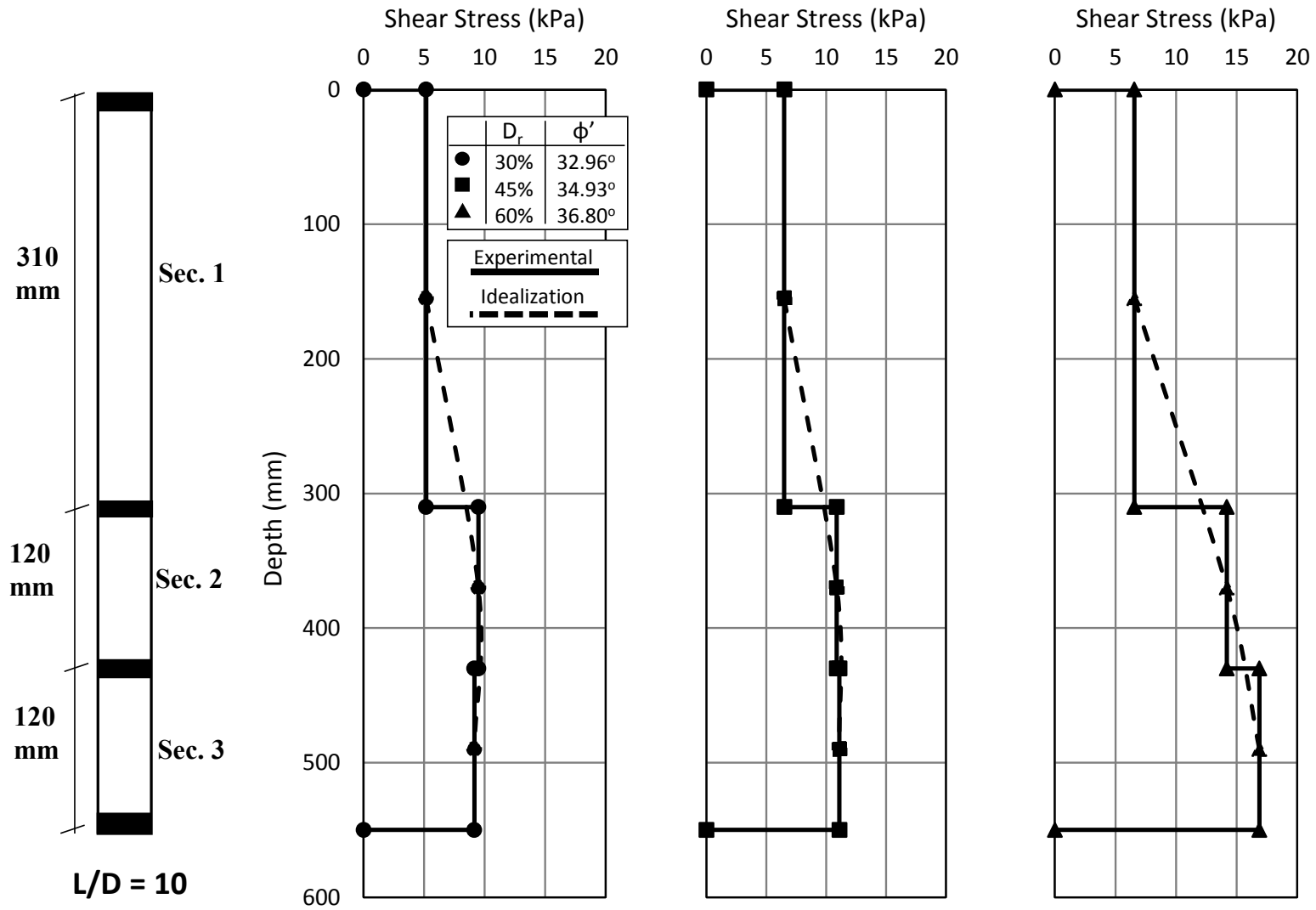


Figure 4-15: Local shear stress distribution for  $L/D = 10$

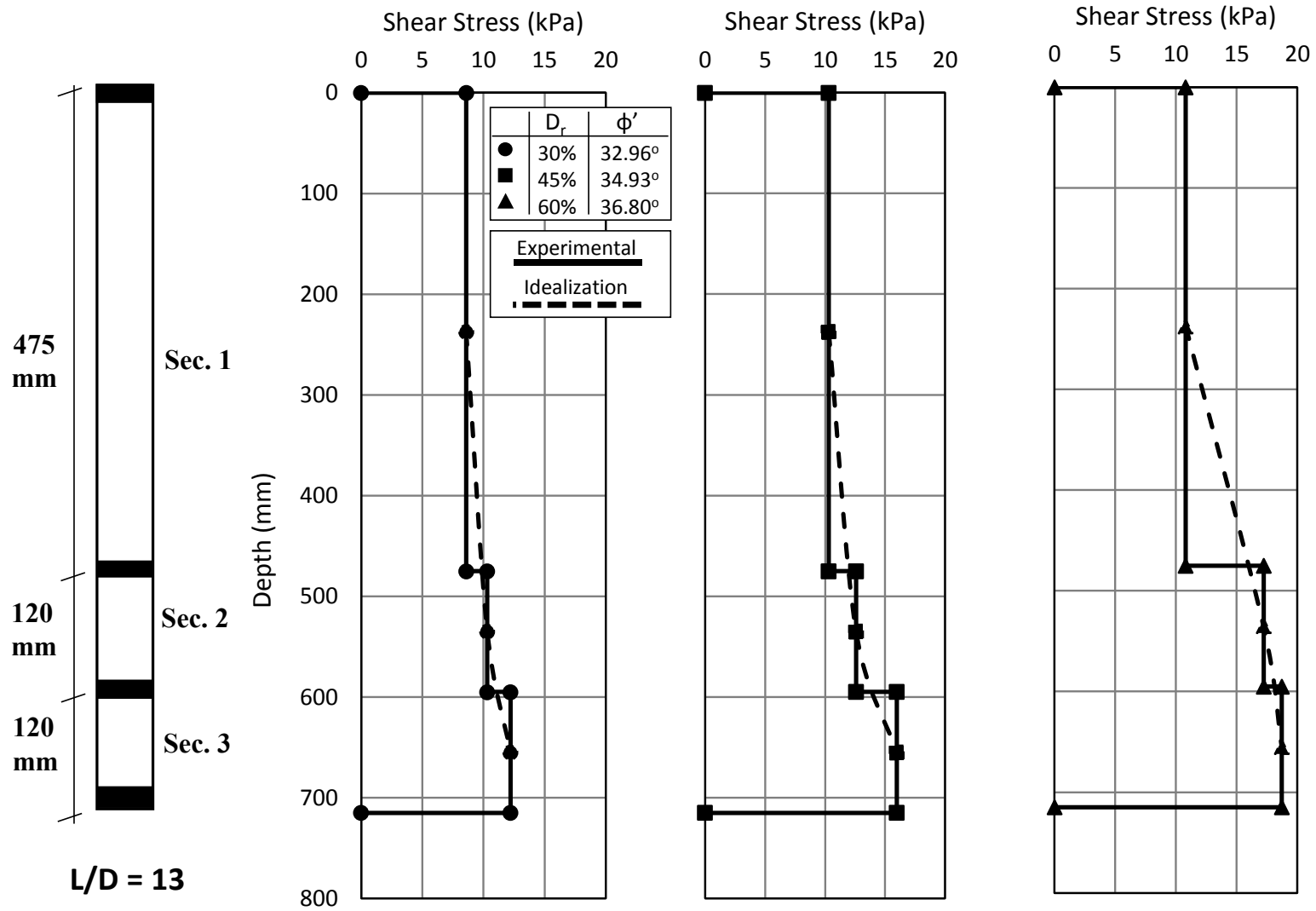


Figure 4-16: Local shear stress distribution for  $L/D = 13$

#### 4.5.2 Lateral Earth Pressure Coefficient at Failure ( $K_s$ )

The lateral earth pressure coefficient ( $K_s$ ) at failure was back-calculated from the local shear stress for each section, to compare them with the values proposed in the literature, using Equation 2.10:

$$Q_s = (0.5 K_s \gamma' L \tan \delta) A_s \quad (\text{Repeated 2-10})$$

Where

( $K_s$ ) = averaged mobilized lateral earth pressure coefficient at failure,

( $\gamma'$ ) = effective unit weight of soil,

( $L$ ) = pile embedment length,

( $\delta$ ) = mobilized pile-sand friction angle,

( $A_s$ ) = pile surface area.

$K_s$  values were calculated for all relative densities (i.e., 30%, 45%, and 60%) and are depicted in Figure 4-17–Figure 4-20 for embedment depth ratios ( $L / D$ ) of 5, 8, 10, and 13, respectively. At the embedment depth ratio  $L / D = 5$  for 30% relative density,  $K_s$  values were 4.2 for Section 1, 4.3 for Section 2, and 0.2 for Section 3. The  $K_s$  distribution at 45% and 60% relative densities at the same embedment depth ratio was similar to that found for 30% relative density; however,  $K_s$  values increased slightly for Section 1 and even more so for Sections 2 and 3 as relative density increased.

In the pile load test performed at the embedment depth ratio of  $L / D = 8$  for 30% relative density, the  $K_s$  values were 3.3 for Section 1, 3.0 for Section 2, and 0.95 for Section 3. The  $K_s$  values for Section 1 for 45% and 60% relative densities were nearly the same as the ones for 30% relative density; again, however,  $K_s$  values for Sections 2 and 3 increased as relative density increased.

The same behaviour continued at embedment depth ratios of  $L / D = 10$  and  $L / D = 13$ , at which  $K_s$  values for Sections 2 and 3 tended to be approximate as embedment depth ratio increased. Such behaviour is in line with the results of researchers such as Sabry (2005) and Flynn and McCabe (2015). Because  $K_s$  values inferred from local shear stress measured were significantly greater than those recommended in the literature (i.e., 0.5–2.0 for displacement piles), the recommended values are liable to underestimate shaft resistance for driven piles in overconsolidated cohesionless soils.

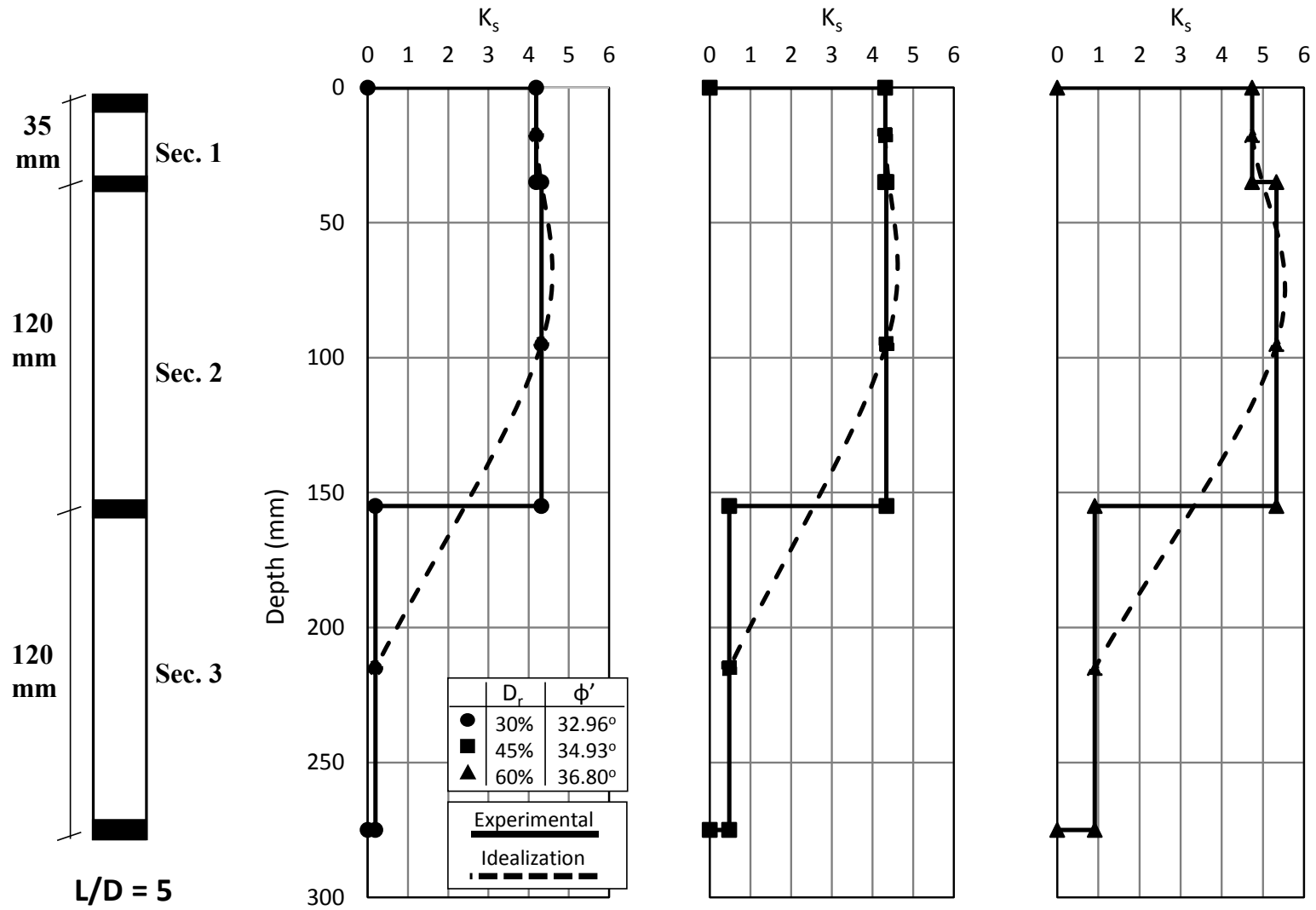


Figure 4-17: Local lateral earth pressure coefficient at failure for  $L/D = 5$

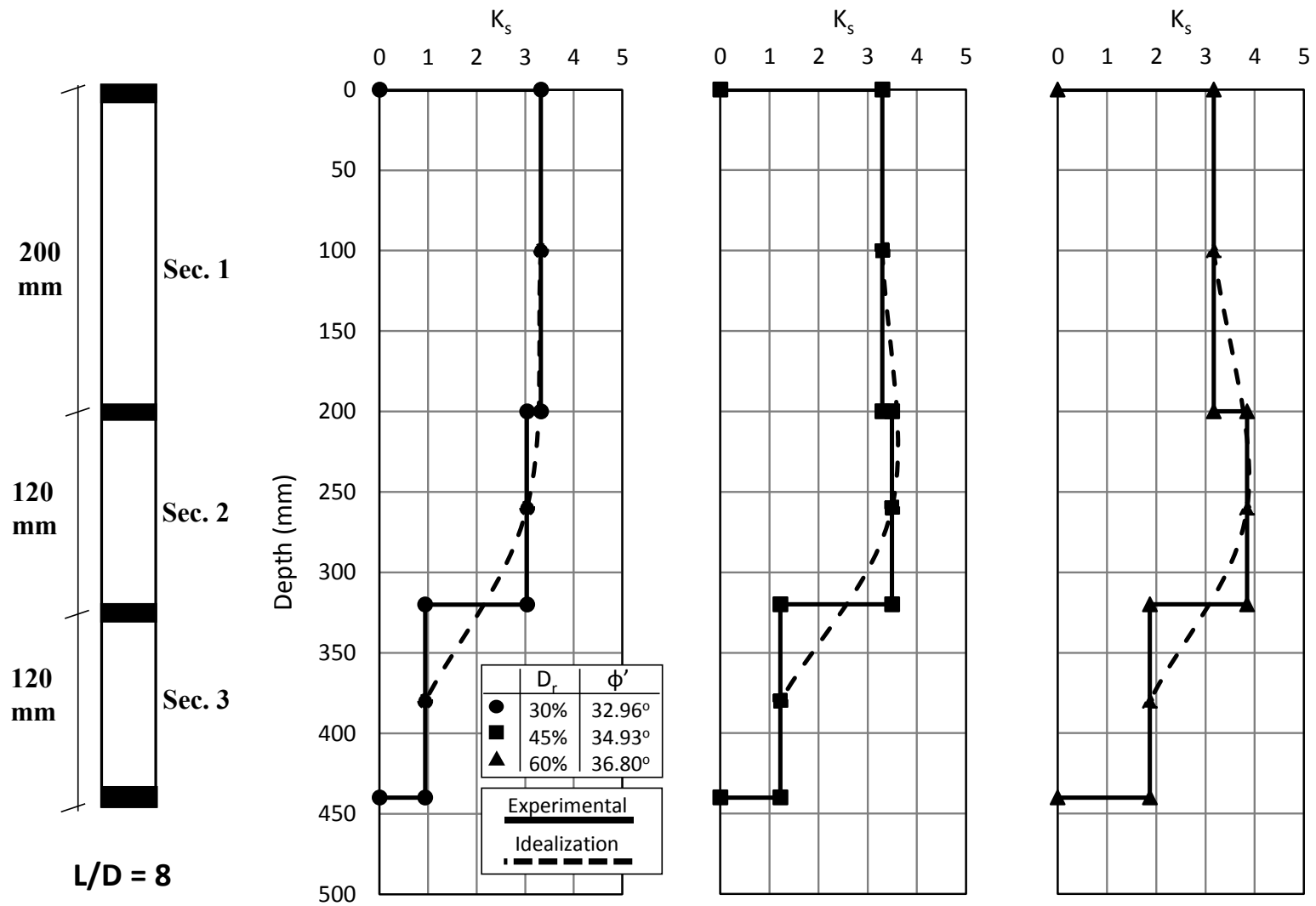


Figure 4-18: Local lateral earth pressure coefficient at failure for  $L/D = 8$

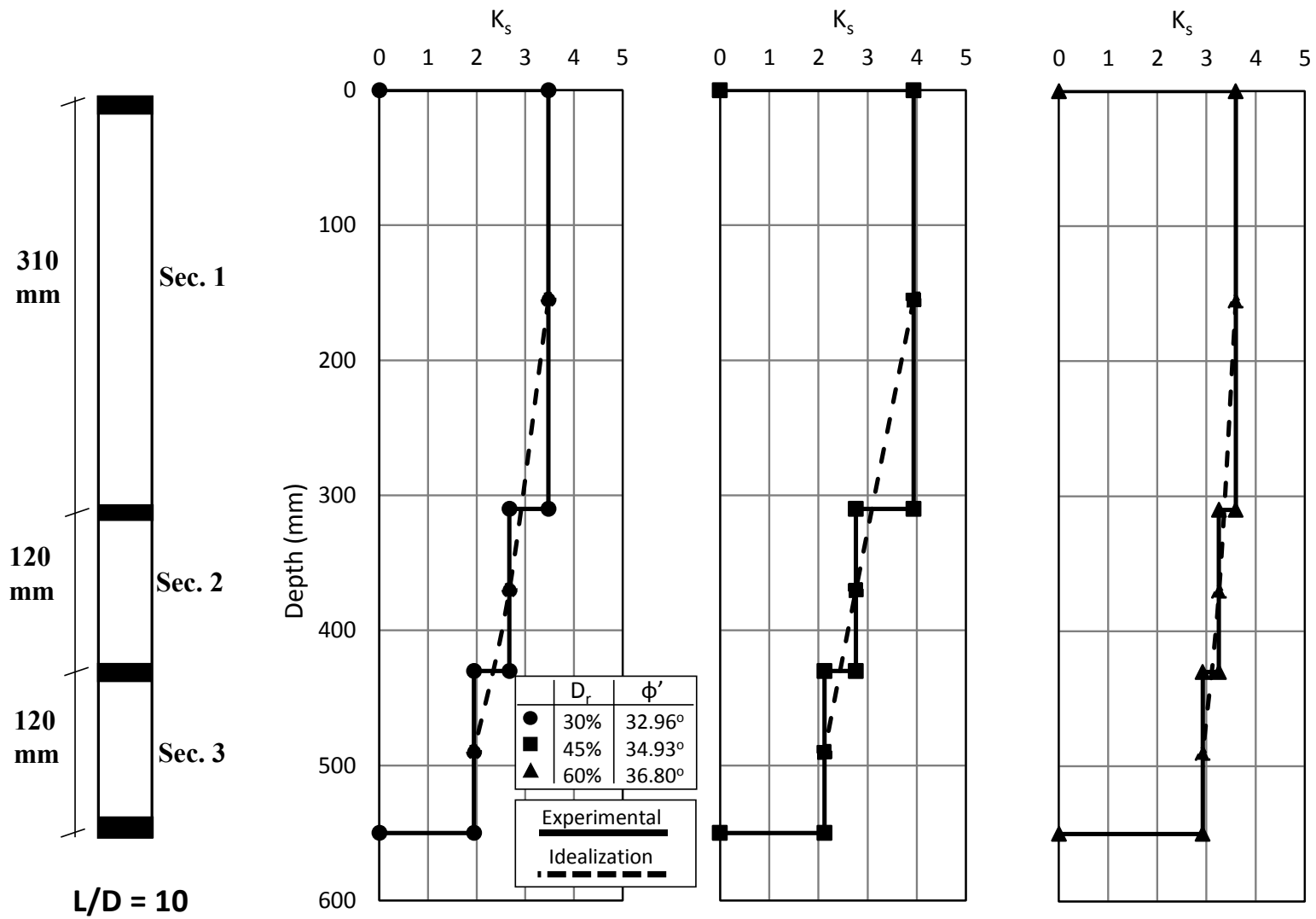


Figure 4-19: Local lateral earth pressure coefficient at failure for  $L/D = 10$

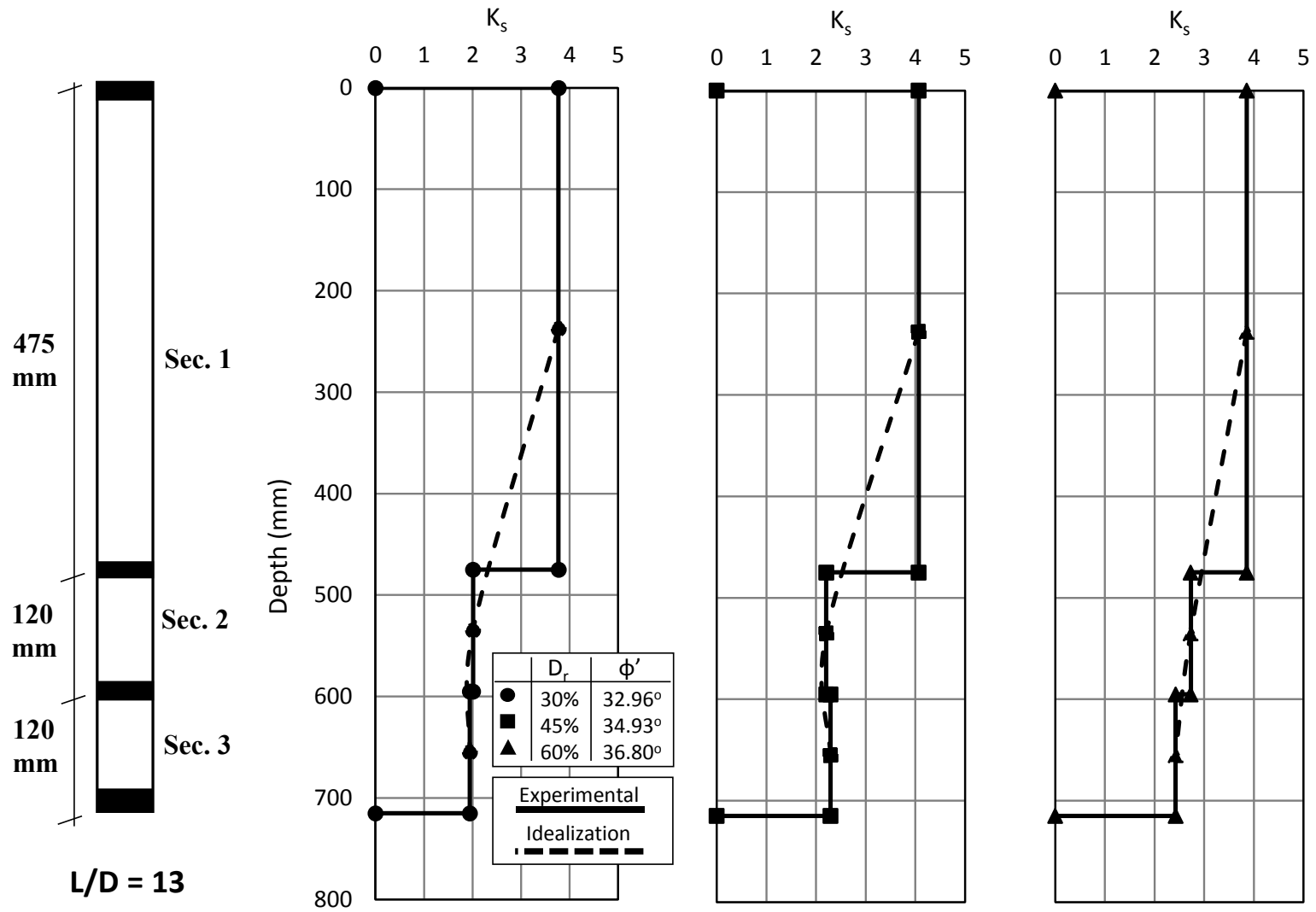


Figure 4-20: Local lateral earth pressure coefficient at failure for  $L/D = 13$

### 4.5.3 Lateral Earth Pressure (LEP)

For all pile load tests performed using the pile with a 55-mm diameter, local shear stresses were used to back-calculate the lateral earth pressure by following Equation 2.6:

$$\tau = \sigma'_h \tan \delta_z \quad (\text{Repeated 2-6})$$

where:

$(\sigma'_h)$  = horizontal effective pressure, which also can be represented as function of the vertical effective stress ( $K_s \sigma'_v$ );

$(\delta_z)$  = mobilized friction angle on the pile-sand interface.

Those values were compared with at-rest lateral earth pressure for normally consolidated soil using the  $K_{0(NC)}$  coefficient and at-rest lateral earth pressure for overconsolidated soil using the  $K_{0(OC)}$  coefficient. Because local lateral earth pressure at failure exceeded the values of both at-rest lateral earth pressures, the values were also compared to Rankine's passive lateral earth pressure using the  $K_p$  coefficient. The earth pressure coefficients were:

$$K_{0(NC)} = 1 - \sin \phi' \quad (\text{Repeated 2-13})$$

$$K_{0(OC)} = (1 - \sin \phi') (OCR)^{(\sin \phi')} \quad (\text{Repeated 2-16})$$

$$K_p = \left[ \frac{1 + \sin \phi'}{1 - \sin \phi'} \right] = \tan^2 \left( 45 + \frac{\phi'}{2} \right) \quad (4-3)$$

where

$(\phi')$  = soil angle of shearing resistance.

Figure 4-21 to Figure 4-24 illustrate the local lateral earth pressure for all relative densities (i.e., 30%, 45%, and 60% for embedment depth ratios ( $L / D$ ) of 5, 8, 10, and 13, respectively. Local lateral earth pressure inferred from the measured local shear stress was significantly greater than the at-rest lateral earth pressure for both normally consolidated and overconsolidated soils. Due to the installation of the pile and the overconsolidation of the soil, it reached the passive lateral earth pressure at the upper section of the pile and decreased with depth, which corroborates Sabry's (2005) numerical results.

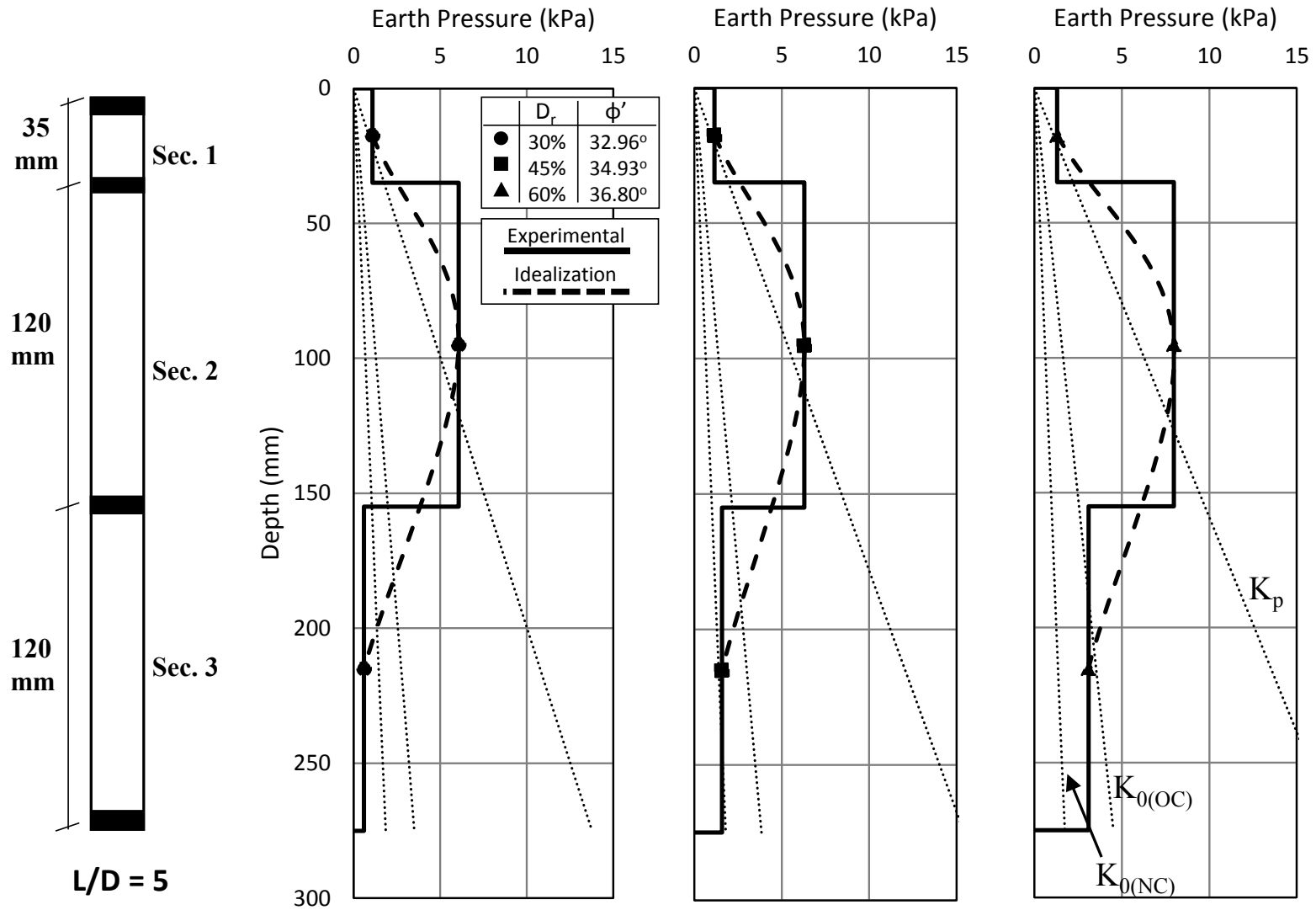


Figure 4-21: Local lateral earth pressure at failure for  $L/D = 5$

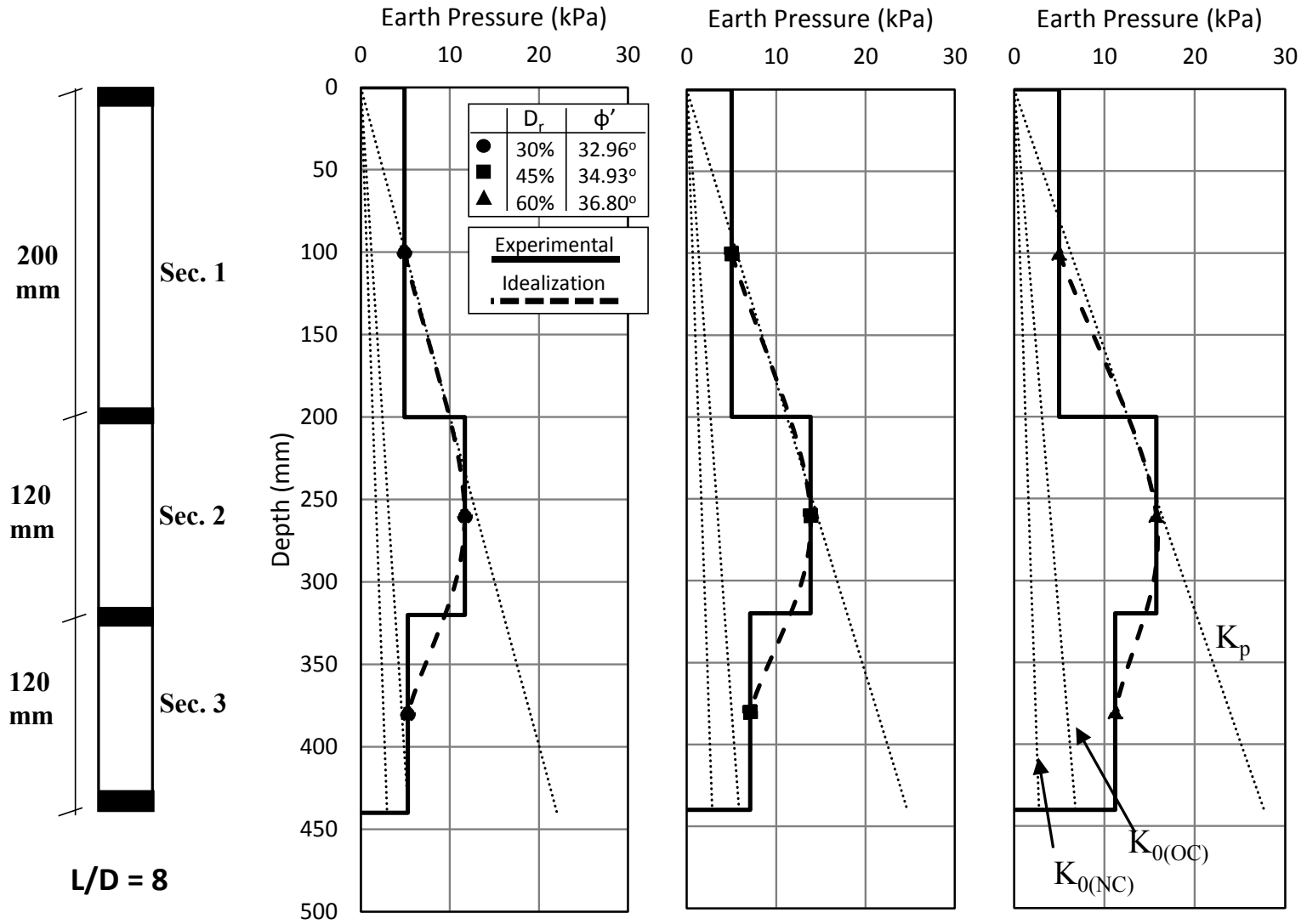


Figure 4-22: Local lateral earth pressure at failure for  $L/D = 8$

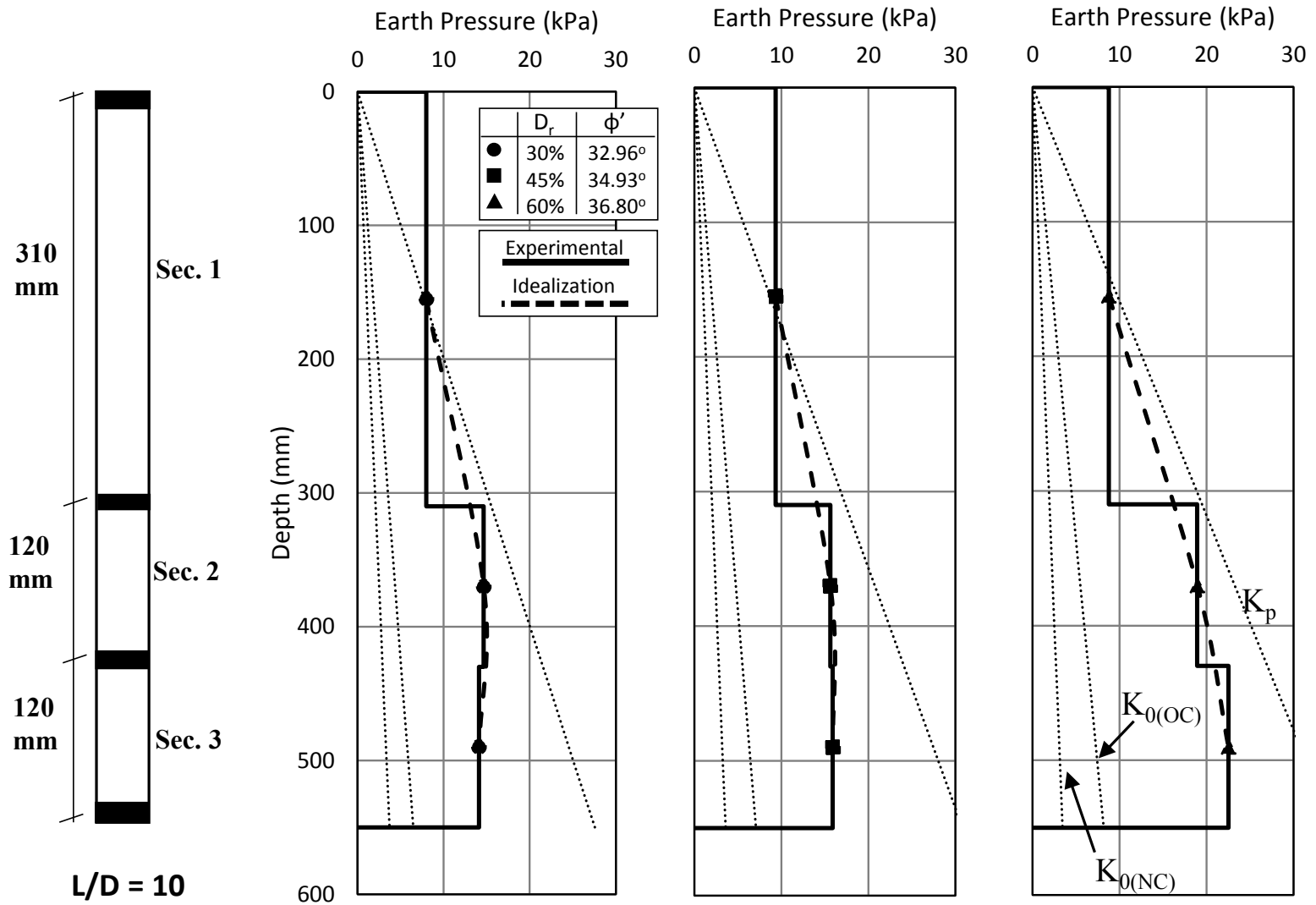


Figure 4-23: Local lateral earth pressure at failure for  $L/D = 10$

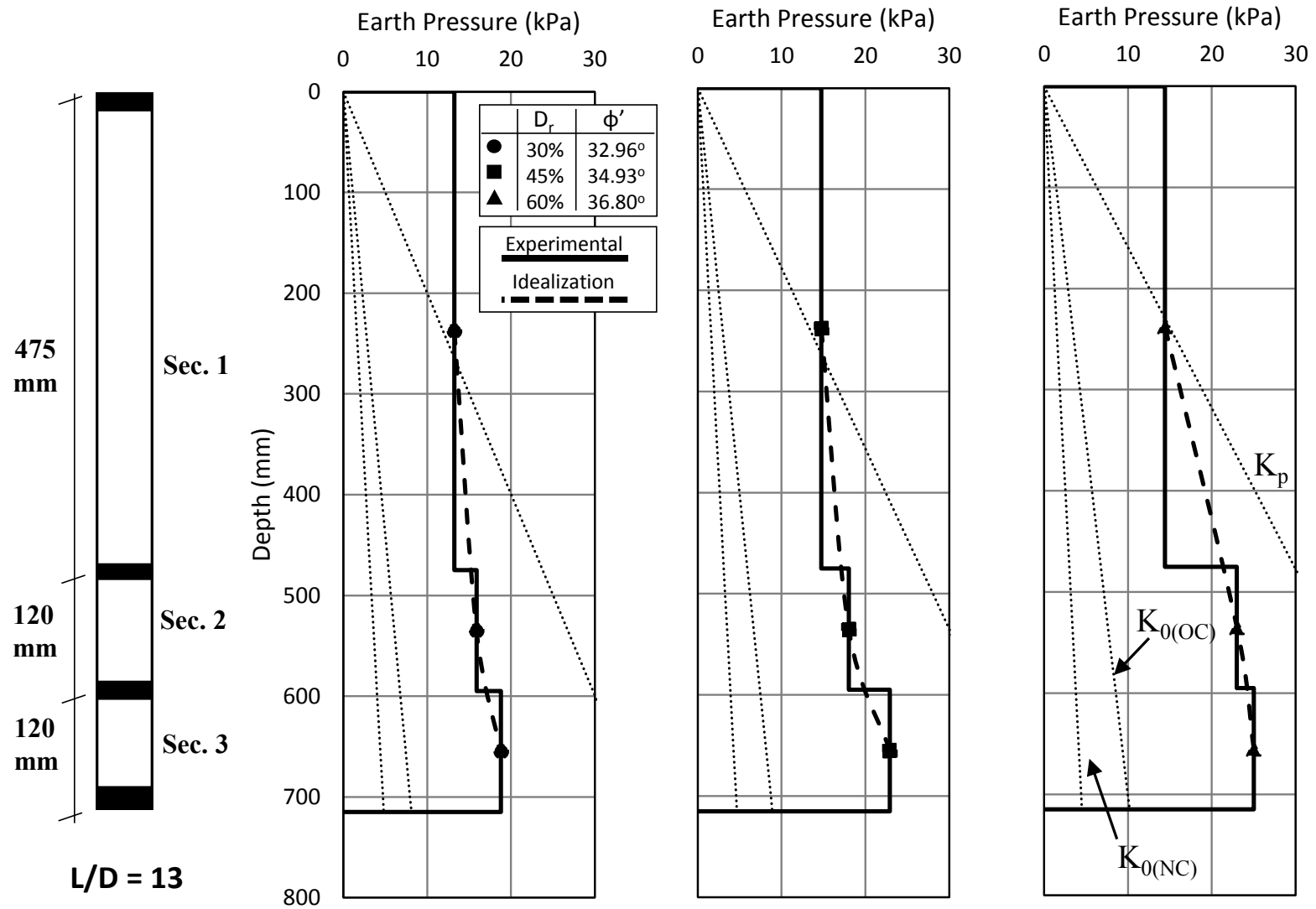


Figure 4-24: Local lateral earth pressure at failure for  $L/D = 13$

## 4.6 Experimental Critical Depth

To investigate critical depth,  $K_s$  values inferred from total shaft resistance for both piles and from local shaft resistance for the pile model 55 mm in diameter were analyzed. Notably,  $K_s$  values inferred from total shaft resistance increased with relative density, and with embedment depth ratio up to a certain depth and thereafter stabilized as shown in Figure 4-25. Such observations uphold the conceptualization of critical depth introduced by Vesic (1967) and Meyerhof (1976) as a function of  $\phi'$  as shown in Figure 2-6. The value of  $\phi'$  is suggested to be adjusted according to the method of installation. For driven piles,  $\phi'$  is calculated as follows:

$$\phi' = 0.75 \phi'_1 + 10 \quad (\text{Poulos \& Davis, 1980}) \quad (4-4)$$

where

$(\phi'_1)$  = effective angle of shearing resistance before installation.

Figure 4-26 compares  $L_c / D$  values according to Vesic's (1967) and Meyerhof's (1976) guidelines with experimental values presented in Figure 4-25. The  $L_c / D$  value was nearly 10 for tests performed at 30% relative density ( $\phi'_1 = 32.96$  degree), and increased to 11 for tests performed at 45% relative density ( $\phi'_1 = 34.93$  degree). As for tests performed at 60% relative density ( $\phi'_1 = 36.80$  degree), the  $L_c / D$  value was 15. It can be seen that these values agree with the critical depth values proposed by Meyerhof (1976).

By contrast, the local shear stress distribution and inferred local  $K_s$  values presented in the previous sections clearly show a nonlinear distribution along the pile shaft with no sign of critical depth. At a certain depth, local shear stress decreased as pile depth increased. Given that reduction, mean total shaft friction remained relatively constant as embedment depth increased, and consequently, critical depth appeared.

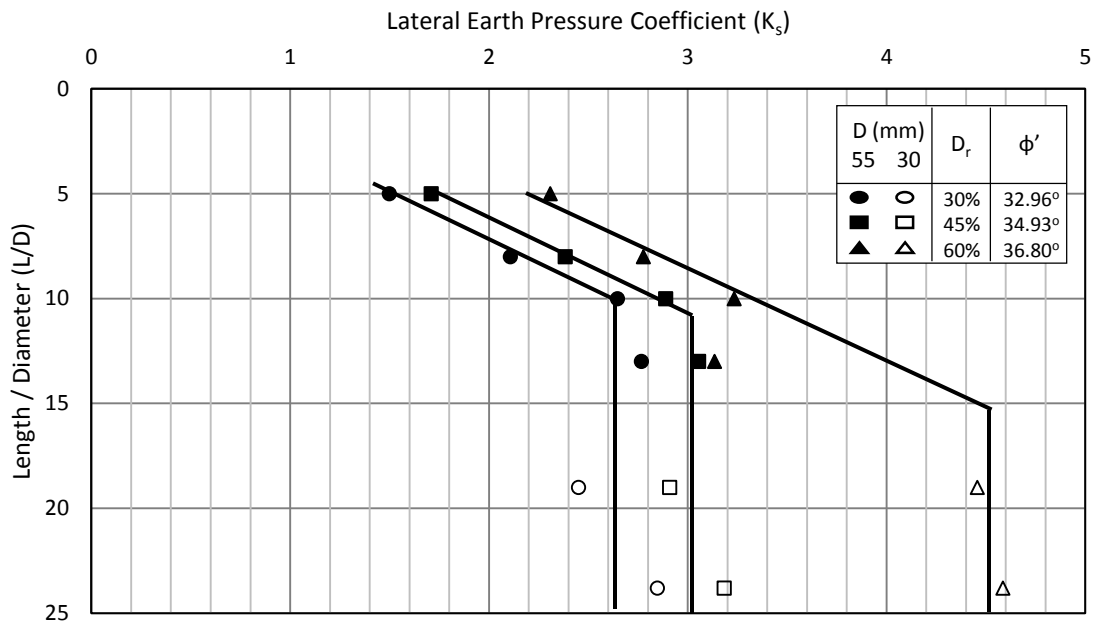


Figure 4-25: Variation of  $K_s$  values with depth for each relative density

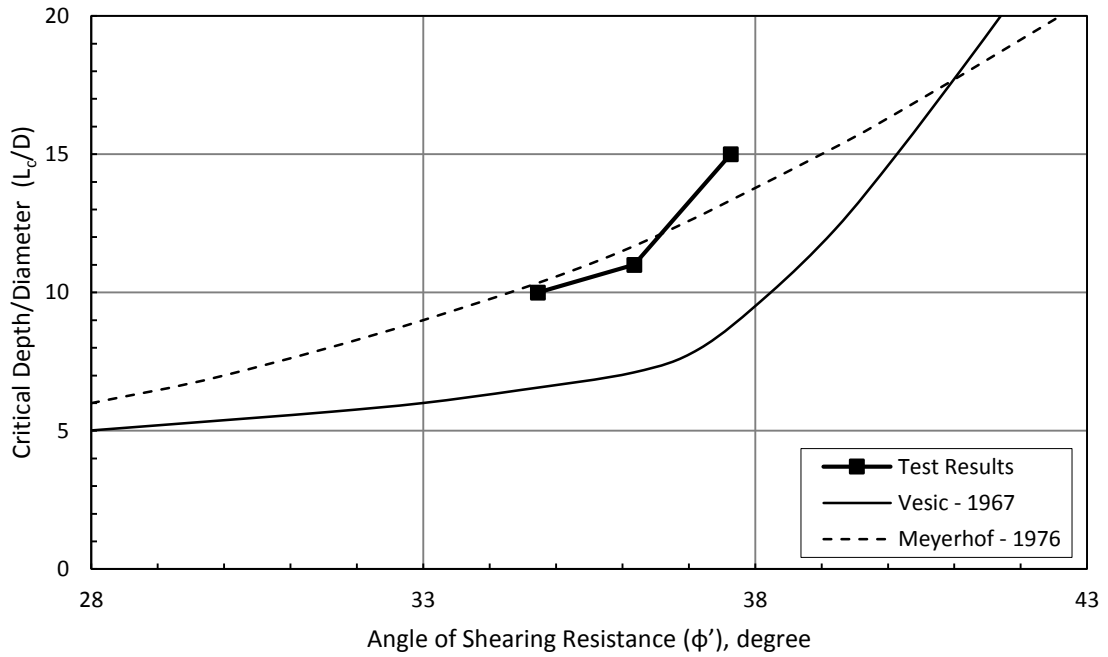


Figure 4-26: Experimental critical depth results

Thus, critical depth ( $L_c$ ) appears only when total shaft resistance is analyzed as an average. Clearly, critical depth appeared in overconsolidated cohesionless soils and was not influenced by the value of OCR. Fellenius and Altaee (1995) and Fellenius (2002) among others are arguing that the critical depth appears when the residual forces, which affect the resistance of piles, are ignored. If considered, the shear stress increases with depth and decreases near the tip of the pile. Although the residual forces were not considered in this experiment, the critical depth appeared when the total shaft resistance was analyzed as an average. Also, the experimental shear stress value increased with depth and decreased near the tip regardless of the residual forces.

Kulhawy (1984) and (1995) referred the appearance of the critical depth to in-situ soil characteristics such as ( $\phi'$ ), ( $K_0$ ) and (OCR), and the fact that their values decreased with depth. Many researchers investigated the appearance of the critical depth experimentally at uniform soils in normally consolidated soils (OCR=1) and observed the critical depth (Vesic, 1967; Meyerhof, 1976). In this experiment, the critical depth was also observed when investigated at uniform soils in overconsolidated soils (OCR>1).

Excluding the effect of residual forces and the in-situ soil characteristics, the critical depth mostly appears due to the effect of sand arching around the piles (Kraft, 1991). When a pile is pushed into the soil, the soil underneath the tip is densified. As the pile goes deeper, it drags the soil in its vicinity which creates a loose sleeve of sand around the pile which makes an ideal condition for arching. Thus, the development of full lateral earth pressure on the pile is prevented (Iskander, 2011).

It can also be attributed to the friction fatigue (Lehane et al., 1993; White and Lehane 2004). It is noted that the local shear stress at a certain depth decreases as the pile depth increases. Because of this reduction, the average total shaft friction remains relatively constant as the embedment depth increases, and consequently, the critical depth appears.

## 4.7 Comparison with Proposed Values in the Literature

The shaft resistance for both pile models were calculated according to the pile geometry, soil properties, and the different design values ( $K_s$ ,  $\beta$ ,  $K_s / K_0$ ) proposed by different researchers as presented in the literature. Figure 4-27 illustrates a comparison between these values and the shaft resistance found experimentally.

It should be mentioned that when low and high value is proposed, the high value was used in this comparison. Also, for  $K_s$  and  $K_s / K_0$  values, the calculated shaft resistance was calculated once considering a limiting value according to the critical depth proposed by Meyerhof (1976), and another without limiting the shaft resistance. In addition, the values proposed by Coyle and Castello (1980) was calculated only for the tests performed at 30% and 45% relative density since the authors did not propose any values for piles driven in soils with an angle of shearing resistance higher than 36 degree. Moreover, the  $R^2$  values were found according to the values ( $K_s$ ,  $\beta$ ,  $K_s / K_0$ ) that were found without limiting the shaft resistance.

It can be concluded from Figure 4-27, as well as from the negative  $R^2$  values that the shaft resistance of driven piles in overconsolidated cohesionless soils are significantly underestimated. To estimate the shaft resistance of driven piles in overconsolidated cohesionless soils more adequately, an empirical model is presented in the following section.

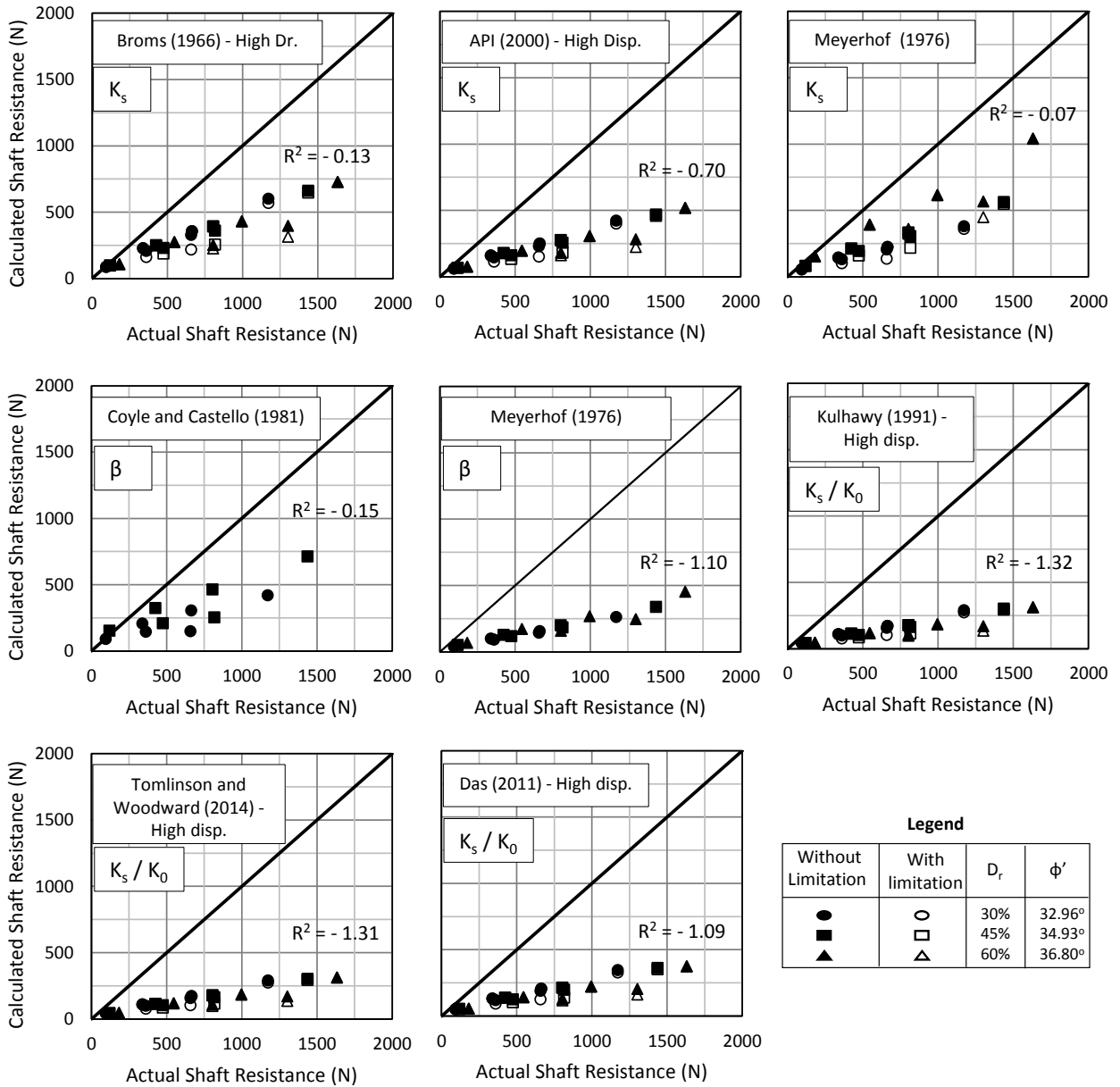


Figure 4-27: Comparison between the actual and the calculated shaft resistance using values proposed by different authors

## 4.8 Empirical Model

It is more practical to correlate test results with the results of a well-defined field test such as the cone penetration test, which has proven valuable for soil profiling and been used in many pile design methods, including those of the University of Western Australia (Lehane et al. , 2005) and Imperial College (Lehane et al., 1993; Chow, 1997).

### 4.8.1 Model Development

Since the cone penetration test was not performed, the end resistance ( $q_c$ ) for all relative densities was estimated according to Mayne's (1991) equation (Eq. 2.26):

$$K_0 = \frac{(P_a / \sigma'_v) (q_c/P_a)^{1.6}}{145 \exp \left\{ \left[ \frac{(q_c/P_a)/(\sigma'_v/P_a)^{0.5}}{12.2 \text{ OCR}^{0.18}} \right]^{0.5} \right\}} \quad (\text{Repeated 2-26})$$

where:

( $K_0$ ) = at rest lateral earth pressure coefficient,

( $q_c$ ) = cone tip resistance,

( $P_a$ ) = a reference stress equal to one atmosphere (1 bar = 100 kPa),

( $\sigma'_v$ ) = vertical effective stress, and

(OCR) = overconsolidation ratio.

The at-rest lateral earth pressure coefficient ( $K_0$ ) can be found using Equation 2.16 (Mayne & Kulhawy, 1982);

$$K_{0(OC)} = (1 - \sin \phi') (\text{OCR})^{(\sin \phi')} \quad (\text{Repeated 2-16})$$

OCRs were measured as presented in Figure 3-10, and accordingly,  $K_0$  values were calculated using Equation 2.16. Consequently, the  $q_c$  value that equalized both sides of Equation 2.26 was identified. Using Equation 2.22 (Lehane et al., 1993), the  $\sigma'_{rf}$  value was calculated as  $\tau_f / \tan \delta_f$  for every section of the pile model 55 mm in diameter and normalized by the corresponding mean end cone resistance ( $q_c$ ) between the load cell levels against the normalized distance from the pile base ( $h / D$ ), as shown in Figure 4-28. The  $\sigma'_{rf} / q_c$  values for tests performed at the same embedment depth ratio were averaged due to their proximity. A similar analytical approach was successfully used by Flynn and McCabe (2015):

$$\tau_f = \sigma'_{rf} \tan \delta_f \quad \text{(Repeated 2-22)}$$

where

$(\tau_f)$  = unit shaft resistance at failure,

$(\sigma'_{rf})$  = radial effective stresses at failure,

$(\delta_f)$  = pile-soil interface friction angle.

For  $h / D$  greater than 3.3,  $\sigma'_{rf} / q_c$  values decreased with increasing  $h / D$  for piles tested at the embedment depth ratio  $L / D = 5$ . As the embedment depth ratio increased to  $L / D = 8$  and 10,  $\sigma'_{rf} / q_c$  decreased at a slower rate. For  $L / D = 13$ ,  $\sigma'_{rf} / q_c$  increased. For  $h / D$  less than 3.3,  $\sigma'_{rf} / q_c$  values decreased with decreased  $h / D$ . As embedment depth ratio increased,  $\sigma'_{rf} / q_c$  values decreased at a slower rate up to a certain  $L / D$ , at which  $\sigma'_{rf} / q_c$  seemed to stabilize. Thus,  $\sigma'_{rf} / q_c$  values clearly depended on the  $L / D$  ratio.

For  $h / D$  greater than 3.3,  $\sigma'_{rf} / q_c$  values seemed to be matched by a power function, as expressed in Equation 4.5. Using that equation, regression analysis was performed with the dataset for the 12 pile load tests to determine the values of factors 'a' and 'b' that adequately described the distribution of  $\sigma'_{rf} / q_c$  values along the pile shaft at different embedment depth ratios. The equation was:

$$(\sigma'_{rf}/q_c) = a (h/D)^b \quad (4-5)$$

where:

$(h/D)$  = normalized distances from the pile base.

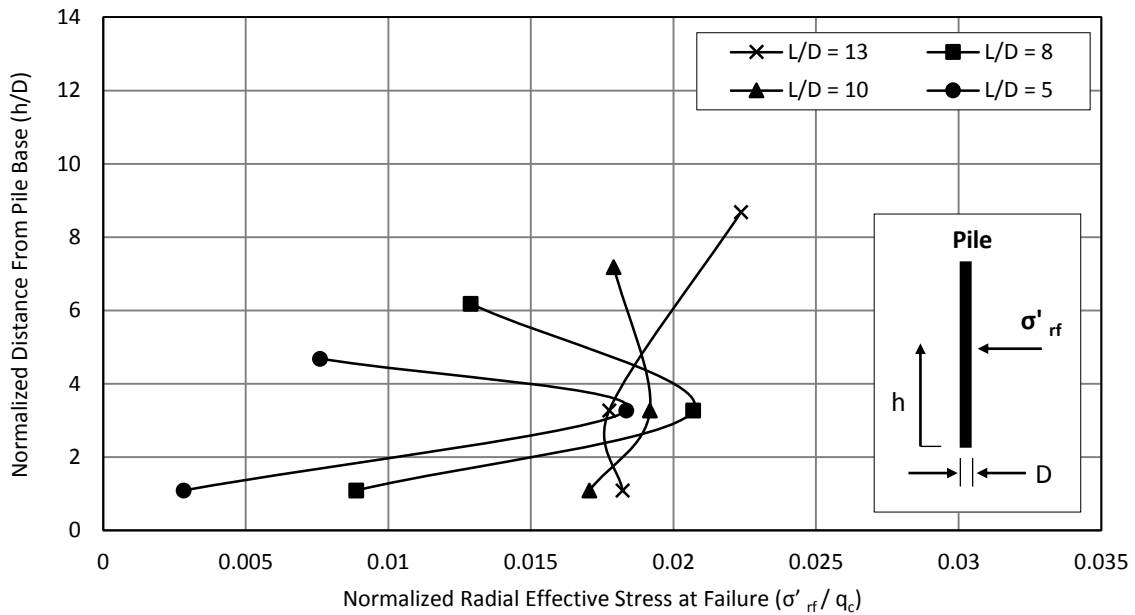


Figure 4-28: Ratio of  $(h/D)$  versus the ratio of  $(\sigma'_{rf}/q_c)$

Because  $\sigma'_{rf} / q_c$  values at  $h / D = 3.3$  were similar, they were averaged to simplify analysis. Based on the best fit (Figure 4-29), the values of factors 'a' and 'b' were determined and plotted (Figure 4-30) against the embedment depth ratio, from which the following relationships were empirically identified:

$$a = 1.0843(L/D)^{-1.667} \quad (4-6)$$

$$b = 0.48 e^{-7.372E-5 (L/D)} - 4.83 e^{-0.2(L/D)} \quad (4-7)$$

For  $h / D$  less than 3.3, it was reasonable to assume that  $\sigma'_{rf} / q_c$  equaled half of that found at  $h / D = 3.3$  for embedment depth ratio ( $L / D$ ) equal to or less than 8. For higher embedment depth ratios, the same  $\sigma'_{rf} / q_c$  value found at  $h / D = 3.3$  was used.

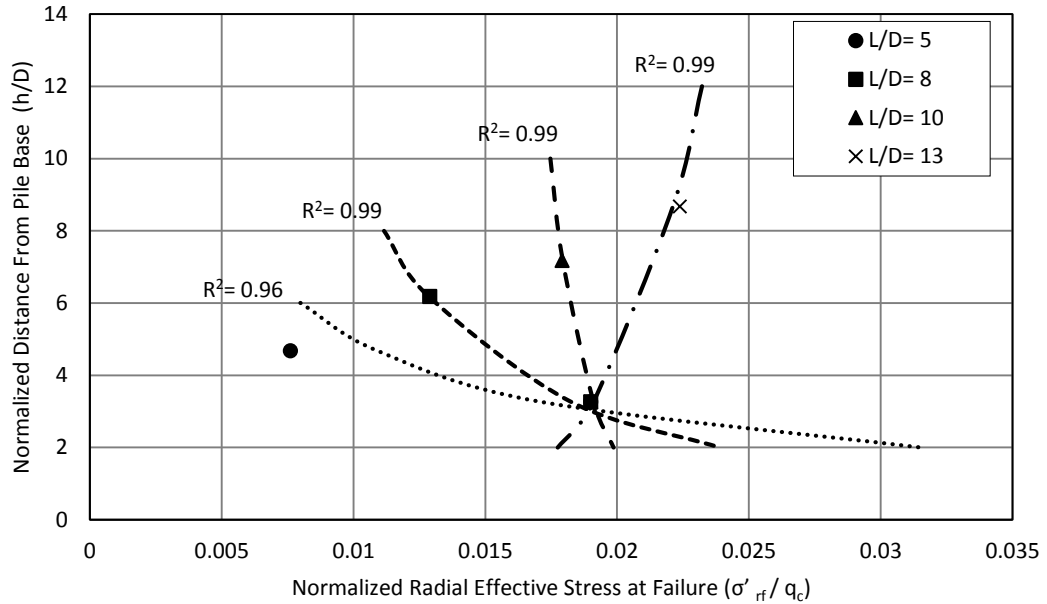


Figure 4-29: Regression analysis for the ratio of ( $h/D$ ) versus the ratio of ( $\sigma'_{rf}/q_c$ )

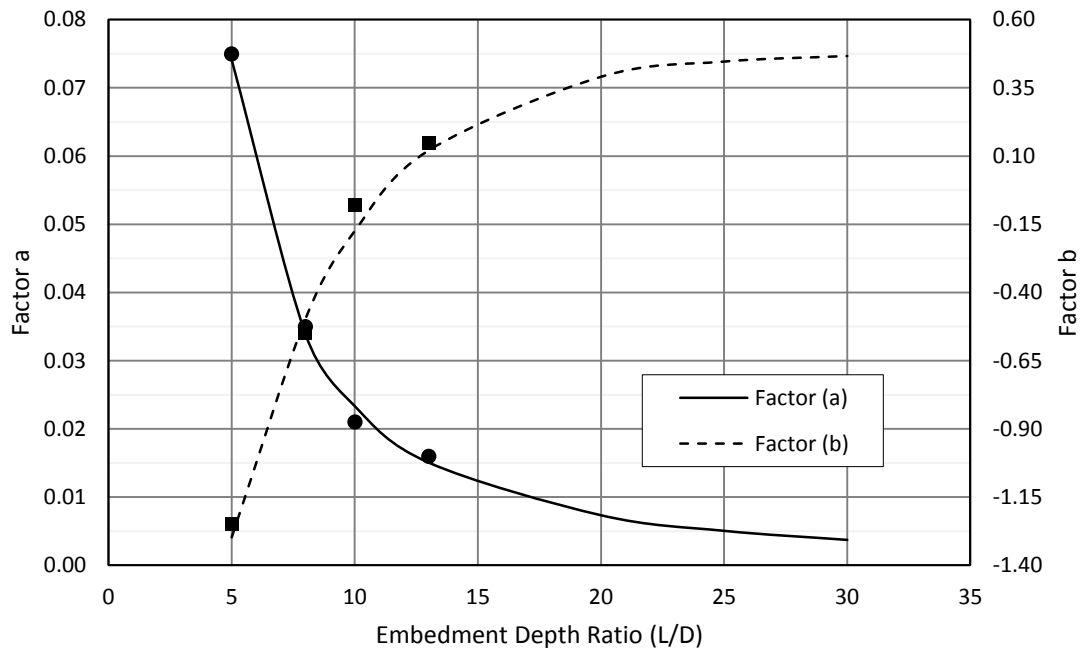


Figure 4-30: Factor (a) and (b) versus the ratio of depth to diameter ( $L/D$ )

## 4.8.2 Validation

Experimental results were compared to those predicted by the proposed equations. Up to  $L/D = 20$ , the comparison (Figure 4-31) revealed that the predicted shear stresses agreed well with the actual values. The test performed at an embedment depth ratio ( $L/D = 23.8$ ) at 60% relative density showed an error of -50%. This error was observed for pile model of 30 mm, and was a result of the high confinement around the pile shaft at 60% relative density, and the minor disturbance that occurred during installation.

To validate the proposed equations with field tests, the results of the field pile load test performed in an OC cohesionless soil reported by Beringen et al. (1979) were analyzed using Equations 4.5–4.7 to determine  $\sigma'_{rf} / q_c$  values along the pile shaft. Those authors used a closed-ended pile 6.75 m long with a diameter of 0.356 m instrumented with strain gages at the ground surface and below ground surface levels at depths of 3.25 m, 4.75 m, 6.25 m, and 6.75 m, which divided the pile into four sections. Because the authors used different failure criteria (tip settlement = 15% D), the tangential method was used to determine ultimate load, and accordingly, total shear stress and its distribution were determined at that load as well. Thus,  $\sigma'_{rf}$  was calculated assuming the pile–soil interface angle equal to  $\delta = 0.75 \phi'$ . That assumption aligns with values proposed by different researchers (Potyondy, 1961; Broms, 1966; Stas & Kulhawy, 1984), as shown in Table 2-4. The nearest cone penetration test to the pile load test location was used to describe the  $q_c$  profile.

The value of  $\sigma'_{rf}$ , for each section was normalized by the corresponding mean ( $q_c$ ) between strain gage levels (Figure 4-32) and plotted against the normalized distance from the pile base ( $h / D$ ). The  $\sigma'_{rf} / q_c$  values calculated by using Equation 4.5 with factors 'a' and 'b' were calculated according to Equations 4.6 and 4.7 for an embedment depth ratio of  $L / D = 18.9$ . The calculated values of  $\sigma'_{rf} / q_c$  agreed with the field pile load test results. The appeared slight difference between the actual  $\sigma'_{rf} / q_c$

and that calculated caused an overestimation of the shaft resistance by 8%, as will be explained in the design example given hereafter. Although the proposed equation was validated, those equations nevertheless need to be tested at greater embedment depth ratios, and the pile–soil interface angle ( $\delta_f$ ) should be carefully selected to obtain accurate results.

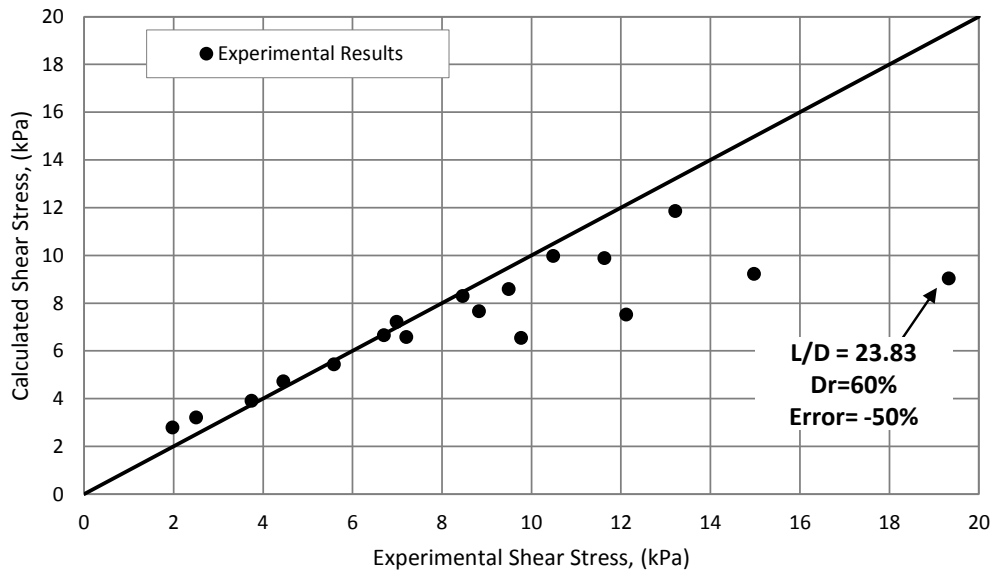


Figure 4-31: Comparison between experimental and predicted shear stress

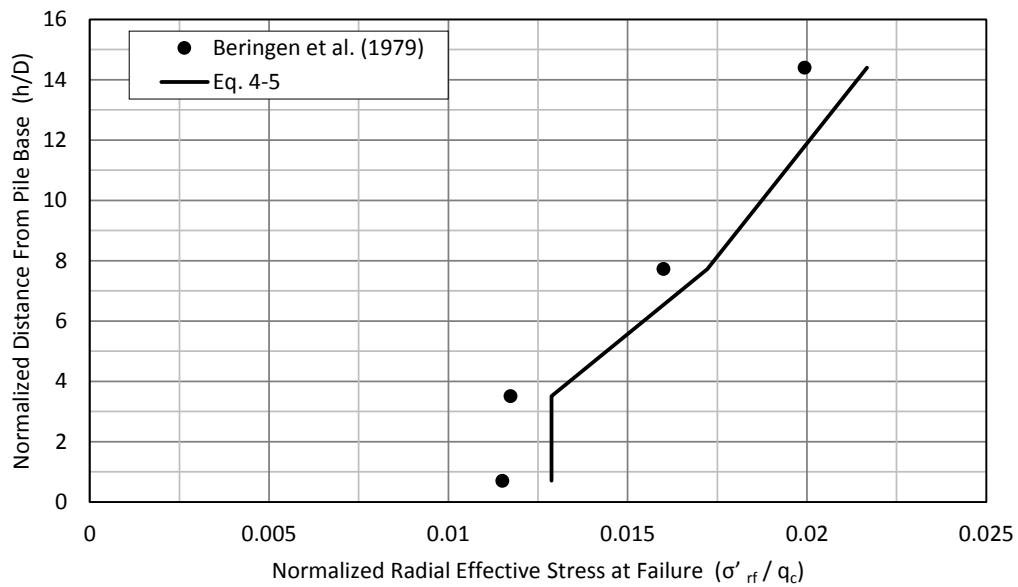


Figure 4-32: Calculated values of  $(\sigma'_{rf}/q_c)$  for the field pile load test reported by Beringen et al. (1979)

### 4.8.3 Design Procedure

The following procedure is recommended for predicting the total shear stress for displacement piles in overconsolidated cohesionless soils as well as its distribution along the pile shaft:

- 1- Divide the pile length into sections of  $2.2 D$  starting from the base of the pile.
- 2- Calculate the  $h / D$  ratio at the middle of each section starting from the base of the pile.
- 3- Calculate factors 'a' and 'b' using Equations 4.6 and 4.7 according to embedment depth ratio ( $L / D$ ).
- 4- Calculate  $\sigma'_{rf} / q_c$  for each section using Equation 4.5 and factors 'a' and 'b' found in Step 3.  
For the first section, from the base of the pile,  $\sigma'_{rf} / q_c$  equals half of that at  $h / D = 3.3$  for any embedment depth ratio ( $L / D$ ) equal to or less than 8; otherwise, it equals  $\sigma'_{rf} / q_c$  at  $h / D = 3.3$ .
- 5- Calculate the mean  $q_c$  value for each section considering the values between the two levels of the section.
- 6- Calculate  $\sigma'_{rf}$  for each section using the corresponding mean  $q_c$  value from Step 5 and  $\sigma'_{rf} / q_c$  value from Step 4.
- 7- Calculate  $\tau_f$  for each section according to Equation 2.22 using the pile–soil interface angle  $\delta_f$ .
- 8- Calculate total shear stress using the length of each section.

#### 4.8.4 Design Example

The field pile load test reported by Beringen et al. (1979) was used to demonstrate the recommended design procedure. The results of the  $q_c$  profile for the soil as well as the load–settlement curve of the pile load test appear in Figure 4-33. The tangential method was used to define ultimate load and, accordingly, shaft resistance.

The following summarize the parameters and results related to the pile load test:

$$D = 0.356 \text{ m}, \quad L = 6.75 \text{ m}$$

$$Q_u = 2,520 \text{ kN}, \quad Q_s = 1,330 \text{ kN}$$

$$\phi' = 38^\circ, \quad \delta_f = 0.75 \phi' \text{ (assumed according to recommendations presented in Table 2-4)}$$

The pile was divided into equal sections of  $2.2 D$ , except for section at the top of the pile where the remaining length was used as presented in Figure 4-33. Accordingly, the height ( $h$ ) from the base of the pile and the  $h / D$  ratio were calculated at the middle of each section. All calculation steps appear in Table 4-4.

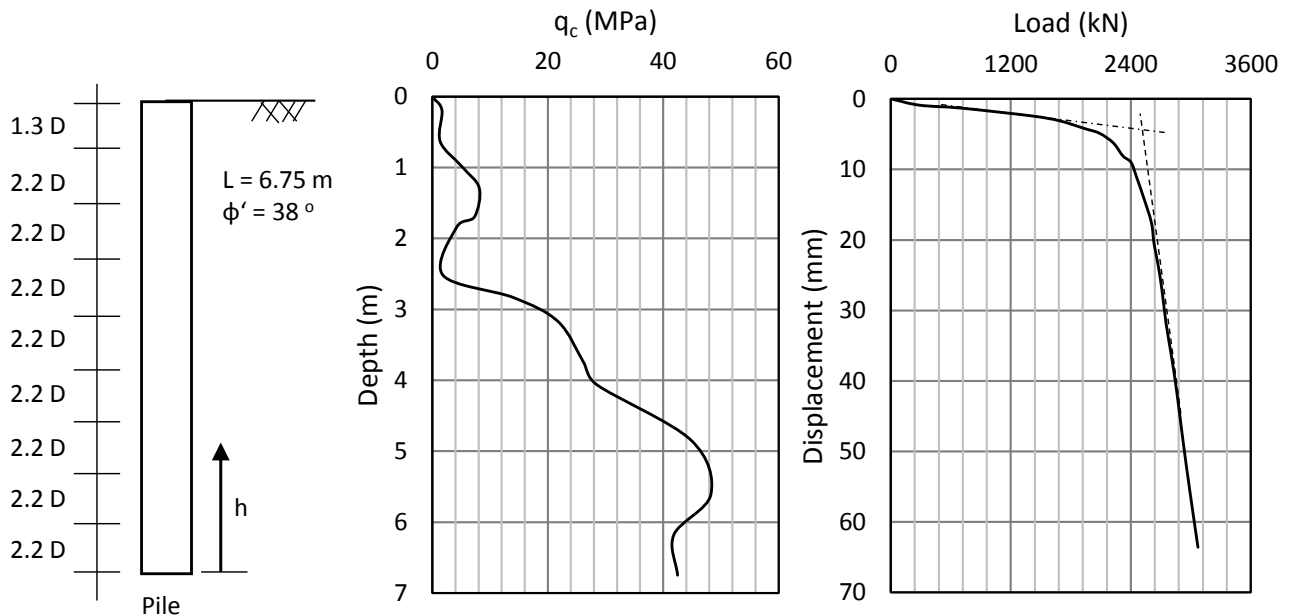


Figure 4-33: The pile load test reported by Beringen et al. (1979), (a) the pile configuration and soil parameter, (b)  $q_c$  profile, and (c) the pile load-settlement curve

According to the embedment depth ratio  $L / D = 18.96$ , factors a and b were calculated using Equations 4.6, and 4.7 as follows:

$$a = 1.0843(18.96)^{-1.667} = 0.00803$$

$$b = 0.48 e^{-7.372E-5 (18.96)} - 4.83 e^{-0.2(18.96)} = 0.3704$$

Using values of factors a and b, the value of  $\sigma'_{rf} / q_c$  was calculated for each section using Equation 4.5, as illustrated below for Section 1:

$$(\sigma'_{rf}/q_c)_{Sec.1} = a (h/D)^b = 0.00803 (18.28)^{0.3704} = 0.0236$$

After the mean  $q_c$  value of the two levels of each section was determined, the  $\sigma'_{rf}$  value was calculated using  $\sigma'_{rf} / q_c$  and the mean  $q_c$  for each section, as illustrated below for Section 1:

$$\left(\frac{\sigma'_{rf}}{q_c}\right)_{Sec.1} = 0.0236 \quad \text{and} \quad (q_{c \text{ avg.}})_{Sec.1} = 1,458.7 \text{ kPa}$$

$$(\sigma'_{rf})_{Sec.1} = 0.0236 \times 1458.69 = 34.39 \text{ kPa}$$

Using the  $\sigma'_{rf}$  value, the  $\tau_f$  value was calculated for each section according to Equation 2.22, as demonstrated below for Section 1:

$$(\tau_f)_{Sec.1} = (\sigma'_{rf})_{Sec.1} \tan \delta_f = 34.39 \tan(0.75 \times 38) = 18.67 \text{ kPa}$$

Mean total shear stress was calculated using the length of each section, as follows:

$$(\tau_f)_{Avg.} = \frac{\sum_{i=1}^n (\tau_f)_{Sec.i} L_i}{L_{Total}} = 191.28 \text{ kPa}$$

Estimated shaft resistance was calculated according to:

$$Q_{s, \text{ estimated}} = \tau_{f \text{ Avg.}} (\pi D L) = 191.28 (\pi \times 0.356 \times 6.75) = 1,441.17 \text{ kN} \quad (\text{Error} \approx 8\%)$$

Table 4-4: Illustration of the calculation steps for the pile load test reported by Beringen et al. (1979)

Section (1)  i	Length / D (2)	Length (m) (3)	h (m) (4)	h/d (5) at mid section	$(\sigma'_{rf}/q_c)$ (6) Eq. 4-5 = a (5) <sup>b</sup>	$q_{c \text{ avg}}$ (kPa) (7)	$\sigma'_{rf}$ (kPa) (8) = (6) X (7)	$\tau_f$ (kPa) (9) Eq. 2-2 = (8) X tan $\delta$
1	1.36	0.48	6.51	18.28	0.0236	1458.69	34.39	18.67
2	2.20	0.78	5.87	16.50	0.0227	3995.13	90.67	49.23
3	2.20	0.78	5.09	14.30	0.0215	5642.08	121.44	65.94
4	2.20	0.78	4.31	12.10	0.0202	6281.72	127.10	69.01
5	2.20	0.78	3.52	9.90	0.0188	20694.87	388.72	211.06
6	2.20	0.78	2.74	7.70	0.0171	30217.63	517.14	280.78
7	2.20	0.78	1.96	5.50	0.0151	42767.50	646.15	350.83
8	2.20	0.78	1.17	3.30	0.0125	46850.80	585.81	318.07
9	2.20	0.78	0.39	1.10	0.0125	43033.43	538.08	292.15

## Chapter 5 : Analytical Model

### 5.1 General

Conventional theories for predicting the capacity of a single pile in sand have generated a range of discrepancies (Hanna & Nguyen, 2002; Poulos & Davis, 1980). In particular, to predict shaft resistance of a pile driven in normally consolidated sand, many theories have derived from limit equilibrium analysis on a cylindrical zone of influence around the pile shaft (Terzaghi, 1943; Meyerhof, 1951; Skempton et al., 1953; Berezantzev et al., 1961).

The models of those theories have made different assumptions and thus pose wide range of discrepancy as shown in Figure 1-1. Also, many field pile load tests (i.e. Vesic, 1970; Lehane et al., 1993; Gavin and O’Kelly, 2007; Flynn and McCabe, 2015) showed that the shaft resistance distribution along the pile’s shaft is nonlinear. This disputes the assumption of using a cylindrical zone of influence around the pile shaft where the forces will be applied horizontally perpendicular to a parallel line to the pile’s center line.

Due to these reasons, an analytical model is proposed based on limit equilibrium analysis using the horizontal slice method to predict the shaft resistance of a single pile driven into a normally consolidated sand. In the model presented here, an inclined failure surface around the pile is assumed where Coulomb’s failure criterion is satisfied along that surface, and the shear and normal stresses on the failure surface are accounted for.

It should be mentioned that the horizontal slice method has previously been able to analyze the stability of reinforced slopes (Shahgholi et al., 2001; Nouri et al., 2006) and to estimate the capacity of pullout piles (Su et al., 2014).

## 5.2 Model Development

In the analysis, an inclined failure plane around the pile shaft was assumed (Figure 5-1). The horizontal slice method was used on the failure zone around the pile shaft, at which ultimate load occurs. The soil in the model was assumed to be homogeneous and isotropic and to obey Coulomb's failure criterion. It was also assumed that the failure surface did not pass below the pile tip. Figure 5-2 presents the forces applied to the failure zone, including:

- 1-  $F_x$  = normal pressure applied on the pile shaft,
- 2-  $F_y$  = shear stress along the pile shaft,
- 3-  $Q$  = vertical overburden pressure applied to the round bottom area of the failure surface,
- 4-  $T_Q$  = shear stress from the overburden pressure assuming full soil mobilization,
- 5-  $W$  = weight of the soil inside the failure zone,
- 6-  $N$  = normal pressure applied to the side failure surface, which is an area of a truncated cone,  
and
- 7-  $T$  = shear stress from the normal pressure applied on the side failure surface assuming full soil mobilization.

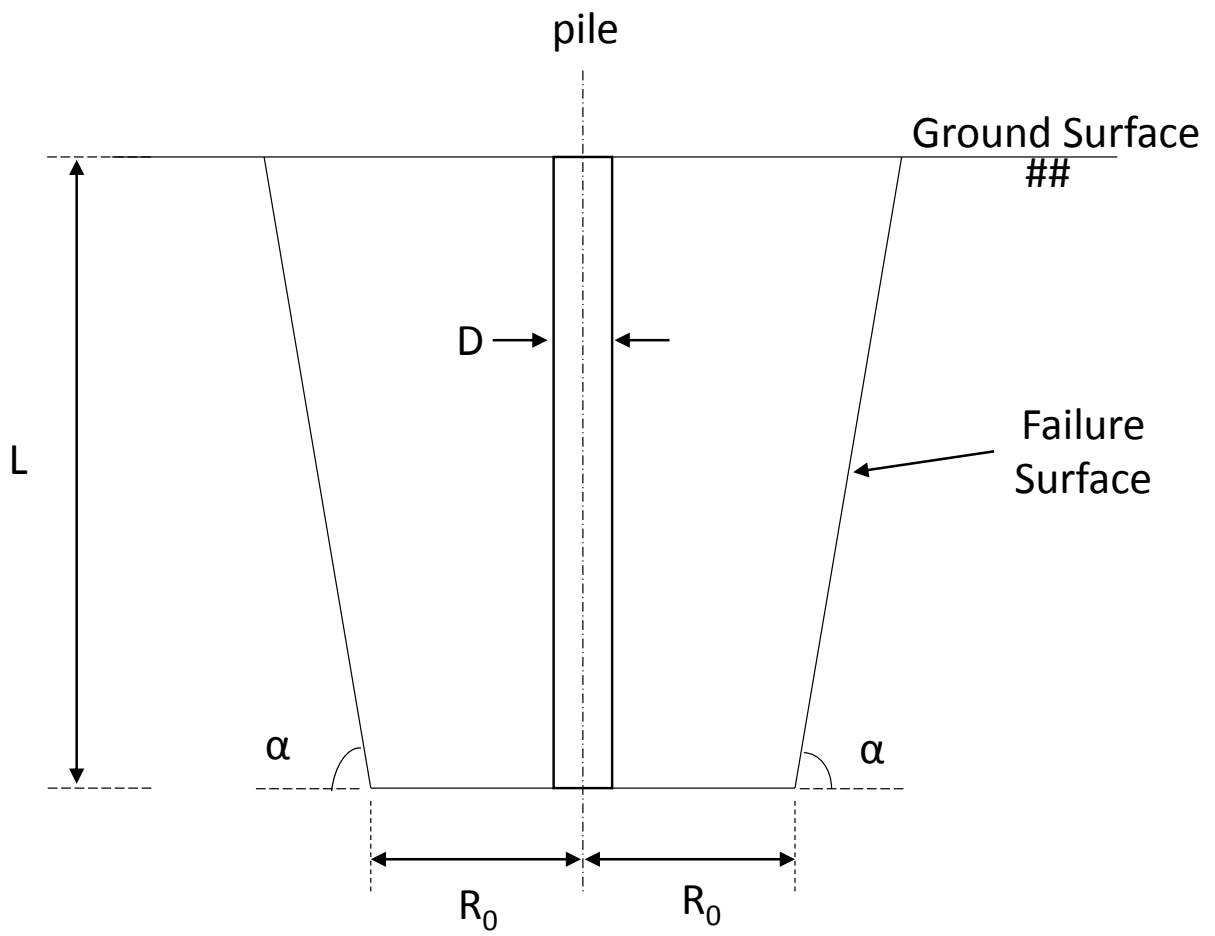


Figure 5-1: Assumed failure zone around the pile's shaft

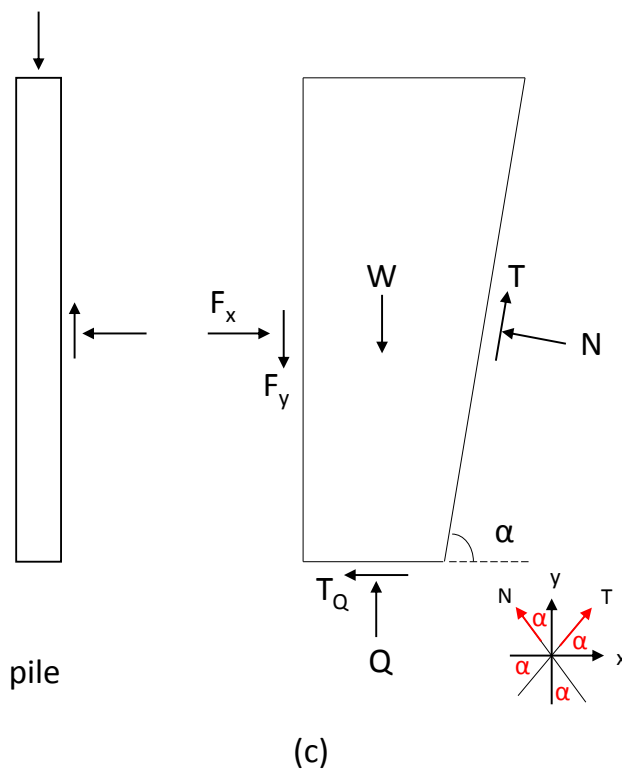
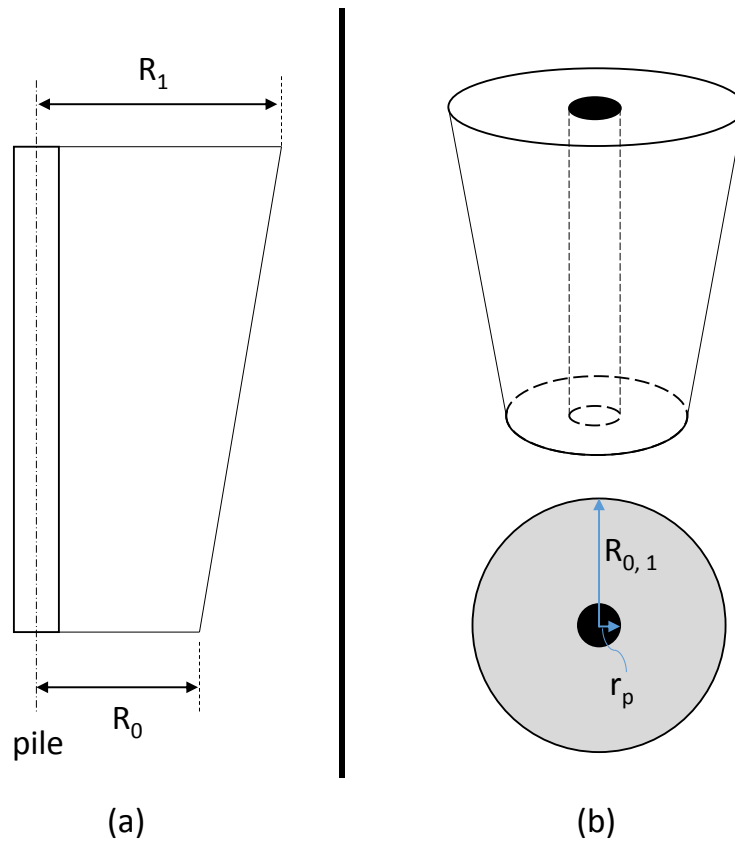


Figure 5-2: (a) one slice of the failure zone, (b) side and bottom area illustration, and (c) forces on the slice

Stresses  $F_x$  and  $F_y$  were applied to the pile shaft. Thus, the shaft area was defined as:

$$\text{Area}_{\text{pile shaft}} = \pi D L \quad (5-1)$$

where:

D: pile diameter, and

L: pile length.

By contrast, the stresses N and T were applied to the side area of the truncated cone (Figure 5-2). The side area was calculated according to the following equation:

$$\text{Area}_{\text{plane}} = \pi (R_0 + R_1) \sqrt{((R_0) - (R_1))^2 + L^2} \quad (5-2)$$

where:

$R_0$  and  $R_1$ : radius of influence at the pile tip and ground surface level, respectively, from the center of the pile to the limit of the failure surface.

Vertical overburden pressure (Q) and its corresponding shear stress ( $T_Q$ ) were applied to the bottom area of the failure zone (Figure 5-2b). That area was calculated according to the following equation:

$$\text{Area}_{\text{bottom}} = \pi \left[ (R_0)^2 - \left( \frac{D}{2} \right)^2 \right] \quad (5-3)$$

To calculate the weight of the soil, the volume of the failure zone around the pile shaft was calculated as the volume of the truncated cone minus the volume of the pile, as follows:

$$\text{Volume}_{\text{soil}} = \left\{ \frac{L}{3} \pi [(R_0)^2 + (R_1)^2 + ((R_0)(R_1))] \right\} - \pi \left( \frac{D}{2} \right)^2 L \quad (5-4)$$

Accordingly, the weight of the soil was calculated based on the unit weight of soil and the volume of the truncated cone according to the following equation:

$$W = \gamma (\text{Volume}_{\text{soil}}) \quad (5-5)$$

where:

$\gamma$ = unit weight of soil.

The radius of influence ( $R_0$ ) at tip level was calculated as a function of the pile's diameter ( $D$ ) and the soil's angle of shearing resistance ( $\phi'$ ) according to Equation 5.6 (Berezantzev et al., 1961). The radius of influence ( $R_1$ ) at the ground surface level was calculated based on the radius of influence ( $R_0$ ) at tip level and the inclination angle of the failure surface ( $\alpha$ ) using a trigonometric equations.

$$R_0 = \frac{D}{2} \left\{ \frac{1 + \sqrt{2} e^{\left(\frac{\pi - \phi'}{2}\right) \tan \frac{\phi'}{2}}}{\sin\left(\frac{\pi - \phi'}{2}\right)} \right\} \quad (5-6)$$

where:

$\phi'$ = angle of shearing resistance.

Using Mohr–Coulomb's failure criterion, shear stress along the pile shaft ( $F_y$ ) was calculated as:

$$F_y = F_x \tan \delta \quad (5-7)$$

where:

$F_x$ = normal pressure on the pile's shaft,

$\delta$ = pile-soil interface angle.

Shear stress at the failure surface was calculated according to Equation 5.8 assuming a fully mobilized angle of shearing resistance:

$$T = N \tan \phi' \quad (5-8)$$

where:

N= normal pressure on the inclined failure surface.

Vertical overburden pressure (Q) applied on the bottom failure surface and its corresponding shear stress ( $T_Q$ ) were calculated as:

$$Q = \gamma L \quad (5-9)$$

$$T_Q = Q \tan \phi' \quad (5-10)$$

Using limit equilibrium analysis, two equations were derived as a result of the force summation in horizontal and vertical directions. The parameters in Equations 5.1–5.10 were known except the values of:

1. Shear stress along the pile's shaft ( $F_y$ ),
2. Normal stress applied to the inclined failure surface (N), and
3. The inclination angle of the failure surface ( $\alpha$ ).

To determine those parameters, a database of 36 field and laboratory pile load tests were collected from extensive published data of various pile diameters, embedment depths, and soil angles of shearing resistance. Those tests were used to establish the relationship between the embedment depth ratio of the pile (L / D) and the inclination angle of the failure surface ( $\alpha$ ). The inclination angle of the

failure surface ( $\alpha$ ) could thus be determined independently. Accordingly, the other two unknown parameters can be found using two equations.

The inclination angle ( $\alpha$ ) varies from 0 to 180 degree. Since the direction of the forces N and T applied at the failure surface and their horizontal and vertical component depend on the inclination angle ( $\alpha$ ), three cases for equilibrium were possible (Figure 5-3), as detailed in what follows.

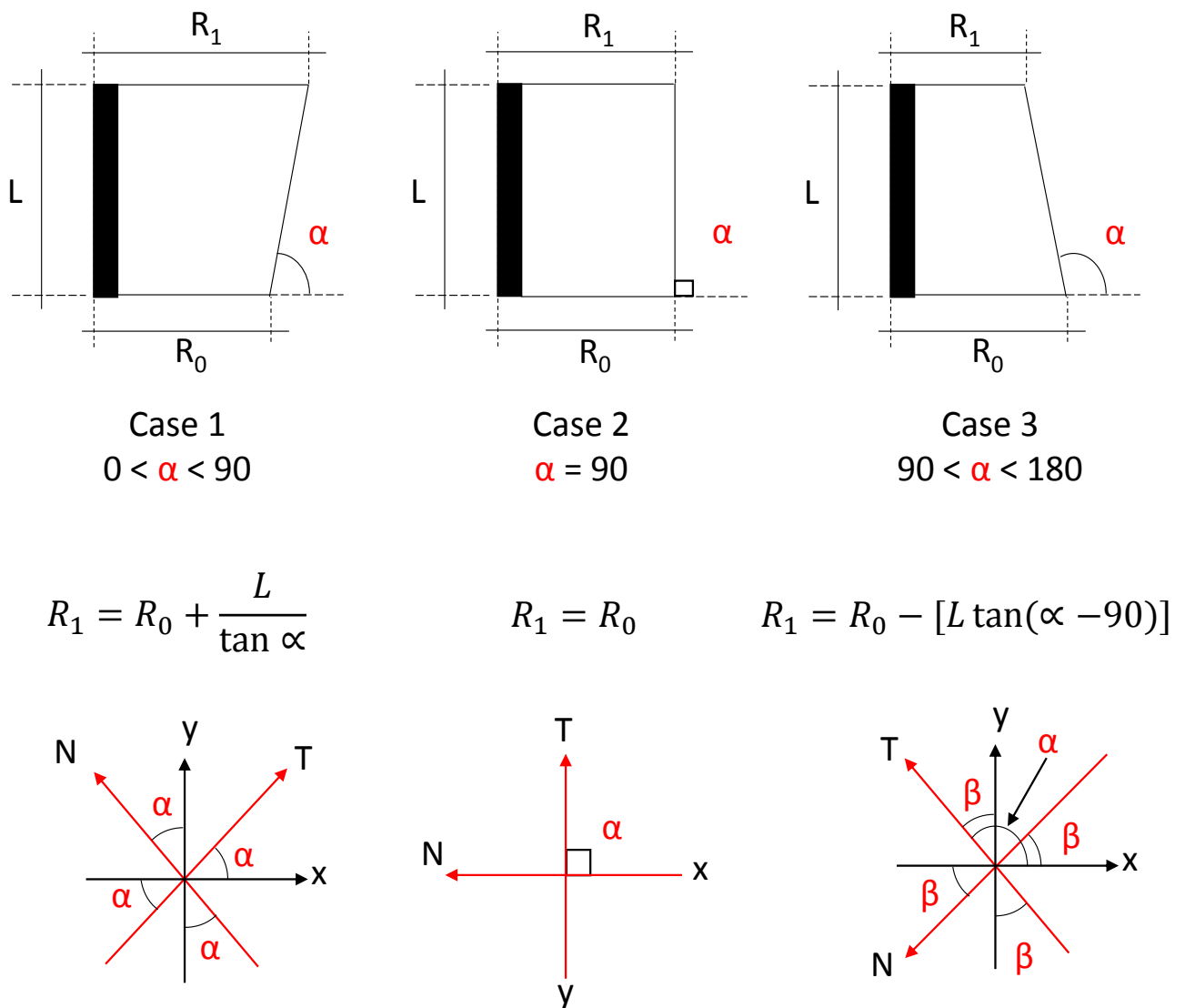


Figure 5-3: Three possible cases for the inclination angle

**A- The equilibrium of forces for the case  $0 < \alpha < 90$  appears below.**

1- The equilibrium of forces in the horizontal direction yields ( $\sum F_x = 0$ ).

$$F_x (\text{Area}_{\text{pile shaft}}) + T \cos \alpha (\text{Area}_{\text{plane}}) = N \sin \alpha (\text{Area}_{\text{plane}}) + T_Q (\text{Area}_{\text{bottom}}) \quad (5-11)$$

Substituting (Eq.5-7) in (Eq.5-11) gives:

$$\frac{F_y}{\tan \delta} (\text{Area}_{\text{pile shaft}}) + T \cos \alpha (\text{Area}_{\text{plane}}) = N \sin \alpha (\text{Area}_{\text{plane}}) + T_Q (\text{Area}_{\text{bottom}}) \quad (5-12)$$

Substituting (Eq.5-8) in (Eq.5-12) gives:

$$\frac{F_y}{\tan \delta} (\text{Area}_{\text{pile shaft}}) + N \tan \phi' \cos \alpha (\text{Area}_{\text{plane}}) = N \sin \alpha (\text{Area}_{\text{plane}}) + T_Q (\text{Area}_{\text{bottom}}) \quad (5-13)$$

Accordingly, the normal force N can be written as follows;

$$N = \frac{\left\{ \frac{F_y}{\tan \delta} (\text{Area}_{\text{pile shaft}}) \right\} - T_Q (\text{Area}_{\text{bottom}})}{(\text{Area}_{\text{plane}}) \{ \sin \alpha - [\tan \phi' \cos \alpha] \}} \quad (5-14)$$

2- The equilibrium of forces in the vertical direction yields ( $\sum F_y = 0$ ).

$$F_y (\text{Area}_{\text{pile shaft}}) + W = Q (\text{Area}_{\text{bottom}}) + N \cos \alpha (\text{Area}_{\text{plane}}) + T \sin \alpha (\text{Area}_{\text{plane}}) \quad (5-15)$$

Also, substituting (Eq.5-8) in (Eq.5-15) gives;

$$F_y (\text{Area}_{\text{pile shaft}}) + W = Q (\text{Area}_{\text{bottom}}) + N \cos \alpha (\text{Area}_{\text{plane}}) + N \tan \phi' \sin \alpha (\text{Area}_{\text{plane}}) \quad (5-16)$$

Accordingly, the shaft resistance of the pile  $F_y$  can be written as follows;

$$F_y = \frac{Q(\text{Area}_{\text{bottom}}) - W + N (\text{Area}_{\text{plane}}) \{ \cos \alpha + [\tan \phi' \sin \alpha] \}}{\text{Area}_{\text{pile shaft}}} \quad (5-17)$$

Equation 5.13 derived from horizontal equilibrium analysis and Equation 5.16 derived from vertical equilibrium analysis can be rewritten in the following forms, respectively:

$$a_1 F_y + b_1 N = c_1 \quad (5-18)$$

Where

$$a_1 = \frac{\text{Area}_{\text{pile shaft}}}{\tan \delta}$$

$$b_1 = -(\text{Area}_{\text{plane}}) \{ \sin \alpha - [\tan \phi' \cos \alpha] \}$$

$$c_1 = T_Q(\text{Area}_{\text{bottom}})$$

$$a_2 F_y + b_2 N = c_2 \quad (5-19)$$

Where

$$a_2 = \text{Area}_{\text{pile shaft}}$$

$$b_2 = -(\text{Area}_{\text{plane}}) \{ \cos \alpha + [\tan \phi' \sin \alpha] \}$$

$$c_2 = Q(\text{Area}_{\text{bottom}}) - W$$

**B- The equilibrium of forces for the case  $\alpha = 90$  appears below.**

1- The equilibrium of forces in the horizontal direction yields ( $\sum F_x = 0$ ).

$$F_x (\text{Area}_{\text{pile shaft}}) = N (\text{Area}_{\text{plane}}) + T_Q (\text{Area}_{\text{bottom}}) \quad (5-20)$$

Substituting (Eq.5-7) in (Eq.5-20) gives:

$$\frac{F_y}{\tan \delta} (\text{Area}_{\text{pile shaft}}) = N (\text{Area}_{\text{plane}}) + T_Q (\text{Area}_{\text{bottom}}) \quad (5-21)$$

Accordingly, the normal force N can be written as follow;

$$N = \frac{\left\{ \frac{F_y}{\tan \delta} (\text{Area}_{\text{pile shaft}}) \right\} - T_Q (\text{Area}_{\text{bottom}})}{(\text{Area}_{\text{plane}})} \quad (5-22)$$

2- The equilibrium of forces in the vertical direction yields ( $\sum F_y = 0$ ).

$$F_y (\text{Area}_{\text{pile shaft}}) + W = Q (\text{Area}_{\text{bottom}}) + T (\text{Area}_{\text{plane}}) \quad (5-23)$$

Also, substituting (Eq.5-8) in (Eq.5-23) gives;

$$F_y (\text{Area}_{\text{pile shaft}}) + W = Q (\text{Area}_{\text{bottom}}) + N \tan \phi' (\text{Area}_{\text{plane}}) \quad (5-24)$$

Accordingly, the shaft resistance of the pile  $F_y$  can be written as follow;

$$F_y = \frac{Q(\text{Area}_{\text{bottom}}) - W + N (\text{Area}_{\text{plane}}) \tan \phi'}{\text{Area}_{\text{pile shaft}}} \quad (5-25)$$

Equation 5.21 derived from horizontal equilibrium analysis and Equation 5.24 derived from vertical equilibrium analysis can be written as follows, respectively:

$$a_3 F_y + b_3 N = c_3 \quad (5-26)$$

Where

$$a_3 = \frac{\text{Area}_{\text{pile shaft}}}{\tan \delta}$$

$$b_3 = -(\text{Area}_{\text{plane}})$$

$$c_3 = T_Q(\text{Area}_{\text{bottom}})$$

$$a_4 F_y + b_4 N = c_4 \quad (5-27)$$

Where

$$a_4 = \text{Area}_{\text{pile shaft}}$$

$$b_4 = -(\text{Area}_{\text{plane}}) \tan \phi'$$

$$c_4 = Q(\text{Area}_{\text{bottom}}) - W$$

**C- The equilibrium of forces for the case  $\alpha > 90$  appears below.**

1- The equilibrium of forces in the horizontal direction yields ( $\sum F_x = 0$ ).

$$F_x (\text{Area}_{\text{pile shaft}}) = N \cos \beta (\text{Area}_{\text{plane}}) + T \sin \beta (\text{Area}_{\text{plane}}) + T_Q (\text{Area}_{\text{bottom}}) \quad (5-28)$$

Substituting (Eq.5-7) in (Eq.5-28) gives:

$$\frac{F_y}{\tan \delta} (\text{Area}_{\text{pile shaft}}) = N \cos \beta (\text{Area}_{\text{plane}}) + T \sin \beta (\text{Area}_{\text{plane}}) + T_Q (\text{Area}_{\text{bottom}}) \quad (5-29)$$

Substituting (Eq.5-8) in (Eq.5-29) gives;

$$\frac{F_y}{\tan \delta} (\text{Area}_{\text{pile shaft}}) = N \cos \beta (\text{Area}_{\text{plane}}) + N \tan \phi' \sin \beta (\text{Area}_{\text{plane}}) + T_Q (\text{Area}_{\text{bottom}}) \quad (5-30)$$

Accordingly, the normal force N can be written as follow;

$$N = \frac{\left\{ \frac{F_y}{\tan \delta} (\text{Area}_{\text{pile shaft}}) \right\} - T_Q (\text{Area}_{\text{bottom}})}{(\text{Area}_{\text{plane}}) \{ \cos \beta + [\tan \phi' \sin \beta] \}} \quad (5-31)$$

2- The equilibrium of forces in the vertical direction yields ( $\sum F_y = 0$ ).

$$F_y (\text{Area}_{\text{pile shaft}}) + W + N \sin \beta (\text{Area}_{\text{plane}}) = Q (\text{Area}_{\text{bottom}}) + T \cos \beta (\text{Area}_{\text{plane}}) \quad (5-32)$$

Also, substituting (Eq.5-8) in (Eq.5-31) gives;

$$F_y (\text{Area}_{\text{pile shaft}}) + W + N \sin \beta (\text{Area}_{\text{plane}}) = Q (\text{Area}_{\text{bottom}}) + N \tan \phi' \cos \beta (\text{Area}_{\text{plane}}) \quad (5-33)$$

Accordingly, the shaft resistance of the pile  $F_y$  can be written as follow;

$$F_y = \frac{Q(\text{Area}_{\text{bottom}}) - W + N (\text{Area}_{\text{plane}}) \{ [\tan \phi' \cos \beta] - \sin \beta \}}{\text{Area}_{\text{pile shaft}}} \quad (5-34)$$

Equation 5.30 derived from horizontal equilibrium analysis and Equation 5.33 derived from vertical equilibrium analysis can be written as follows, respectively:

$$a_5 F_y + b_5 N = c_5 \quad (5-35)$$

Where

$$a_5 = \frac{\text{Area}_{\text{pile shaft}}}{\tan \delta}$$

$$b_5 = -(\text{Area}_{\text{plane}}) \{ \cos \beta + [\tan \phi' \sin \beta] \}$$

$$c_5 = T_Q(\text{Area}_{\text{bottom}})$$

$$a_6 F_y + b_6 N = c_6 \quad (5-36)$$

Where

$$a_6 = \text{Area}_{\text{pile shaft}}$$

$$b_6 = -(\text{Area}_{\text{plane}}) \{ [\tan \phi' \cos \beta] - \sin \beta \}$$

$$c_6 = Q(\text{Area}_{\text{bottom}}) - W$$

### 5.3 Data Analysis

Software was developed to analyze the 36 field and laboratory pile load tests (Table 5-1) in order to determine the inclination angle ( $\alpha$ ) that would satisfy the equilibrium in light of the three possible cases. The flowchart presented in Figure 5-4 highlights the steps followed to obtain the results. The tangential method was applied to determine ultimate load for the pile from reported load–settlement curves, and accordingly, shaft resistance was determined. Because the data reported by Stas and Kulhawy (1984) were tabulated, they were used as originally reported. Also, the value of  $R_1$  was constrained to have a minimum value equal to the pile’s diameter in order to prevent negative values. The pile–soil interface angle ( $\delta$ ), which depends upon the pile’s surface roughness and hardness as well as upon the soil’s grain size, shape, and mineral type (Yang et al., 2015), was assigned as a percentage of the soil angle of shearing resistance ( $\phi'$ ). Broms (1966) proposed an interface angle of 20 degree for all steel piles and  $0.75 \phi'$  for all concrete piles, whereas the interface angle proposed by Stas and Kulhawy (1984) ranges from  $0.8\text{--}0.9 \phi'$  for rough steel piles and  $0.9\text{--}1.0 \phi'$  for concrete. Later, Jardine et al. (1992) revealed that interface angle decreases as mean grain size ( $d_{50}$ ) increases and ranges from 36 to 23 degree. Regardless of mean grain size, CUR (2001) recommended using an interface angle of 29 degree for steel piles. Following large-displacement ring shear interface tests on various materials and grain sizes, Ho et al. (2011) reported results similar to Jardine et al.’s (1992) except lower values and less reduction as mean grain size ( $d_{50}$ ) increased and thus recommended an interface angle of 26–31 degree. For concrete piles, Barmopoulos et al. (2009) found a relationship between interface angle and the ratio of pile roughness to mean grain size ( $d_{50}$ ) that generally suggests an interface angle of 29 degree.

To obtain consistent results, values proposed by Stas and Kulhawy (1984) were adopted in the analysis reported here—that is, an interface angle of  $0.9 \phi'$  for both steel and concrete piles, given the

assumption of rough surfaces—because the dataset used in the model derives from different sources, most of which do not provide data regarding pile roughness, and because soil grain size presented, if at all, ranged widely. For tests performed with a sandpaper cover, the interface angle equaled the angle of shearing resistance.

The inclination angle at which forces on the pile and the failure zone are in equilibrium was determined for each pile load test in the database using the analytical model presented earlier. Although the exact inclination angle for pile load tests reported by Hanna and Nguyen (2003) could not be identified due to the constraint applied in analysis ( $R_1 \geq D$ ), the inclination angles reported yielded a minimum error of -20%. Such angles were deemed acceptable because the error was considerably small and because the angles predicted lower shear stress than actual values, which increased safety.

Table 5-1: Summary of the database for pile load tests in sand

Reference	Serial No	Test Name	Material / Type	D (m)	L (m)	L/D	$\phi'$ (degree)	$\gamma$ (kN/m <sup>3</sup> )	Shaft Resistance (kPa)	$\delta$ (degree)
Lehane et al. (1993)	1	LB1C	S / F	0.1020	5.95	58.33	33.00	12.50	31.47	29.70
	2	LB2C	S / F	0.1020	1.80	17.65	36.00	16.90	20.80	32.40
Tavenas (1971)	3	J-2	S / F	0.3230	8.84	27.37	34.00	15.39	20.16	30.60
	4	J-3	S / F	0.3230	11.89	36.80	34.00	15.39	24.72	30.60
	5	J-4	S / F	0.3230	14.94	46.24	34.00	15.39	25.44	30.60
	6	J-5	S / F	0.3230	17.98	55.68	34.00	15.39	25.92	30.60
	7	J-6	S / F	0.3230	21.03	65.11	34.00	15.39	25.20	30.60
Stas & Kulhawy (1984)	8	136/1	C / F	0.2804	7.99	28.48	30.00	11.50	29.20	27.00
	9	136/3	C / F	0.2408	7.99	33.16	30.00	11.14	41.40	27.00
Vesic (1970)	10	H-11	S / F	0.4572	3.02	6.61	31.00	15.88	34.43	27.90
	11	H-12	S / F	0.4572	6.12	13.39	33.00	13.40	66.86	29.70
	12	H-13	S / F	0.4572	8.86	19.39	35.00	12.63	66.52	31.50
	13	H-14	S / F	0.4572	11.99	26.22	35.90	12.25	76.96	32.31
	14	H-15	S / F	0.4572	15.01	32.83	36.00	12.00	75.33	32.40
Paik et al. (2003)	15	CEP	S / F	0.356	6.87	19.30	33.30	13.52	53.10	29.97
Altaee et al. (1992)	16	Test 1	C / F	0.2850	11.00	38.60	31.00	13.91	58.89	27.90
	17	Test 2	C / F	0.2850	15.00	52.63	31.00	12.82	93.15	27.90
Hanna & Nguyen (2003)	18	D-76	SP / L	0.0762	0.76	10.00	40.00	15.65	13.37	40.00
	19	D-77	SP / L	0.0762	1.52	20.00	40.00	15.65	18.84	40.00
Mansur & Kufman (1958)	20	2	S / F	0.5334	19.81	37.14	30.00	10.10	73.19	27.00
	21	4	S / F	0.4318	20.12	46.59	30.00	9.85	102.24	27.00
	22	5	S / F	0.4318	13.72	31.76	29.00	10.20	53.55	26.10
Vesic (1967)	23	25	S / L	0.0508	0.25	5.00	35.04	14.14	2.29	31.53
	24	26	S / L	0.0508	0.25	5.00	30.90	13.12	1.84	27.81
	25	28	S / L	0.0508	0.51	10.00	36.04	14.37	2.35	32.43
	26	29	S / L	0.0508	0.51	10.00	30.47	13.01	2.17	27.42
	27	31	S / L	0.0508	0.76	15.00	35.90	14.34	2.41	32.31
	28	32	S / L	0.0508	0.76	15.00	31.33	13.23	1.82	28.19
	29	34	S / L	0.0508	1.02	20.00	35.63	14.28	2.28	32.07
	30	35	S / L	0.0508	1.02	20.00	30.22	12.94	1.64	27.20
	31	46	S / L	0.1016	1.02	10.00	35.77	14.31	2.29	32.19
	32	47	S / L	0.1016	1.02	10.00	31.08	13.16	1.84	27.97
	33	50	S / L	0.1016	2.03	20.00	30.16	12.93	2.35	27.15
Mansur & Hunter (1970)	34	1	S / F	0.3658	16.18	44.25	32.00	13.84	68.41	28.80
	35	2	S / F	0.4572	16.09	35.20	32.00	13.68	66.19	28.80
	36	3	S / F	0.5180	16.15	31.19	32.00	12.07	53.18	28.80

S : Steel , C : concrete , SP : Sand Paper , F : Field Test , L : Laboratory Test

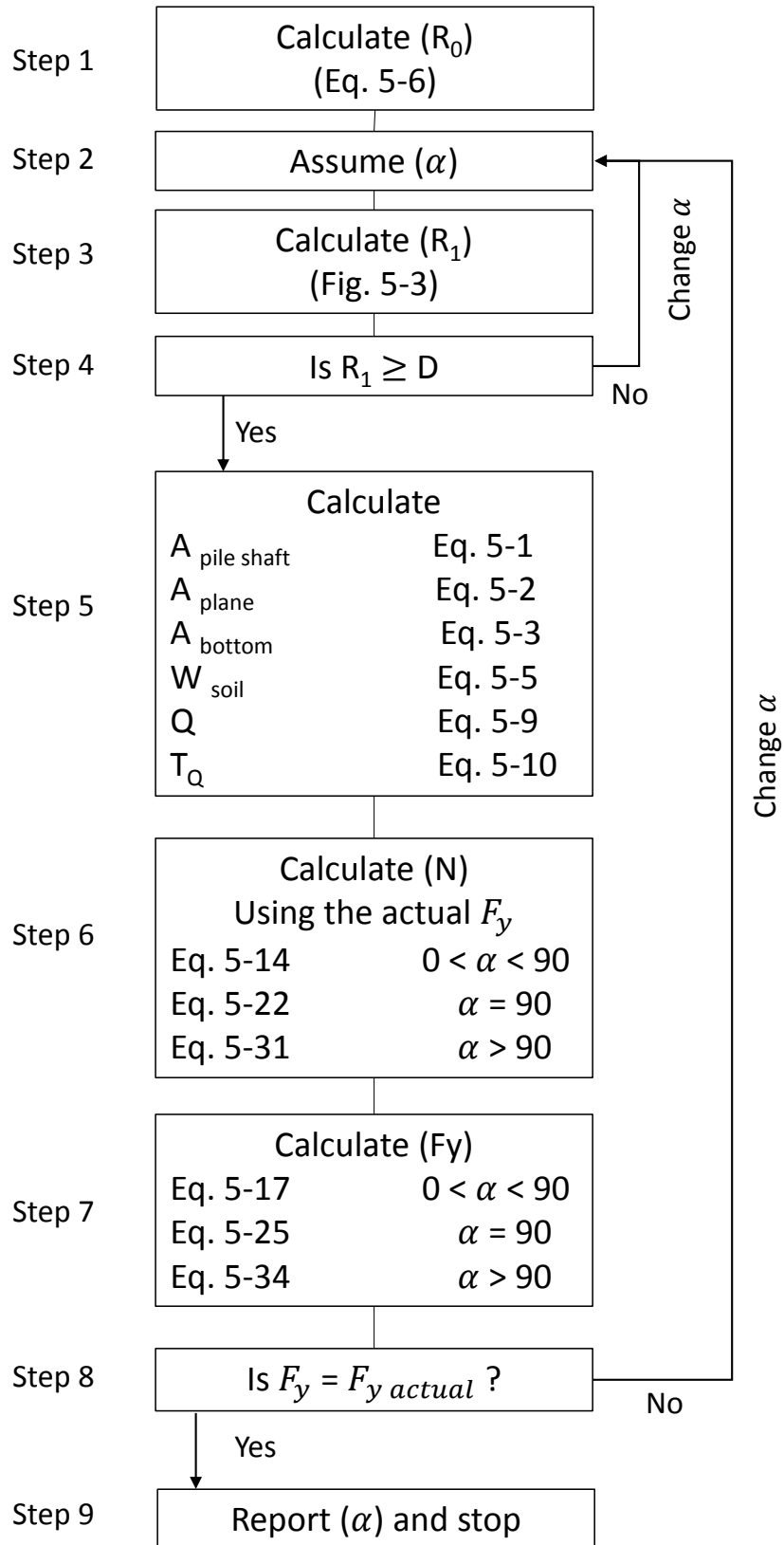


Figure 5-4: Steps of calculating the inclination angle

## 5.4 Results of Analysis

The inclination angles ( $\alpha$ ) for all pile load tests listed in the database appear in Figure 5-5 against the embedment depth. The inclination angle increased as the angle of shearing resistance ( $\phi'$ ) increased and decreased as the ratio of pile length to pile diameter (i.e.,  $L / D$ ) increased. Figure 5-6 illustrates the general behaviour of the inclination angle with depth.

The inclination angles for piles tested in soils with the same angle of shearing resistance ( $\phi'$ ) were aligned and demonstrated a certain pattern in relation to the  $L / D$  ratio. Moreover, the inclination angle for piles tested in soil with angles of shearing resistance of 30–31 degree, 32–33 degree, and 34–35 degree showed the same pattern with  $L / D$  ratio as well.

Accordingly, a relationship was detected between inclination angle and the  $L / D$  ratio for angles of shearing resistance of 30–31 degree, 32–33 degree, and 34–35 degree, respectively. That relationship (Figure 5-5) was extrapolated for the angle of shearing resistance of 36–37 degree, 38–39 degree, and 40–41 degree, which agreed well with inclination angles in that range. Therefore, inclination angle ( $\alpha$ ) can be determined by using the angle of shearing resistance ( $\phi'$ ) and the  $L / D$  ratio.

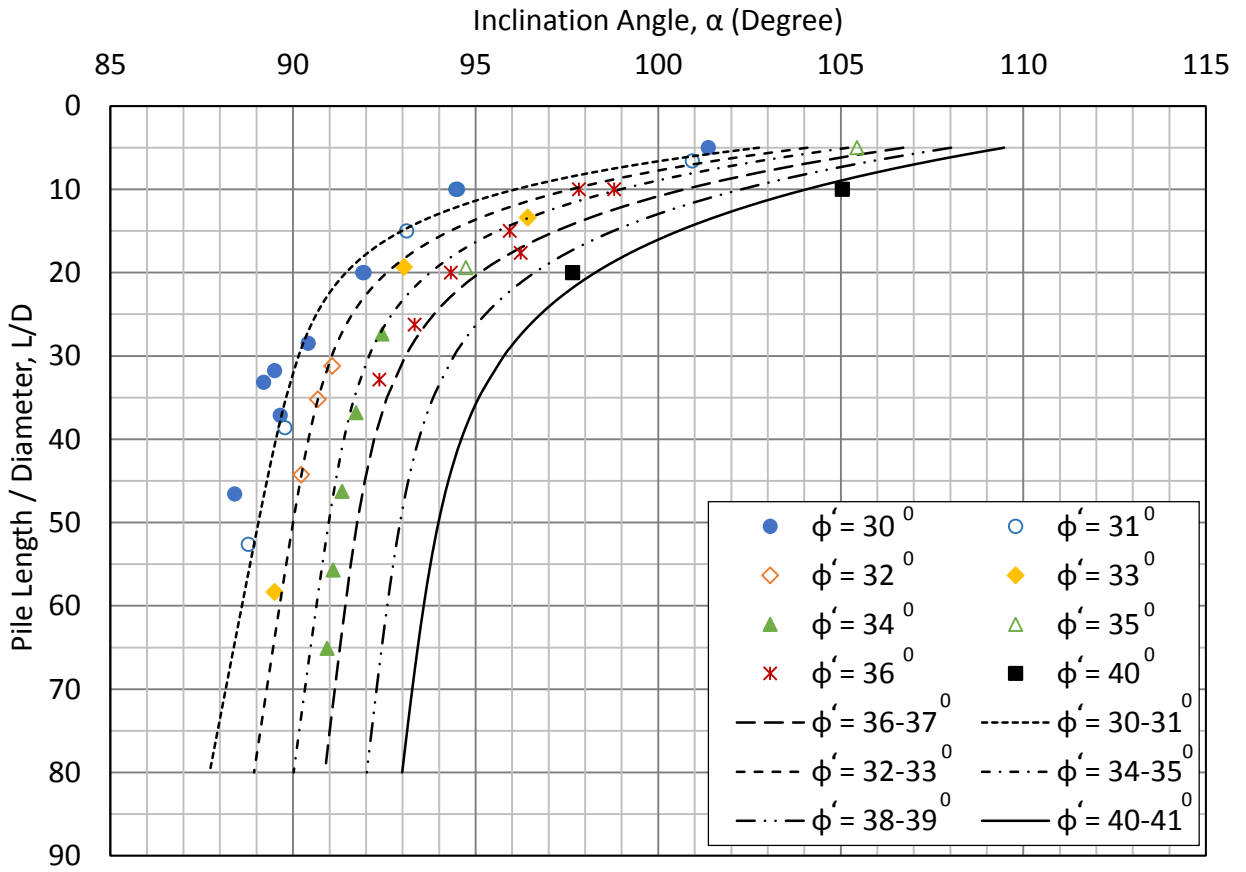


Figure 5-5: Results of the inclination angles

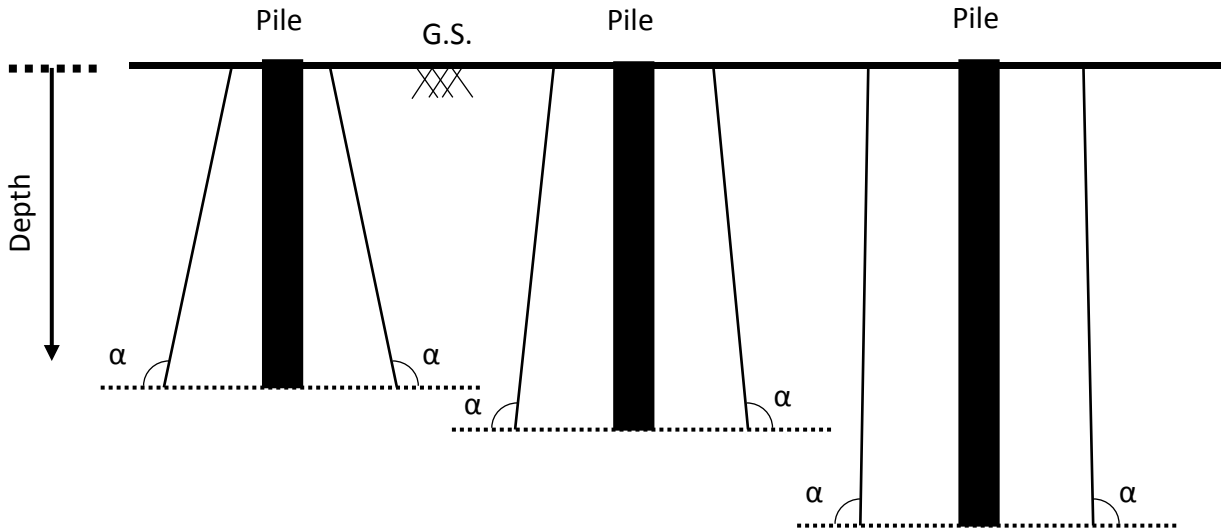


Figure 5-6: Illustration of the inclination angle behaviour with depth

## 5.5 Design Procedure

According to the previous analysis, the following steps can be used to calculate the shear resistance ( $F_y$ ) of driven piles in normally consolidated soil:

- 1- Determine the inclination angle (Figure 5-5) based on the  $L / D$  ratio and angle of shearing resistance ( $\phi'$ ).
- 2- Specify the case of analysis and, accordingly, the two equations:
  - a. Equation 5.18 and 6.19      for  $0 < \alpha < 90$
  - b. Equation 5.26 and 6.27      for  $\alpha = 90$
  - c. Equation 5.35 and 6.36      for  $\alpha > 90$
- 3- Calculate the corresponding three parameters for each equation according to inclination angle, pile geometry, and soil properties (Eqs. 5.1–5.10).
- 4- Solve the two equations, according the case of analysis specified in step 2, to determine the shaft resistance ( $F_y = Q_s$ ).

## 5.6 Validation

For validation, an independent database was used to compare the predicted shear stress along the pile shaft using the proposed inclination angle chart with field measurements. Table 5-2 summarizes the database, which comprised 8 field pile load tests collected from published geotechnical research. The design procedure presented earlier was used to calculate shear resistance ( $F_y$ ), the results of which appear in Table 5-3, with the percentage of error illustrated in Figure 5-7. Inclination angles for all piles exceeded  $90^\circ$  except that for the first pile load test (No. 1). Predicted shaft resistance agreed well with actual shaft resistance ( $\pm 30\%$ ).

Table 5-2: Independent database of field pile load tests for validation

Reference	Serial No	Test Name	Material	D (m)	L (m)	L/D	$\phi'$ (degree)	$\gamma$ (kN/m <sup>3</sup> )	Shaft Resistance (kPa)	$\delta$ (degree)
BCP-committee (1971)	1	C6	Steel	0.20	11.00	55.00	30.0	13.40	47.74	27.0
Briaud et al. (1989)	2	Single	Steel	0.27	9.14	33.49	35.4	10.93	22.02	31.9
Coyle et al. (1973)	3	C-CH	Concrete	0.44	8.69	19.57	34.0	10.3	32.64	30.6
Stas & Kulhawy (1984)	4	152/2	Concrete	0.32	21.33	66.67	34.0	9.24	38.46	30.6
	5	153/1	Steel	0.45	3.01	6.60	33.0	14.60	29.43	29.7
Vesic (1970)	6	H-2	Concrete	0.44	15.24	34.32	36.0	12.00	61.40	32.4
Gregersen et al. (1973)	7	A	Concrete	0.28	8.00	28.57	30.0	11.25	24.02	27.0
Fellenius (1986)	8	Single	Steel	0.27	9.10	33.33	35.0	9.81	22.8	31.5

Table 5-3: The results of the validation database

Reference	Serial No	$\alpha$ (degree)	Equations	a	b	c	$F_y = Q_s$ (kPa)	Error (%)
BCP-committee (1971)	1	88.9	Equ.6-18	13.56	-36.96	47.94	61.64	29.10%
			Equ.6-19	6.91	-22.29	-49.44		
Briaud et al (1989)	2	92.3	Equ.6-35	12.62	-34.89	129.52	24.22	9.98%
			Equ.6-36	7.84	-22.74	75.14		
Coyle et al. (1973)	3	93.55	Equ.6-35	20.50	-51.25	250.49	40.65	24.52%
			Equ.6-36	12.12	-30.13	150.19		
Stas and Kulhawy (1984)	4	90.55	Equ.6-35	36.27	-100.02	286.52	36.22	-5.81%
			Equ.6-36	21.45	-66.07	98.32		
	5	102	Equ.6-35	7.60	-17.81	113.40	27.69	-5.90%
			Equ.6-36	4.33	-6.84	82.77		
Vesic (1970)	6	92.5	Equ.6-35	33.50	-95.56	684.84	45.01	-26.69%
			Equ.6-36	21.26	-63.25	412.18		
Gregersen et al. (1973)	7	90.4	Equ.6-35	13.81	-29.33	57.37	28.77	19.79%
			Equ.6-36	7.04	-16.66	9.32		
Fellenius (1986)	8	92	Equ.6-35	12.74	-35.08	109.12	27.38	20.09%
			Equ.6-36	7.80	-22.78	58.10		

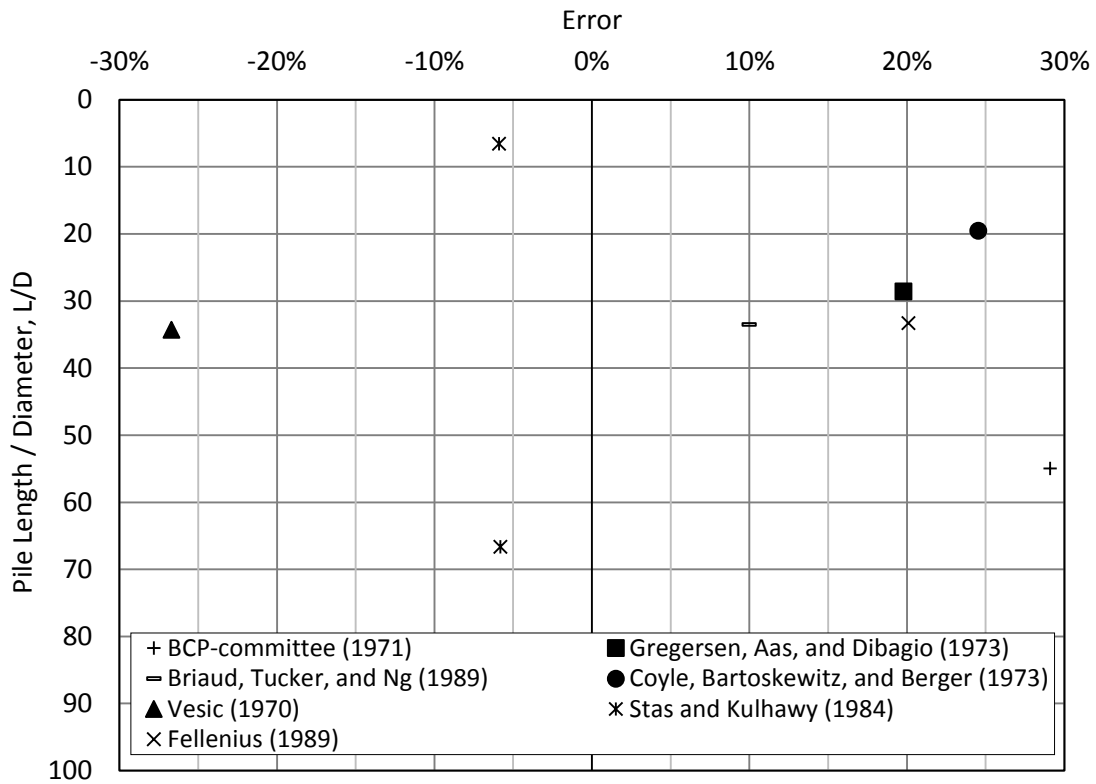


Figure 5-7: Error between the predicted and actual shaft resistance

## 5.7 Critical Depth

As Figure 5-5 suggests, a sudden change occurred in the decreasing rate of the inclination angle with the  $L / D$  ratio, which confirms that critical depth exists when shear stress along the pile shaft is analyzed as an average. The tangential method was used to identify the intercept point for each curve in Figure 5-5; the intercept point represents the critical depth for the corresponding angle of shearing resistance. Figure 5-8 presents the deduced critical depth with respect to the angle of shearing resistance along with values proposed by Vesic (1964) and Meyerhof (1976). Critical depth existed between the  $L / D$  ratios of 10 and 20, which agrees with the results of Vesic (1964) and Meyerhof (1976), and increased linearly with as the angle of shearing resistance increased. Moreover, the

deduced critical depth exceeded values proposed by Vesic (1964) and Meyerhof (1976), which, it bears noting, were based on small-scale laboratory tests, whereas the deduced values using the analytical model were found based on a large database of mostly field pile load tests.

The deduced values seem to agree more with the values proposed by Meyerhof (1976) since they behaved nearly linearly with the angle of shearing resistance, as observed analytically. However, the difference between the deduced values and Meyerhof's (1976) values was considerable at a low angle of shearing resistance and decreased as that angle increased.

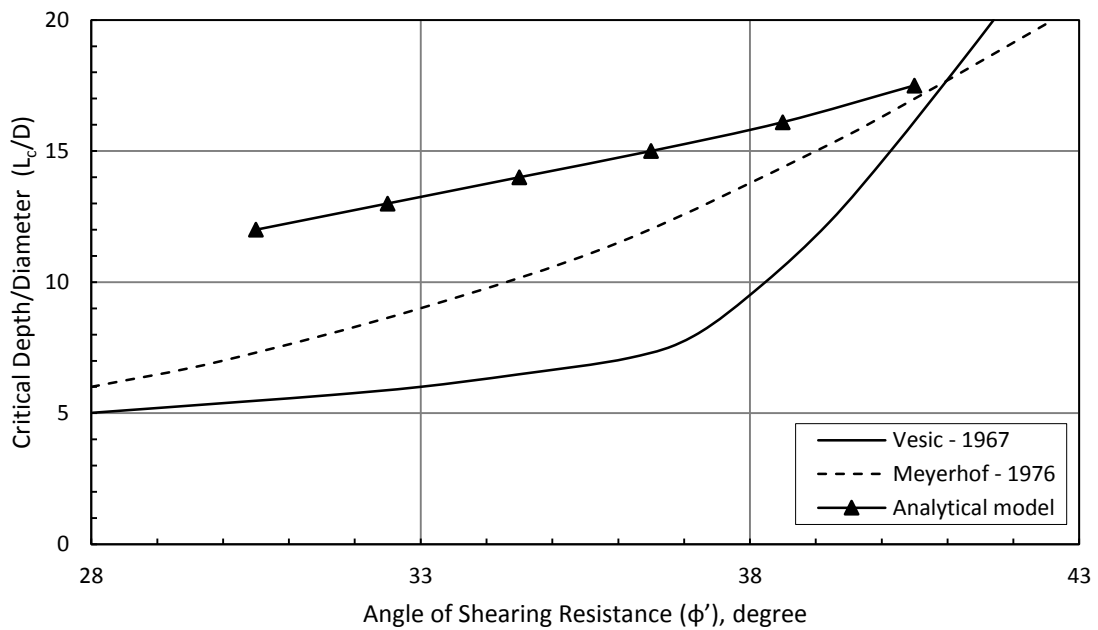


Figure 5-8: Results of critical depth

## 5.8 Discussion

An analytical model was developed based on limit equilibrium analysis using the horizontal slice method to predict the shaft resistance of piles in normally consolidated cohesionless soils. The model was developed with the aid of 36 pile load tests collected from the literature. The results obtained from the model agreed well with field pile load test. Moreover, a critical depth was observed, which is generally in line with the literature.

The analytical model developed was used to determine the shaft resistance in normally consolidated sand ( $OCR = 1$ ) for a pile model 55 mm in diameter used experimentally. Figure 5-5 was used to find the inclination angle for each pile load test performed using the pile model 55 mm in diameter. Using the soil properties, shaft resistance was determined following the steps presented earlier, the results of which appear in Table 5-4. Shaft resistance was less than that observed experimentally (Table 3-11) due to the effect of OCR. The error between experimentally and analytically determined shaft resistances appears in Figure 5-9. Because error increased along with embedment depth, the effect of the OCR increased as embedment depth increased, although the OCR value decreased as  $L / D$  increased.

Table 5-4: Shaft resistance of 55 mm pile model at normally consolidated sand

Pile Model	$D_r$ (%)	L (m)	L/D	$\phi' = \delta$ (degree)	$\gamma$ (kN/m <sup>3</sup> )	$\alpha$ (degree)	$F_y$ kPa	$Q_s$ (N)
55 mm	30	0.275	5	33	14.78	104.09	2.20	104.54
		0.44	8	33	14.78	99.69	2.69	204.57
		0.55	10	33	14.78	97.61	2.70	256.63
		0.715	13	33	14.78	95.67	2.61	322.32
	45	0.275	5	34.9	15.26	105.21	2.23	106.17
		0.44	8	34.9	15.26	101.01	2.79	211.89
		0.55	10	34.9	15.26	98.97	2.84	270.26
		0.715	13	34.9	15.26	96.90	2.77	341.64
	60	0.275	5	36.84	15.73	106.71	2.27	107.80
		0.44	8	36.84	15.73	102.74	2.98	226.70
		0.55	10	36.84	15.73	100.72	3.13	297.11
		0.715	13	36.84	15.73	98.40	2.95	364.47

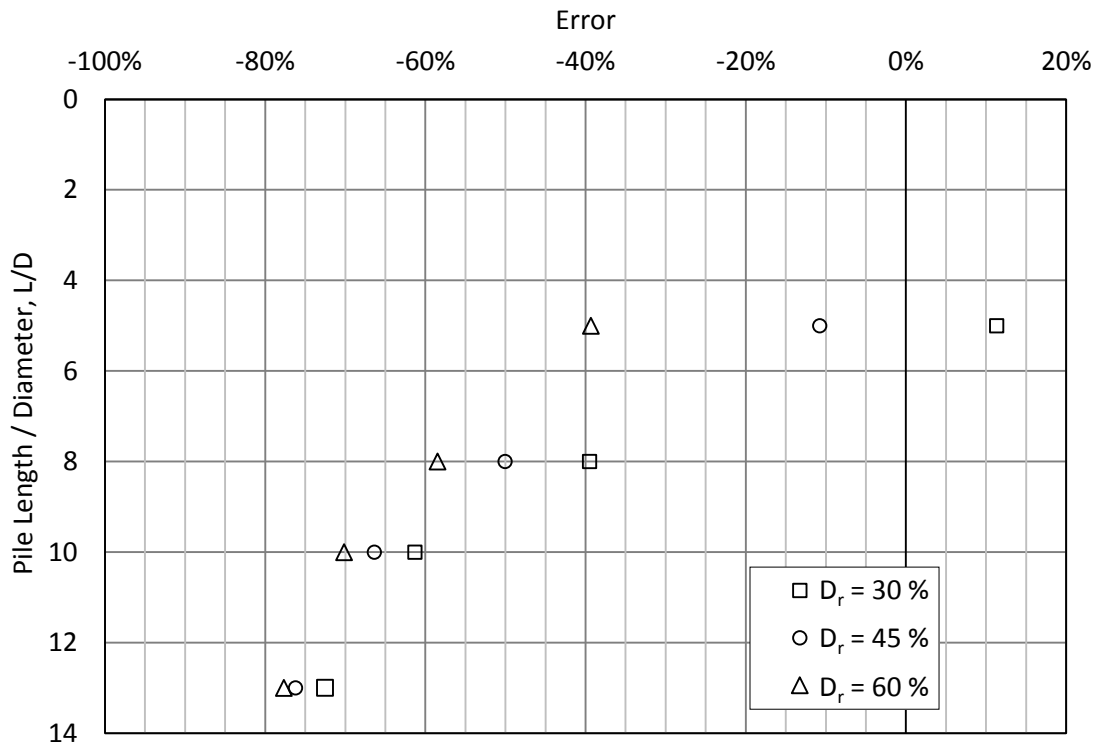


Figure 5-9: Difference between experimental and analytical shaft resistance

## Chapter 6 : Numerical Investigation

### 6.1 General

In the previous chapters, shaft resistance was determined for the pile model 55 mm in diameter at different relative densities and embedment depths, both experimentally in overconsolidated sand and analytically at normally consolidated sand. The values of  $\beta$  found for all case yielded two values: one for overconsolidated sand ( $OCR > 1$ ), the other for normally consolidated sand ( $OCR = 1$ ). Nevertheless, more data are needed to establish a reliable relationship between shaft resistance and the value of  $\beta$ . To that end, numerical analysis—an increasingly popular method in geotechnical engineering during the last two decades given the significant improvement of computer hardware and software (Kusakabe & Kobayashi, 2010)—was used to develop a three-dimensional numerical model for every pile load test performed experimentally using the pile model 55 mm in diameter. Those models were validated with the experimental results and used to determine the shaft resistance for various values of  $\beta$  at different relative densities and embedment depths.

Among the many commercial software programs currently available to develop two- and three-dimensional numerical models, popular ones for geotechnical studies include PLAXIS, FLAC, and ABAQUS. Although ABAQUS is a general-purpose software based on finite element (FE) analysis, it is widely used in modeling problems related to soil–structure interaction (Zhan et al., 2012). Thus, ABAQUS was used to develop a three-dimensional numerical model using the FE analysis, an effective method for scrutinizing piles in sand. To simulate a pile load test in ABAQUS, the constitutive model that governs the behaviour of the material, geometric, boundary, and initial conditions, as well as the model's discretization, should be specified.

## 6.2 Model Development

To describe the complex behaviour of soil in different loading conditions, several comprehensive constitutive models have been developed, among which the elasto-plastic Mohr–Coulomb constitutive model was adopted in the study conducted for this thesis. To solve geotechnical problems dealing with cohesionless soils, the Mohr–Coulomb model is widely applied in FE analysis due to its simplicity, sufficient accuracy, and minimal costs of computation (Zhan et al., 2012).

The Mohr–Coulomb model is an elastic, perfectly plastic model that combines Hooke’s law and the generalized form of Coulomb’s failure criterion. The chief soil parameters in the model are Young’s modulus ( $E$ ), Poisson’s ratio ( $\nu$ ), the internal friction angle ( $\phi'$ ), cohesion ( $c'$ ), and the dilation angle ( $\psi$ ). The first two parameters describe the elastic behaviour of soil, whereas the last three describe its plastic behaviour and yield.

Young’s modulus ( $E$ ) and Poisson’s ratio ( $\nu$ ) describe Hooke’s law of linear isotropic elasticity, the simplest stress–strain relationship of which is:

$$\sigma = E \varepsilon \quad (6-1)$$

where ( $\sigma$ ) is the normal stress, ( $E$ ) is the modulus of elasticity, and ( $\varepsilon$ ) is the normal strain.

For a cubic soil element (Figure 6-1), each side is subjected to three stress components: one of normal stress and two of shear stress.

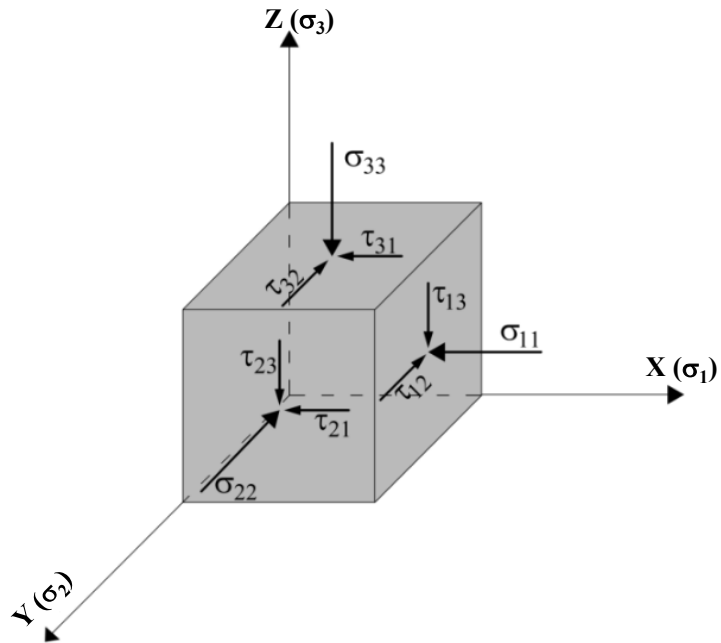


Figure 6-1 Stresses on a soil element in three-dimensional space

For the soil element presented in the previous figure, the following equations represent Hooke's law for a general stress condition.

$$\varepsilon_{11} = \frac{1}{E}(\sigma_{11} - \nu\sigma_{22} - \nu\sigma_{33})$$

$$\varepsilon_{22} = \frac{1}{E}(\sigma_{22} - \nu\sigma_{11} - \nu\sigma_{33})$$

$$\varepsilon_{33} = \frac{1}{E}(\sigma_{33} - \nu\sigma_{11} - \nu\sigma_{22})$$

(6-2)

$$\varepsilon_{12} = \frac{(1+\nu)}{E}\tau_{12}$$

$$\varepsilon_{23} = \frac{(1+\nu)}{E}\tau_{23}$$

$$\varepsilon_{31} = \frac{(1+\nu)}{E}\tau_{31}$$

where ( $\nu$ ) is Poisson's ratio, defined as:

$$\nu = \frac{\text{Lateral Strain}}{\text{Axial Strain}} = -\frac{\varepsilon_{22}}{\varepsilon_{11}} = -\frac{\varepsilon_{33}}{\varepsilon_{11}} \quad (6-3)$$

The previous strain equations along with Poisson's ratio can be presented in a matrix form as:

$$\begin{bmatrix} \varepsilon_{11} \\ \varepsilon_{22} \\ \varepsilon_{33} \\ \varepsilon_{12} \\ \varepsilon_{13} \\ \varepsilon_{23} \end{bmatrix} = \begin{bmatrix} 1/E & -\nu/E & \nu & 0 & 0 & 0 \\ -\nu/E & 1/E & -\nu/E & 0 & 0 & 0 \\ -\nu/E & -\nu/E & 1/E & 0 & 0 & 0 \\ 0 & 0 & 0 & 1/2G & 0 & 0 \\ 0 & 0 & 0 & 0 & 1/2G & 0 \\ 0 & 0 & 0 & 0 & 0 & 1/2G \end{bmatrix} \begin{bmatrix} \sigma_{11} \\ \sigma_{22} \\ \sigma_{33} \\ \tau_{12} \\ \tau_{13} \\ \tau_{23} \end{bmatrix} \quad (6-4)$$

Knowing that shear strain, presented in Equation 6.5, is a function of the modulus of elasticity (E) and Poisson's ratio ( $\nu$ ), Equation 6.4 can be inverted to determine three-dimensional stresses, as shown in Equation 6.6:

$$G = \frac{E}{2(1+\nu)} \quad (6-5)$$

$$\begin{bmatrix} \sigma_{11} \\ \sigma_{22} \\ \sigma_{33} \\ \tau_{12} \\ \tau_{13} \\ \tau_{23} \end{bmatrix} = \frac{E}{(1+\nu)(1-2\nu)} \begin{bmatrix} 1-\nu & \nu & \nu & 0 & 0 & 0 \\ \nu & 1-\nu & \nu & 0 & 0 & 0 \\ \nu & \nu & 1-\nu & 0 & 0 & 0 \\ 0 & 0 & 0 & 1-2\nu & 0 & 0 \\ 0 & 0 & 0 & 0 & 1-2\nu & 0 \\ 0 & 0 & 0 & 0 & 0 & 1-2\nu \end{bmatrix} \begin{bmatrix} \varepsilon_{11} \\ \varepsilon_{22} \\ \varepsilon_{33} \\ \varepsilon_{12} \\ \varepsilon_{13} \\ \varepsilon_{23} \end{bmatrix} \quad (6-6)$$

The plastic behaviour of the soil, which indicates a permanent deformation of soil particles, is more dominant than its elastic behaviour. Thus, in the Mohr–Coulomb model, plastic behaviour depends upon two parameters from Coulomb's failure criterion: the friction angle ( $\phi'$ ) and cohesion ( $c'$ ), and the dilation angle ( $\psi$ ). The latter parameter derives from an unassociated flow rule, which helps to realistically describe the irreversible change in volume due to shearing (Brinkgreve, 2005).

The failure or yield in the Mohr–Coulomb criterion occurs when the shear stress reaches the failure envelope, which depends upon the normal stress in a linear relationship. Figure 6-2 depicts the Mohr–Coulomb yield model, in which the failure envelope is the best straight line that touches the Mohr circles.

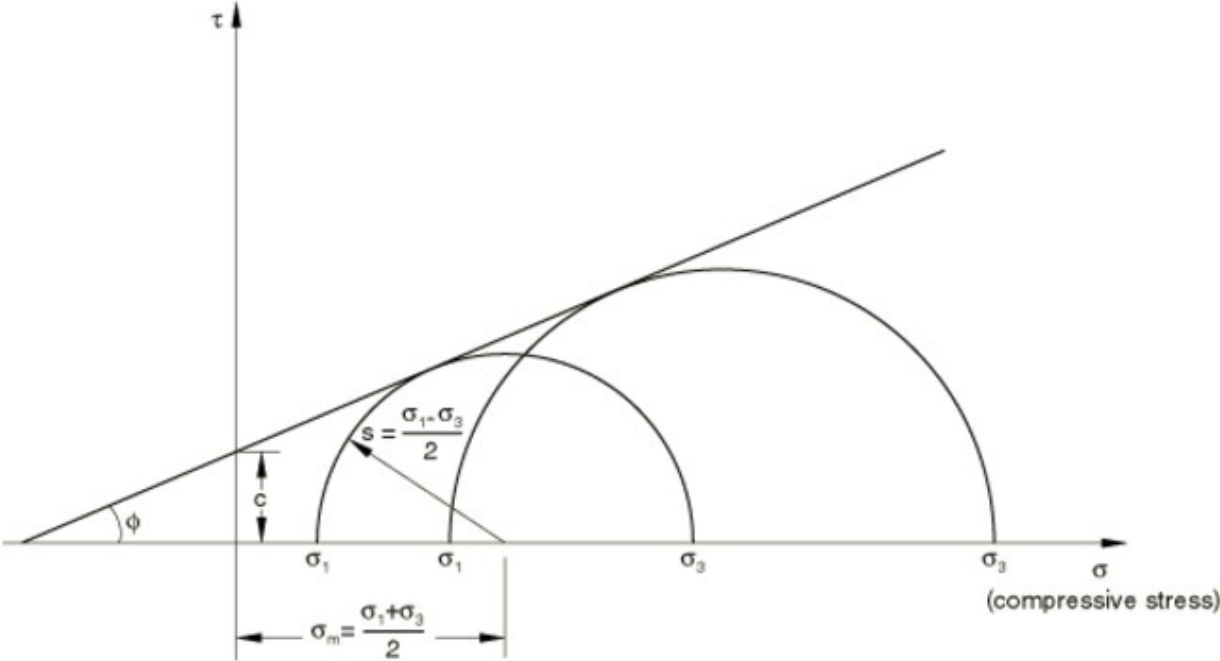


Figure 6-2: Mohr-Coulomb yield model (Hibbitt et al., 2016)

The lateral earth pressure coefficient was introduced into the model via a feature in ABAQUS. For the pile material, an elastic model was adopted that depends upon Hooke’s law, the chief parameters of which are Young’s modulus (E) and Poisson’s ratio ( $\nu$ ).

The dimensions of the setup for the experimental pile load tests were duplicated in ABAQUS. The soil had an area of  $1\text{ m} \times 1\text{ m}$  and a height of  $1.2\text{ m}$ , and the pile was  $55\text{ mm}$  in diameter with various heights— $275\text{ mm}$ ,  $440\text{ mm}$ ,  $550\text{ mm}$ , and  $715\text{ mm}$ —as in the experimental tests.

To be able to apply different lateral earth pressure coefficients, the soil was divided into five layers. The soil around the pile was divided into three layers according to the heights of the pile sections determined experimentally. Underneath the pile tip was a layer of height 5 times the diameter, followed by the last layer with a remaining height of the total tank height. Figure 6-3 depicts the soil layers for the numerical model built for the pile at a depth of  $550\text{ mm}$ .

Tank dimensions in the analysis were fixed in all models. Pressure exerted on the sides of the tank up to reaching ultimate load were determined to assess the boundary effect and ensure the validity of the experimental results.

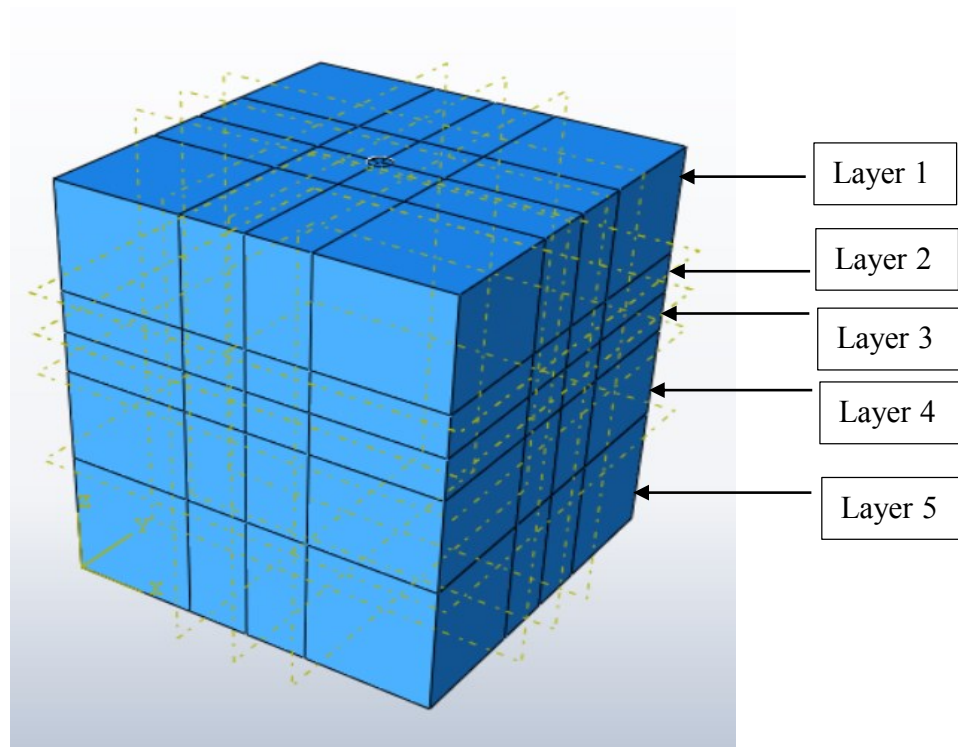


Figure 6-3: Soil layers in model built for pile at  $550\text{ mm}$  depth

The boundary condition is a major point in FE analysis. To simulate the experimental tests, the bottom side of the sand was fixed in all directions (i.e., X, Y, and Z), whereas the vertical sides were fixed at the axis perpendicular to the side to prevent horizontal displacement (Khodair & Abdel-Mohti, 2014). Figure 6-4 depicts the boundary conditions used in all of the models.

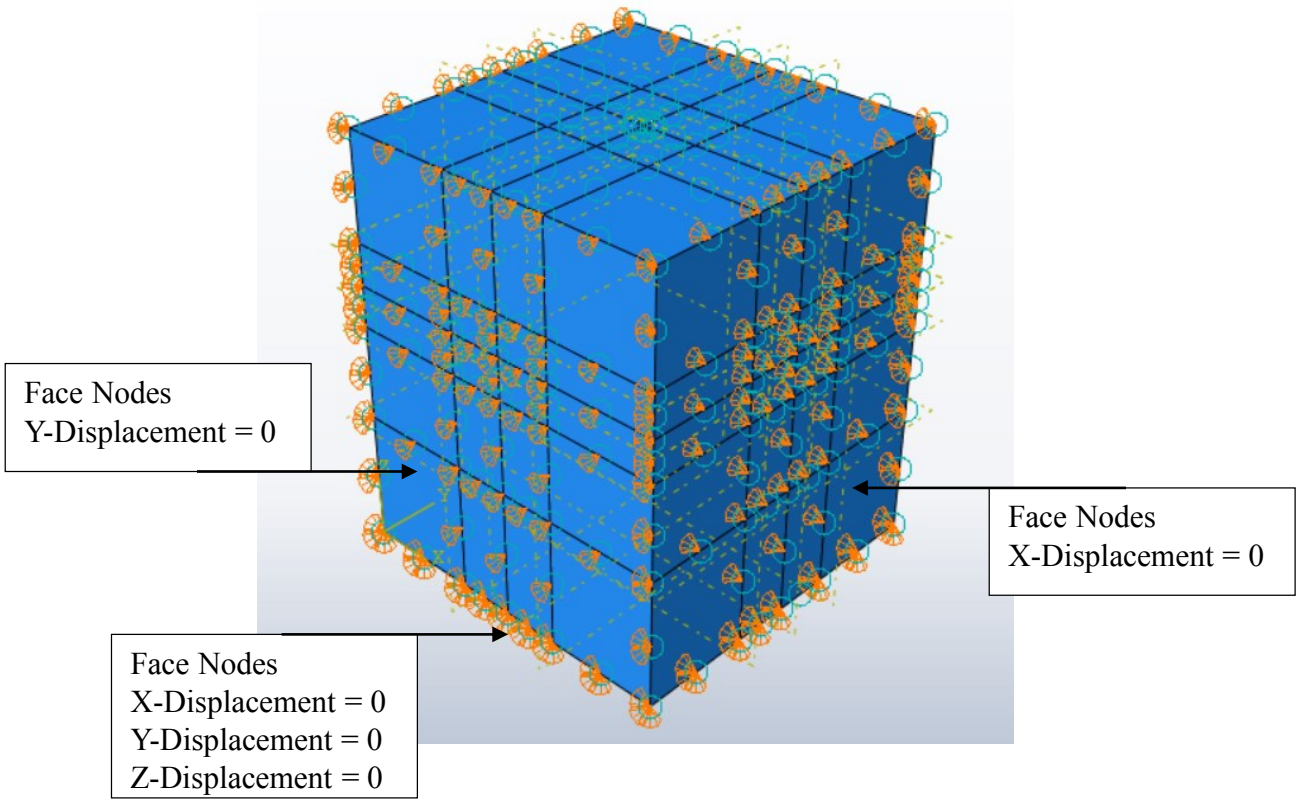


Figure 6-4: Boundary conditions

ABAQUS provides different types of elements, including beams, shells, and continuum (e.g., solid and fluid), the selection of which depends upon the nature of the problem being investigated. In the model reported here, solid elements were chosen for both the soil and pile for three-dimensional FE analysis. For solid elements, ABAQUS provides tetrahedra, triangular wedges, and hexahedra, among others (Figure 6-5).

The 8-nodal hexahedral element was deemed more accurate than the 4-nodal tetrahedral and 6-nodal wedge elements to analyze the problem at hand, as well as poses the least computing cost. To generate a hexahedral element, five tetrahedral elements are required, the first-order type of which needs a number of nodes that increases from 4 to 20, as well as two triangular wedge elements, the first-order type of which needs a number of nodes that increases from 6 to 12.

Because a higher-order element increases the number of nodes exponentially, selecting the first-order 8-nodal hexahedral element is more reasonable than the other two since the computing cost relates directly to the number of nodes. Moreover, the 8-nodal hexahedral element reduces the number of elements during discretization, which in turn reduces error unlike the other two types of elements. Last, the 8-nodal hexahedral element is easier to visualize than the other two types of elements (Hibbitt et al., 2016). Therefore, an 8-nodal hexahedral element was selected to perform the analysis.

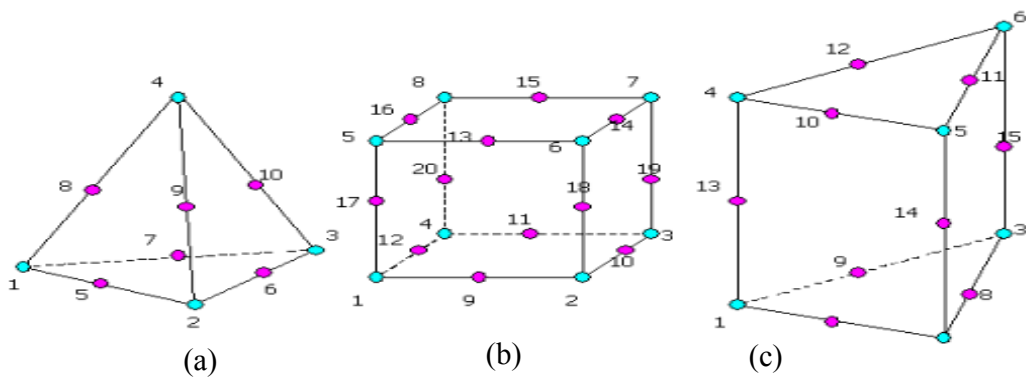


Figure 6-5: Solid elements: (a) tetrahedron, (b) hexahedra, (c) triangular wedge.

Mesh size influences stresses obtained from ABAQUS. Although the smaller the element size, the more accurate the results, reducing the element size increases the number of elements, which in turn increases the number of nodes and thus the computing cost. To obtain accurate results with the least computing cost, finer elements were strategically maintained in the vicinity of the pile and coarser elements at a further distance from the pile.

Shalabi and Bader (2014) experimentally studied the effect of pile driving on the densification of sand around a pile. Their results revealed that the horizontal movement of sand corresponding to the process of pile driving extended to nearly 3 times the pile's diameter. Accordingly, the mesh at a distance 3 times the diameter (3D) around the pile needed to be densified.

To that end, the partition technique was used to densify the mesh around the pile and steadily increase the size as the distance from the pile increased. Outside the 3D zone, the size of the elements increased while a fixed base was used to discretize the soil. The size of the element in the 3D zone, outside the 3D zone, and along the Z direction was selected according to mesh analysis. Figure 6-6 illustrates the mesh used in a model built for the pile embedment depth of 550 mm ( $L / D = 10$ ).

The analysis of soil–structure contact problems involves geometry, interface stress conditions, and the development of algorithms (Wriggers, 1995). Among the many concepts available to simulate the interaction of a pile and soil material, including the p–y spring (i.e., Winkler spring), the zero thickness interface element, the thin layer interface element, and the master–slave concept, ABAQUS adopts the master–slave concept, which is widely used for its ability to simulate contact behaviour. In applying the concept, the mechanical contact properties in ABAQUS are defined to control the tangential and normal stress components in the contact area. The surface-to-surface contact option is preferred over the node-to-surface option in pile–soil interaction problems because it is more accurate and prevents large penetrations of the two surfaces during contact (Hibbitt et al., 2016).

In using the master–slave approach, one of the surfaces should be set as the master surface—ideally the one with higher stiffness—and the other as the slave surface. In the study reported here, the pile surface was the master and the soil surface was the slave. Surface-to-surface contact connected the nodes on the master surface (i.e., the pile) to the face of the slave surface (i.e., the soil) so that each node on the latter experienced the same motion as the closest point on the former (Khodair & Abdel-Mohti, 2014; Vakili, 2015).

Thereafter, the mechanical contact feature in ABAQUS was used to define the normal and tangential interactions of the pile and the soil. Normal interaction was defined as hard contact, whereas the frictional coefficient for tangential interaction was defined as  $\tan\delta = \tan\phi'$ .

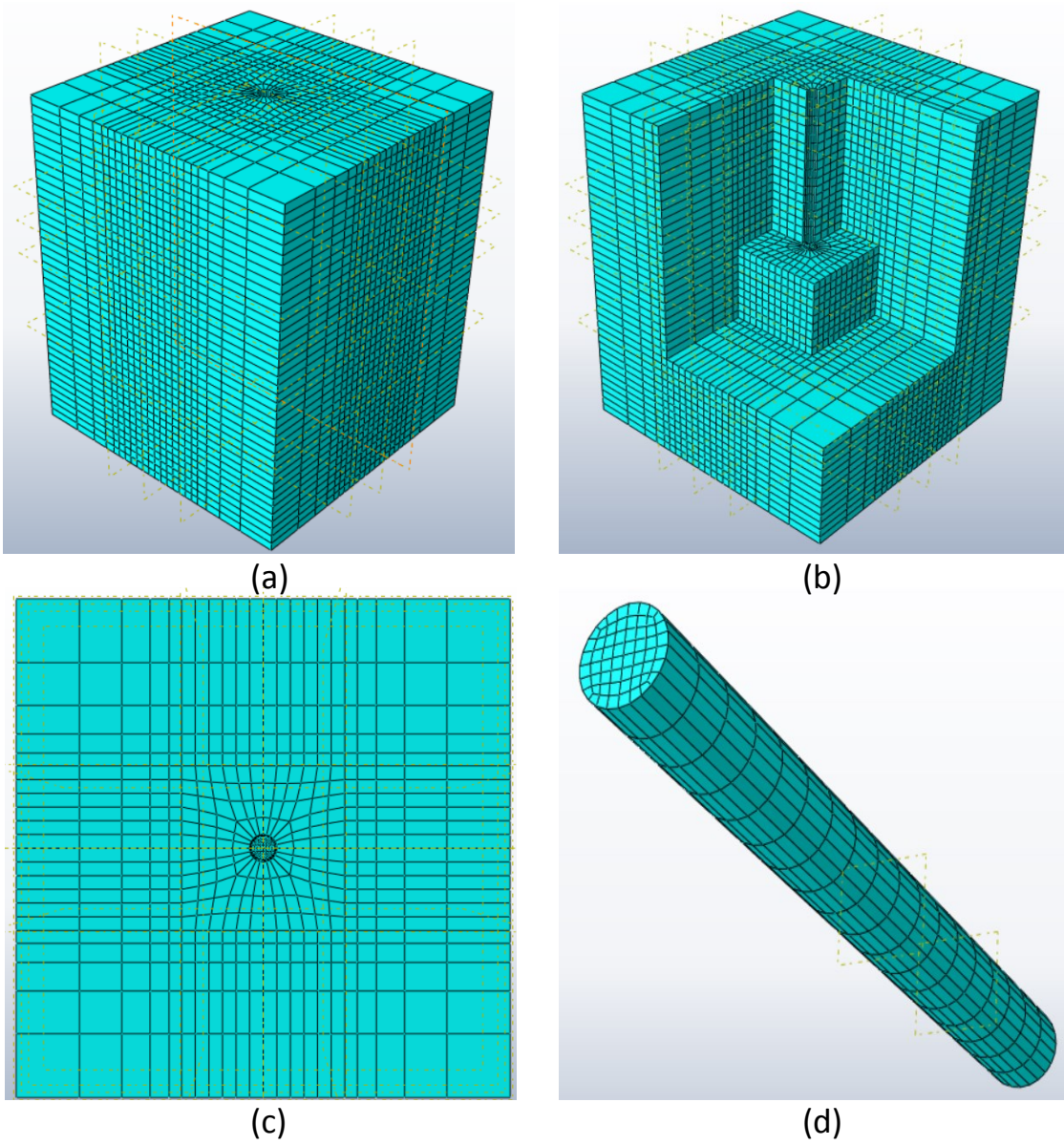


Figure 6-6: (a) Model mesh, (b) inside elements, (c) top view of the model, and (d) pile mesh

Several FE analyses were performed to examine the effect of mesh size (i.e., number of elements) on shaft and tip resistance. The mesh size was altered in every analysis, whereas the material properties were maintained. Shaft and tip resistance was determined for all analyses and compared. To study the influence of mesh size and reduce the number of elements, the soil was divided into two zones horizontally: inside the 3D zone and outside the 3D zone (Figure 6-7).

Because the inside zone, which was a square around the pile 6D long, was more critical in the analysis than the outside zone, the mesh size in the square around the pile was set to be smaller than the zone outside the square. Several numerical trials (Table 6-1, Figure 6-8) revealed that having five elements in the horizontal directions (i.e., X and Y) outside the square zone around the pile with a base of 5 was justified, whereas having 12 elements in both directions was justified inside the square around the pile (Figure 6-9).

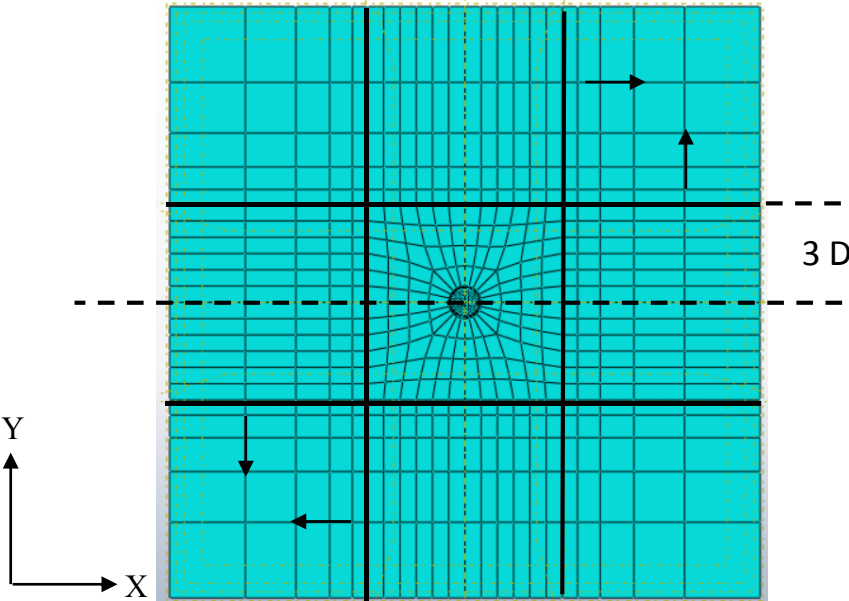


Figure 6-7: Top view of the model for 3D zone mesh size illustration

Table 6-1: Mesh analysis for X and Y directions

Location	Base	Number of element	Length (mm)	Shaft Resistance (N)	Tip Resistance (N)
Outside of 3D Zone	5	4	31.50	689.05	3001.25
	5	5	25.62	688.62	3001.35
	5	6	21.56	688.36	2945.68
Inside the 3D Zone	N/A	6	55.00	688.62	3001.35
	N/A	10	33.00	689.33	3005.55
	N/A	12	27.00	690.19	3008.65

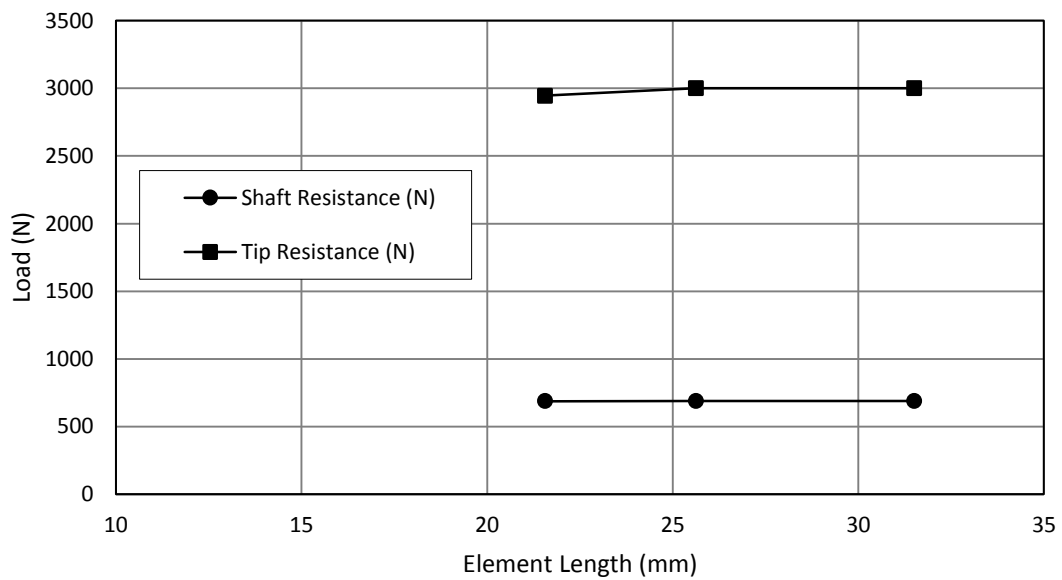


Figure 6-8: Influence of the element size outside the 3D zone on the pile capacity

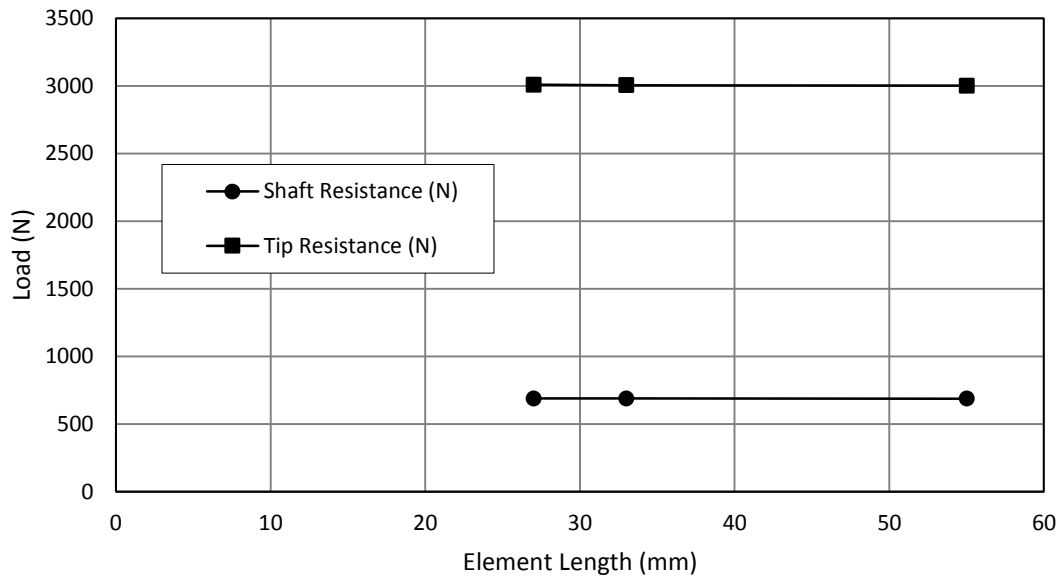


Figure 6-9: Influence of the element size inside the 3D zone on the pile capacity

To study the influence of vertical element length, the soil was divided into two parts (Figure 6-10). The first part encompassed the soil around the pile shaft, in which several numerical trials were performed to test different element lengths (Table 6-2, Figure 6-11). It was determined that having 20 elements was justified for the first part in the Z direction. The second part was the soil underneath the pile tip, for which the justified number of elements in the Z direction was 22 (Figure 6-12). As Table 6-1 and Table 6-2 show, shaft resistance was nearly the same at different element sizes, which corroborated the use of the numerical model to study shear stress.

In sum, the total number of nodes and elements in the numerical model was 23,162 and 21,280, respectively, for the pile with a diameter of 55 mm at a depth of 550 mm ( $L / D = 10$ ). Although the number of nodes and elements differed when the length of the pile changed, the same ratios and element lengths found in sensitivity analysis were used in all numerical models.

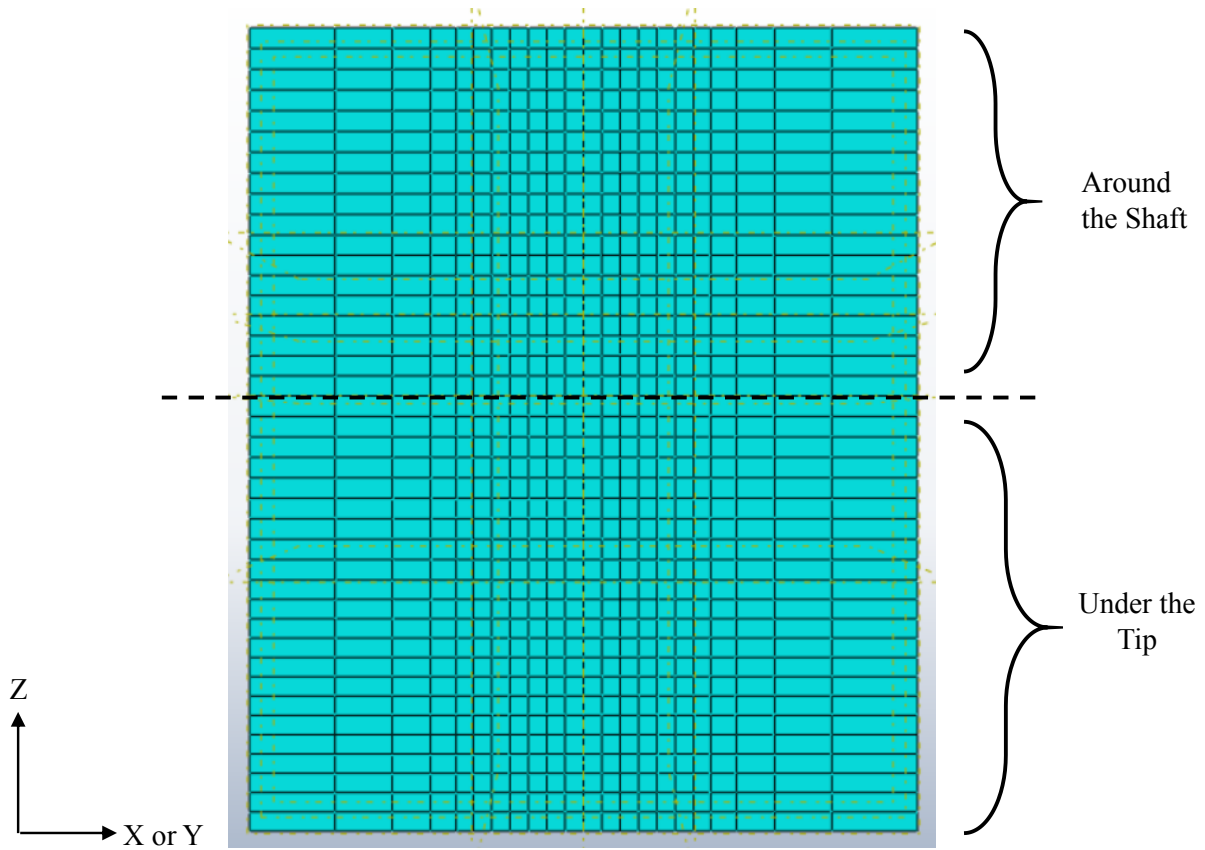


Figure 6-10: Side view of the model for mesh size illustration at Z direction

Table 6-2: Mesh analysis for Z directions

Location	Size	Number of element	Length (mm)	Shaft Resistance (N)	Tip Resistance (N)
Z direction (around Shaft)	40	14	39.28	698.34	2981.54
	30	20	27.50	690.19	3008.65
	25	22	25.00	689.17	3009.47
Z direction (under Tip)	50	14	46.42	691.35	3070.40
	40	16	40.60	689.46	3015.01
	30	22	29.54	690.19	3008.65

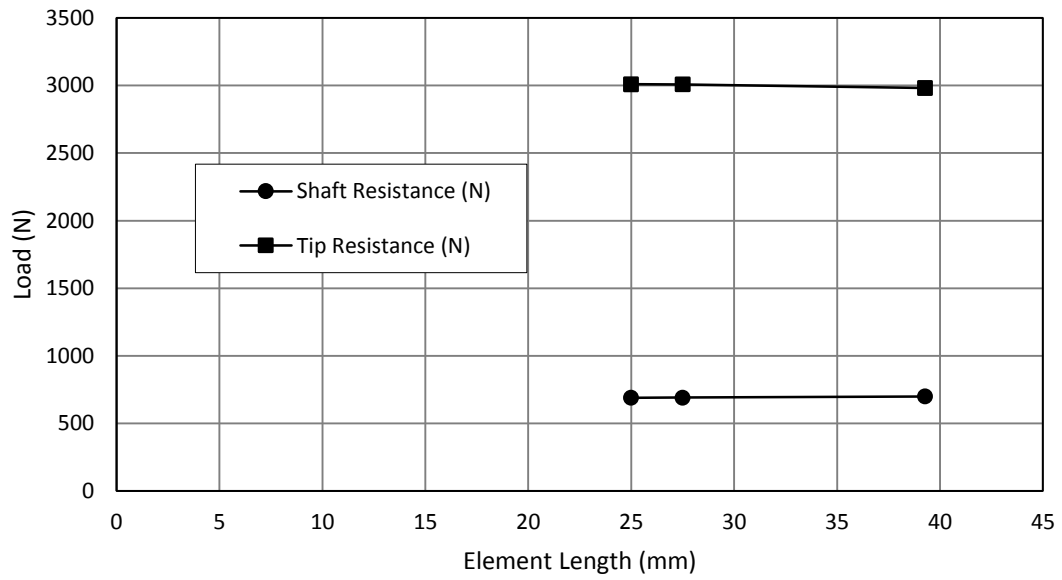


Figure 6-11: Influence of the element size on the pile capacity for Z direction around the pile shaft

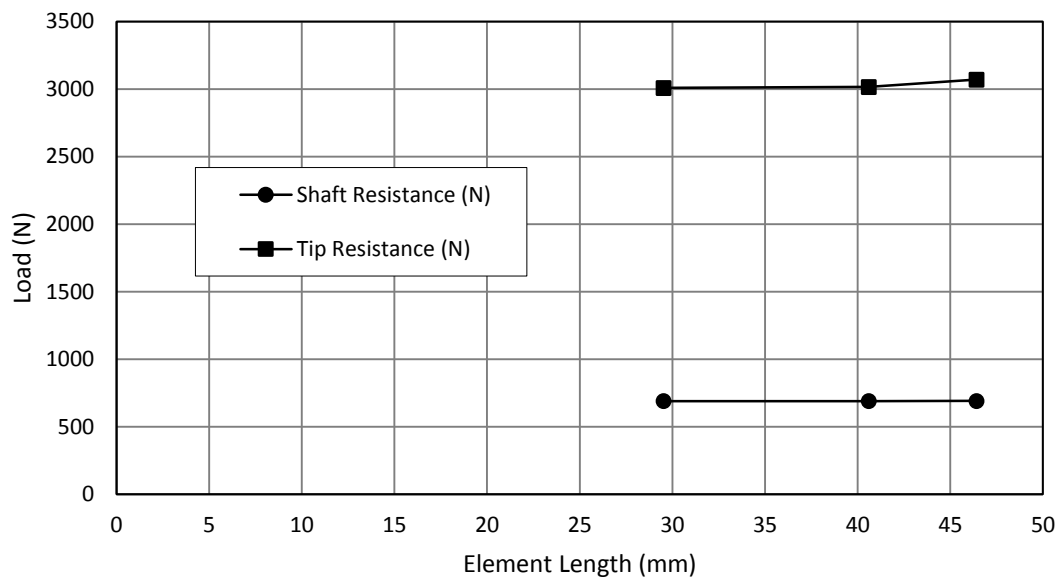


Figure 6-12: Influence of the element size on the pile capacity for Z direction underneath the pile tip

### 6.3 Model Validation

All pile load tests performed experimentally using the pile model 55 mm in diameter at 30%, 45%, and 60% relative densities were used to validate the model. The same parameters used and back-calculated in the experimental analysis for those pile load tests, including soil density ( $\rho$ ), angle of shearing resistance ( $\phi'$ ), and overburden pressure ( $\sigma_v$ ), were used in the numerical model. Validation was performed twice. In the first validation, a different lateral earth pressure coefficient ( $K_s$ ) was used for each soil layer (Figure 6-3), which was back-calculated according to the shaft resistance for each section of the pile. In the second validation, the  $K_s$  value was introduced as a mean value that was back-calculated from the total shaft of the pile.

Other parameters estimated from known correlations included the modulus of elasticity ( $E$ ), the dilation angle ( $\psi$ ), and Poisson's ratio ( $\nu$ ). Cohesion ( $c'$ ) was assigned a relatively high value because the tested soil was overconsolidated cohesionless soil, which shows apparent cohesion when tested in triaxial tests (Lambe & Whitman, 1969). Furthermore, because the numerical model encounters numerous convergence problems that prematurely terminate analysis when cohesion is not introduced or assigned a value that is too small, a value of 0.02 MPa was determined to be convenient to validate and use in the numerical model.

The modulus of elasticity ( $E$ ) was estimated according to Equation 6.7 (Coduto, 2001), which is a function of the OCR, the  $N_{60}$  value, and two empirical factors. The  $N_{60}$  value, which is the corrected blow count of the standard penetration count, was calculated according to Equation 6.8 as a function of  $\phi'$  and the angle of shearing resistance (Bowles, 2002). The two empirical factors were related to the type of soil (Table 6-3). The dilation angle ( $\psi$ ) was calculated according to Bolton's (1986) findings (Eq. 6.9). The value of Poisson's ratio ( $\nu$ ) has varied from 0.1 to 0.3 for loose sands and from 0.3 to 0.4 for dense sands (Hanna & Al-Romhein, 2008).

$$E_s = \beta_0 \sqrt{OCR} + \beta_1 N_{60} \quad (6-7)$$

$$\phi' = \sqrt{20 N_{60}} + 20 \quad (6-8)$$

$$\psi = (\phi' - 33) \quad (6-9)$$

Table 6-3: Factors for Eq.6-7 after (Coduto, 2001)

Soil Type	$\beta_0$ (kPa)	$\beta_1$ (kPa)
Clean Sand (SW and SP)	5000	1200
Silty Sand and clayey sand (SM and SC)	2500	600

The soil and pile properties used in the validation are summarized in Table 6-4. To use ABAQUS to simulate a pile load test, the lateral earth pressure coefficient ( $K_s$ ) should be introduced into the model. The pile capacity was determined twice, first by introducing  $K_s$  values found experimentally for every soil layer. The  $K_s$  values were introduced into the first three layers in the numerical model according to the back-calculated values from the experiment; the layer underneath the tip was assumed to have the same value as the third layer; and the  $K_s$  value for the last layer was set as the initial  $K_0$  value. In the second validation, mean  $K_s$  values were used for the first four layers of soil.

Table 6-4: Material properties

Parameter	Soil			Pile	Unit
$D_r$ , Relative density	30	45	60	-	(%)
E, Modulus of elasticity	18	22	26.3	200,000	MPa
$\rho$ , Density	1.51E-06	1.56E-06	1.60E-06	7.50E-05	Kg/mm <sup>3</sup>
$\nu$ , Poisson's ratio	0.25	0.27	0.3	0.3	-
$\psi$ , Dilation angle	0	1.9	3.85	-	degree
$\phi'$ , Angle of shearing resistance	33	34.9	36.85	-	degree

The first step in analysis was geostatic, in which initial stresses were specified according to the soil unit weight. ABAQUS uses those values as initial values in the process of convergence during analysis because initial stresses exert considerable impact on subsequent steps. Deviation of those stresses from actual events would result in incorrect soil displacements in the model, which would in turn cause instabilities, at which point analysis would end. As shown in Figure 6-13, the numerical vertical stress matched the theoretical vertical stress ( $\gamma H$ ).

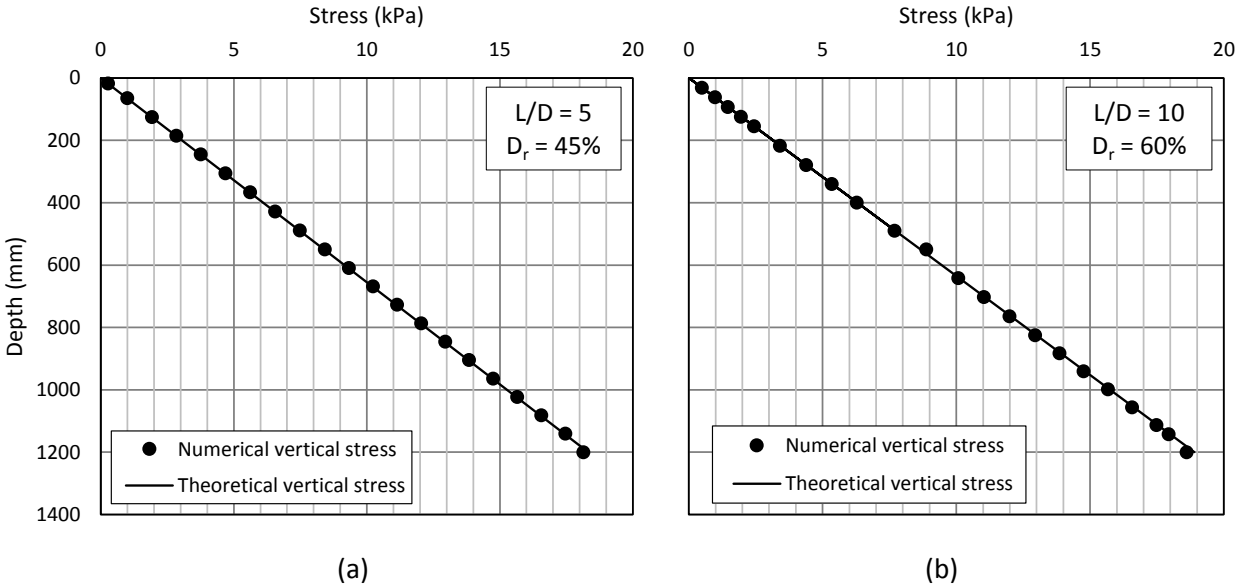


Figure 6-13: Geostatic analysis for (a)  $D_r = 45\%$  and  $L/D = 5$ , (b)  $D_r = 60\%$  and  $L/D = 10$

The second step in analysis was the pile load test, in which the pile was displaced 20 mm downward as in the experimental test. The total applied load to displace the pile for the specified distance was determined, as was total shear stress along the sides of the pile. Tip resistance was calculated by subtracting shaft resistance from total resistance.

Figure 6-14 illustrates typical load–settlement curve results for pile load test performed at 550 mm at various embedment depths and 45% relative density. The tangential method, which was used to define the failure experimentally, was also used to interpret the numerical results and determine ultimate load (i.e., failure). According to the ultimate load of the total pile resistance, tip and shaft resistance were found. The stress distribution at failure appears in Figure 6-15.

Values of total resistance, tip resistance, and shaft resistance were found and compared to the experimental results, as presented in Table 6-5 and Table 6-6, for the first validation (i.e., with different  $K_s$  values throughout the layers) and the second validation (i.e., with the mean  $K_s$  value), respectively. Shaft resistance found using different values of  $K_s$  deviated from experimental results mostly by  $\pm 10\%$ , whereas deviation was mostly  $\pm 14\%$  when the mean value of  $K_s$  was used. Obtaining an acceptable level of confidence on the numerical simulation by the experimental results, the subsequent stages of analysis can be trusted.

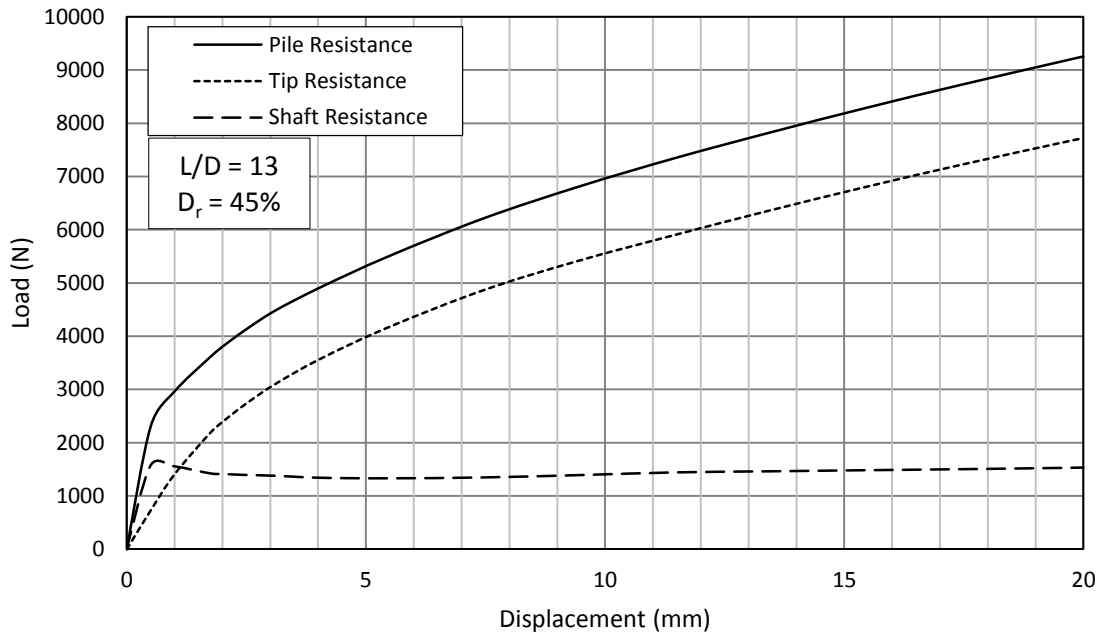


Figure 6-14: Results of the numerical pile load test for (C-55-45%-13)

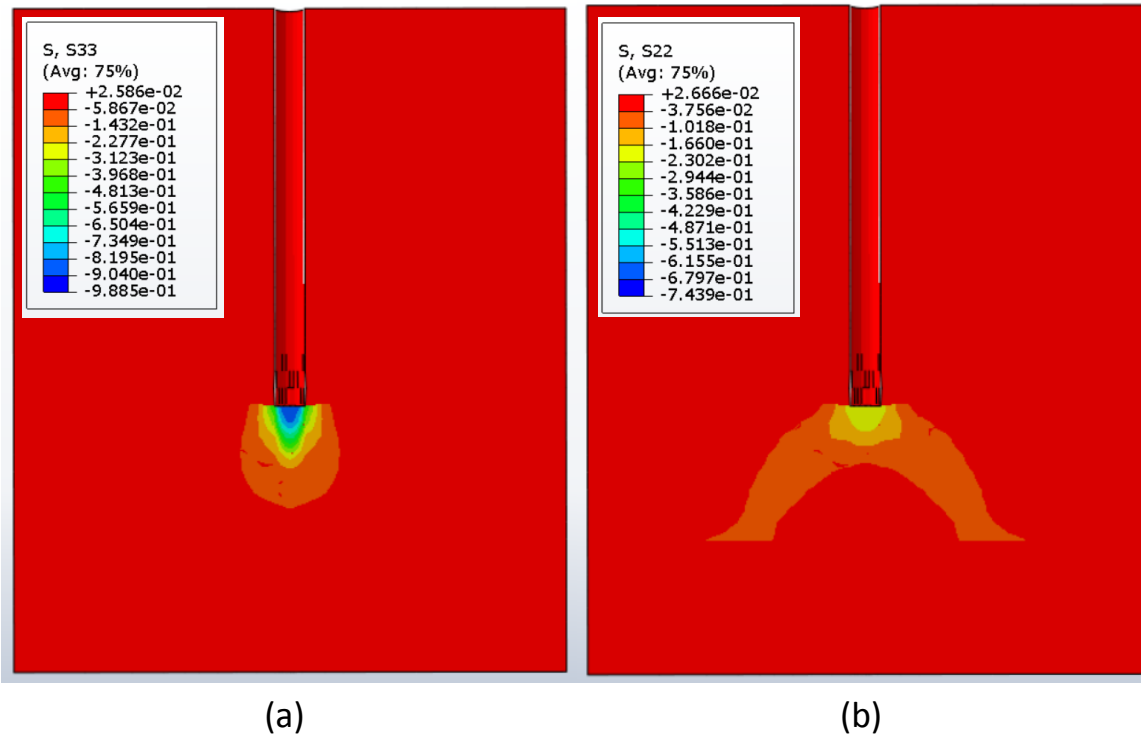


Figure 6-15: Stress distribution at failure (a) vertical, (b) lateral

Table 6-5: Numerical results and comparison with experimental results using different  $K_s$  values

L/D	$D_r$ (%)	Numerical Result			Error		
		Total Resistance (N)	Tip Resistance (N)	Shaft Resistance (N)	Total Resistance (%)	Tip Resistance (%)	Shaft Resistance (%)
5	30	1021.19	927.56	93.63	-8.4%	-9.2%	-0.3%
8		2271.81	1899.30	372.51	1.5%	0.0%	10.1%
10		3374.27	2728.96	645.32	-0.1%	0.6%	-2.7%
13		4426.96	3268.07	1158.89	-6.8%	-8.7%	-1.1%
5	45	1688.45	1558.18	130.27	-12.1%	-13.5%	9.5%
8		3330.74	2863.86	466.88	-0.8%	-2.4%	10.0%
10		4527.08	3764.88	762.20	0.1%	1.2%	-5.2%
13		5142.32	3806.87	1335.45	-17.2%	-20.2%	-7.0%
5	60	2668.53	2491.72	176.81	0.7%	0.9%	-0.5%
8		4550.98	4007.08	543.91	0.5%	0.6%	-0.6%
10		6056.78	5159.87	896.91	0.0%	1.9%	-10.0%
13		7327.81	5810.09	1517.71	-11.0%	-12.0%	-7.0%

Table 6-6: Numerical results and comparison with experimental results using an average  $K_s$  values

L/D	$D_r$ (%)	Numerical Result			Error		
		Total Resistance (N)	Tip Resistance (N)	Shaft Resistance (N)	Total Resistance (%)	Tip Resistance (%)	Shaft Resistance (%)
5	30	1278.82	1181.59	97.23	14.7%	15.7%	3.5%
8		2299.41	2009.82	289.59	2.7%	5.8%	-14.4%
10		3331.39	2709.22	622.17	-1.3%	-0.1%	-6.2%
13		4407.66	3312.07	1095.60	-7.2%	-7.5%	-6.5%
5	45	2234.37	2113.30	121.07	16.3%	17.3%	1.8%
8		3447.63	3035.87	411.76	2.7%	3.5%	-3.0%
10		4522.90	3798.47	724.43	0.0%	2.1%	-9.9%
13		5422.89	4117.61	1305.28	-12.7%	-13.7%	-9.1%
5	60	2461.63	2306.68	154.95	-7.1%	-6.6%	-12.8%
8		4729.44	4243.74	485.70	4.4%	6.5%	-11.3%
10		5556.58	4644.88	911.70	-8.3%	-8.2%	-8.5%
13		7258.43	5787.99	1470.43	-11.8%	-12.3%	-9.9%

Lateral earth pressure exerted on the sides of the tank was measured before the pile load test (i.e., after the geostatic step) and at ultimate load to assess whether any boundary effects from the sides of the tank had occurred. Vertical stresses on all elements from the pile's tip to the bottom of the tank were also measured before starting the pile load test and at ultimate load to assess the effect of the bottom side on the tip results. Results presented in Figure 6-16 are typical of pile load tests performed at embedment depths of 440 mm and 550 mm at 45% and 60% relative densities, respectively. No change in those stresses occurred on the tank boundary, which reflects the reliability of the experimental results.

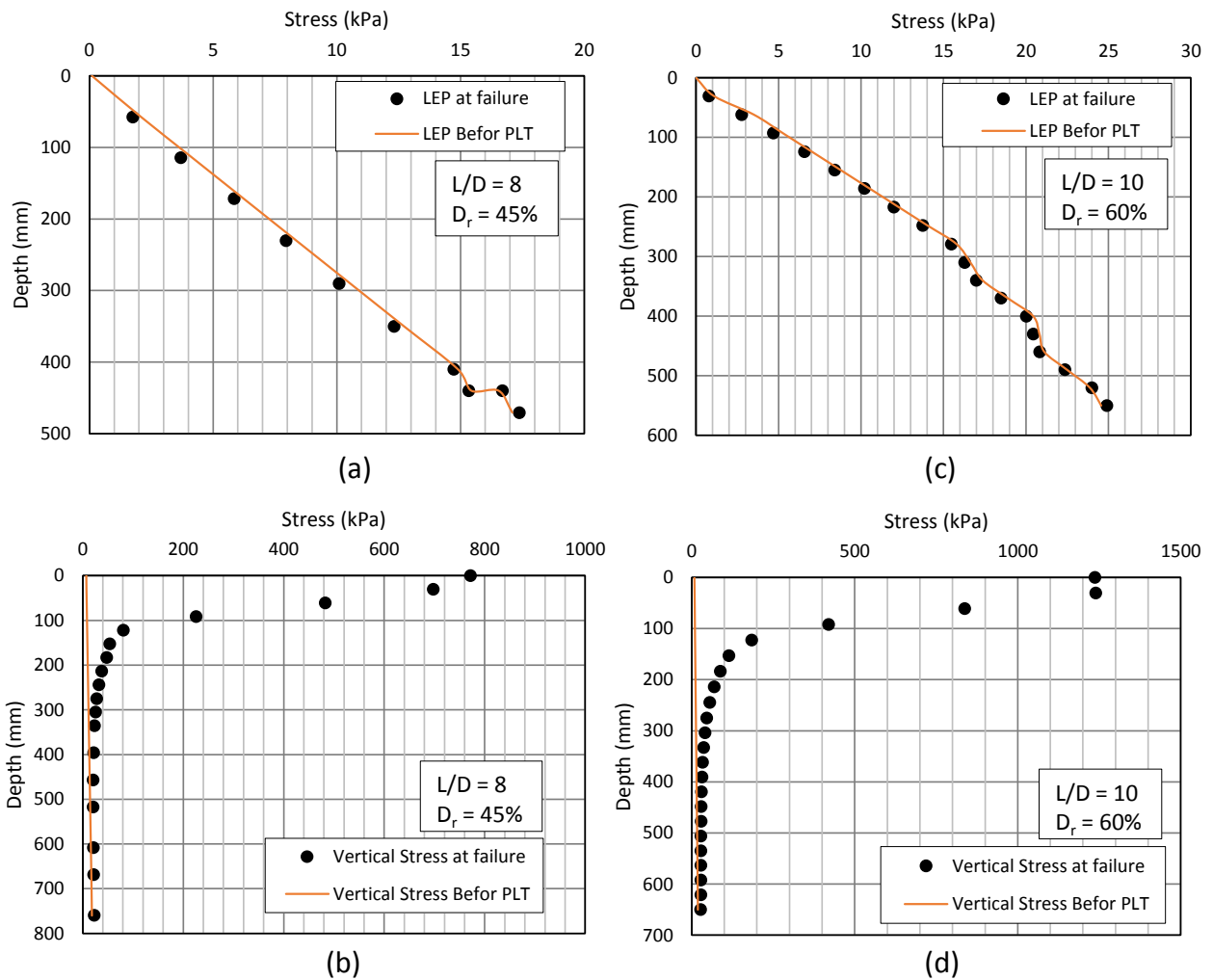


Figure 6-16: Stresses before pile load test and at ultimate load on (a & c) the tank sides, and on (b & d) the bottom of the tank.

## 6.4 Pile Load Tests

The numerical models developed were used to perform 200 pile load tests at different embedment depths and with different soil properties to examine the effect of  $\beta$  ( $\beta = K_s \tan\delta$ ) on shaft resistance. Five different soils were used in this study. The soil properties were altered according to the procedure explained in the previous sections. The variation of the modulus of elasticity with the angle of shearing

resistance was found by using Equation 6.7 (Figure 6-17). The value of Poisson's ratio was selected according to relative density, in relation to which it has varied from 0.1 to 0.3 for loose sands and from 0.3 to 0.4 for dense sands (Hanna & Al-Romhein, 2008). The dilation angle was calculated according to Equation 6.9 (Bolton, 1986). The soil properties used, which reflect the properties of the sand used experimentally, are summarized in Table 6-7.

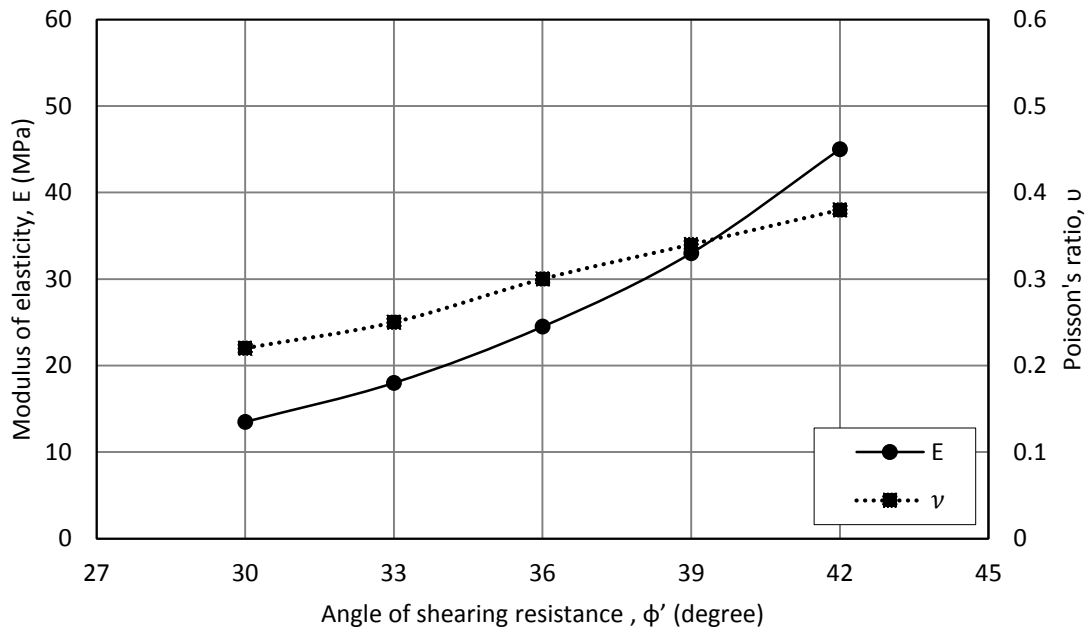


Figure 6-17: Variation of modulus of elasticity and Poisson's ratio with angle of shearing resistance

Table 6-7: Soil properties of the sand used for pile load test

Parameter	Soil 1	Soil 2	Soil 3	Soil 4	Soil 5	Unit
$\phi'$ , Angle of shearing resistance	30	33	36	39	42	degree
E, modulus of elasticity	13.5	18	24.5	33	45	MPa
$\rho$ , Density	1.44E-06	1.51E-06	1.58E-06	1.66E-06	1.73E-06	kg/mm <sup>3</sup>
$\nu$ , Poisson's ratio	0.22	0.25	0.3	0.34	0.38	
$\psi$ , Dilation angle	0	0	3	6	9	degree

The variation of shaft resistance for the pile tested at an embedment depth ratio ( $L / D$ ) of 8 appears in Table 6-8 and Figure 6-18.

Table 6-8: Shaft resistance with variable values of  $\beta$  for embedment depth ratio ( $L/D$ ) of 5

L/D	Test No	$\beta$	Shaft Resistance (N)				
			$\phi'$ (degree)	$\phi'$ (degree)	$\phi'$ (degree)	$\phi'$ (degree)	$\phi'$ (degree)
			30	33	36	39	42
10	1	0.5	81.59	81.48	89.26	91.17	100.53
	2	1	110.85	112.83	114.03	120.74	127.32
	3	1.5	139.16	140.56	144.97	158.45	171.24
	4	2	171.32	174.76	182.60	186.60	225.93
	5	2.5	207.68	208.03	220.60	231.53	246.31
	6	3	219.76	220.39	232.16	250.29	277.52
	7	3.5	246.52	259.18	274.53	300.75	341.51
	8	4	284.89	288.84	311.48	346.39	367.94
	9	4.5	305.56	318.12	355.62	383.13	438.41
	10	5	359.54	361.94	372.23	411.17	493.97

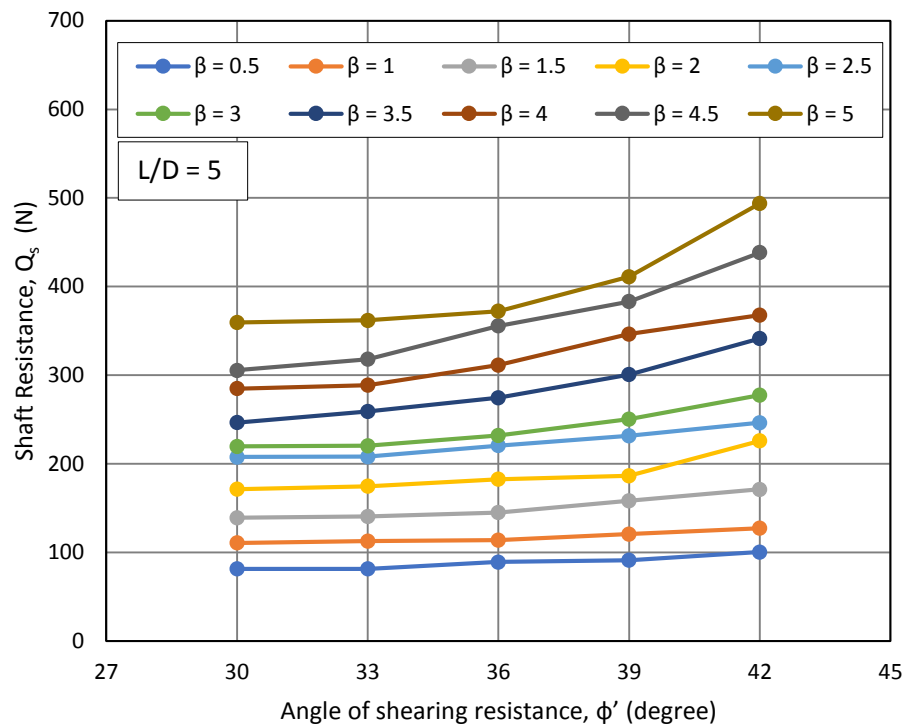


Figure 6-18: Shaft resistance with variable values of  $\beta$  for embedment depth ratio ( $L/D$ ) of 5

The variation of shaft resistance for the pile tested at an embedment depth ratio ( $L / D$ ) of 8 appears in Table 6-9 and Figure 6-19.

Table 6-9: Shaft resistance with variable values of  $\beta$  for embedment depth ratio ( $L/D$ ) of 8

L/D	Test No	$\beta$	Shaft Resistance (N)				
			$\phi'$ (degree)	$\phi'$ (degree)	$\phi'$ (degree)	$\phi'$ (degree)	$\phi'$ (degree)
			30	33	36	39	42
10	1	0.5	203.25	208.96	213.81	224.43	248.81
	2	1	282.80	305.85	315.79	343.65	383.30
	3	1.5	398.24	405.16	402.38	460.90	491.51
	4	2	471.80	499.64	532.43	582.45	608.84
	5	2.5	584.97	599.82	640.59	694.66	692.39
	6	3	703.80	712.03	738.27	799.62	811.86
	7	3.5	789.90	799.09	829.79	884.92	928.48
	8	4	897.46	923.35	953.16	1004.55	1119.37
	9	4.5	1061.15	1059.32	1072.48	1117.42	1295.43
	10	5	1167.33	1196.35	1237.08	1349.73	1422.70

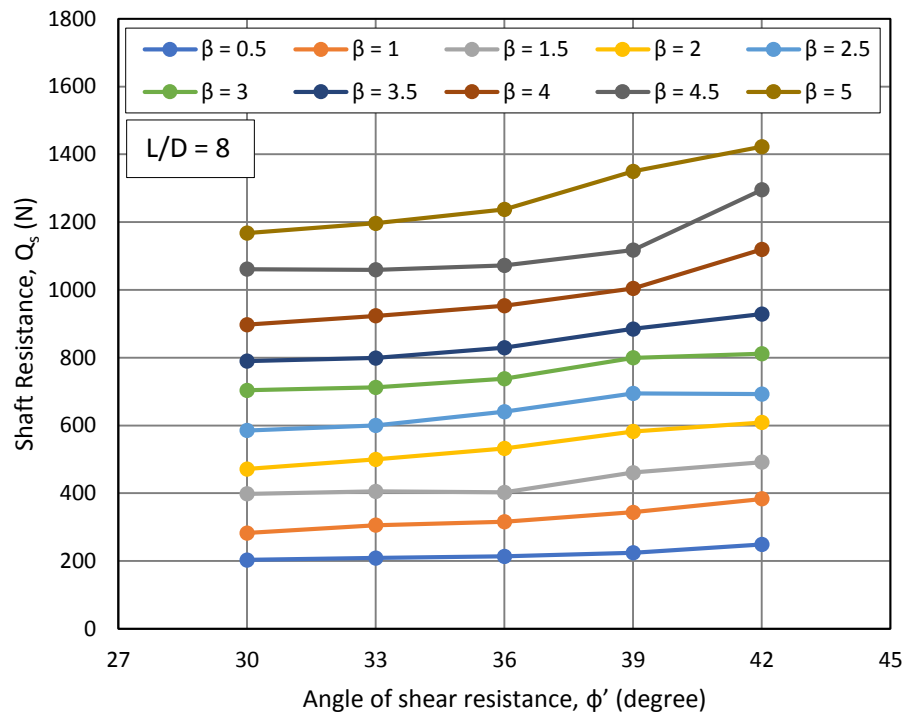


Figure 6-19: Shaft resistance with variable values of  $\beta$  for embedment depth ratio ( $L/D$ ) of 8

The variation of shaft resistance for the pile tested at an embedment depth ratio ( $L / D$ ) of 8 appears in Table 6-10 and Figure 6-20.

Table 6-10: Shaft resistance with variable values of  $\beta$  for embedment depth ratio ( $L/D$ ) of 10

L/D	Test No	$\beta$	Shaft Resistance (N)				
			$\phi'$ (degree)	$\phi'$ (degree)	$\phi'$ (degree)	$\phi'$ (degree)	$\phi'$ (degree)
			30	33	36	39	42
10	1	0.5	234.44	246.57	249.16	301.44	338.50
	2	1	391.27	419.63	452.20	489.07	552.98
	3	1.5	551.56	586.96	629.51	686.90	770.89
	4	2	704.69	757.56	814.46	874.56	990.33
	5	2.5	861.99	920.53	993.23	1073.24	1211.60
	6	3	1017.52	1077.42	1165.94	1256.26	1435.14
	7	3.5	1210.15	1274.55	1335.22	1537.60	1701.41
	8	4	1417.02	1495.23	1523.60	1716.18	1988.45
	9	4.5	1635.19	1685.69	1791.27	1919.86	2328.81
	10	5	1826.81	1841.59	2017.06	2356.26	2777.15

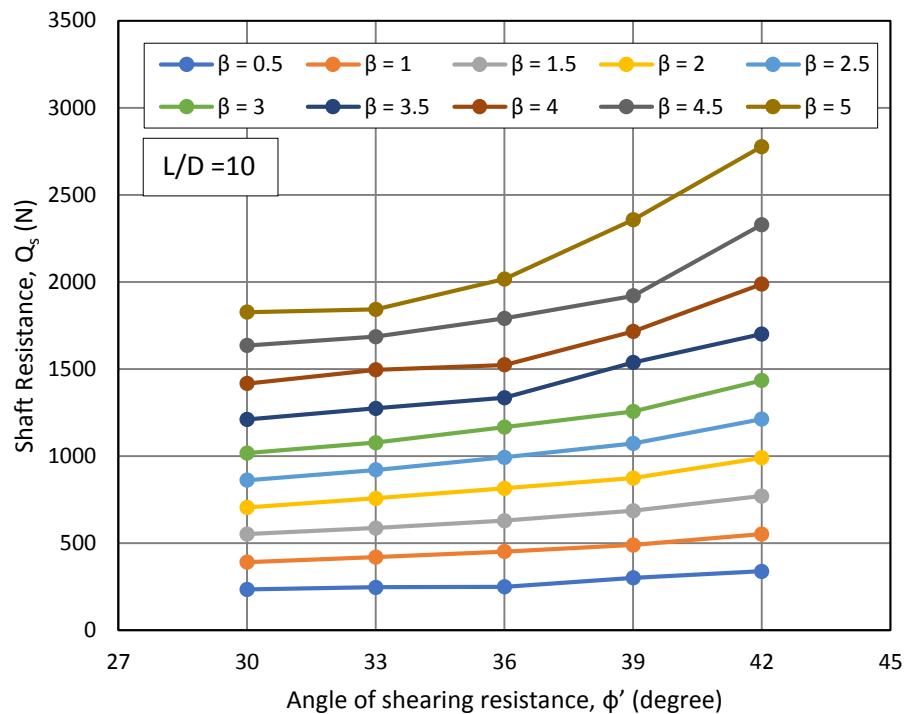


Figure 6-20: Shaft resistance with variable values of  $\beta$  for embedment depth ratio ( $L/D$ ) of 10

The variation of shaft resistance for the pile tested at an embedment depth ratio ( $L / D$ ) of 8 appears in Table 6-11 and Figure 6-21.

Table 6-11: Shaft resistance with variable values of  $\beta$  for embedment depth ratio ( $L/D$ ) of 13

L/D	Test No	$\beta$	Shaft Resistance (N)				
			$\phi'$ (degree)	$\phi'$ (degree)	$\phi'$ (degree)	$\phi'$ (degree)	$\phi'$ (degree)
			30	33	36	39	42
13	1	0.5	391.01	400.73	408.91	415.70	497.39
	2	1	653.51	674.86	703.39	761.21	838.97
	3	1.5	938.42	968.19	1011.34	1105.22	1181.44
	4	2	1255.44	1342.49	1324.75	1411.85	1469.93
	5	2.5	1566.86	1632.00	1604.24	1778.30	1936.95
	6	3	1906.01	1987.21	2030.61	2281.66	2721.29
	7	3.5	2261.04	2349.68	2414.14	2701.59	3874.39
	8	4	2617.56	2742.86	2984.70	3289.55	5315.40
	9	4.5	2964.74	3197.95	3491.80	3956.41	6092.37
	10	5	3310.43	3506.32	3840.00	4634.68	6962.77

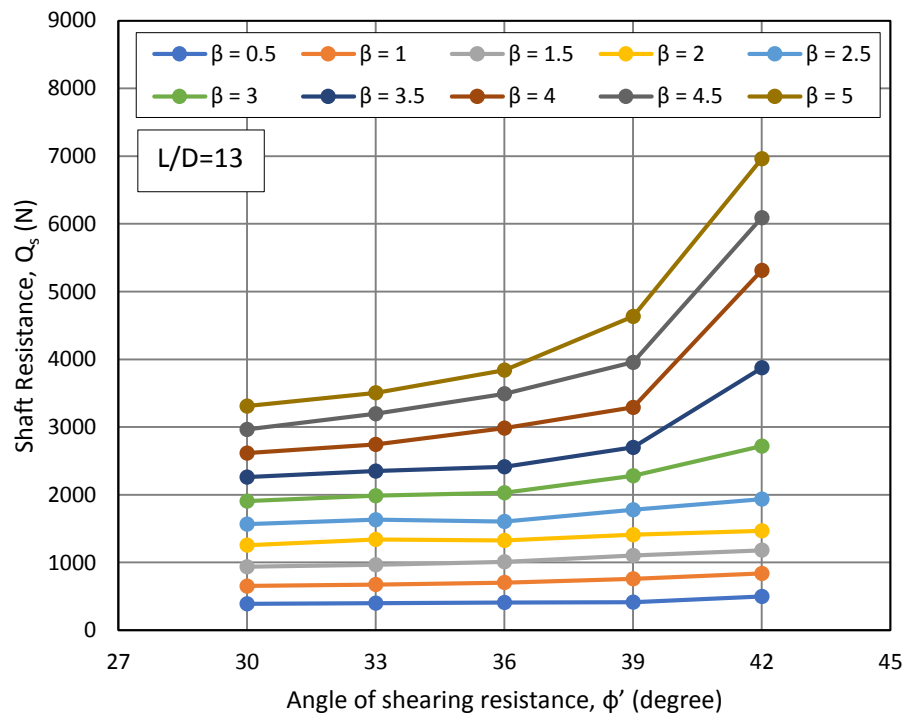


Figure 6-21: Shaft resistance with variable values of  $\beta$  for embedment depth ratio ( $L/D$ ) of 13

## 6.5 Analysis

It can be noted from Figure 6-18 to Figure 6-21 that the shaft resistance increases with the increase of  $\beta$  value. Moreover, the shaft resistance increases as the embedment depth ( $L/D$ ) increases for the same  $\beta$  value. It can also be noted that at a certain embedment depth ( $L/D$ ), the shaft resistance changes almost linearly with the increase of the angle of shearing resistance ( $\phi'$ ) at low  $\beta$  values. As the  $\beta$  value increases the shaft resistance increases nonlinearly with the increase of the angle of shearing resistance ( $\phi'$ ). This behaviour is more pronounced at high embedment depth ( $L/D$ ) ratios.

By interpolation, the relationship between  $\beta$  values and shaft resistance at the angle of shearing resistance ( $\phi'$ ) of 32.97 ( $\approx 33$ ) degree, 34.9 ( $\approx 35$ ) degree, and 36.84 ( $\approx 37$ ) degree for embedment depth ratios ( $L / D$ ) of 5, 8, 10 and 13 was determined (Figure 6-22, Figure 6-23, Figure 6-24 and Figure 6-25, respectively). The  $\beta$  values back-calculated from the analytical and experimental shaft resistance at every embedment depth ratio and angle of shearing resistance appear in the same figures. In sum, the experimental and analytical  $\beta$  values agreed with results found numerically.

For the embedment depth ratio of  $L / D = 5$  (Figure 6-22), the experimental and analytical  $\beta$  values at the angle of shearing resistance ( $\phi'$ ) of 32.97 ( $\approx 33$ ) degree were similar. As the angle of shearing resistance ( $\phi'$ ) increased, the difference between the two values increased with greater experimental  $\beta$  values. Since the analytical  $\beta$  value represents the normally consolidated state ( $OCR = 1$ ) and experimental  $\beta$  values represent the overconsolidated state ( $OCR > 1$ ), the effect of the OCR at the angle of shearing resistance ( $\phi'$ ) of 32.97 ( $\approx 33$ ) degree was remarkably small. As the angle of shearing resistance increased, the effect of the OCR became more pronounced.

For embedment depth ratios ( $L / D$ ) of 8, 10, and 13 (Figure 6-23, Figure 6-24 and Figure 6-25, respectively), a greater difference is clear between the analytical and experimental  $\beta$  values, which indicates the greater effect of the OCR at higher embedment depth ratios. For the same angle of shearing resistance ( $\phi'$ ), the effect of the OCR on  $\beta$  increased as the embedment depth ratio increased.

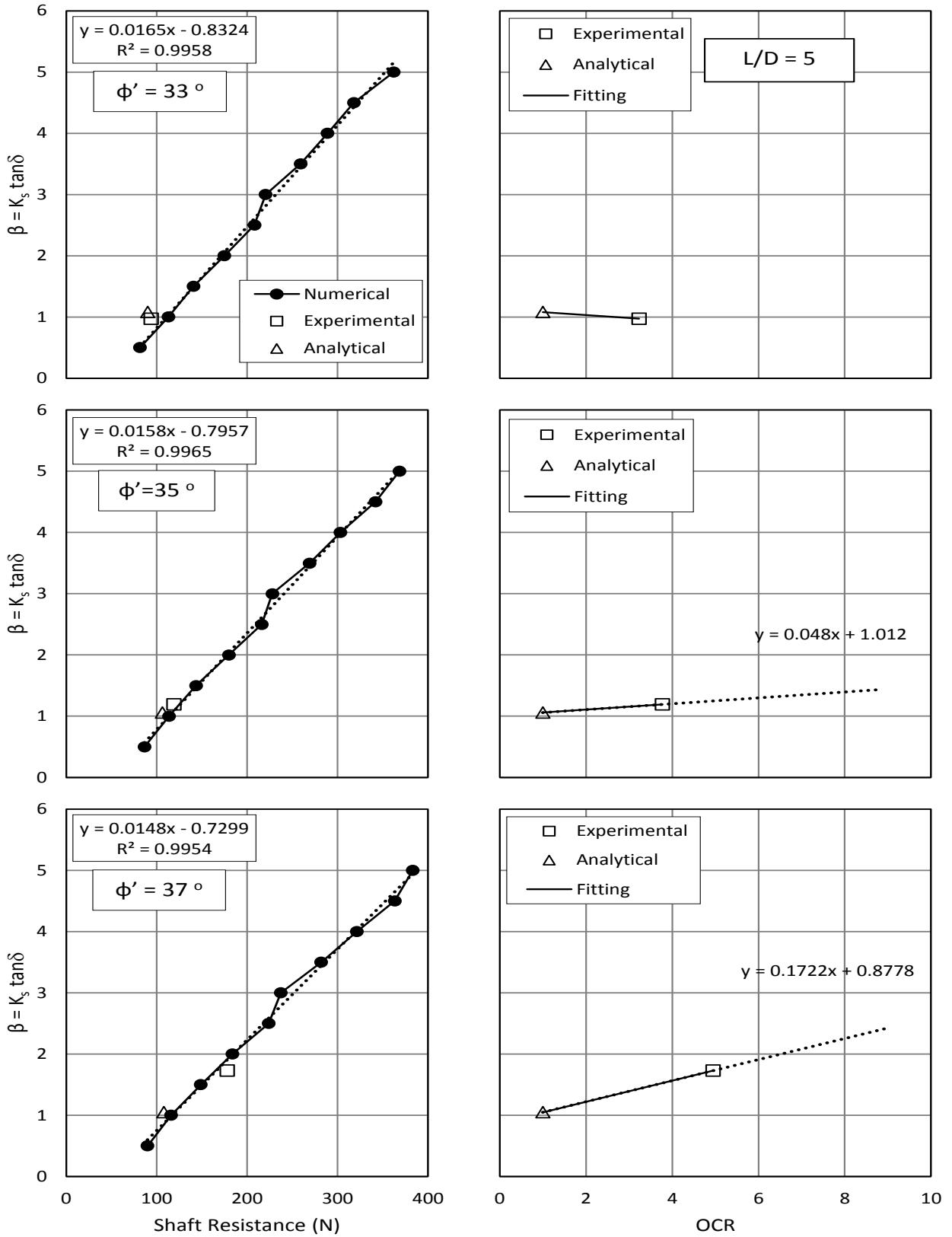


Figure 6-22:  $\beta$  value versus shaft resistance and OCR for  $L/D = 5$

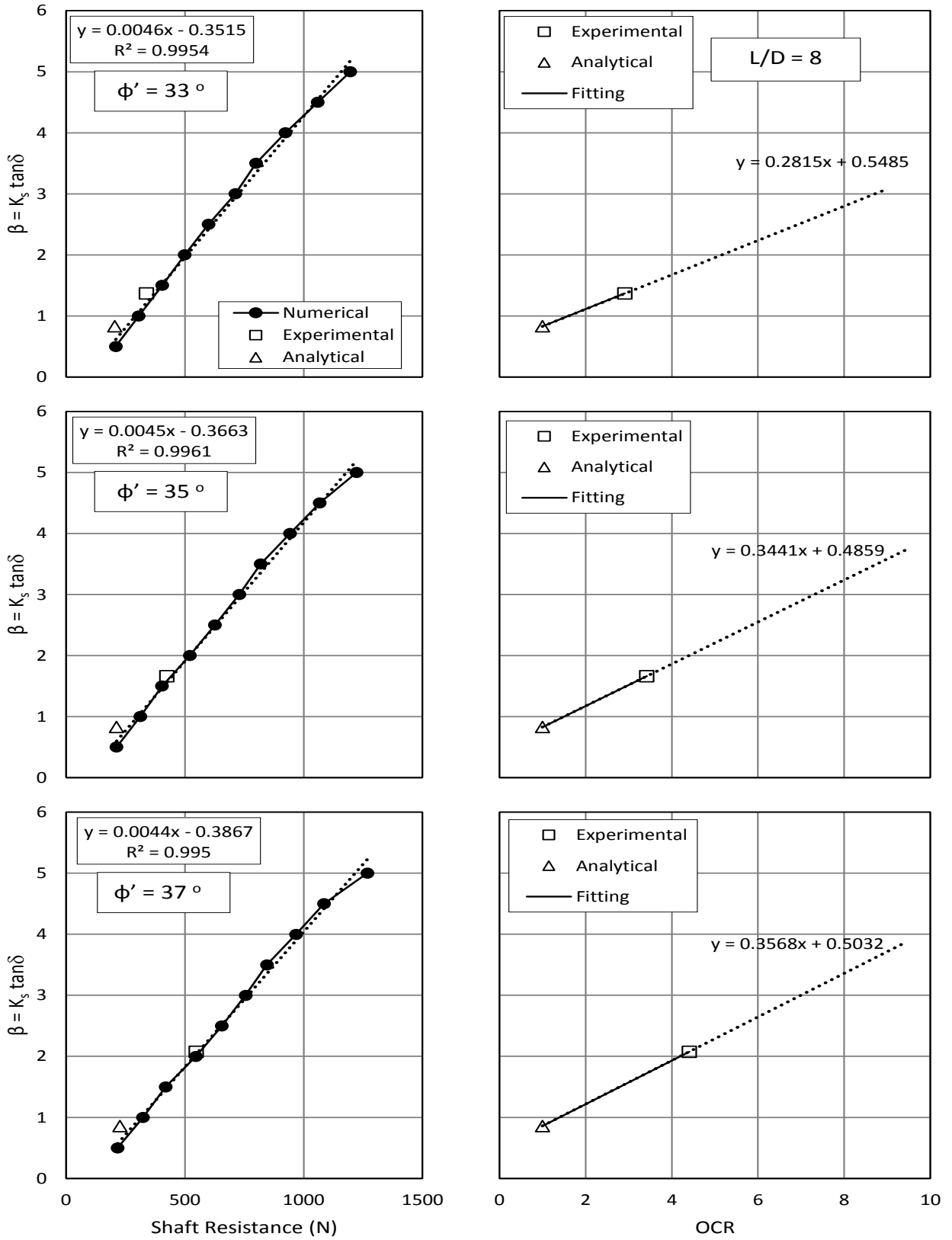


Figure 6-23:  $\beta$  value versus shaft resistance and OCR for  $L/D = 8$

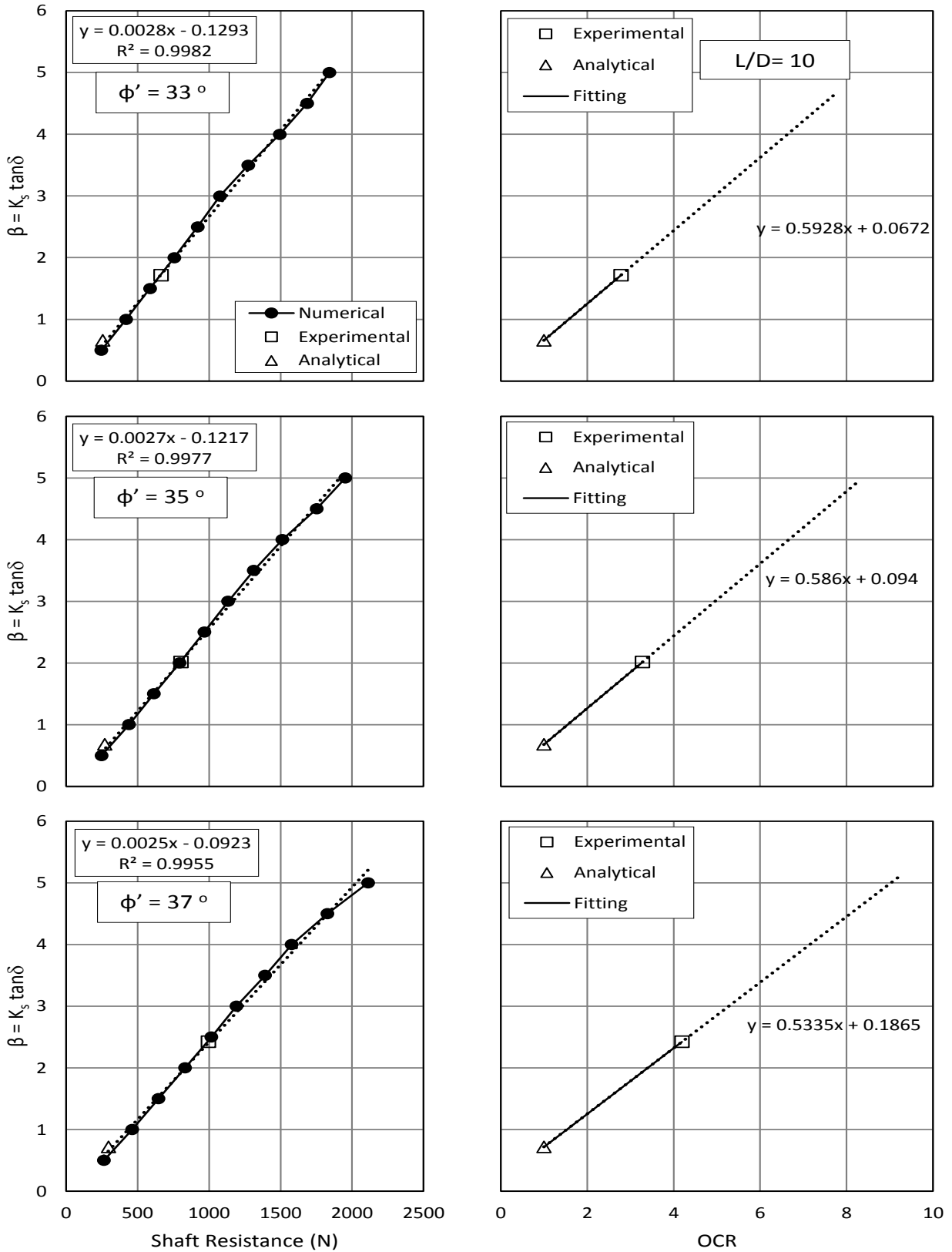
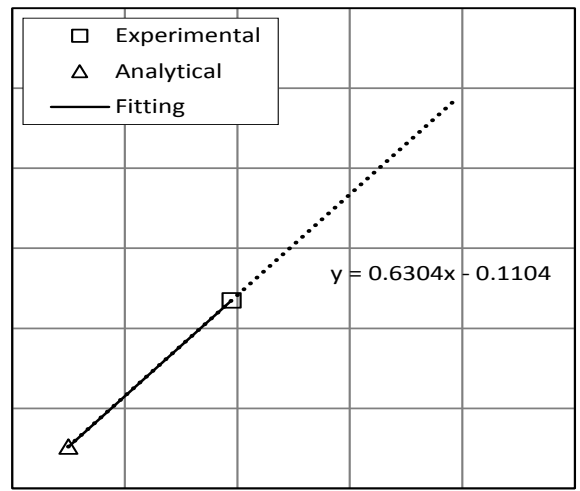
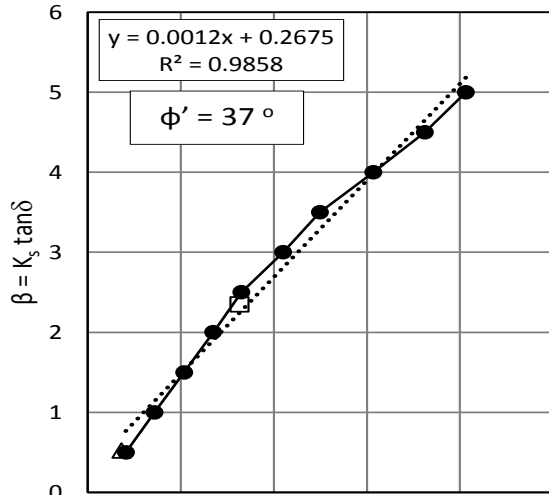
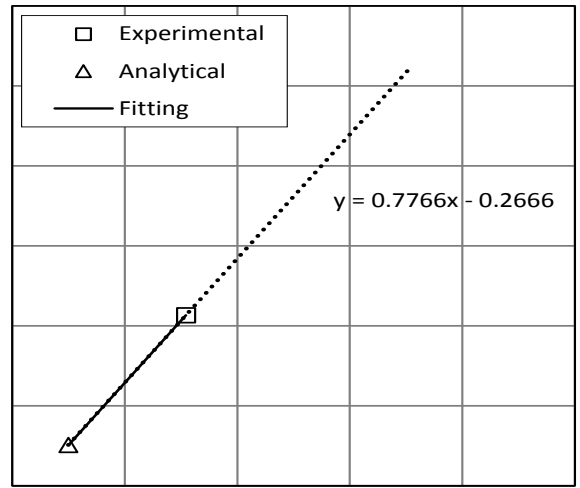
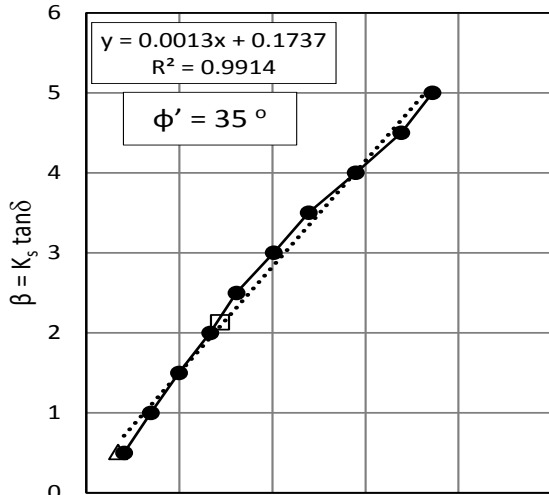
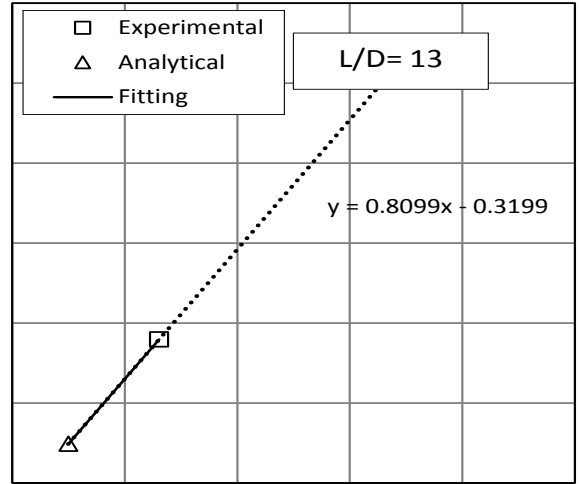
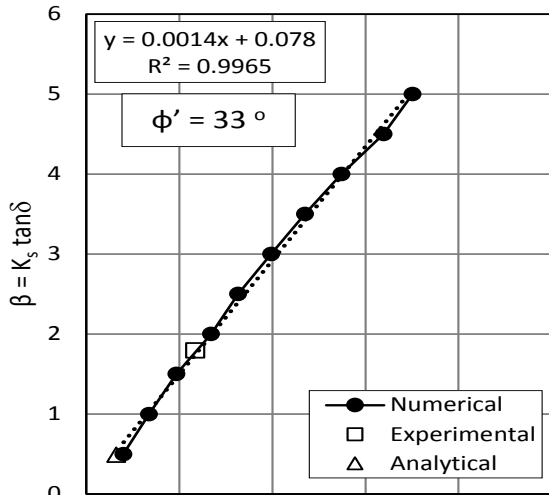


Figure 6-24:  $\beta$  value versus shaft resistance and OCR for  $L/D = 10$



Shaft Resistance (N)

OCR

Figure 6-25:  $\beta$  value versus shaft resistance and OCR for  $L/D = 13$

## 6.6 Design Charts

Using the OCR values for the analytical  $\beta$  value ( $\text{OCR} = 1$ ) and the experimental  $\beta$  value (mean from Figure 3-10), a linear relationship was established between the  $\beta$  value and the OCR for the range of angles of shearing resistance ( $\phi'$ ) and the range of embedment depth ratios ( $L / D$ ) presented in the previous section (Figure 6-22 to Figure 6-25). For different OCR values, the analytical and experimental  $\beta$  values at the embedment depth ratio ( $L / D$ ) of 5 and angle of shearing resistance ( $\phi'$ ) of 32.97 degree, given their proximity, were set as the same value.

The relationship between the  $\beta$  values and the embedment depth ratios of 5, 8, 10, and 13 was thus determined for OCR values ranging from 1 to 10 at angles of shearing resistance ( $\phi'$ ) of 32.97 ( $\approx 33$ ) degree, 34.90 ( $\approx 35$ ) degree, and 36.84 ( $\approx 37$ ) degree. To extrapolate the values and cover a wider range of embedment depth ratios ( $L / D$ ), a logarithmic relationship was identified for each OCR value ( $R^2 > 0.95$ ) using the four points at  $L / D$  of 5, 8, 10 and 13. These charts were also extrapolated to generate another chart at angle of shearing resistance ( $\phi'$ ) of 39 degree.

Figure 6-26, Figure 6-27, Figure 6-28 and Figure 6-29 were generated for angles of shearing resistance ( $\phi'$ ) of 33 degree, 35 degree, 37 degree, and 39 degree, respectively, and can be used as design charts to predict  $\beta$  at different embedment depths ratios ( $L/D$ ) and OCR values. It should be mentioned that these figures are limited for OCRs up to 10, and embedment depth ratios up to 30.

The charts indicate that  $\beta$  increases as the OCR increases, that the rate of change for  $\beta$  paired with a small OCR is smaller than that at a greater OCR value, and that  $\beta$  at the same OCR decreases as the angle of shearing resistance ( $\phi'$ ) increases.

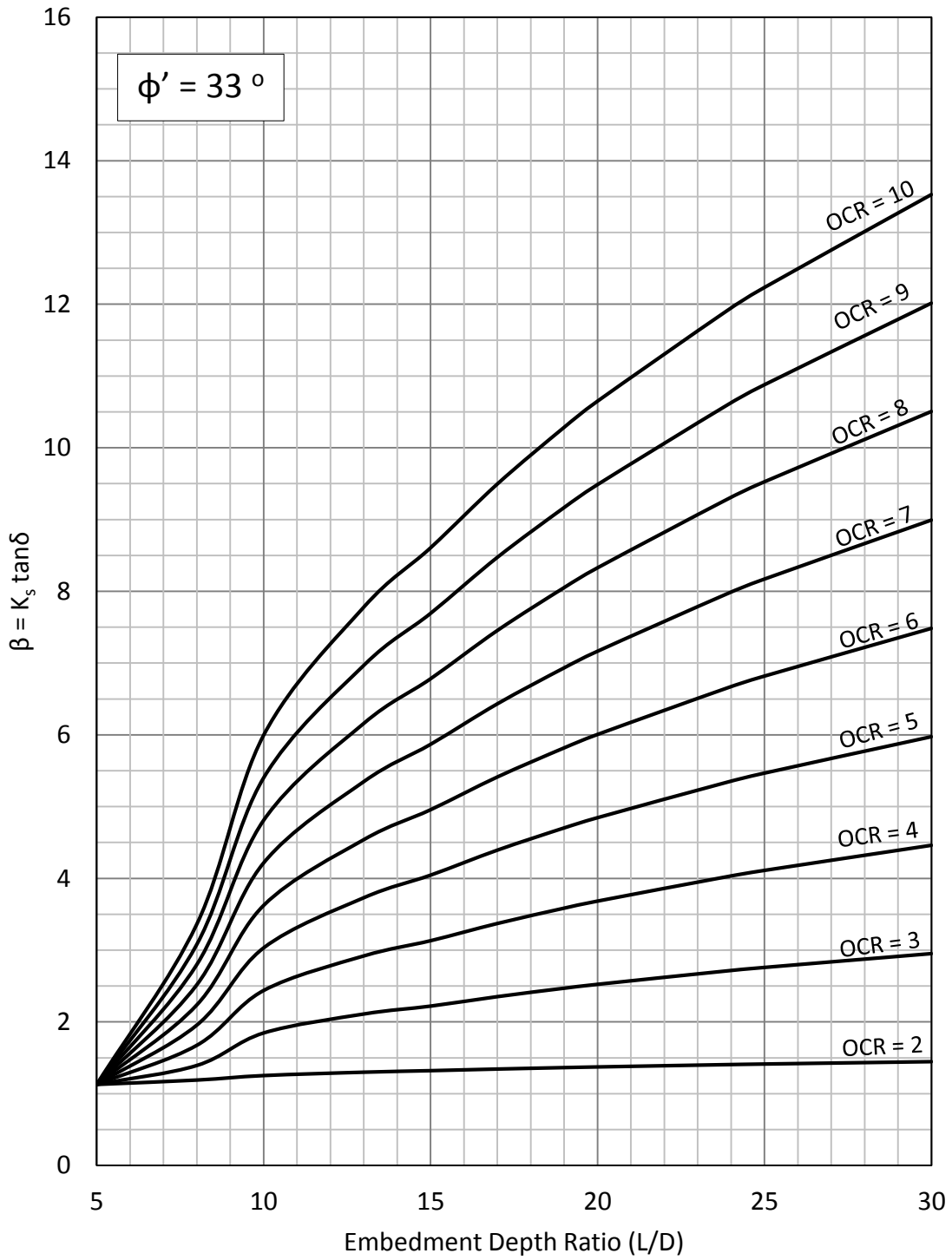


Figure 6-26:  $\beta$  value versus embedment depth ratio for  $\phi' = 33$  degree

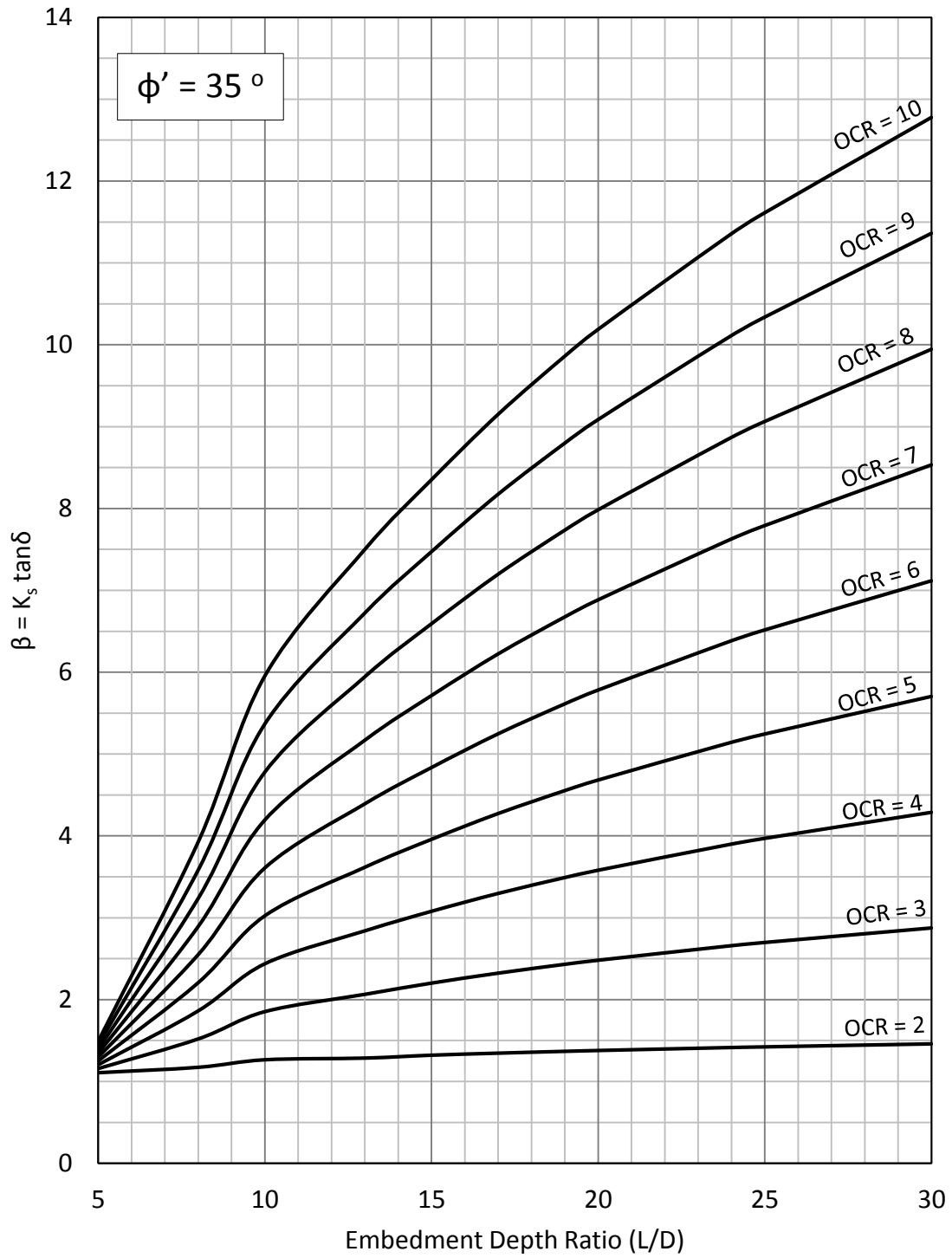


Figure 6-27:  $\beta$  value versus embedment depth ratio for  $\phi' = 35$  degree

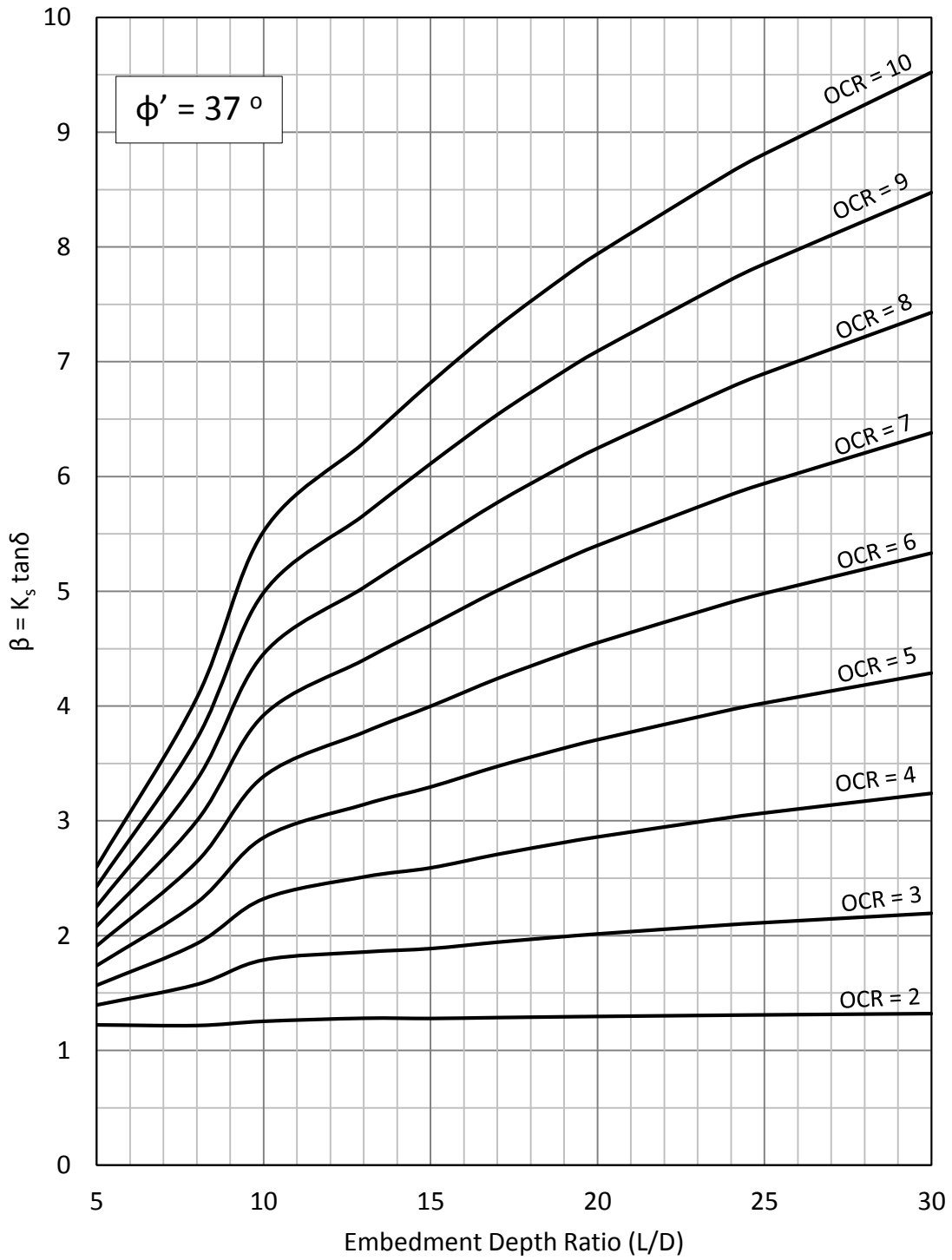


Figure 6-28:  $\beta$  value versus embedment depth ratio for  $\phi' = 37$  degree

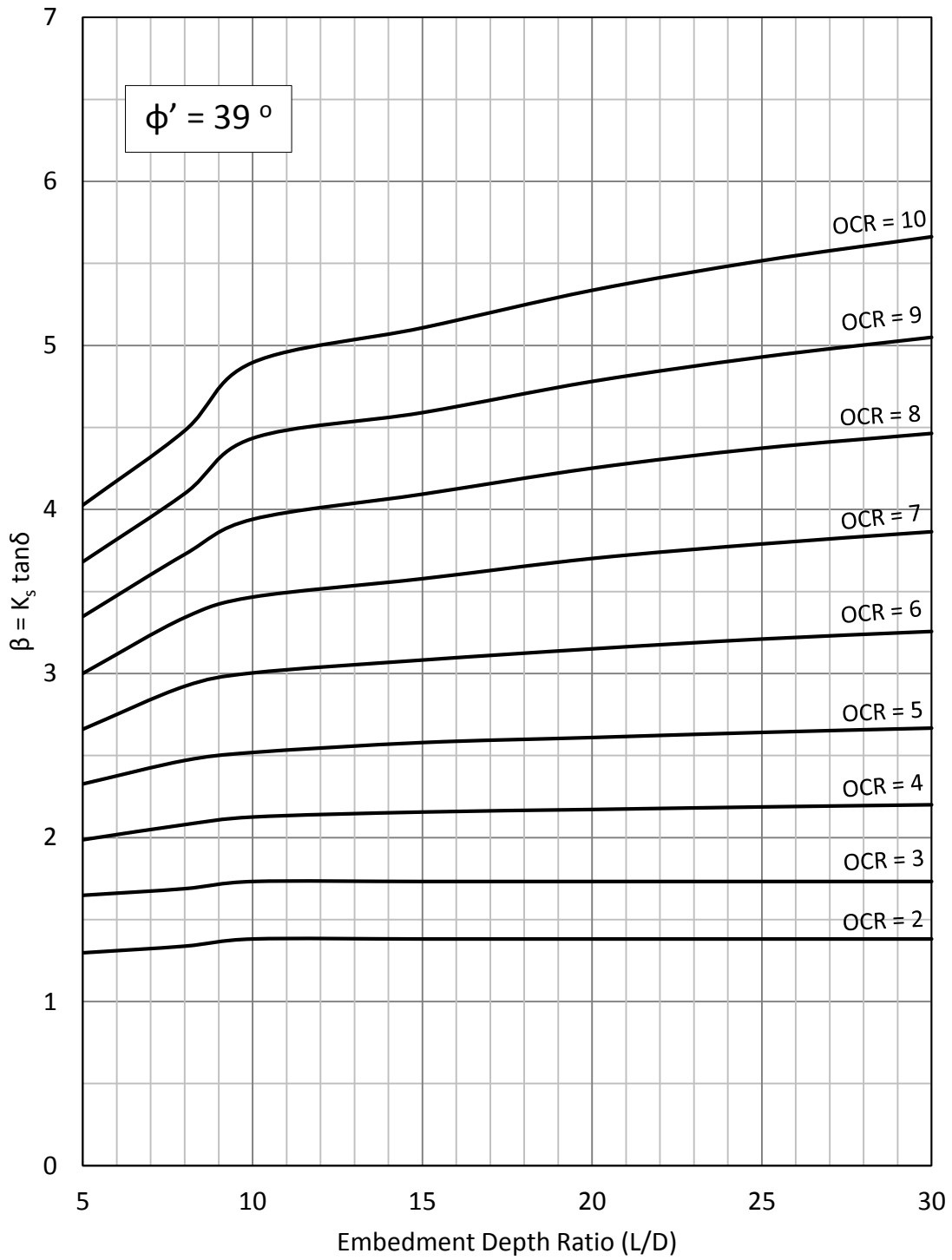


Figure 6-29:  $\beta$  value versus embedment depth ratio for  $\phi' = 39$  degree

## 6.7 Validation

Due to the lack of published record on pile load test in overconsolidated cohesionless soils, the design charts were validated using the experimental results of the pile model of 30 mm in diameter as well as the field pile load test reported by Beringen et al. (1979).

As for the pile model 30 mm in diameter, the experimental results were analyzed to validate the proposed design charts. Figure 3-10 was used to calculate the average OCR values along the pile shaft.

The percentage of error between the actual  $\beta$  values and that predicted from the design charts presented earlier are illustrated in Table 6-12. Predicted  $\beta$  values agreed well with actual  $\beta$  values ( $\pm 30\%$ ).

Moreover, the results of the field pile load test performed in overconsolidated cohesionless soil reported by Beringen et al. (1979) were analyzed to validate the proposed design charts. The OCR was estimated according to Mayne's (1991) equation (Eq. 2.26):

$$K_0 = \frac{(P_a / \sigma'_v) (q_c / P_a)^{1.6}}{145 \exp \left\{ \left[ \frac{(q_c / P_a) / (\sigma'_v / P_a)^{0.5}}{12.2 \text{ OCR}^{0.18}} \right]^{0.5} \right\}} \quad (\text{Repeated 2-26})$$

where:

$(K_0)$  = at rest lateral earth pressure coefficient,

$$= (1 - \sin \phi') (\text{OCR})^{(\sin \phi')} \quad (\text{Repeated 2-16})$$

$(q_c)$  = cone tip resistance,

$(P_a)$  = a reference stress equal to one atmosphere (1 bar = 100 kPa),

$(\sigma'_v)$  = vertical effective stress, and

$(\text{OCR})$  = overconsolidation ratio.

Knowing the  $q_c$  profile (Figure 4-33) and soil properties ( $\phi' = 38$  degree,  $\gamma_{\text{eff}} = 16.1 \text{ kN/m}^3$ ), the mean OCR value that equalizes both sides of Equation 2.26 was calculated, after which the  $\beta$  value was back-calculated according to the shaft resistance of the pile and the soil properties. As a result, the OCR and  $\beta$  value were found to be 5.5 and 3.23, respectively. The design charts presented earlier (Figure 6-26 to Figure 6-29) were used to determine the  $\beta$  value at OCR = 5.5 and the embedment depth ratio of  $L / D = 19$  for the angle of shearing resistance of 33, 35, 37, and 39 degree.

Accordingly, the relationship between the angle of shearing resistance ( $\phi'$ ) and  $\beta$  value for an OCR = 5.5 and  $L / D = 19$  was identified and extrapolated (Figure 6-30). The  $\beta$  value at  $\phi' = 38^\circ$  was determined from the extrapolation of the best fitting line ( $R^2 = 0.99$ ), which yielded a value of 3.50. Ultimately, the error between the predicted and actual  $\beta$  value was -8%. The error presented is not high and could be justified by the accuracy of the reported data by Beringen et al. (1979) where it may not be accurate enough, and/or the actual field condition may not be as reported.

Table 6-12: Error between the predicted and actual  $\beta$  values for the pile model of 30 mm diameter

Tests	$\phi'$ (degree)	L/D	OCR	$\beta$ (Experimental)	$\beta$ (Chats)	Error (%)
D=30 mm	33	19	2.78	1.59	2.10	-32%
		23.8	2.61	1.85	2.00	-8%
	35	19	3.28	2.03	2.60	-28%
		23.8	3.09	2.22	2.60	-17%
	37	19	4.19	3.34	3.00	10%
		23.8	3.90	3.44	2.90	16%

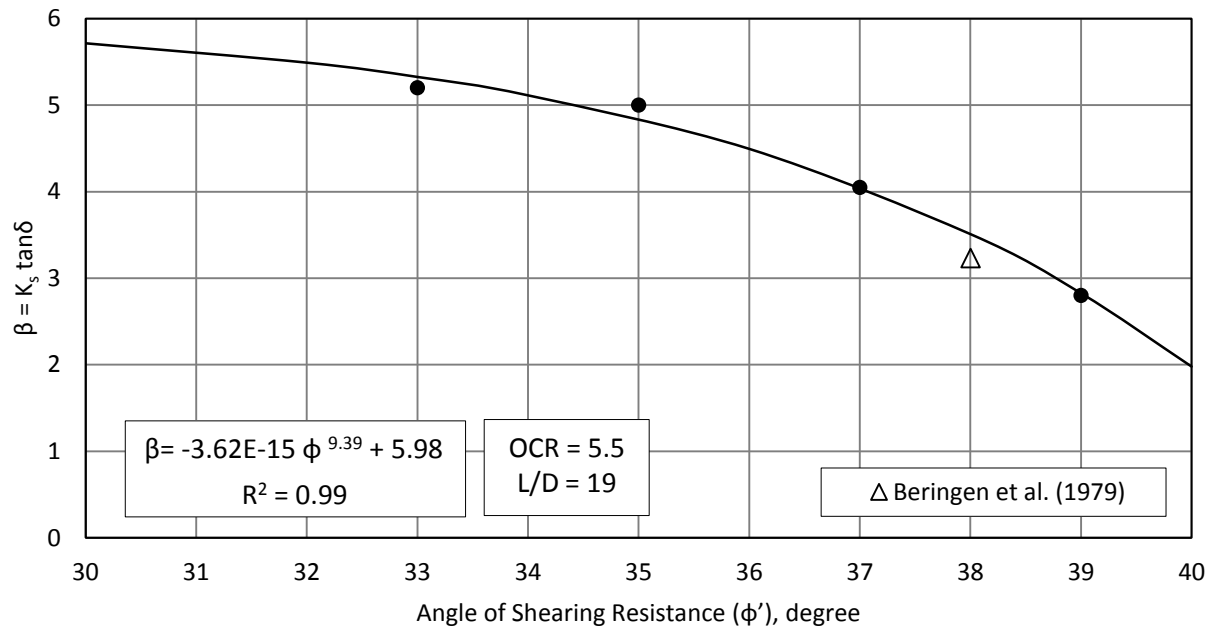


Figure 6-30:  $\beta$  value versus angle of shearing resistance for OCR = 5.5 and L/D = 19

## **Chapter 7 : Conclusion and Recommendations**

### **7.1 General**

The capacity of driven piles in overconsolidated cohesionless soils has been investigated experimentally, analytically and numerically in this thesis. Emphasis to the effect of overconsolidation on the shaft resistance and the concept of critical depth were highlighted.

Experimentally, laboratory tests were performed on a prototype instrumented model, to evaluate the effect of dynamic compaction on relative density and the induced stresses in cohesionless soils to produce uniform overconsolidated cohesionless soils. Pile load tests were conducted on two pile models in overconsolidated cohesionless soils.

Analytically, the limit equilibrium technique was used to predict the shaft resistance of a single pile driven into normally consolidated cohesionless soil. A database of 36 field and laboratory pile load tests collected from the literature to validate the theory developed.

Numerically, three-dimensional numerical model was developed to perform 200 pile load tests to examine the mobilized lateral earth pressure on the shaft resistance.

### **7.2 Conclusion**

Based on the experimental, analytical and numerical investigations conducted on the shaft resistance of displacement piles, the following conclusions were drawn:

1. The dynamic compaction method adopted in the experimental investigation was successfully used to produce uniform unit weight, and overconsolidation in the testing tank. This was achieved by controlling the applied energy on each layer.

2. Design procedure was developed to determine the required energy level to be applied on each layer to produce a uniform homogeneous sand in the testing tank. Design charts are presented to estimate the number of drops needing to be applied on each layer for a desired relative density throughout a testing tank and the overconsolidation ratio (OCR) values.
3. The experimental set-up was equipped to measure the in-situ stress in the sand mass and accordingly the overconsolidation ratio (OCR). The OCR has significant effect on the capacity of closed-end displacement piles in cohesionless soil.
4. Bearing capacity factors ( $N_q$ ) deduced from the present experimental investigation agreed well with theoretical values proposed by Meyerhof (1953), which validate the present experimental investigation. The embedment depth significantly influenced the  $N_q$  values at low relative density, and its effect decreases as the relative density increases.
5. The ratio of pile displacement to pile diameter ( $W_s / D$ ) at the peak for the shaft resistance vary from the typical value (2%) and increases with the increase of the embedment depth ratio and the relative density.
6. The experimental values of the average lateral earth pressure coefficient  $K_s$  and the values of the local  $K_s$  deduced from the measured local shear stress, were significantly greater than those traditionally recommended for displacement piles, and accordingly, the  $K_s / K_0$  ratio.
7. Critical depth ( $L_c / D$ ) appeared only when total shaft resistance was analyzed as a mean. The critical depth agrees well with Meyerhof's (1976) results which indicates that the OCR neither affects its appearance nor its value. Analytically, the sudden drop in the rate of the inclination angle ( $\alpha$ ) with the ( $L / D$ ) ratio confirms the presence of the critical depth when shear stress along the pile's shaft is analyzed as a mean. Also, the deduced critical depth agreed with

previously reported values (Meyerhof, 1976) in ( $L / D$ ) ratio range of 10 to 20 and increased linearly as angles of shearing resistance ( $\phi'$ ) increased.

8. At a given depth, local shear stress decreases with the increase of the pile depth and, accordingly, the mean total shaft friction remained relatively unchanged and accordingly, the critical depth appeared.
9. Shear stress distribution along the pile's shaft showed some dependency on the embedment depth ratio ( $L / D$ ). Semi-empirical factors were proposed as function of the embedment depth ratio to determine shear stress distribution along the pile shaft. The proposed design procedure can be used to estimate the shear stress distribution for displacement piles in overconsolidated cohesionless soils.
10. The inclination angle ( $\alpha$ ) of the failure surface increases with the increase of the angle of shearing resistance ( $\phi'$ ) and decreases with the increase of the ratio of pile length to pile diameter ( $L / D$ ). The experimental values of the inclination angle ( $\alpha$ ) and ( $L / D$ ) ratio for various angles of shearing resistance ( $\phi'$ ) were the base to develop design charts to predict the pile capacity. The proposed design procedure can be used to estimate shear stress for displacement piles in normally consolidated cohesionless soils.
11. Shaft resistance increased as the value of the coefficient  $\beta$  increases, and for the same  $\beta$  value, shaft resistance increases with the increase of the embedment depth ( $L / D$ ). For a given embedment depths ( $L / D$ ), shaft resistance change almost linearly as the angle of shearing resistance ( $\phi'$ ) increases for low  $\beta$  values. For higher values of  $\beta$ , shaft resistance increases nonlinearly with the increase of the angle of shearing resistance ( $\phi'$ ), which is more pronouncedly at higher embedment depth ( $L / D$ ) ratios.

12. For a given angle of shearing resistance ( $\phi'$ ), the effect of the OCR on the value of the coefficient  $\beta$  increases with the increase of the embedment depth ratio ( $L / D$ ). For a given OCR and embedment depth, the value of  $\beta$  decreases with the increase of the angle of shearing resistance.
13. Design theory is proposed to estimate the value of  $\beta$  for different OCR values at different embedment depth ratios ( $L / D$ ) and different angles of shearing resistance ( $\phi'$ ).

### **7.3 Recommendation for Future Work**

Given the conclusions regarding how the OCR affects the shaft resistance of closed-ended driven piles in cohesionless soils, seven recommendations are suggested for future work:

- 1- To examine the case of piles driven into overconsolidated layered soil;
- 2- To examine the case pile groups in overconsolidated cohesionless soil;
- 3- To examine the case of battered piles in overconsolidated cohesionless soil;
- 4- To examine the effect of water tables;
- 5- To examine the case of an open-ended driven piles in cohesionless soils;
- 6- To experimentally investigate the pile–soil interface angle ( $\delta$ ); and
- 7- To experimentally investigate the effects of pile diameter ( $D$ ) on the shaft resistance of driven piles in overconsolidated cohesionless soil.

## References

- Al-Mhaidib, A. (2012). Experimental study on the effect of compressive loads on uplift capacity of model piles in sand. *International Journal of Geotechnical Engineering*, 6(1), 133-137.
- Altaee, A., Fellenius, B. H., & Evgin, E. (1992). Axial load transfer for piles in sand. I. Tests on an instrumented precast pile. *Canadian Geotechnical Journal*, 29(1), 11-20.
- Ansari, Y., Kouretzis, G. P., & Sloan, S. W. (2018). Development of a prototype for modelling soil-pipe interaction and its application for predicting the uplift resistance to buried pipe movements in sand. *Canadian Geotechnical Journal*, In press.
- API. (2000). *Recommended practice for planning, designing and constructing fixed offshore platforms-working stress design*. 2A-WSD, 21.
- Barmopoulos, I. H., Ho, T. Y., Jardine, R. J., & Anh-Minh, N. (2009). The large displacement shear characteristics of granular media against concrete and steel interfaces. *In Characterization and Behavior of Interfaces. Proceedings of the Research Symposium on Characterization and Behavior of Interfaces, Atlanta, Georgia, USA*, (pp. 16-23). IOS Press, Amsterdam, the Netherlands.
- Barnes, G. (2016). *Soil mechanics: principles and practice*. Palgrave macmillan.
- Basu, P., Loukidis, D., Prezzi, M., & Salgado, R. (2011). Analysis of shaft resistance of jacked piles in sands. *International Journal for Numerical and Analytical Methods in Geomechanics*, 35(15), 1605-1635.
- BCP-Committee. (1971). Field tests on piles in sand. *Soils and Foundations*. 11(2), 29-49.

- Berezantzev, V. G., Khristoforov, V., & Golubkov, V. (1961). Load bearing capacity and deformation of piled foundations. *In Proceedings of the 5th International Conference on Soil Mechanics and Foundation Engineering*, 2, pp. 11-15. Paris.
- Beringen, F., Windle, D., & Van Hooydonk, W. (1979). Results of loading tests on driven piles in sand. *International Conference of the Institution of Civil Engineers on Recent Developments in the Design and Construction of Piles*, (pp. 213-225). London.
- Bolton, M. D. (1986). The strength and dilatancy of sands. *Geotechnique*, 36(1), 65-78.
- Bolton, M. D. (1991). *A guide to soil mechanics*. Universities Press.
- Boulon, M., & Foray, P. (1986). Physical and numerical simulation of lateral shaft friction along offshore piles in sand. *Proceedings of the 3rd International Conference on Numerical methods in Offshore piling*, (pp. 127-147). Nantes, France.
- Bowles, J. (2002). *Foundation analysis and design*. New York: McGraw-Hill.
- Briaud, J. L., Tucker, L. M., & Ng, E. (1989). Axially loaded 5 pile group and single pile in sand. *In Proceeding, 12th International Conference on Soil Mechanics and Foundation Engineering*, 2, pp. 1121-1124. Balkema Rotterdam.
- Brinch, J. (1963). Discussion of hyperbolic stress-strain response: cohesive soil: by Robert L. Kondner. *Journal of the Soil Mechanics and Foundations Division*, 89(4), 241-242.
- Brinkgreve, R. B. (2005). Selection of soil models and parameters for geotechnical engineering application. *In Soil constitutive models: Evaluation, selection, and calibration*, (pp. 69-98).
- Broms, B. B. (1966). Methods of calculating the ultimate bearing capacity of piles - A summary. *Sols-Soils*, 18-32.
- Broms, B. B., & Silberman, J. O. (1964). Skin friction resistance for piles in cohesionless soils. *Sols-Soils*, 10, 33-41.

- Chari, T. R., & Meyerhof, G. G. (1983). Ultimate capacity of rigid single piles under inclined loads in sand. *Canadian Geotechnical Journal*, 20(4), 849-854.
- Chow, F. (1997). *Investigations into displacement pile behaviour for offshore foundations*. Ph.D. thesis. Imperial College. London.
- Chow, Y. K. (1986). Analysis of vertically loaded pile groups. *International Journal for Numerical and Analytical Methods in Geomechanics*, 10(1), 59-72.
- Coduto, D. P. (2001). *Foundation design: principles and practices*. Prentice Hall.
- Coyle, H. M., & Castello, R. R. (1981). New design correlations for piles in sand. *Journal of Geotechnical and Geoenvironmental Engineering*, 107(7), 965-986.
- Coyle, H. M., Bartoskewitz, R. E., & Berger, W. J. (1973). *Bearing capacity prediction by wave equation analysis-state of the art*. Research Report 125-8. Texas A&M University. College Station. Texas.
- Cresswell, A., Barton, M., & Brown, R. (1999). Determining the maximum density of sands by pluviation. *Geotechnical Testing Journal*, 22(4), 324-328.
- CUR (Centre for Civil Engineering Research and Codes). (2001). *Bearing capacity of steel pipe piles*. Report 2001-8. Gouda. The Netherlands: Centre for Civil Engineering Research and Codes.
- Das, B. M. (2011). *Prinsiple of foundation engineering, 7th edition*. Global Engineering: Christopher M. Shortt, Cengage Learning.
- Das, B. M. (2012). *Fundamentals of geotechnical engineering*. Cengage Learning; 4 edition.
- Davisson, M. T. (1972). High capacity piles. *Proceedings, Soil Mechanics Lecture Series on Innovations in Foundation Construction*, (pp. 81-112).

- DiCamillo, F. (2014). Effects of stress history of sand on the shaft resistance of large displacement piles. *Masters thesis*. Concordia University.
- Dorr, H. (1922 ). Die Tragfaehigkeit der Pfaehle. *Verlag W. Ernst & Sohn*. Berlin .
- Duncan, J. M., & Seed, R. B. (1986). Compaction-induced earth pressures under K 0-conditions. *Journal of Geotechnical Engineering*, 112(1), 1-22.
- El-Emam, M. (2011). Experimental and numerical study of at-rest lateral Earth pressure of overconsolidated sand. *Advances in Civil Engineering*, 2011, 1-12.
- Fellenius, B. H. (1975). Test loading of piles and new proof testing procedure. *Journal of Geotechnical and Geoenvironmental Engineering*, 101(9), 855–869.
- Fellenius, B. H. (1986). *The FHWA static testing of a single pile and a pile group*. Report on the analysis of soil and installation data plus Addendum Report. The Federal Highway Administration. FHWA. Washington. Prediction Symposium.
- Fellenius, B., & Altaee, A. (1995). The critical depth – How it came into being and why it does not exist. *Civil Engineers, Geotechnical Engineering Journal*, 113(2) 107-111.
- Fellenius, H. B. (2002). Determining the resistance distribution in piles. Part 1: notes on shift of no-load reading and residual load. *Geotechnical News Magazine*, 20(2), 35 - 38.
- Fioravante, V. (2002). On the shaft friction modelling of non-displacement piles in sand. *Soils and Foundations, The Japanese Geotechnical Society*, 42(2), 23-33.
- Fleming, K., Weltman, A., Randolph, M., & Elson, K. (2008). *Piling engineering*. CRC press.
- Flynn, K. N., & McCabe, B. A. (2015). Shaft resistance of driven cast-in-situ piles in sand. *Canadian Geotechnical Journal*, 53(1), 49-59.
- Foray, P., Balachowski, L., & Colliat, J. L. (1998). Bearing capacity of model piles driven into dense overconsolidated sands. *Canadian Geotechnical Journal*, 35(2), 374-385.

- Franke, E., & Muth, G. (1985). Scale effect in 1g model tests on horizontally loaded piles. *In Proceedings of the 11th International Conference of Soil Mechanics and Foundations*, 2, pp. 1011-1014. San Francisco.
- Garnier, J., & Konig, D. (1998). Scale effects in piles and nails loading tests in sand. *In Centrifuge*, 98, 205-210.
- Garnier, J., Gaudin, C., Springman, S. M., Culligan, P. J., Goodings, D., Konig, D., & ..... Thorel, L. (2007). Catalogue of scaling laws and similitude questions in geotechnical centrifuge modelling. *International Journal of Physical Modelling in Geotechnics*, 7(3), 1.
- Gavin, K. G., & O'Kelly, B. C. (2007). Effect of friction fatigue on pile capacity in dense sand. *Journal of Geotechnical and Geoenvironmental Engineering*, 133(1), 63-71.
- Gavin, K. G., Cadogan, D., & Casey, P. (2009). Shaft capacity of continuous flight auger piles in sand. *Journal of Geotechnical and Geoenvironmental Engineering*, 135(6), 790-798.
- Gogoi, N., Bordoloi, S., & Sharma, B. (2014). A model study of micropile group efficiency under axial loading condition. *International Journal of Civil Engineering Research*, 323-332.
- Gregersen, O. S., Aas, G., & Dibiagio, E. (1973). Load tests on friction piles in loose sand. *Proceeding 8th International Conference on Soil Mechanics*, 2, pp. 109-117. Moscow.
- Hanna, A. M., & Al-Romhein, R. (2008). At-rest pressure of overconsolidated cohesionless soil. *Journal of Geotechnical and Geoenvironmental Engineering, ASCE, Vol. 134, No. 3*, 408-412.
- Hanna, A. M., & Ghaly, A. M. (1992). Effects of  $K_0$  and overconsolidation on uplift capacity. *Journal of geotechnical engineering*, 118 (9), 1449-1469.
- Hanna, A. M., & Nguyen, T. Q. (2002). An axisymmetric model for of ultimate capacity of a single pile in sand. *Japanese Geotechnical Society, Vol. 42*, pp. 47-58.

- Hanna, A. M., & Soliman-Saad, N. (2001). Effect of compaction duration on the induced stress levels in a laboratory prepared sand bed. *Geotech Test J ASTM*, 24(4), 430-438.
- Hanna, A., & Al Khoury, I. (2005). Passive earth pressure of overconsolidated cohesionless backfill. *Journal of geotechnical and geoenvironmental engineering*, 131(8), 978-986.
- Hanna, A., & Nguyen, T. Q. (2003). Shaft resistance of single vertical and batter piles driven in sand. *Journal of Geotechnical and Geoenvironmental Engineering*, 129(7), 601-607.
- Hibbitt, H., Karlsson, B., & Sorensen, P. (2016). Abaqus analysis user's manual version 2016. *Dassault Systèmes Simulia Corp, Providence*.
- Ho, T., Jardine, R., & Anh-Minh, N. (2011). Large-displacement interface shear between steel and granular media. *Géotechnique*, 61 (3), 221–234.
- Iskander, M. (2011). *Behavior of Pipe Piles in Sand*. Springer Berlin Heidelberg.
- Jaky, J. (1944). The coefficient of earth pressure at rest. *Journal of the Society of Hungarian Architects and Engineers*, 335-358.
- Jardine, R. J., Chow, F. C., Overy, R., & Standing, J. (2005). *ICP design methods for driven piles in sands and clays*. ICE Publishing. Retrieved from <http://app.knovel.com/hotlink/toc/id:kpICPDMDP1/icp-design-methods-driven/icp-design-methods-driven>
- Jardine, R. J., Lehane, B. M., & Everton, S. J. (1992). Friction coefficients for piles in sands and silts. *In Offshore site investigation and foundation behaviour*, (pp. 661–677). London.
- Khodair, Y., & Abdel-Mohti, A. (2014). Numerical analysis of pile–soil Interaction under axial and lateral loads. *International Journal of Concrete Structures and Materials*, 8(3), 239-249.
- Kim, S.-R., & Chung, S.-G. (2012). Equivalent head-down Load vs. movement relationships evaluated from bi-directional pile load tests. *KSCE Journal of Civil Engineering*, 1170-1177.

- Kishida, H. (1967). Ultimate bearing capacity of piles driven into loose sand. . *Soils and Foundations*, 7(3), 20-29.
- Ko, J., Jeong, S., & Lee, J. K. (2016). Large deformation FE analysis of driven steel pipe piles with soil plugging. *Computers and Geotechnics*, 71, 82-97.
- Kraft, L. M. (1991). Performance of axially loaded pipe piles in sand. *Journal of Geotechnical Engineering*, 117(2), 272-296.
- Kulhawy, F. (1984). Limiting tip and side resistance: Fact or fallacy? *ASCE Spec. Conf. on Analysis and Design of Pile Foundation*, (pp. 80-98).
- Kulhawy, F. H. (1991). Drilled shaft foundations. *Foundation Engineering Handbook* (pp. 537-552). Springer US.
- Kulhawy, H. (1995). Discussion of the critical depth – How it came into being and why it does not exist. *Civil Engineers, Geotechnical Engineering Journal*, 244-245.
- Kusakabe, O., & Kobayashi, S. (2010). Foundation. *Japanese Geotechnical Society*, 903-313.
- Ladd, R. S. (1978). Preparing test specimens using undercompaction. *ASTM Geotechnical Testing Journal*, 1(1), 16-23.
- Lambe, T. W., & Whitman, R. V. (1969). *Soil mechanics*. New York: John Wiley & Sons.
- Le Kouby, A., Dupla, J. C., Canou, J., & Francis, R. (2013). Pile response in sand: experimental development and study. *International Journal of Physical Modelling in Geotechnics*, 13(4), 122-137.
- Lee, J., Yun, T. S., Lee, D., & Lee, J. (2013). Assessment of K<sub>0</sub> Correlation to Strength for Granular Materials. *Soils and Foundations*, 53(4), 584-595.
- Lee, K. M., & Xiao, Z. R. (2001). A simplified nonlinear approach for pile group settlement analysis in multilayered soils. *Canadian Geotechnical Journal*, , 38(5), 1063-1080.

- Lehane, B. M., & Gavin, K. G. (2001). Base resistance of jacked pipe piles in sand. *Journal of Geotechnical and Geoenvironmental Engineering*, 127(6), 473-480.
- Lehane, B. M., Gaudin, C., & Schneider, J. A. (2005). Scale effects on tension capacity for rough piles buried in dense sand. *Géotechnique*, 55(10), 709-719.
- Lehane, B., Jardine, R., Bond, A., & Frank, R. (1993). Mechanisms of shaft friction in sand from instrumented pile tests. *Journal of Geotechnical Engineering*, 19-35.
- Lehane, B., Scheider, J. A., & Xu, X. (2005). CPT based design of driven piles in sand for offshore structures. *Internal Report No. GEO:05345*. Perth, Australia: University of Western Australia.
- Mansur, C. I., & Hunter, A. H. (1970). Pile tests - Arkansas river project. *Journal of Soil Mechanics and Foundations Division*, 96(SM5), 1545-1582.
- Mansur, C. I., & Kaufman, R. I. (1958). Pile tests, low-sill structure, Old River, Louisiana. *Transactions of the American Society of Civil Engineers*, 123(1), 715-743.
- Mayne, P. W. (1991). Tentative method for estimating  $\sigma_v'$  from qc data in sands. *In proceeding, 1st International Symp. on Calibration Chamber Testing*, (pp. 249-256). Elsevier, Potsdam, NY.
- Mayne, P. W., & Kulhawy, F. H. (1982). Ko-OCR relationships in soil. *Journal of the Geotechnical Engineering Division*, vol. 108, no. 6, pp. 851-872.
- Mazurkiewicz, B. K. (1972). *Test loading of piles according to Polish regulations*. Report No.35. Royal Swedish Academy of Engineering Sciences, Committee on Pile Research.
- Meyerhof, G. (1951). The ultimate bearing capacity of foundations. *Geotechnique*, 2(4), 301-332.
- Meyerhof, G. (1976). Bearing capacity and settlement of pile foundations. *Journal of the Geotechnical Engineering Division, ASCE, Vol. 102, No. GT3*, pp.195-228.

- Meyerhof, G. G., & Hanna, A. M. (1978). Ultimate bearing capacity of foundations on layered soils under inclined load. *Canadian Geotechnical Journal*, 15(4), 565-572.
- Murthy, V.N.S. (2002). *Geotechnical engineering: principles and practices of soil mechanics and foundation engineering*. CRC Press.
- NAVFAC (Naval Facilities Engineering Command). (1986). *Foundations and earth Structures*. Design Manual, 7.
- Niazi, F. S., & Mayne, P. W. (2013). Cone penetration test based direct methods for evaluating static axial capacity of single piles. *Geotechnical and Geological Engineering*, 31(4), 979-1009.
- Nouri, H., Fakher, A., & Jones, C. J. (2006). Development of horizontal slice method for seismic stability analysis of reinforced slopes and walls. *Geotextiles and Geomembranes*, 24(3), 175-187.
- Paik, K., Salgado, R., Lee, J., & Kim, B. (2003). Behavior of open-and closed-ended piles driven into sands. *Journal of Geotechnical and Geoenvironmental Engineering*, 129(4), 296-306.
- Potts, D. M., Zdravkovic, L., & Zdravković, L. (2001). *Finite element analysis in geotechnical engineering: application*. Thomas Telford.
- Potyondy, J. G. (1961). Skin friction between various soils and construction materials. *Geotechnique*, 11(4), 339-353.
- Poulos, H. G., & Davis, E. H. (1980). *Pile foundation analysis and design*. John Wiley and Sons.
- Prakash, S., & Sharma, H. D. (1990). *Pile foundations in engineering practice*. John Wiley & Sons.
- Rajakakse, R. (2008). *Geotechnical engineering calculations and rules of thumb*. Butterworth-Heinemann.

- Rakotonindriana, J., Le Kouby, A., Buttigieg, S., Derkx, F., Thorel, L., & Garnier, J. (2010). Design of an instrumented model pile for axial cyclic loading. *In 7th international Conference on Physical Modelling in Geotechnics*, (p. 991).
- Randolph, M. F., Dolwin, J., & Beck, R. (1994). Design of driven piles in sand. *Geotechnique*, 44(3), 427-48.
- Rankine, W. M. (1857). On the stability of loose earth. *Philosophical Transactions of the Royal Society of London*, 147, 9-27.
- Sabry, M. (2005). Insitu stresses and capacity of driven piles in sand. *PhD thesis*. Concordia University.
- Sedran, G., Stolle, D. F., & Horvath, R. G. (2001). An investigation of scaling and dimensional analysis of axially loaded piles. *Canadian geotechnical journal*, 38(3), 530-541.
- Shahgholi, M., Fakher, A., & Jones, C. J. (2001). Horizontal slice method of analysis. *Geotechnique*. 51(10), 881-885.
- Shalabi, F., & Bader, T. A. (2014, Jan). Effect of sand densification due to pile-driving on pile resistance. *International Journal of Civil Engineering (IJCE)*, Vol. 3(Issue 1), 17-30.
- Sivakugan, N., & Das, B. M. (2010). *Geotechnical engineering: a practical problem solving approach*. J. Ross Publishing.
- Skempton, A., Yassin, A., & Gibson, R. (1953). Theorie de la force portante des pieux. *In Annales de l'Institut Technique du Batiment et des Travaux Publics*, 6 (63-64), 285-290.
- Stas, C. V., & Kulhawy, F. H. (1984). *Critical evaluation of design methods for foundations under axial uplift and compression loading*. Electric Power Research Institute.
- Su, Q., Zhang, X., Yin, P., & Zhao, W. (2014). Ultimate capacity analysis and determination of the position of failure surface for uplift piles. *Mathematical Problems in Engineering*.

- Tavenas, F. A. (1971). Load tests results on friction piles in sand. *Canadian Geotechnical Journal*, 8(1), 7-22.
- Terzaghi, K. (1943). *Theoretical soil mechanics*. New York: Wiley.
- Terzaghi, K., Peck, R. B., & Mesri, G. (1996). *Soil Mechanics in Engineering Practice*. John Wiley & Sons.
- Tomlinson, M. J. (1986). *Foundation design and construction*. New York: John Wiley and Sons.
- Tomlinson, M., & Woodward, J. (2014). *Pile design and construction practice*. CRC Press.
- Toolan, F. E., Lings, M. L., & Mirza, U. A. (1990). An appraisal of API RP2A recommendations for determining skin friction of piles in sand. *In Offshore Technology Conference*. Offshore Technology Conference.
- Towhata, I. (2008). *Geotechnical earthquake engineering*. Springer Science & Business Media.
- Ulitskii, V. M. (1995). History of pile foundation engineering. *Soil Mechanics and Foundation Engineering*, 110-114.
- Vakili, R. (2015). *Load sharing mechanism of piled-raft foundation in sand*. PhD thesis, Concordia University.
- Vesic, A. S. (1964). Investigations of bearing capacity of piles in sand. *Proc. N. Am. Conf. on Deep Foundation*. Mexico City.
- Vesic, A. S. (1967). *A study of bearing capacity of deep foundations*. Final Report, Project B-189, Georgia Institute of Technology, Atlanta, Ga.
- Vesic, A. S. (1970). Tests on instrumented piles, Ogeechee River site. *Journal of Soil Mechanics & Foundations Div.*
- Vesic, A. S. (1973). Analysis of ultimate loads of shallow foundations. *Journal of the Soil Mechanics and Foundations Division, ASCE, 11 No. 11*, A230.

- Vesic, A. S. (1977). Design of pile foundations. *National Cooperative Highway Research Program Synthesis of Practice No. 42*, 32-48.
- White, D. J., & Lehane, B. M. (2004). Friction fatigue on displacement piles in sand. *Géotechnique*, 54(10), 645-658.
- Wrana, B. (2015). Pile load capacity - calculation methods. *Studia Geotechnica et Mechanica*, 37(4), 83-93.
- Wriggers, P. (1995). Finite element algorithms for contact problems. *Archives of Computational Methods in Engineering*, 4, 1-49.
- Wroth, C. P. (1973). General theories of earth pressure and deformation. *5th European Conf. on Soil Mechanics and Foundation Engineering*, 2, pp. 33–52. Madrid, Spain.
- Yang, Z., Jardine, R., Guo, W., & Chow, F. (2015). *A comprehensive database of tests on axially loaded piles driven in sand*. Academic Press.
- Zhan, Y. G., Wang, H., & Liu, F. C. (2012). Modeling vertical bearing capacity of pile foundation by using ABAQUS. *Electronic Journal of Geotechnical Engineering*, 17, 1855-1865.